Graduate Theses and Dissertations   Graduate School

2008

Mathematical modeling of polymer exchange membrane fuel cells

Colleen Spiegel
University of South Florida

Follow this and additional works at: http://scholarcommons.usf.edu/etd

Part of the American Studies Commons

Mathematical Modeling of

Polymer Exchange Membrane Fuel Cells

by

Colleen Spiegel

A dissertation submitted in partial fulfillment
of the requirements for the degree of
Doctor of Philosophy
Department of Electrical Engineering
College of Engineering
University of South Florida

Major Professor: Shekhar Bhansali, Ph.D.
Ken Buckle, Ph.D.
Lee Stefanakos, Ph.D.
Julie Harmon, Ph.D.
Yogi Goswami, Ph.D.

Date of Approval:
November 4, 2008

Keywords: PEM fuel cell, flow field, thermal model, microchannels

DEDICATION

To my husband, Brian, who inspires me to be a better person every day,
encourages me to pursue all of my dreams, and has the patience and endurance to stand
by me while I work at them.

To my son, Howard, who had to endure endless sleepless nights (in the womb and
out) while I was completing this dissertation.

ACKNOWLEDGMENTS

To my parents, Chris and Shirley, and my in-laws, Mark and Susan (pseudo parents), for helping to watch Howard while I completed this dissertation.

To Dr. Bhansali, who encouraged me to pursue my passion. Thank you for encouraging me to stick with the topic that I am most passionate about.

TABLE OF CONTENTS

LIST OF TABLES

viii

LIST OF FIGURES

xiii

MATHEMATICAL MODELING OF
POLYMER EXCHANGE MEMBRANE FUEL CELLS

Colleen Spiegel

ABSTRACT

Fuel cells are predicted to be the power delivery devices of the future. They have many advantages such as the wide fuel selection, high energy density, high efficiency and an inherent safety which explains the immense interest in this power source. The need for advanced designs has been limited by the lack of understanding of the transport processes inside the fuel cell stack. The reactant gases undergo many processes in a fuel cell that cannot be observed. Some of these processes include convective and diffusional mass transport through various types of materials, phase change and chemical reaction. In order to optimize these variables, an accurate mathematical model can provide a valuable tool to gain insight into the processes that are occurring.

The goal of this dissertation is to develop a mathematical model for polymer electrolyte-based fuel cells to help contribute to a better understanding of fuel cell mass, heat and charge transport phenomena, to ultimately design more efficient fuel cells. The model is a two-phase, transient mathematical model created with MATLAB. The model was created by using each fuel cell layer as a control volume. In addition, each fuel cell layer was further divided into the number of nodes that the user inputs into the model. Transient heat and mass transfer equations were created for each node. The catalyst

layers were modeled using porous electrode equations and the Butler-Volmer equation. The membrane model used Fick's law of diffusion and a set of empirical relations for water uptake and conductivity. Additional work performed for this dissertation includes a mathematical model for predicting bolt torque, and the design and fabrication of four fuel cell stacks ranging in size from macro to micro scale for model validation. The work performed in this dissertation will help improve the designs of polymer electrolyte fuel cells, and other polymer membrane-based fuel cells (such as direct methanol fuel cells) in the future.

1
INTRODUCTION

Energy is a vital part of modern society, enabling life after dark, the movement of people and goods, and the continuous advancement of technology. Available conventional energy sources, such as crude oil and natural gas, have been used to serve the growth of the population for stationary and transportation purposes. However, the use of fossil fuels for power has resulted in many negative consequences; some of these include severe pollution, extensive mining of the world's resources, and political control and domination of countries that have extensive resources. All the while, the global demand for power will increase rapidly due to the large growth in global population. In addition, there is approximately 30 years left of fossil fuels to provide energy for transportation and stationary applications. A power source is needed that is energy efficient, has low pollutant emissions and has an unlimited supply of fuel.

There are many types of renewable energy technologies that have been researched for several decades; some of these include hydro, wind, solar, tidal and biofuels. However, conventional energy sources like petroleum-based products have not been replaced because these alternatives have lower reliability, low concentration and costly implementation. For example, wind energy may be only available in certain geographical locations, and may not be uniform or steady. Solar has enormous potential to be a major local energy source; nevertheless, the photovoltaic arrays can be costly due to the competing cost of polysilicon with electronic manufacturers.

In spite of these challenges, there is a growing interest in renewable energy worldwide. Many of these sources can be replenished continuously, which enhances the security of the energy supplies. There is also an increasing concern for the environment that makes many of these alternative energy options attractive. These factors have increased the research and development for seeking new power sources and energy technologies around the world.

Hydrogen is a clean fuel, and in principal, can be produced abundantly and safely. It can be created from many types of energy sources, unlike gasoline, which can only be refined from crude oil. Although hydrogen has less volumetric energy density than gasoline, the energy density can be increased by storing it in pressurized tanks, or in liquid or solid forms. Hydrogen can also be used like gasoline, directly in an internal combustion engine. In comparison, fuel cell technology can be used to directly create electrical energy.

Fuel cells are now closer to commercialization than ever, and they have the ability to fulfill all of the global power needs while meeting the efficiency and environmental expectations thereof. Of the many types of fuel cells, the type most commonly used for transportation and portable applications is polymer electrolyte membrane (PEM) fuel cells. PEM-type fuel cells traditionally use hydrogen as the fuel, but also have the ability to use many types of fuel – these range from hydrogen to ethanol to biomass-derived materials. These fuels can either be directly fed into the fuel cell, or sent to a reformer to extract pure hydrogen, which is then directly fed to the fuel cell. PEM fuel cells operate at temperatures between 20º and 80 º C, which enable a startup time comparable with the internal combustion engine. PEM fuel cells are able to obtain net power densities of over

1 kW/liter, which makes them competitive with the internal combustion engine for transportation applications [1]. There are numerous advantages and challenges for PEM fuel cells. Some advantages include:

1. Fuel cells have the potential for a high operating efficiency.

2. There are many types of fuel sources and methods of supplying fuel to a fuel cell.

3. Fuel cells have a highly scalable design.

4. Fuel cells produce no pollutants.

5. Fuel cells are low maintenance because they have no moving parts.

6. Fuel cells do not need to be recharged, and they provide power instantly when supplied with fuel.

Some limitations common to all fuel cell systems include the following:

1. Fuel cells are costly due to the need for materials with very specific properties. There is an issue with finding low-cost replacements.

2. Fuel reformation technology can be expensive, heavy and requires power in order to run.

3. If another fuel besides hydrogen is fed into the fuel cell, the performance gradually decreases over time due to catalyst degradation and electrolyte poisoning.

Mathematical modeling studies can aid in overcoming these challenges. Since fuel cells are very small, and many of the layers have thicknesses in the micron range, local values of significant properties such as concentration, pressure and current density cannot be directly measured. The creation of mathematical models can help supply

information about the processes that are occurring inside of the fuel cell. In addition, mathematical models can help to eliminate unnecessary time-consuming experimental investigations due to a better understanding of the phenomena that occur inside the cell. This understanding leads to better designs and optimized operating conditions. In practice, it is essential to combine experimental prototyping with simulations to achieve the optimal design cycle.

1.1 Background Information

Typical fuel cells operate at a voltage ranging from 0.6 – 0.8 V, and produce a current per active area (current density) of 0.2 to 1 A/cm^2. A fuel cell consists of a negatively charged electrode (anode), a positively charged electrode (cathode), and an electrolyte membrane. Hydrogen is oxidized on the anode and oxygen is reduced on the cathode. Protons are transported from the anode to the cathode through the electrolyte membrane, and the electrons are carried to the cathode over the external circuit. The electrons are transported through conductive materials to travel to the load when needed. On the cathode-side, oxygen reacts with protons and electrons forming water and producing heat. Both, the anode and cathode, contain a catalyst to create electricity from the electrochemical process as shown in Figure 1.1.
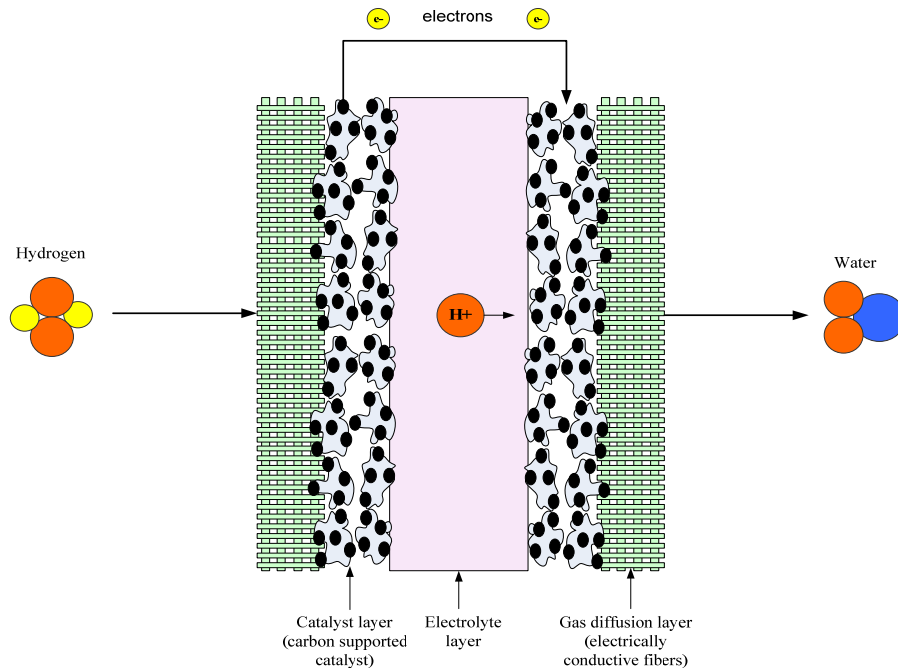
Figure 1.1. A single PEM fuel cell [2]

The conversion of the chemical energy of the reactants to electrical energy, heat and liquid water occurs in the catalyst layers, which have a thickness in the range of 5 to 30 microns (μm). A typical PEM fuel cell has the following reactions:

Anode: H_2 (g) $\rightarrow$ 2H^+ (aq) + 2e^- (1)

Cathode: ½ O_2 (g) + 2H^+ (aq) + 2e^- $\rightarrow$ H_2O (2)

Overall: H_2 (g) + ½ O_2 (g) $\rightarrow$ H_2O (l) + electric energy + waste heat (3)
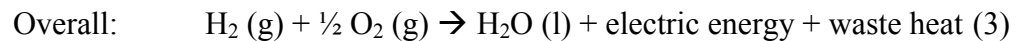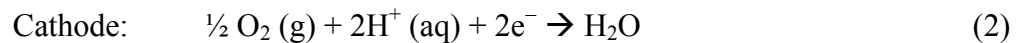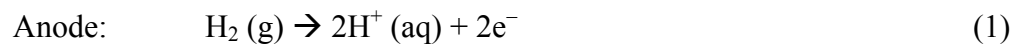
Reactants are transported by diffusion and convection to the catalyzed electrode surfaces where the electrochemical reactions take place. The water and waste heat generated by the fuel cell must be continuously removed, and may present critical issues for PEM fuel cells.

Since most applications have voltage or power requirements that cannot be satisfied by a single cell, many cells are connected in series to make a fuel cell stack. These repeating cells are separated by flow field plates. Increasing the number of cells in the stack increases the voltage, while increasing the surface area of the cells increases the current. A PEM fuel cell stack is made up of bipolar plates, membrane electrode assemblies (MEA), and end plates as shown in Figure 1.2.
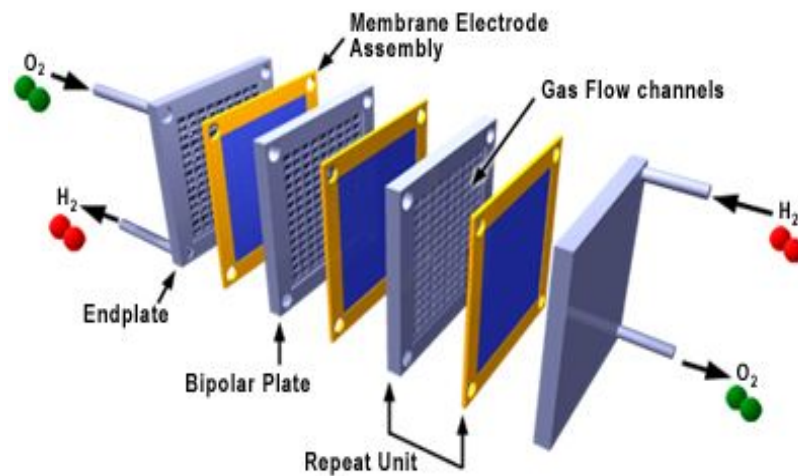
Figure 1.2. An exploded view of a polymer electrolyte membrane fuel cell stack [3]

The bipolar plates are constructed of graphite or metal, and they simultaneously distribute gases through flow channels to the MEA while transporting electrons to the load. The gas flow channels allow the anode and cathode reactants to enter the MEA, where the electrochemical reactions occur. Therefore, the active area of the fuel cell is normal to the y-direction. The MEA typically has a thickness of $500 - 600$ μm, and consists of five layers: the proton exchange membrane, the anode and cathode catalyst layers and the anode and cathode gas diffusion layers. The components in the fuel cell

stack are summarized in more detail in Table 1.1. Sections 1.2 through 1.6 describe the

PEM components, stack, operating conditions and basic testing in more detail.

Table 1.1

Basic PEM fuel cell components

Component	Description	Common Types
Proton Exchange Membrane	Enables hydrogen protons to travel from the anode to the cathode.	Nafion membrane 112, 115, 117
Catalyst Layers	Breaks the fuel into protons and electrons. The protons combine with the oxidant to form water at the fuel cell cathode. The electrons travel to the load.	Platinum/carbon catalyst.
Gas Diffusion layers	Allows fuel/oxidant to travel through the porous layer, while collecting electrons.	Carbon cloth or Toray paper.
Flow Field Plates	Distributes the fuel and oxidant to the gas diffusion layer.	Graphite, stainless steel.
Gaskets	Prevent fuel leakage, and helps to distribute pressure evenly.	Silicon, Teflon
End plates	Holds stack layers in place.	Stainless steel, graphite, polyethylene, PVC

1.1.1 Polymer Exchange Membrane

The polymer electrolyte membrane is essential for a PEM fuel cell to work properly. When fuel enters the fuel cell stack, it travels to the catalyst layer where it gets broken into protons (H^+) and electrons. The electrons travel to the external circuit to power the load, and the hydrogen protons travel through the electrolyte until they reach the cathode to combine with oxygen to form water. The PEMFC electrolyte must meet the following requirements in order for the fuel cell to work properly:

1. High ionic conductivity

2. Present an adequate barrier to the reactants

3. Be chemically and mechanically stable

4. Low electronic conductivity

5. Ease of manufacturability/availability

6. Preferably low-cost

The membrane layer contains the solid polymer membrane, liquid water, water vapor and trace amounts of H_2, O_2, or CO_2 depending upon the purity of the H_2 coming into the system.

1.1.2 Gas Diffusion Layer

The gas diffusion layers (GDL) are between the catalyst layer and the bipolar plates in the fuel cell stack. They provide electrical contact between electrodes and the bipolar plates, and distribute reactants to the catalyst layers. The layers also allow reaction product water to exit the electrode surface and permit the passage of water

between the electrodes and the flow channels. The gas diffusion layers provide five functions for a PEM fuel cell:

1. Electronic conductivity
2. Mechanical support for the proton exchange membrane
3. Porous media for the catalyst to adhere to
4. Reactant access to the catalyst layers
5. Product removal.

The diffusion layer is made of electrically conductive porous materials such as carbon or Toray paper. The thickness of the diffusion layer is usually 0.25 – 0.40 mm. The conductivity of the paper can be improved by filling it with electrically conductive powder, such as carbon black. To help remove water from the pores of the carbon paper, the diffusion layer can be treated with PTFE. Some fuel cell developers forgo the diffusion layer altogether, and platinum is sputtered directly on the proton exchange structure.

1.1.3 Catalyst Layer

The fuel cell catalyst layers are where the electrochemical reactions occur. As mentioned previously, at the anode catalyst layer, the hydrogen is broken into protons and electrons. At the cathode catalyst layer, oxygen combines with the protons to form water. The catalyst layer should have a high surface area, and preferably be low cost. These catalyst layers are often the thinnest in the fuel cell (5 to 30 μm), but are often the most complex due to multiple phases, porosity, and electrochemical reactions. It is a

challenge to find a low-cost catalyst that is effective at creating electricity from the electrochemical reactions.

The catalyst layers are usually made of a porous mixture of carbon supported platinum or platinum/ruthenium. In order to catalyze reactions, catalyst particles must have contact with the protonic and electric conductors. There also must be passages for reactants to reach catalyst sites and for reaction products to exit. The contacting point of the reactants, catalyst, and electrolyte is conventionally referred to as the three-phase interface. In order to achieve acceptable reaction rates, the effective area of active catalyst sites must be several times higher than the geometrical area of the electrode. Therefore, the electrodes are made porous to form a three-dimensional network, in which the three-phase interfaces are located.

The reactions in the catalyst layers are exothermic; therefore, heat must be transported out of the cell. The heat can be removed through the convection in the flow channels, and conduction in the solid portion of the catalyst layers, gas diffusion media and bipolar plates. Since liquid water is produced by the PEM fuel cell, the condensation and evaporation of water affects the heat transfer in a PEM fuel cell. Therefore, the water and heat management in the fuel cell are closely linked.

1.1.4 Bipolar Plates

After the membrane electrode assembly (MEA) has been pulled together, the cell(s) must be placed in a fuel cell stack to evenly distribute fuel and oxidant to the cells, and collect the current to power the desired devices. In a fuel cell with a single cell, there

are no bipolar plates (only single-sided flow field plates). Yet, in fuel cells with more

than one cell, there is usually at least one bipolar plate (flow fields exist on both sides of

the plate). Bipolar plates perform many roles in fuel cells. They distribute fuel and

oxidant within the cell, separate the individual cells in the stack, collect the current, carry

water away from each cell, humidify gases, and keep the cells cool. Bipolar plates also

have reactant flow channels on both sides, forming the anode and cathode compartments

of the unit cells on the opposing sides of the bipolar plate. In order to simultaneously

perform these functions, specific plate materials and designs are used. Commonly used

designs can include straight, serpentine, parallel, interdigitated or pin-type flow fields.

Materials are chosen based upon chemical compatibility, resistance to corrosion, cost,

density, electronic conductivity, gas diffusivity/impermeability, manufacturability, stack

volume/kW, material strength, and thermal conductivity. The materials most often used

are stainless steel, titanium, nonporous graphite, and doped polymers. Several composite

materials have been researched and are beginning to be mass produced.

1.1.4.1 Flow Field Designs

In fuel cells, the flow field should be designed to minimize pressure drop, while

providing adequate and evenly distributed mass transfer through the gas diffusion layer to

the catalyst surface for reaction. The three most popular channel configurations for PEM

fuel cells are serpentine, parallel, and interdigitated flow, which are shown in Figures 1.3

through 1.6. The serpentine flow path is continuous from start to finish. An advantage of

the serpentine flow path is that it reaches the entire active area of the electrode by

eliminating areas of stagnant flow. A disadvantage of serpentine flow is the fact that the

11

reactant is depleted through the length of the channel, so that an adequate amount of the gas must be provided to avoid excessive polarization losses. For high current density operation, very large plates, or when air is used as an oxidant, alternate designs have been proposed based upon the serpentine design.
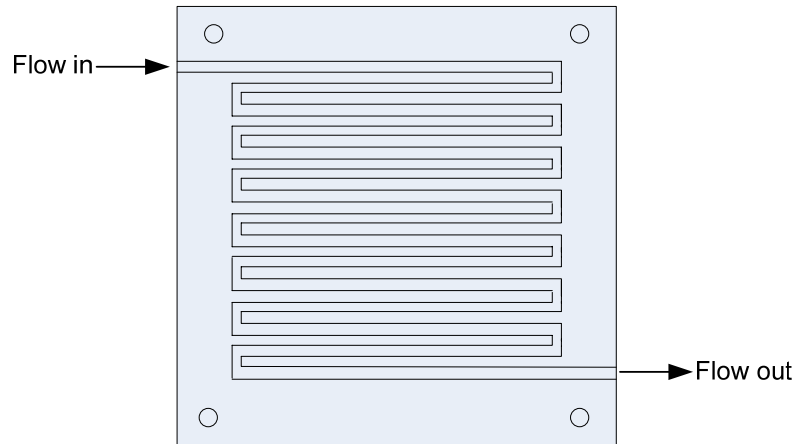
Figure 1.3. A serpentine flow field design [2]
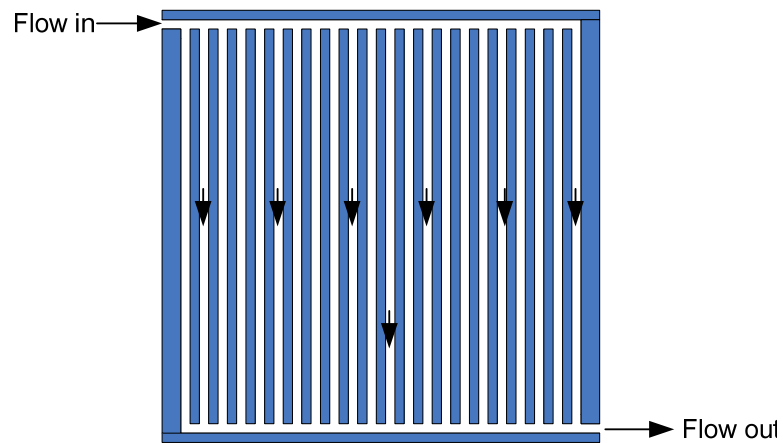
Figure 1.4. A parallel flow field design [2]

Several continuous flow channels can be used to limit the pressure drop and reduce the amount of power used for pressurizing the air through a single serpentine channel. This design allows no stagnant area formation at the cathode surface due to water accumulation. The reactant pressure drop through the channels is less than the serpentine channel, but still an important parameter to consider.

Flow out

Flow in
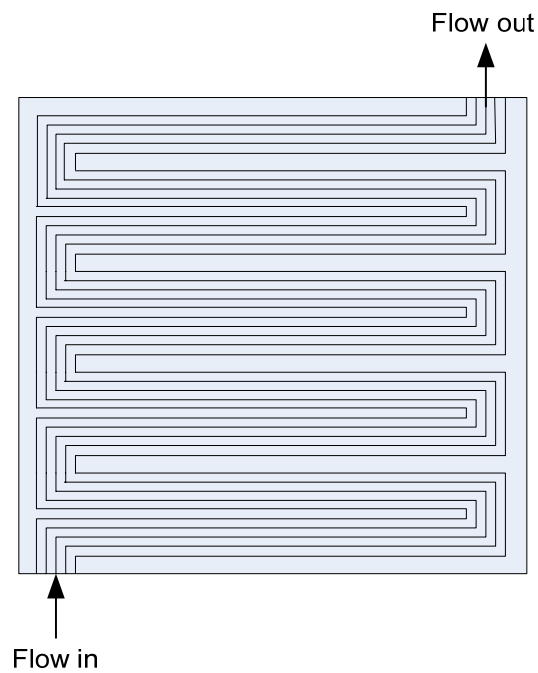
Figure 1.5. Multiple serpentine flow channel design [2]

The reactant flow for the interdigitated flow field design is parallel to the electrode surface. Often, the flow channels are not continuous from the plate inlet to the plate outlet. The flow channels are dead-ended, which forces the reactant flow, under pressure, to go through the porous reactant layer to reach the flow channels connected to

the stack manifold. This design can remove water effectively from the electrode structure, which prevents flooding and enhances performance. The interdigitated flow field enables the gas to be pushed into the active layer of the electrodes where forced convection avoids flooding and gas diffusion limitations. This design is sometimes noted in the literature as outperforming conventional flow field designs, especially on the cathode side of the fuel cell. The interdigitated design is shown in Figure 1.6.
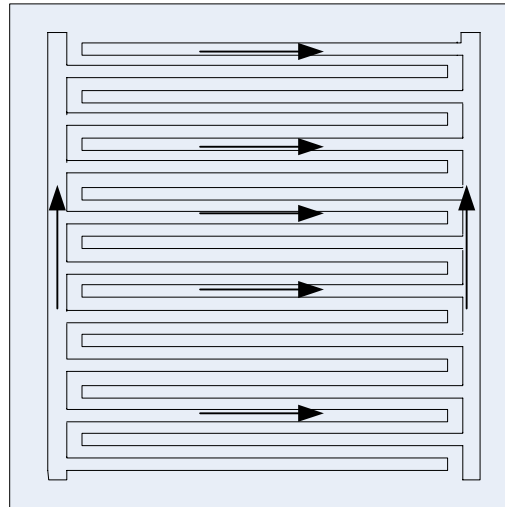
Figure 1.6. Interdigitated flow channel design [2]

1.1.5 Stack Design and Configuration

In the traditional bipolar stack design, the fuel cell stack has many cells in series, and the cathode of one cell is connected to the anode of the next cell. The MEAs, gaskets, bipolar plates and end plates are the typical layers of the fuel cell. The stack is clamped by bolts, rods, or another pressure device to clamp the cells together. For an efficient fuel

cell design, the following should be considered:

1. Fuel and oxidant should be uniformly distributed through each cell, and
    across their surface area.

2. The temperature must be uniform throughout the stack.

3. The membrane must not dry out or become flooded with water.

4. The resistive losses should be kept to a minimum.

5. The stack must be properly sealed to ensure no gas leakage.

6. The stack must be sturdy and able to withstand the necessary
    environments it will be used in.

The most common fuel cell configuration is shown in Figure 1.7. Each cell (MEA) is separated by a plate with flow fields to distribute the fuel and oxidant. The majority of fuel cell stacks are of this configuration regardless of fuel cell size, type or fuel used.
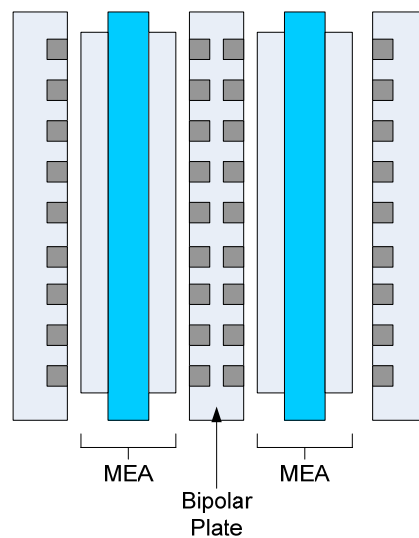
Figure 1.7. Typical fuel cell stack configuration (a two-cell stack) [2]

Fuel cell performance is dependent upon the flow rate of the reactants. Uneven

flow distribution can result in uneven performance between cells. Reactant gases need to

be supplied to all cells in the same stack through common manifolds. Some stacks rely on

external manifolds, while others use an internal manifold system. One advantage of an

external manifold is its simplicity, which allows a low pressure drop in the manifold, and

permits good flow distribution between cells. A disadvantage is that the gas may flow in

cross flow, which can cause uneven temperature distribution over the electrodes and gas

leakage. One, of the most common methods, is ducts formed by the holes in the separator

plates that are aligned once the stack is assembled. An example of this type of manifold is

shown in Figure 1.8.
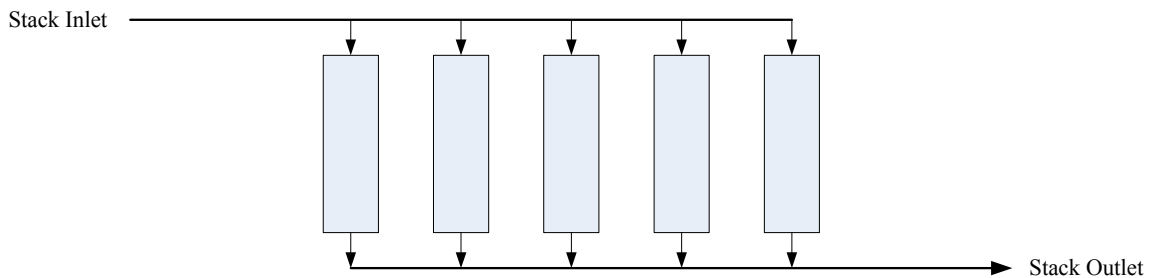
Figure 1.8. A Z-type manifold [4]

1.1.6 Operating Conditions

There is a wide range of operating conditions that can be used for PEM fuel cells.

The range of operating conditions and the optimal conditions are summarized in Table

1.2. The fuel cell performance is determined by the pressure, temperature, and humidity

based upon the application requirements, and can often be improved (depending upon

16

fuel cell type) by increasing the temperature, pressure, humidity and optimizing other

important fuel cell variables. The ability to increase these variables is application-

dependent, since system issues, weight and cost play important factors when optimizing

certain parameters.

Table 1.2

Operating conditions of PEMFCs in literature

Operating Parameter	Range of Conditions	Optimal Conditions
Temperature	20°– 90 °C	60°– 80°C
Pressure	1 – 3 atm	2 – 3 atm
Humidity	50 – 100 % RH	100 % RH
Oxidant	Air or O_2	O_2

The range of temperatures in the literature for PEM fuel cells are 20° – 90 °C, and

it is well known that higher temperatures result in better fuel cell performance. The

polymer membrane that is used for the majority of PEMFCs limits the upper temperature

to below the glass transition temperature of the polymer. In addition, proton conductivity

of the membrane is affected by the water content in the membrane; therefore, the

temperature is also limited by the amount of liquid water content in the membrane.

However, it may not be advantageous for the fuel cell system design to require high

operating temperatures. The pressure range for most PEMFCs in literature is from 1 – 3

atm. Fuel cells that operate at 3 atm require additional equipment to regulate and monitor

the pressure. Consequently, it may not be advantageous to run the fuel cell system above

ambient pressure. The relative humidity should be monitored since it changes daily under

ambient conditions. The humidity, pressure, temperature, and hydrogen and oxidant flow

rates should all be monitored and controlled depending upon ambient conditions and

system requirements.

1.1.7 Polarization Curves

The traditional measure of characterizing a fuel cell is through a polarization

curve – which is a plot of cell potential versus current density. This I-V curve is the most

common method for characterizing and comparing fuel cell efficiency to other published

data. The polarization curve illustrates the voltage-current relationship based upon

operating conditions such as temperature, humidity, applied load, and fuel/oxidant flow

rates. Figure 1.9 shows a typical polarization curve for a single PEM fuel cell, and the

regions of importance.
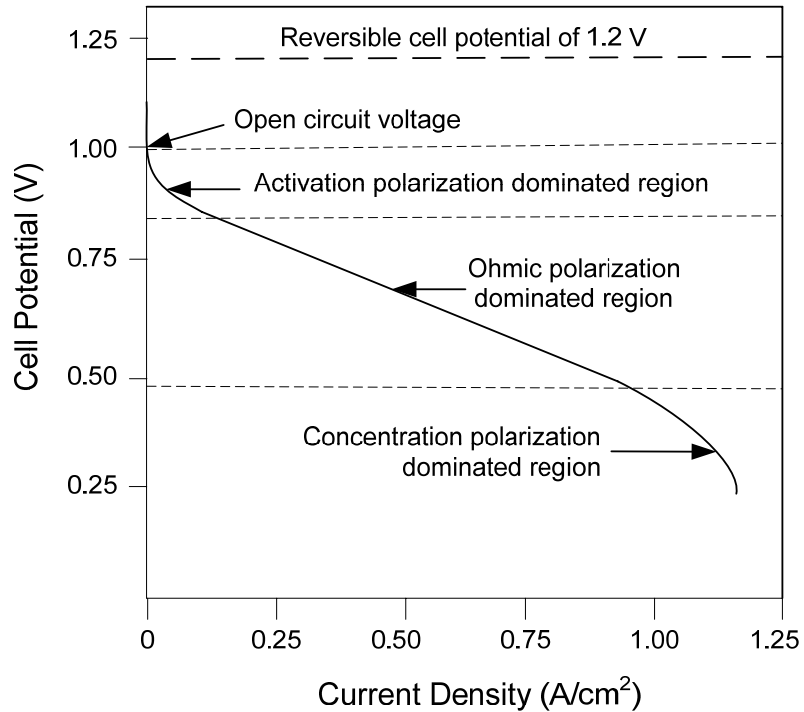
Figure 1.9. Example of a PEMFC polarization curve [4]

As shown in Figure 1.9, the polarization curve can be divided into three regions:

1. the activation overpotential region,

2. the ohmic overpotential region, and

3. the concentration overpotential region.

In the activation overpotential region, voltage losses occur when the electrochemical reactions are slow in being driven from equilibrium to produce current. The reduction of oxygen is the electrochemical reaction that is responsible for most of the activation overpotential. As the PEM fuel cell produces more current, the activation losses increase at a slower rate than the ohmic losses. The ohmic overpotential is due to the resistance of the transport of charged species in the polymer electrolyte membrane, catalyst and gas diffusion layers and bipolar plates.

19

The concentration overpotential is due to mass transport limitations; the rates of the electrochemical reactions within the catalyst layers are hindered by a lack of reactants. The mass transport limitations are due to both diffusional limitations in the electrode backing layer and water flooding in the cathode catalyst layer. At high current densities, the amount of liquid water produced in the cathode catalyst layer becomes greater than the amount of water that can be removed from the flow in the gas channels.

1.2 Previous Modeling Approaches

Mathematical models provide detailed information about the processes occurring within the fuel cell. The processes include mass, momentum, species, energy and charge transport, and can be described mathematically by using the control volume approach commonly used in engineering sciences. The model developed in this dissertation provides a good balance between micro-scale and macro-scale models. In micro-scale models, transport phenomena is commonly modeled at the molecular level, and macro-scale models look at the overall system complexity to predict certain variables, without considering the molecular effects. Many of the micro-scale models (such as the interactions between the ion, water and polymer molecules) are impractical for the entire PEM fuel cell stack since the number of computations required creates long computation times. Therefore, the mathematical models reviewed in this chapter are macro-scale models. Many of the molecular interactions have been simplified, for example, using diffusion coefficients to represent the interactions between molecules. There are two main classifications of macro-scale mathematical models: (1) An MEA centered approach, and (2) an along-the-channel approach.

The MEA-centered approach considers the membrane to be the most important aspect of the fuel cell, and models this layer in detail, while making simplifying assumptions for the other layers. The along-the-channel model concentrates on modeling the flow channels coupled with the processes that occur within the MEA. This approach uses many of the same equations as the membrane-centered approach it is based upon.

1.2.1 MEA-Centered Approach

Most of the modeling efforts that use the MEA-centered approach are variations or combinations of the two original models: the models of Bernardi and Verbrugge [5, 6] and Springer et al. [7, 8]. Both of these models made steady-state and isothermal assumptions. The species transport was assumed to be one-dimensional through the MEA, and transport in the gas channels was one-dimensional along the channel.

In the channel portion of the model of Bernardi and Verbrugge [5, 6], no pressure drop was assumed, and the species transport was through convection only. The electrode layers assumed no pressure drop, and the species transport was through diffusion only. The Stefan-Maxwell equations were used to describe the diffusive fluxes, and the conservation of momentum equation was written as Darcy's law. Charge transport was modeled using Ohm's law. The polymer electrolyte layer consisted of a porous network of channels, and was assumed to be fully hydrated. The ion transport was governed by the Nernst-Plank equation, and the liquid water transport was described by Schlogl's equation. The catalyst layers were considered to be porous media, with the diffusion of the reactant gases characterized by Fick's law. The oxidation of hydrogen in the anode

21

catalyst layer, and the reduction of oxygen in the cathode catalyst layer, were modeled using the Butler-Volmer equation.

Bernardi and Verbrugge [5, 6] assumed that the water and charge transport in the polymer electrolyte membrane was constant. However, the water content in a fuel cell membrane is not constant during the production of current. In addition, the protonic conductivity is highly dependent upon water content.

The other pioneering fuel cell model is by Springer et al [7], which included the modeling of variable membrane hydration. A semi-empirical governing equation is used, which consists of a Fickian equation combined with an osmotic drag coefficient. The diffusional velocity depends upon a potential gradient, and is a function of membrane hydration. The water diffusion coefficient, electroosmotic coefficient and the electrical conductivity are all dependent upon membrane hydration, which was found to be a function of the relative humidity of the gases. The gas flow channels and the gas diffusion media were modeled in a similar manner as the Bernardi and Verbrugge [5, 6] models. However, the modeling of the catalyst layers was simplified, and the electrochemical reactions were assumed to occur at the catalyst/gas diffusion media interface.

Most other fuel cell models in the literature are based upon the Bernardi and Verbrugge [5, 6] and Springer et al. [7, 8] approaches. The Bernardi and Verbrugge [5, 6] used an oxygen reduction rate constant for the exchange current density several times larger than the experimental value in order to obtain agreement with the experimental data. Weisbrod et al. [9] combined the detailed catalyst layer model of Bernardi and Verbrugge [5, 6] with the variable hydration membrane model of Springer et al. [7, 8].

Gloaguen and Durand [10] were able to improve this by assuming that the catalyst layer consists of a solid matrix with void space occupied by reactant gas. Eikerling and Kornyshev [11] modeled the cathode catalyst layer with high and low overpotentials, and developed solutions for poor electrical conductivity and poor oxygen transport.

Marr and Li [12] used the membrane model of Bernardi and Verbrugge [5, 6], and improved the gas flow channel and catalyst layer formulations. The pressure in the flow channels was allowed to vary with the assumption of one-dimensional pipe flow. The average concentration going to the gas diffusion media was assumed to differ from the average concentrations in the bulk flow of the channel. The average concentrations at the interface were calculated using a log mean concentration relationship. Marr and Li [12] also used the basic catalyst layer model of Bernardi and Verbrugge [5, 6], but occupied the void space of the catalyst layer with polymer electrolyte and liquid water.

Baschuk and Li [13] allowed the void space to be occupied by gaseous reactants, liquid water, and polymer electrolyte by varying a parameter called the degree of water flooding to simulate the concentration overpotential region of the polarization curve. Two- phase flow was added to the model by Pisani et al. [14]. This model used the liquid water governed by Darcy's law. The permeability of the electrode backing and catalyst layers was dependent upon the liquid water saturation.

Heat transfer in PEM fuel cells is of interest since heat is produced due to the exothermic reaction in the catalyst layers. In addition, the water management of a PEM fuel cell is coupled with the thermal management. In order to model the heat transfer in a PEM fuel cell, the conservation of energy must be applied to the fuel cell. The model of Bevers et al. [15] and Wohr et al. [16] included mass, species, momentum and energy

transport in the gas diffusion, catalyst and membrane layers. Although the temperature was allowed to vary within the fuel cell, the temperature of the gases/fluid in the solid and void space were assumed to be equal. The Dusty Gas model was used to describe the mass, momentum and species transport for the reactants in the gas diffusion and catalyst layers. The flow of the gaseous reactants and liquid water were coupled with porosity, since the presence of liquid water decreases the available pore volume. The electrochemical reactions were modeled using the Butler-Volmer equation and heat generation due to entropy changes and charge transfer resistance, or reversible and irreversible heat generation, were included. The transfer of water and protons in the polymer electrolyte layer was modeled with the Stefan-Maxwell equation.

A non-isothermal model was also developed by Rowe and Li [16], and was similar to the models developed by Bevers et al. [15] and Wohr et al. [17] in that the gas/fluid and solid temperatures were assumed to be equal. However, this model also included mass and species transport in a similar manner to the Bernardi and Verbrugge [5, 6] models.

In the one-dimensional models described thus far, the gas flow in the channels and gas diffusion media was solved separately, and the water produced in the PEM fuel cell was removed by the flow channels. Reactant depletion along the channels also affects the electrochemical reactions in the catalyst layers. Fuller and Newman [18] modeled this interaction between the gas flow channels and the MEA. The variation in temperature and reactant concentration was integrated along the gas flow channel, and combined with the MEA model. The Fuller and Newman [18] model assumed no pressure drop, and the species transport in the gas diffusion and catalyst layers was assumed to be through

24

diffusion only. However, this model differed from both Bernardi and Verbrugge [5, 6] and Springer et al. [7, 8] in modeling transport in the polymer electrolyte. Concentration solution theory was used to model the water and proton transport. The conservation of energy was applied by assuming that sections of the MEA were of uniform temperature, and the temperature was varied along the flow direction of the gas flow channel.

Nguyen and White [19] also developed a quasi- two-dimensional, PEM fuel cell model. This model was similar to Nguyen and White [19] except that the polymer electrolyte membrane layer was modeled using the variable hydration model of Springer et al. [7, 8], and the catalyst layer was considered to be an interface.

Thirumalai and White [20] added pressure drop to the model assuming that gas flow channels could be modeled as a pipe network. Yi and Nguyen [21] further developed the model by allowing the bipolar plate, MEA and the gas flow within the channels to have different temperatures. van Bussel et al. [22] developed a transient, quasi-two-dimensional model, based on the one-dimensional model of Springer et al. [7, 8] .

Another method of modeling the MEA with the gas flow channels is to model the MEA in a multi-dimensional manner, and simulate variations along the channel as boundary conditions. Singh et al. [23] developed a two-dimensional model using the same approach as Bernardi and Verbrugge [5, 6]. Kazim et al. [24] applied the conservation of mass, momentum and species for modeling the cathode backing layer. The catalyst layer was assumed to be an interface, and the conservation of momentum was expressed in the form of Darcy's law. Bradean et al. [25] extended this model by including the conservation of energy.

Two phase flow has also been modeled using a quasi-two-dimensional approach. He et al. [26] modeled the cathode backing layer of a PEM fuel cell with the catalyst layer is considered to be a surface, and the effect of the gas flow channels were included as a boundary condition. The conservation of mass, momentum, and species were applied to both the liquid and the gas phases and then solved separately. The conservation of momentum was expressed by Darcy's law for the liquid and gas phase. The definition of capillary pressure was used so that the liquid phase velocity was proportional to the gas phase velocity and the gradient of saturation. The mass transport between the liquid and gas phases was expressed by an interfacial source term that was proportional to the water vapor partial pressure and the liquid water saturation pressure.

Natarajan and Nguyen [27] also developed a two-phase, two-dimensional model of the cathode electrode backing layer, which was extended to a quasi-three-dimensional model in Natarajan and Nguyen [28]. The gas flow in the channels was incorporating by assuming it was one dimensional along the flow direction. This was used as boundary conditions for the 2-D analysis.

1.2.2 Channel-Centered Approach

Since the MEA-centered approach does not solve the Navier-Stokes equations, the transport in the gas flow channels cannot be fully coupled with the MEA processes. Therefore, the channel-centered approach was initiated by three research groups: the University of Miami, Pennsylvania State University, and the University of South Carolina. In the channel-centered approach, the governing equations for the entire fuel cell are discretized with the finite volume method.

26

The channel-centered approach started with the model of Gurau et al. [29] at the University of Miami. The Gurau et al. [29] model was a single-phase, two-dimensional model that included the gas flow channels, electrode backing layers, catalyst layers, and polymer electrolyte membrane layer. The model was united since the equations representing the conservation of mass, momentum, species, and energy in each layer had the same general form, and differed through the source terms. Schlogl's equation was used to model the transport of liquid water for the polymer electrolyte membrane, and this model was similar to the model of Bernardi and Verbrugge [5, 6]. The gas diffusion media was modeled using a generalized Darcy's equation, and the catalyst layer was assumed to consist of a solid matrix with void space filed with the polymer electrolyte membrane. Ohm's law was used to model the current flow, and the electrical conductivity in the membrane was allowed to vary with membrane hydration using the model of Springer et al. [7, 8]. Fick's law was used to mode the diffusional flux of each species. Zhou and Liu [30] extended the two-dimensional model of Gurau et al. [28] into three-dimensions, while You and Liu [31] developed a two-phase, isothermal, two-dimensional model of the cathode gas flow channels, electrode backing layer and catalyst layer.

The channel-centered approach at the University of South Carolina started with a three-dimensional, single-phase model. The commercial CFD software FLUENT was used to create the model which included the conservation of mass, momentum, and species for the gas flow channels, gas diffusion media, catalyst layers and the polymer electrolyte membrane. The model of Springer et al. [6, 7] was used to model the water and current transport in the polymer electrolyte membrane layer, and Fick's law was used

to describe the diffusional flux. The catalyst and polymer electrolyte membrane layers were modeled as surfaces since the water transport, current flow and reaction rate was not allowed to vary. Shimpalee and Dutta [32] added the conservation of energy, and then time dependence in Shimpalee et al. [33, 34]. Two-phases were added to the three dimensional model in Shimpalee et al. [35], and the interfacial mass transfer rate was proportional to the difference between the water vapor partial pressure and the saturation pressure.

The Pennsylvania State University research group began their channel-centered approach with a two-phase, two-dimensional model of the cathode flow channel and diffusion media. The catalyst layer was treated as a surface, and modeled with a boundary condition. The conservation of mass, momentum, and species were applied to both the gas and liquid phases, and then added together. Darcy's law was used for the conservation of momentum in the cathode electrode backing layer, and the velocity of the liquid water was found to be a function of the capillary pressure and gravitational body force. The capillary pressure was a function of the saturation of the liquid water in the electrode backing void space.

Um et al. [36] presented a single phase, isothermal, two-dimensional, transient model using a similar formulation to Gurau et al. [29] and then extended to three dimensions in Um et al. [36]. Wang and Wang [37] and Wang and Wang [38] have recently presented a single phase model that uses the membrane water transport equations of Springer et al. [7, 8]. The recent models do not assume that the catalyst and polymer electrolyte layers are one-dimensional, but use the procedure introduced by Kulikovsky [39] to couple the gas phase and membrane water transport.

Kulikovsky [39] created a three-dimensional model of the flow channel and gas diffusion media, and then coupled this with one-dimensional model of the transport in the catalyst layers and polymer electrolyte. The Springer et al. [7] model was used to model the transport in the polymer membrane, and the gas transport in the catalyst layer was assumed to be from Knudsen diffusion only. The water flux in the catalyst layer was due to a gradient in the gas phase water concentration, and the hydration of the membrane, which were related through the hydration versus relative humidity curves of Springer et al. [7].

Siegel et al. [40] solved the gas phase and liquid water transport separately, and coupled them with an interfacial mass transfer term that was analogous to Newton's law of cooling for convective heat transfer. Siegel et al. [40] assumed that the void space of the catalyst layer was filled with both gas and polymer electrolyte. The membrane model of Springer et al. [7, 8] was used to describe the water and current transport in the polymer electrolyte, and the conservation of mass, momentum and species was applied to the gas phase.

Berning et al. [41] developed a three dimensional, single-phase fuel cell model that included the gas flow channels, electrode backing layers, and polymer electrolyte membrane layer; the catalyst layers were treated as interfaces in a similar manner as Shimpalee et al. [32]. The conservation of mass, momentum, species and energy was used, and the conservation of energy for the gas and solid phases were considered separately, therefore, the temperatures of the gas and solid phases could differ. The heat transfer through the solid and gas phases were modeled with a convective heat transfer coefficient.

29

1.3 Summary and Comparison of PEM Fuel Cell Mathematical Models

Fuel cell models must be robust and accurate and be able to provide solutions to fuel cell problems quickly. A good model should predict fuel cell performance under a wide range of fuel cell operating conditions. Even a modest fuel cell model will have large predictive power. A few important parameters to include in a fuel cell model are the cell, fuel and oxidant temperatures, the fuel or oxidant pressures, the cell potential, and the weight fraction of each reactant. Some of the parameters that must be solved for in a mathematical model are shown in Figure 1.10.
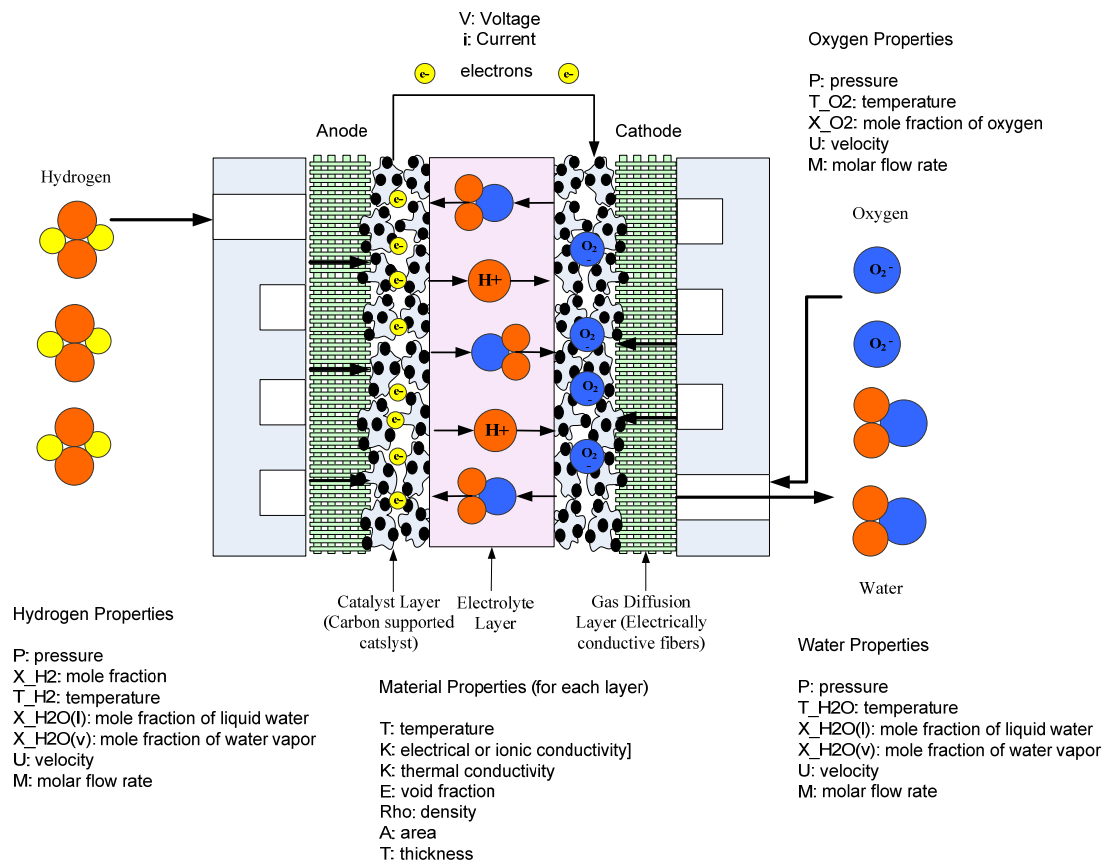
Figure 1.10. Parameters that need to be solved in a mathematical model [4]

The necessary improvements for fuel cell performance and operation demand better design, materials, and optimization. These issues can only be addressed if realistic mathematical process models are available. Table 1.3 shows a summary of equations or characteristics of fuel cell models presented in Section 1.2.

Table 1.3

Comparison of the characteristics of recent mathematical models

Model Characteristic	Description/Equations
No. of Dimensions	1, 2 or 3
Mode of Operation	Dynamic or Steady-State
Phases	Gas, Liquid or a Combination of Gas & Liquid
Kinetics	Tafel-Type Expressions, Butler-Volmer Equations, Or Complex Kintics Equations
Mass Transport	Nernst-Plank + Schogle, Stafan-Maxwell Equation, Or Nernst-Plank + Drag Coefficient

Most models in the early 1990s were 1-D, models in the late 1990s to early 2000s were 2-D, and more recently there have been a few 3-D models for certain fuel cell components. Although 2-D and 3-D models would seem to have more predictive power than 1-D models, most of them in the literature use the same equations and methodology of a 1-D model, but apply it to 3 dimensions. As shown in Table 1.3, most published models have steady-state voltage characteristics and concentration profiles, and the electrode kinetic expressions are simple Tafel-type expressions. Some models use Butler-

Volmer–type expressions, or more realistic, complex multi-step reaction kinetics for the electrochemical reactions. It is well known that there are two phases (liquid and gas) that coexist under a variety of operating conditions. Inside the cathode structure, water may condense and block the way for fresh oxygen to reach the catalyst layer. However, most published models only examine a single phase.

An important feature of each model is the mass transport descriptions of the anode, cathode, and electrolyte. Simple Fick diffusion models or Nerst-Planck mass transport expressions are often used. The convective flow is typically calculated from Darcy's law using different formulations of the hydraulic permeability coefficient. Some models use Schlogl's formulations for convective flow instead of Darcy's law, which also accounts for electroosmotic flow, and can be used for mass transport inside the PEM. Another popular type of mass transport description is the Maxwell-Stefan formulation for multi-component mixtures. This has been used for gas-phase transport in many models, but this equation would be better used for liquid-vapor-phase mass transport.

A very simple method of incorporating electroosmotic flow in the membrane is by applying the drag coefficient model, which assumes a proportion of water and fuel flow to proton flow. The swelling of polymer membranes is modeled through empirical or thermodynamic models for PEM fuel cells. Most models assume a fully hydrated membrane. In certain cases, the water uptake is described by an empirical correlation, and in other cases a thermodynamic model is used based upon the change of Gibbs free energy inside the PEM based upon water content.

A model is only as accurate as its assumptions allow it to be. The assumption needs to be well understood in order to understand the model's limitations and to

accurately interpret its results. Common assumptions used in fuel cell modeling are:

1. Ideal gas properties

2. Incompressible flow

3. Laminar flow

4. Isotropic and homogeneous electrolyte, electrode, and bipolar material
   structures

5. A negligible ohmic potential drop in components

6. Mass and energy transport is modeled from a macro-perspective using
   volume-averaged conservation equations

These concepts can be applied to all polymer membrane-based fuel cell types, regardless of the fuel cell geometry. Even simple fuel cell models will provide tremendous insight into determining why a fuel cell system performs well or poorly. The physical phenomenon that occurs inside a fuel cell can be represented by the solution of the equations presented throughout this dissertation, and are discussed in Chapters $2 - 8$.

1.4 Dissertation Objectives and Outline

The performance of a PEM fuel cell is affected by the processes occurring within each layer of the cell. Due to the thinness of the layers, in-situ measurements are difficult to obtain, therefore, mathematical modeling has become necessary for a better understanding and optimization of PEM fuel cells. Therefore, the objective of this dissertation is to develop a transient, two-phase model of a PEM fuel cell, which differs from most published previous models in several respects:

1. A fully integrated transient heat and mass transfer model that includes all layers in the fuel cell stack.

2. The model uses Fick's law for all types of mass transport in the MEA layers. This allows an accurate prediction of mass transport for a vast range of operating conditions ($20° – 90 °C$).

3. Water uptake by the membrane is accounted for by an empirical model first developed by Springer et al. [7, 8].

4. A complete energy balance is included to account for heat conduction, convection and production.

5. A complete transient mass balance model for all layers is included in the model.

6. Pressure drops throughout the fuel cell are included.

7. Two phases are modeled in the anode and cathode layers.

8. Butler-Volmer type rate descriptions will be used for both electrode reactions.

A comprehensive general engineering formulation is developed that can be used as a starting point for all mathematical models for PEM and other types of low-temperature fuel cells. The numerical solution of the formation is developed using MATLAB to take advantage of the built-in ordinary differential equations solvers. The numerical results from the simulation of the physical and chemical phenomena within the PEM fuel cell are provided.

The general formulation is comprehensive because it includes phenomena in all layers of a PEM fuel cell. The engineering model includes a control volume analysis of

each node in all of the layers within the fuel cell stack. Energy, mass and charge balances were created and pressure drops were calculated for each control volume.

In addition to the complete fuel cell model developed in this dissertation, a model for calculating optimal torque of the fuel cell stack was developed. To validate these models, four fuel cell stacks were constructed. The stacks had active areas of 16 cm^2, 4 cm^2 and two had 1 cm^2. Six different sets of flow field plates were constructed for the 1 cm^2 stacks to be able to compare both macro and micro-sized fuel cell stacks.

Chapter 2 summarizes the general theory for PEM fuel cell models that currently exist in the literature. The heat transfer portion of the mathematical model is included in Chapter 3, and the mass and pressure portion is discussed in Chapter 4. Chapter 5 is devoted to the membrane portion of the model. The bolt torque model is presented in Chapter 6, and the fabrication of micro fuel cells is presented in Chapter 7. Chapter 8 review the results of the mathematical model. A summary and suggestions for future work are given in Chapter 9.

2
GENERAL THEORY AND EQUATIONS

One of the reasons why fuel cell modeling is important is to determine why the actual voltage of a fuel cell is different than the thermodynamically predicted theoretical voltage. As explained by thermodynamics, the maximum possible cell potential is achieved when the fuel cell is operated under the thermodynamically reversible condition. This can be described as the net output voltage of a fuel cell, which is the reversible cell potential minus the irreversible potential at a certain current density [42]:

$$V = V_{rev} - V_{irrev} \tag{4}$$

where $V_{rev} = E_r$ is the maximum (reversible) voltage of the fuel cell, and V_{irrev} is the irreversible voltage loss (overpotential) occurring at the cell.

The actual open circuit voltage of a fuel cell is lower than the theoretical model due to reaction, charge and mass transfer losses. As described in Section 1.8 and shown in Figure 2.1, the performance of a polarization curve can be broken into three sections: (1) activation losses, (2) ohmic losses, and (3) mass transport losses. Therefore, the operating voltage of the cell can be represented as the departure from ideal voltage caused by these polarizations [42]:

$$V = E_r + V_{act} + V_{ohmic} + V_{conc} \tag{5}$$

where V is the cell potential, E_r is the thermodynamic potential or Nernst voltage, V_{act}

is the voltage loss due to activation polarization, V_{ohmic} is the voltage loss due to ohmic

polarization and V_{conc} is the voltage losses due to concentration polarization. The

explanation of the terms in equation 5 and Figure 2.1 stems from the detailed study of

different disciplines. The Nernst voltage comes from thermodynamics, activation losses

are described by electrochemistry, charge transport examines ohmic losses and

concentration losses can be explained by mass transport. Activation and concentration

polarization occurs at both the anode and cathode, while the ohmic polarization

represents resistive losses throughout the fuel cell.
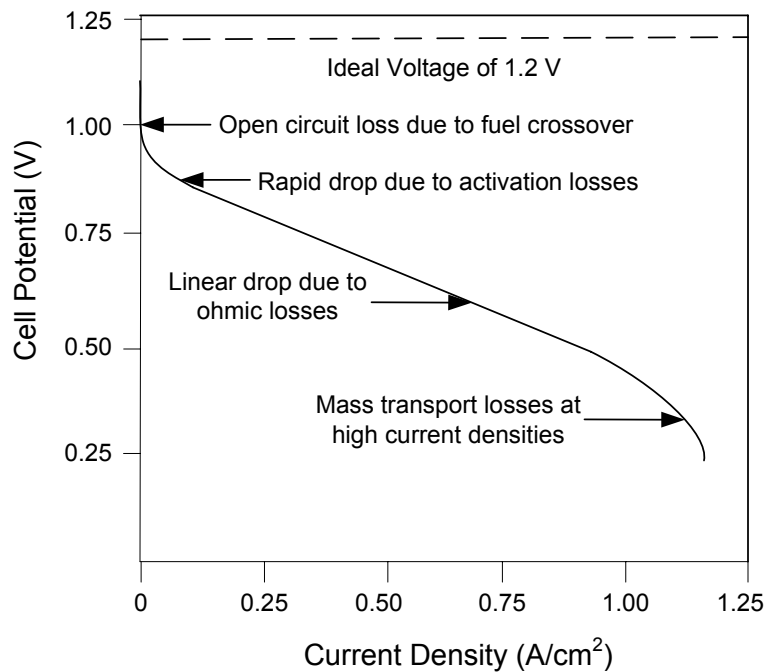
Figure 2.1. Hydrogen–oxygen fuel cell polarization curve at equilibrium [4]

Activation losses mainly occur when the electrochemical reactions are slow in

being driven from equilibrium to produce current. The reduction of oxygen is the

37

electrochemical reaction that is responsible for most of the activation overpotential. As the PEM fuel cell produces more current, the activation losses increase at a slower rate than the ohmic losses.

Ohmic losses are due to the movement of charges from the electrode where they are produced, to the load where they are consumed. The two major types of charged particles are electrons and ions, and both electronic and ionic losses occur in the fuel cell. The electronic loss between the bipolar, cooling and contact plates are due to the degree of contact that the plates make with each other. Ionic transport is far more difficult to predict and model than the fuel cell electron transport. The ionic charge losses occur in the fuel cell membrane when H^+ ions travel through the electrolyte.

Concentration losses are due to reactants not being able to reach the electrocatalytic sites, and can significantly affect fuel cell performance. These mass transport losses can be minimized by optimizing hydrogen, air and water transport in the flow field plates, gas diffusion layer and catalyst layers. This chapter explains the theory and equations relevant to the study of these potential losses through explanation of thermodynamics, electrochemistry, charge transport and mass transport in relation to fuel cells and the work presented in this study.

2.1 Thermodynamics

As shown in Figure 2.1, the thermodynamic potential is the highest obtainable voltage for a single cell. The Nernst equation gives the ideal open circuit potential, and provides a relation between the ideal standard potential for the cell reaction, and the ideal equilibrium potential at the partial pressures of the reactants and products. The

38

relationship between voltage and temperature is derived by taking the free energy,
linearizing about the standard conditions of 25 ºC, and assuming that the enthalpy change
ΔH does not change with temperature [43]:

$$E_r = -\frac{\Delta G_{rxn}}{nF} = -\frac{\Delta H - T\Delta S}{nF}$$

(6)

$$\Delta E_r = \left(\frac{dE}{dT}\right)(T - 25) = \frac{\Delta S}{nF}(T - 25)$$

(7)

where E_r is the standard-state reversible voltage, and ΔG_{rxn} is the standard free-energy
change for the reaction. The change in entropy is negative; therefore, the open circuit
voltage output decreases with increasing temperature. The fuel cell is theoretically more
efficient at low temperatures as shown in Figure 2.2. However, mass transport and ionic
conduction is faster at higher temperatures and this more than offsets the drop in open-
circuit voltage.
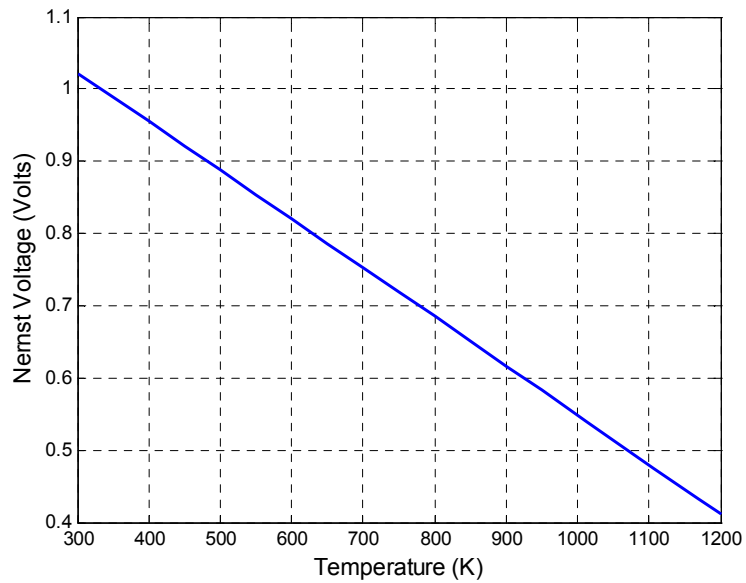
Figure 2.2. Nernst voltage as a function of temperature [4]

39

In the case of a hydrogen–oxygen fuel cell under standard-state conditions:

$$H_2 \text{ (g)} + \frac{1}{2} O_2 \text{ (g)} \rightarrow H_2O \ (\Delta H = -285.8 \text{ KJ/mol}; \Delta G = -237.3 \text{ KJ/mol}) \qquad (8)$$
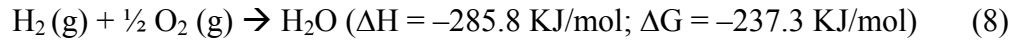
$$E_{H_2/O_2} = -\frac{-237.3 KJ \,/\, mol}{2 mol * 96,485 C \,/\, mol} = 1.229V \qquad (9)$$

At standard temperature and pressure, this is the highest voltage obtainable from a hydrogen–oxygen fuel cell. Most fuel cell reactions have voltages in the 0.8 to 1.0 V range. To obtain higher voltages, several cells have to be connected together in series. For nonstandard conditions, the reversible voltage of the fuel cell may be calculated from the energy balance between the reactants and the products [44]. The theoretical potential for an electrochemical reaction can be expressed by the Nernst equation [43]:

$$V = E_r - \frac{RT}{nF} \ln \frac{a_{H_2O}}{a_{H_2} a_{O_2}^{1/2}} \qquad (10)$$

where V is the actual cell voltage, E_r is the standard-state reversible voltage, R is the universal gas constant, T is the absolute temperature, n is the number of electrons consumed in the reaction, and F is Faraday's constant. Figures 2.3 and 2.4 illustrate the Nernst voltage as a function of the activity of hydrogen and oxygen.
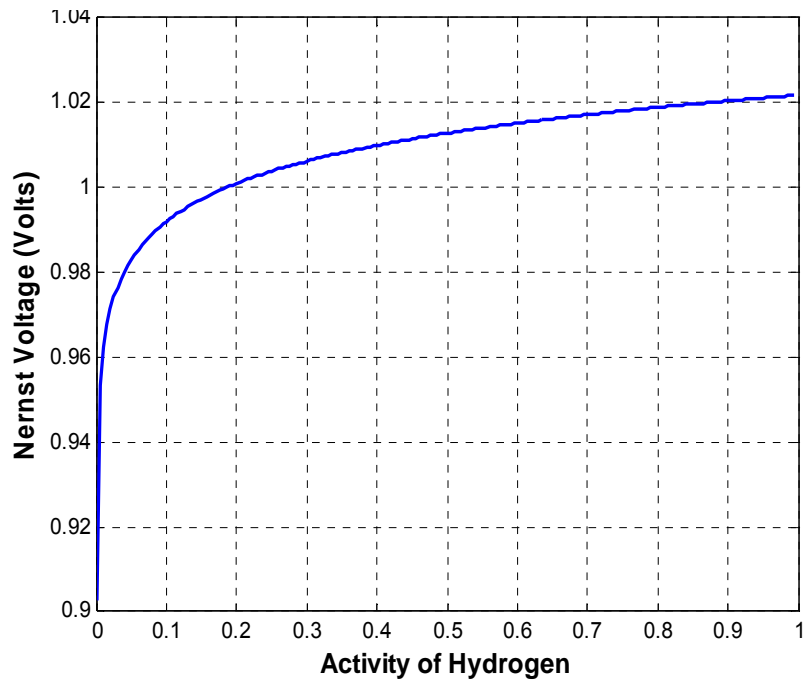
Figure 2.3. Nernst voltage as a function of activity of hydrogen
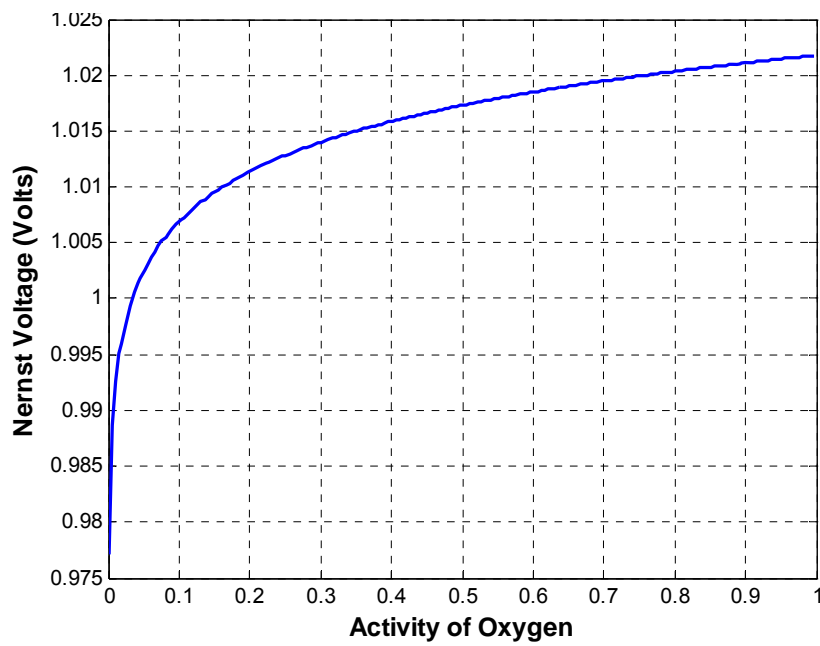
Figure 2.4. Nernst voltage as a function of activity of oxygen

At standard temperature and pressure, the theoretical potential of a hydrogen–air fuel cell can be calculated as follows [43]:

$$E_r = 1.229 - \frac{8.314(J/(mol*K))*298.15}{2*9,6485(C/mol)} \ln \frac{1}{1*0.21^{1/2}} = 1.219V \qquad (11)$$

The potential between the oxygen cathode where the reduction occurs and the hydrogen anode at which the oxidation occurs will be 1.219 volts at standard conditions with no current flowing.

By assuming the gases are ideal (the activities of the gases are equal to their partial pressures, and the activity of the water phase is equal to unity), equation 10 can be written as [43]:

$$V = E_r - \frac{RT}{nF} \ln \left[\prod_i \left(\frac{p_i}{p_0} \right)^{v_i} \right] \qquad (12)$$

The form of the Nernst equation that is relevant for this study is:

$$E_r = -\frac{G_{f,liq}}{2F} - \frac{RT_k}{2F} * \ln \left(\frac{P_{H_2O}}{p_{H_2} * p_{O_2}^{1/2}} \right) \qquad (13)$$

where $G_{f,liq}$ is the free-energy change for the reaction, R is the universal gas constant, T is the absolute temperature, F is Faraday's constant, P_{H_2O} is the partial pressure of water, p_{H_2} is the partial pressure of hydrogen and p_{O_2} is the partial pressure of oxygen.

The saturation pressure of water can be calculated by [19]:

$$\log P_{H_2O} = -2.1794 + 0.02953 * T_c - 9.1837 \times 10^{-5} * T_c^2 + 1.4454 \times 10^{-7} * T_c^3 \quad (14)$$

where T_c is the temperature in °C.

The partial pressure of hydrogen is [19]:

$$p_{H_2} = 0.5 * (P_{H_2} / \exp(1.653 * i / (T_K^{1\,334}))) - P_{H_2O} \qquad (15)$$

The partial pressure of oxygen can be obtained by [19]:

$$p_{O_2} = (P_{air} / \exp(4.192 * i / (T_K^{1\,334}))) - P_{H_2O} \qquad (16)$$

Equation 13 can be used to obtain the thermodynamically reversible voltage at a temperature T. Further details for the parameters in the above equations and thermodynamic discussions can be found from various books [43, 45].

2.2 Voltage Loss Due to Activation Polarization

Activation polarization is the voltage overpotential required to overcome the activation energy of the electrochemical reaction on the catalytic surface [5]. This type of polarization dominates losses at low current density, and measures the catalyst effectiveness at a given temperature. This is a complex three-phase interface problem, since gaseous fuel, the solid metal catalyst, and electrolyte must all make contact. The catalyst reduces the height of the activation barrier, but a loss in voltage remains due to the slow oxygen reaction. The total activation polarization overpotential is 0.1 to 0.2 V, which reduces the maximum potential to less than 1.0 V even under open-circuit conditions [42]. Activation overpotential expressions can be derived from the Butler-Volmer equation. The activation overpotential increases with current density and can be expressed as [46]:

$$V_{act} = \upsilon_{act,anode} + \upsilon_{act,cath} = \frac{RT}{nF\alpha} \ln\left(\frac{i}{i_o}\right)\bigg|_{anode} + \frac{RT}{nF\alpha} \ln\left(\frac{i}{i_o}\right)\bigg|_{cath} \tag{17}$$

where i is the current density, and i_0, is the reaction exchange current density, n is the number of exchange protons per mole of reactant, F is Faraday's constant, and α is the charge transfer coefficient used to describe the amount of electrical energy applied to change the rate of the electrochemical reaction [47]. The exchange current density, i_o is the electrode activity for a particular reaction at equilibrium. In PEMFC, the anode i_o for hydrogen oxidation is very high compared to the cathode i_o for oxygen reduction, therefore, the cathode contribution to this polarization is often neglected. Intuitively, it seems that the activation polarization should increase linearly with temperature based upon Equation 17; however, the purpose of increasing temperature is to decrease activation polarization. In Figure 2.2, increasing the temperature would cause a voltage drop within the activation polarization region.

The exchange current density measures the readiness of the electrode to proceed with the chemical reaction. It is a function of temperature, catalyst loading, and catalyst specific surface area. The higher the exchange current density, the lower the barrier is for the electrons to overcome, and the more active the surface of the electrode. The exchange current density can usually be determined experimentally by extrapolating plots of log i versus υ_{act} to $\upsilon_{act} = 0$. The higher the exchange current density, the better is the fuel cell performance. The effective exchange current density at any temperature and pressure is given by the following equation [46]:

$$i_0 = i_0^{ref} a_c L_c \left(\frac{P_r}{P_r^{ref}}\right)^{\gamma} \exp\left[-\frac{E_r}{RT}\left(1 - \frac{T}{T_{ref}}\right)\right] \tag{18}$$

where i_{0ref} is the reference exchange current density per unit catalyst surface area

(A/cm^2), a_c is the catalyst specific area, L_c is the catalyst loading, P_r is the reactant partial

pressure (kPa), P_r^{ref} is the reference pressure (kPa), γ is the pressure coefficient (0.5 to

1.0), E_c is the activation energy (66 kJ/mol for O_2 reduction on Pt), R is the gas constant

[8.314 J/(mol*K)], T is the temperature, K, and T_{ref} is the reference temperature (298.15

K). The activation losses as a function of exchange current density are shown in Figure

2.5.
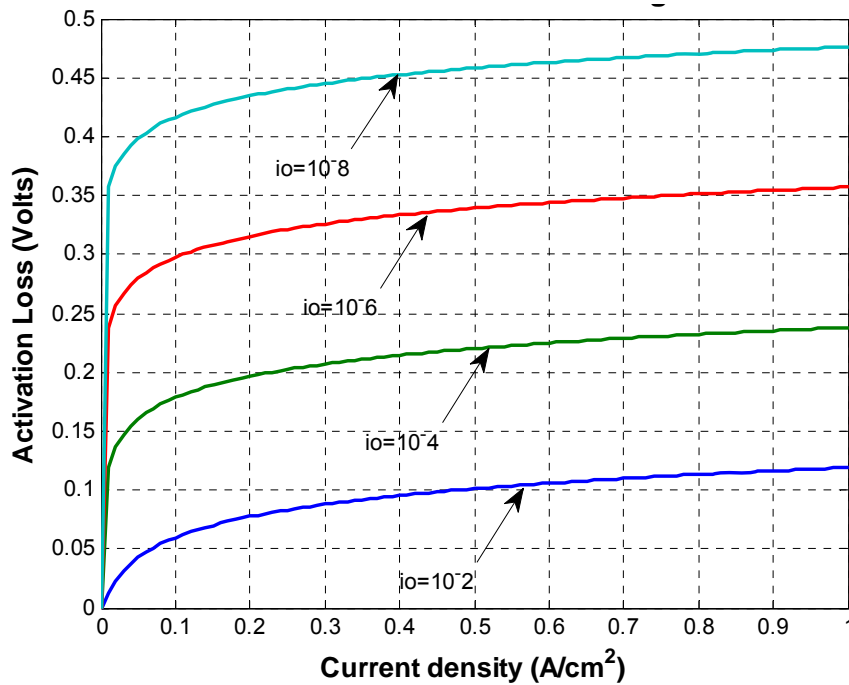
Figure 2.5. Effect of the exchange current density on the activation losses [4]

If the currents are kept low so that the surface concentrations do not differ much

from the bulk values, the Butler-Volmer equation can be written as [46]:

$$i = i_0 \exp\left[\frac{-\alpha n F \upsilon_{act,cath}}{RT}\right] - i_0 \exp\left[\frac{\alpha n F \upsilon_{act,anode}}{RT}\right] \qquad (19)$$

where i is the current density per unit catalyst surface area (A/cm^2), i_0 is the exchange

current density per unit catalyst surface area (A/cm^2), υ_{act} is the activation polarization

(V), n is the number electrons transferred per reaction (–), R is the gas constant [8.314

J/(mol*K)], and T is the temperature (K). The transfer coefficient is the change in

polarization that leads to a change in reaction rate for fuel cells is typically assumed to be

0.5. Figure 2.6 illustrates the affects of transfer coefficient on the activation losses.
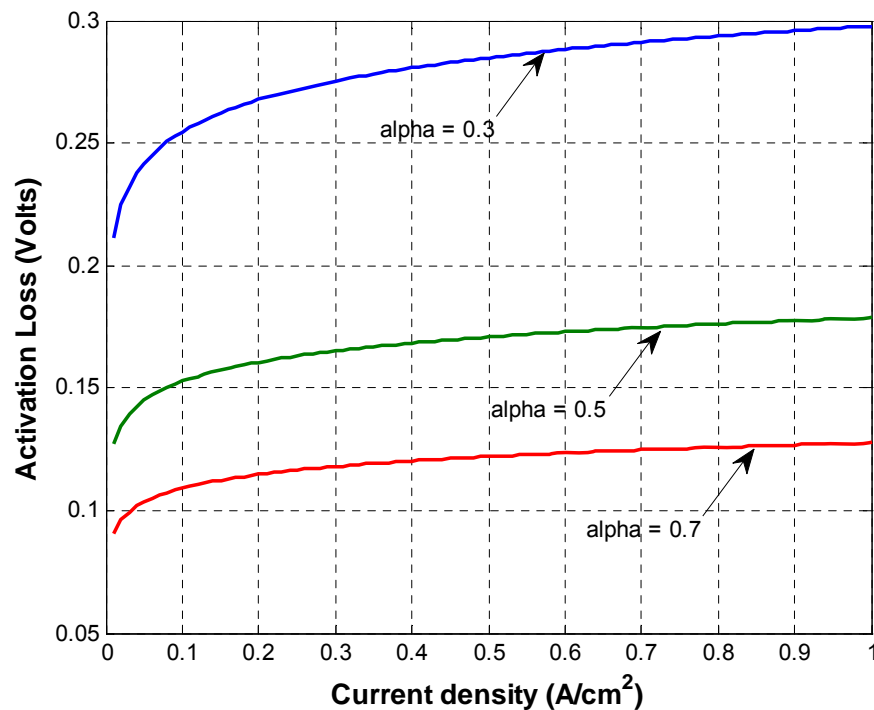
Figure 2.6. Effect of the transfer coefficient on the activation losses [4]

The Butler-Volmer equation is valid for both the anode and cathode reaction in a

fuel cell. It states that the current produced by an electrochemical reaction increases

46

exponentially with activation overpotential [42]. This equation also says that if more current is required from a fuel cell, voltage will be lost. The Butler-Volmer equation applies to all single-step reactions, and can also be used for multi-step approximations with some modifications to the equation.

If the exchange current density is low, the kinetics become sluggish, and the activation overpotential will be larger for any particular net current. If the exchange current is very large, the system will supply large currents with insignificant activation overpotential. If a system has an extremely small exchange current density, no significant current will flow unless a large activation overpotential is applied. The exchange current can be viewed as an "idle" current for charge exchange across the interface. If only a small net current is drawn from the fuel cell, only a tiny overpotential will be required to obtain it. If a net current is required that exceeds the exchange current, the system has to be driven to deliver the charge at the required rate, and this can only be achieved by applying a significant overpotential. When this occurs, it is a measure of the systems ability to deliver a net current with significant energy loss.

In this study, the activation losses are estimated using the Butler-Volmer equation, and can be expressed as [46]:

$$V_{act} = \upsilon_{act,anode} + \upsilon_{act,cath} \tag{20}$$

where the activation losses for the anode are [46, 48]:

$$i = a_{1,2}(1 - S)i_{anode} \tag{21}$$

$$i_{anode} = \left[\frac{p_{H2}}{p_{H2}^{ref}} \exp\left(\frac{\alpha_a F}{RT} \left(\upsilon_{act,anode} \right) \right) - \exp\left(\frac{-\alpha_c F}{RT} \left(\upsilon_{act,anode} \right) \right) \right] \tag{22}$$

and the activation losses for the cathode are [46, 48]:

$$i = a_{1,2}(1-S)i_{cathode} \tag{23}$$

$$i_{cathode} = \left[\frac{p_{O2}}{p_{O2}^{ref}} \exp\left(\frac{-\alpha_c F}{RT}\left(\upsilon_{act,cath} \right) \right) \right] \tag{24}$$

The Butler-Volmer activation losses are illustrated by Figure 2.7.
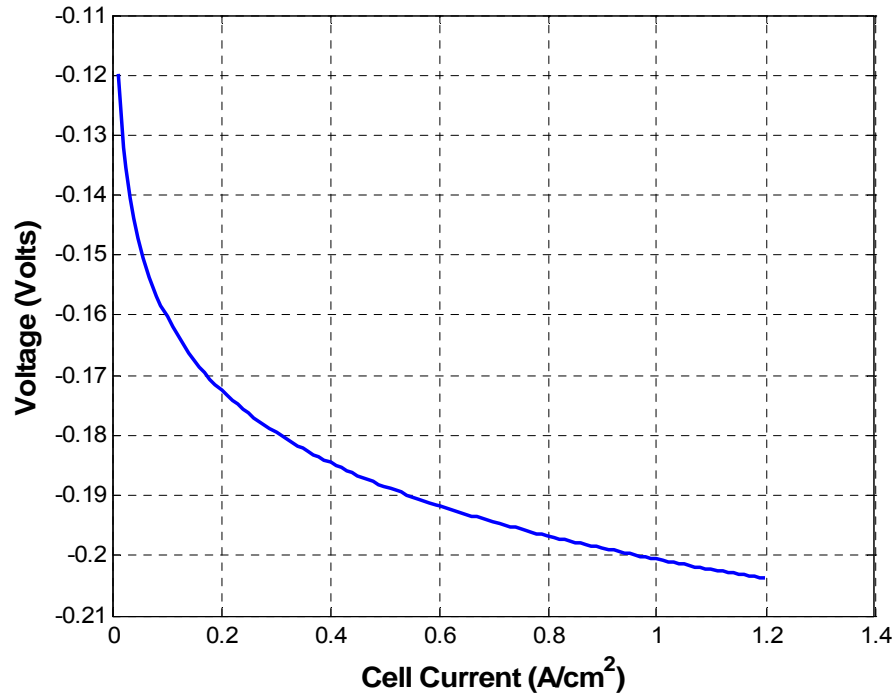
Figure 2.7. Butler-Volmer activation losses [4]

2.3 Voltage Loss Due to Charge Transport

Every material has an intrinsic resistance to charge flow. The material's natural resistance to charge flow causes ohmic polarization, which results in a loss in cell voltage. All fuel cell components contribute to the total electrical resistance in the fuel cell, including the electrolyte, the catalyst layer, the gas diffusion layer, bipolar plates,

interface contacts and terminal connections. The reduction in voltage is called "ohmic loss", and includes the electronic (R_{elec}) and ionic (R_{ionic}) contributions to fuel cell resistance. This can be written as [42]:

$$V_{ohmic} = iR_{ohmic} = i(R_{elec} + R_{ionic}) \tag{25}$$

R_{ionic} dominates the reaction in Equation 25 because ionic transport is more difficult than electronic charge transport. R_{ionic} represents the ionic resistance of the electrolyte, and R_{elec} includes the total electrical resistance of all other conductive components, including the bipolar plates, cell interconnects, and contacts.

The material's ability to support the flow of charge through the material is its conductivity. The electrical resistance of the fuel cell components is often expressed in the literature as conductance (σ), which is the reciprocal of resistance [49]:

$$\sigma = \frac{1}{R_{ohmic}} \tag{26}$$

where the total cell resistance (R_{ohmic}) is the sum of the electronic and ionic resistance. Resistance is characteristic of the size, shape and properties of the material, as expressed by Equation 27 [49]:

$$R = \frac{L_{cond}}{\sigma A_{cond}} \tag{27}$$

where L_{cond} is the length or thickness (cm) of the conductor, A_{cond} is the cross-sectional area (cm^2) of the conductor, and σ is the electrical conductivity (ohm^{-1} cm^{-1}). The current density, i, (A/cm^2), can be defined as [42]:

$$i = \frac{I}{A_{cell}} \tag{28}$$

The total fuel cell ohmic losses can be written as:

$$\upsilon_{ohmic} = iA\sum R = iA\left[\left(\frac{L}{\sigma A}\right)_{anode} + R_{ionic} + \left(\frac{L}{\sigma A}\right)_{cath}\right] \tag{29}$$

where L can either be the length or thickness of the material, or the total "land area". The first term in Equation 29 applies to the anode, the second to the electrolyte and the third to the cathode. In the bipolar plates, the "land area" can vary depending upon flow channel area. As the land area is decreased, the contact resistance increases since the land area is the term in the denominator of the contact resistance:

$$R_{contact} = \frac{R_{contact}}{A_{contact}} \tag{30}$$

where $A_{contact}$ equals the land area. Therefore, with increasing land area, or decreasing channel area, the contact resistance losses will decrease and the voltage for a given current will be higher. This concept is illustrated in Figure 2.8.
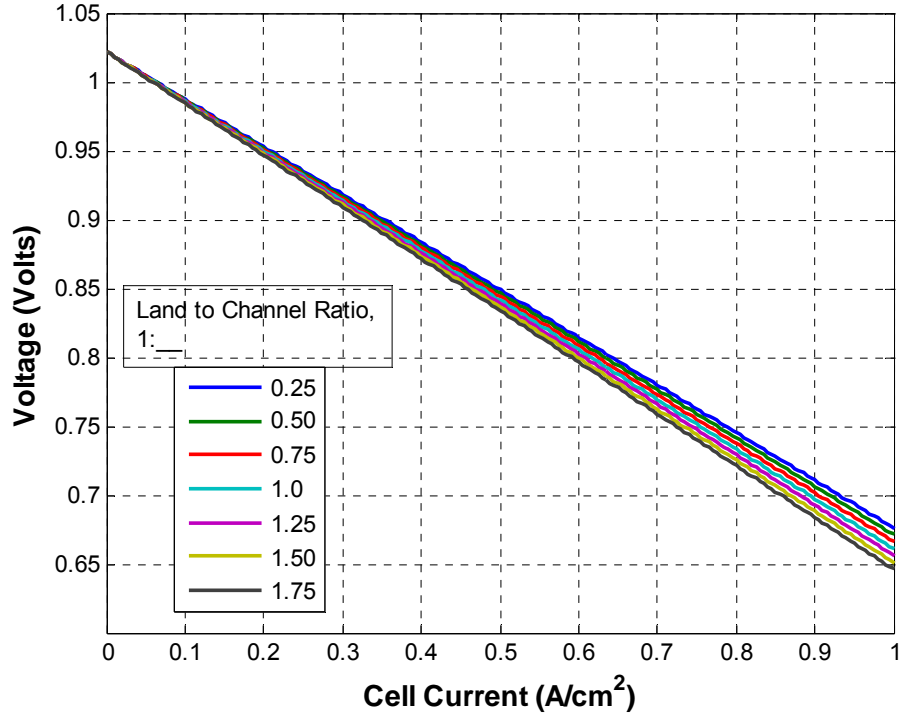
Figure 2.8. Cell voltage and current density based upon land to channel [4]

One of the most effective ways for reducing ohmic loss is to either use a better ionic conductor for the electrolyte layer, or a thinner electrolyte layer. Thinner membranes are also advantageous for PEM fuel cells because they keep the anode electrode saturated through "back" diffusion of water from the cathode. At very high current densities (fast fluid flows), mass transport causes a rapid drop off in the voltage, because oxygen and hydrogen simply cannot diffuse through the electrode and ionize quickly enough, therefore, products cannot be moved out at the necessary speed [42].

Since the ohmic overpotential for the fuel cell is mainly due to ionic resistance in the electrolyte, this can be expressed as [4, 42]:

$$\upsilon_{ohmic} = iR_{ohmic} = iA_{cell}\left(\frac{\delta}{\sigma A_{cell}}\right) = \frac{i\delta}{\sigma} \tag{31}$$

51

where A_{cell} is the active area of the fuel cell, δ is the thickness of the electrolyte layer, and

σ is the conductivity. As seen from Equation 31 and Figures 2.9 and 2.10, the ohmic

potential can be reduced by using a thinner electrolyte layer, or using a higher ionic

conductivity electrolyte.
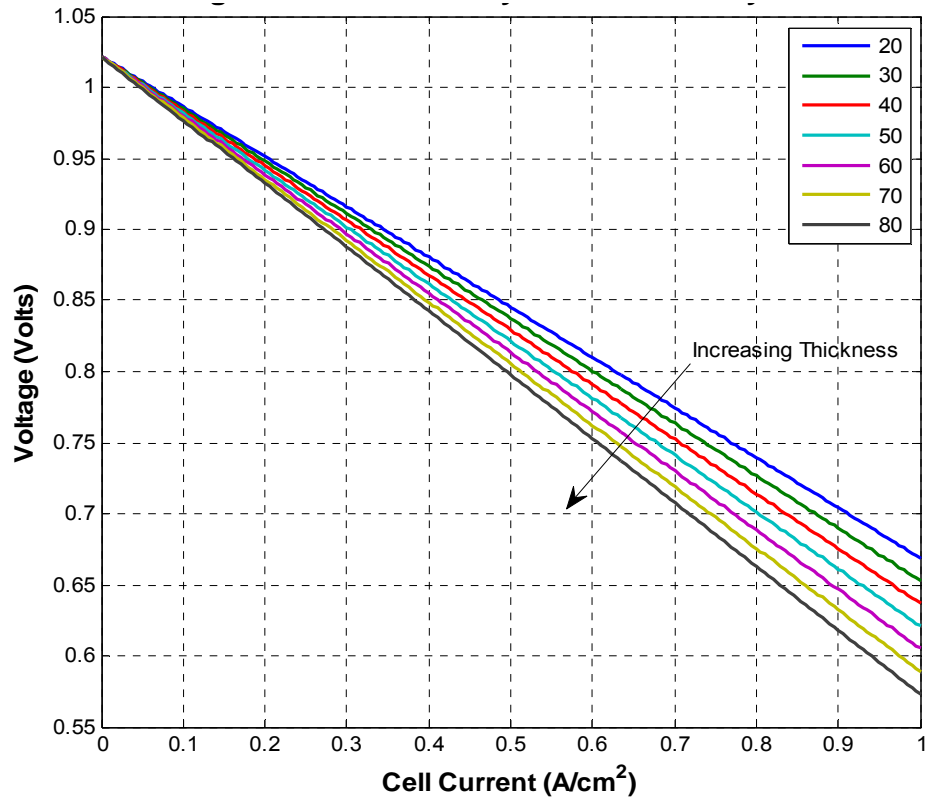
Figure 2.9. Cell voltage and current density due to electrolyte thickness (microns) [4]
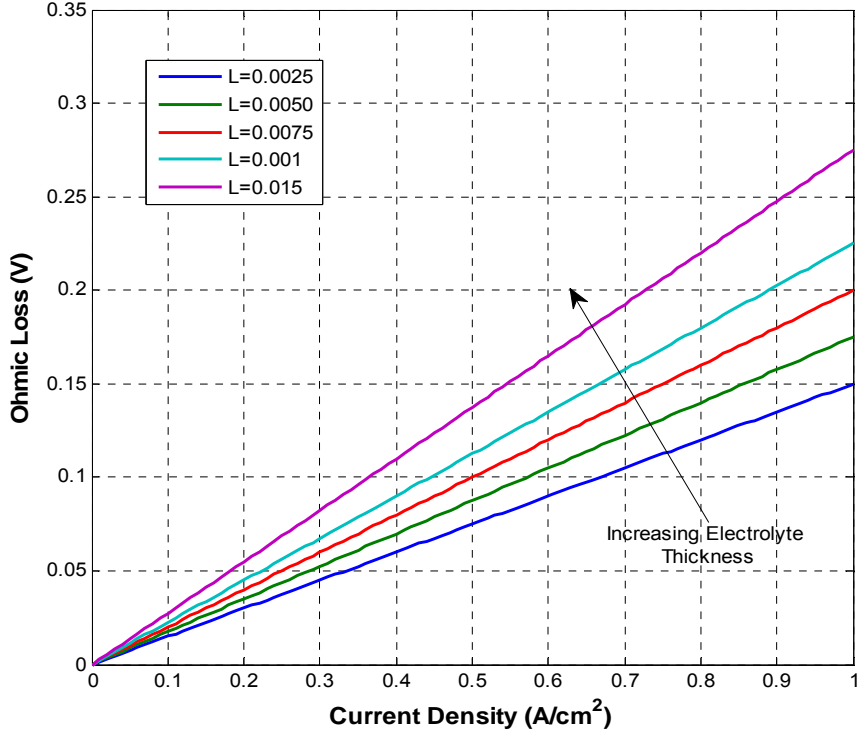
Figure 2.10. Ohmic loss as a function of electrolyte thickness (cm) [4]

2.4 Voltage Loss Due to Mass Transport

As described in Section 2.1, concentration affects fuel cell performance through the Nernst equation since the thermodynamic voltage of the fuel cell is determined by the reactant and product concentrations at the catalyst sites [43]:

$$V = E_r - \frac{RT}{nF} \ln \frac{\prod a_{products}^{v_i}}{\prod a_{reac\tan ts}^{v_i}} \tag{32}$$

In order to calculate the incremental voltage loss due to reactant depletion in the catalyst layer, the changes in Nernst potential using c_R^* values instead of c_R^0 values are represented by the following [42, 43, 46]:

$$V_{conc} = E_r - E_{Nernst} \tag{33}$$

$$V_{conc} = \left(E_r - \frac{RT}{nF} \ln \frac{1}{C_0} \right) - \left(E_r - \frac{RT}{nF} \ln \frac{1}{C_i} \right) \tag{34}$$

$$V_{conc} = \frac{RT}{nF} \ln \frac{C_0}{C_i} \tag{35}$$

where E_r is the Nerst voltage using C_0 values, and E_{Nernst} is the Nernst voltage using C_i values. The ratio i/i_L can be expressed as [42]:

$$\frac{i}{i_L} = 1 - \frac{C_i}{C_0} \tag{36}$$

Therefore, the ratio C_0/C_i (the concentration at the backing/catalyst layer interface can be written as [2, 42]:

$$\frac{C_0}{C_i} = \frac{i_L}{i_L - i} \tag{37}$$

Substituting equation 37 into 35 yields [42, 46]:

$$V_{conc} = \frac{RT}{nF} \ln \left(\frac{i_L}{i_L - i} \right) \tag{38}$$

This expression is only valid for $i < i_L$.

Concentration also affects fuel cell performance through reaction kinetics. The reaction kinetics is dependent upon the reactant and product concentrations at the reaction sites. As mentioned previously, the reaction kinetics can be described by the Butler-Volmer equation [42, 46]:

$$i = i_0 \frac{c_R^*}{c_R^{0*}} \exp(\alpha nF \upsilon_{act,anode} / (RT)) - \frac{c_P^*}{c_P^{0*}} \exp(-(1-\alpha)nF \upsilon_{act,cath} / (RT)) \tag{39}$$

where c_R^* and c_P^* are arbitrary concentrations and i_0 is measured as the reference reactant

and product concentration values c_R^{0*} and c_P^{0*}. In the high current-density region, the

second term in the Butler-Volmer equation drops out and the expression then becomes:

$$i = i_0 \frac{c_R^*}{c_R^{0*}} \exp(\alpha n F \upsilon_{act} / (RT))$$ (40)

In terms of activation over voltage using c_R^* instead of c_R^{0*} [42, 46]:

$$V_{conc} = \frac{RT}{\alpha n F} \frac{c_R^{0*}}{c_R^*}$$ (41)

The ratio can be written as:

$$\frac{c_R^0}{c_R^*} = \frac{i_L}{i_L - i}$$ (42)

The total concentration loss can be written as [42, 46]:

$$V_{conc} = \left(\frac{RT}{nF}\right)\left(1 + \frac{1}{\alpha}\right)\frac{i_L}{i_L - i}$$ (43)

Fuel cell concentration loss (or mass transport loss), may be expressed by the equation

[42, 46]:

$$V_{conc} = c \ln \frac{i_L}{i_L - i}$$ (44)

where c is a constant, and can have the approximate form [42, 46]:

$$c = \frac{RT}{nF}\left(1 + \frac{1}{\alpha}\right)$$ (45)

Actual fuel cell behavior frequently has a larger value than what the Equation 45

predicts. Due to this, c is often obtained empirically. The concentration loss appears at

high current density, and is severe. Significant concentration losses limit fuel cell

performance.

In this study, the mass transport losses can be calculated using the following

equation [4, 46]:

$$V_{conc} = -\left(\frac{RT}{nF} \ln\left(\frac{i_{L,cath}}{i_{L,cath} - i} \right) + \frac{RT}{nF} \ln\left(\frac{i_{L,anode}}{i_{L,anode} - i} \right) \right)$$ (46)

where i_L is the limiting current density, expressed by the following equation [4, 46]:

$$i_L = \frac{nFD_{AB}(C_1 - C_2)}{\delta}$$ (47)

where D_{AB} is the diffusion coefficient, C is the concentration, and δ is the thickness.

3
HEAT TRANSFER MODEL

There are many areas of fuel cell technology that need to be improved in order for it to become commercially viable. Among these areas, the temperature of the fuel cell layers and the heat transfer through the stack are very important for optimal performance. Temperature in a fuel cell is not always uniform, even when there are constant mass flow rates in the channels. Uneven fuel cell stack temperatures are a result of water phase change, coolant temperature, air convection, the trapping of water, and heat produced by the catalyst layer. Figure 3.1 illustrates the heat generation from the catalyst layer for a PEM fuel cell. The membrane has to be adequately hydrated in order for proper ionic conduction through the fuel cell. If the fuel cell is heated too much, the water in the fuel cell will evaporate, the membrane will dry out, and the performance of the fuel cell will suffer. If too much water is produced on the cathode side, water removal can become a problem, which affects the overall cell heat distribution. This ultimately leads to fuel cell performance losses. In addition, the existence of phase change, and the combination of fuel cell phenomena in the stack complicate the heat transfer analysis. In order to precisely predict temperature-dependent parameters and rates of reaction and species transport, the heat distribution throughout the stack needs to be determined accurately. Both detailed experimentation and modeling are needed to optimize the stack design and the electrochemical performance.
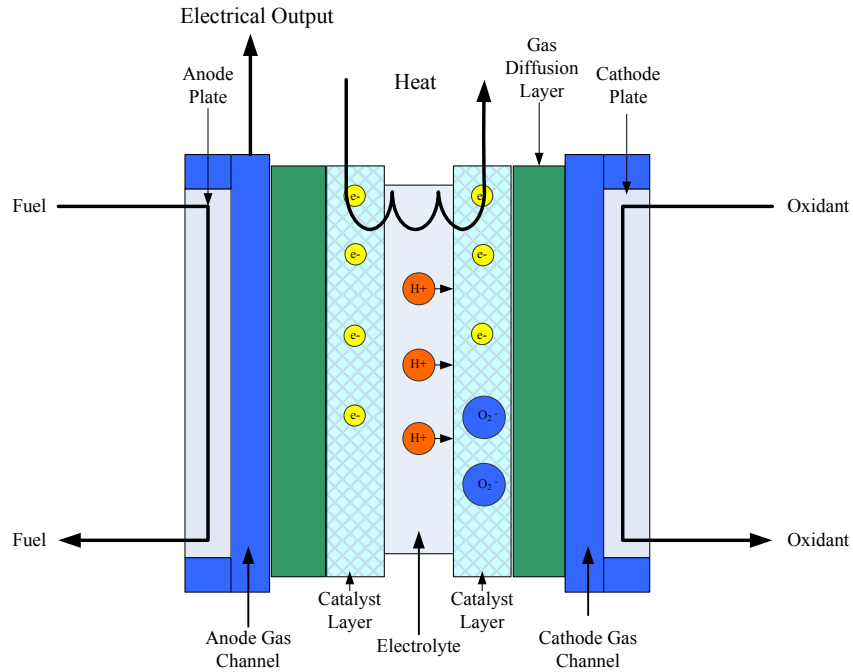
Figure 3.1. Illustration of a polymer electrolyte membrane (PEM) fuel cell with heat

generation from the catalyst layers [2]

The thermal model developed in this dissertation includes the computation of

energy balances and thermal resistances defined around the control volumes in each fuel

cell layer to enable the study of the diffusion of heat through a particular layer as a

function of time or position.

3.1 Model Development

A 1-D transient numerical model is developed for predicting the heat transfer and

temperature distribution through the layers of a fuel cell stack. The numerical model

consists of the calculation of both conductive and convective heat transfer. The energy

balances for each layer include the thermal resistance, the heat generated by the fuel cell

reactions, the heat flows from the nodes on the left and right sides, and the heat loss by the fuel cell gases, liquids and the surroundings. Conductive heat transfer occurs in the solid and porous structures, and convective heat transfer occurs between the solid surfaces and gas streams. Heating and cooling of the stack was examined to determine the accuracy of the model for predicting heating of the fuel cell catalyst layers, and the effect of running coolant through different portions of the fuel cell. The motivation of this work was to build a transient model that can be used to examine the effects of thermal diffusion, catalyst heating, membrane hydration, and material design and selection for a fuel cell stack.

3.1.1 Background and Modeling Approaches

Heat transfer in fuel cell stacks have been studied in the literature during the last decade. The majority of the existing fuel cell stack models in the literature investigate the heat transfer in the stack during steady-state conditions [50,51,52,53], conduct or include heat transfer in a very crude manner, such as using the overall fuel cell stack as the control volume [51, 54]. There are very few studies that have used the fuel cell layers or smaller nodes to analyze the heat transfer; however, these are typically steady-state models, and there has not been any experimental validation of these models. Maggio et al. [50], Park and Li [52] and Zong et al. [53] focused on the fuel cell cooling and flow field plate layers, and the heat transfer to the gases, but did not include the effects that the other layers may have had on the temperature distribution in the stack. Zhang et al. [51] focused on a simple stack thermal model, and incorporated it into a system with thermal model of the balance of plant components. Sundaresan and Moore [55] have presented a

59

zero-dimensional thermal layered model to analyze cold start behavior from a sub-zero environment. This model focuses on cold-start conditions, and each layer only as a single-point temperature, which limits the data that the model can predict. Shan et al. [56] and [57] developed a transient stack system model to study the effect of varying load on the start-up during normal operating conditions. Khandelwal et al. [58] presented a transient stack model for cold-start analysis using a layered model. However, this model did not provide any experimental data like most thermal models in the literature. In addition, there are currently no thermal models that study the heat distribution through a single fuel cell in order to obtain information about the behavior of the catalyst, membrane and gas diffusion layers, and their effect on surrounding flow field layer temperatures.

3.1.2 Methodology

In establishing the methodology for the heat transfer calculations, two important factors should be considered. The fuel cell stack layers are made up of varying materials, each with a different thermal conductivity. There is strong potential for axial conduction through the flow field channel plates, gas diffusion media and catalyst layers. Some of the layers, such as the end plates, gaskets and terminals act as extended heat transfer surfaces, and other layers have a large area that is in direct contact with the fuel (hydrogen), the oxidant (air) and water. Due to the simultaneous coupled conduction and convection within the channels and other layers, conjugate effects must be addressed. Therefore, the heat transfer analysis is conducted by analyzing the fuel cell stack by layer. Appendix G provides the detailed procedure employed for the heat transfer

calculations discussed in this section. The five main steps in the segmental heat transfer analysis are:

1. Definition of the layers and nodes

2. Definition of the boundary conditions

3. An energy balance computation for each node.

4. Definition of the thermal resistance for each potential heat flow path.

5. Calculation of heat transfer coefficients.

6. Calculation of additional parameters such as the heat generated by the catalyst layers.

The following subsections describe each of the above steps in the nodal heat transfer analysis.

3.2 Definitions of Segments and Nodes

Figure 3.2 shows a schematic of the PEMFC stack, and the grid structure used in the fuel cell thermal analysis model. The sections of the geometry under consideration vary depending upon fuel cell stack layers and construction. The main layers under consideration in this model are the end plates, gaskets, terminals, flow field plates, gas diffusion media, catalyst and membrane layers. The flow field plate layers are subdivided into two separate layers due to part of the layer containing both conductive and convective heat transfer, and the other part only containing conductive heat transfer. Although only a small percentage of the total layer area in the end plates, gaskets and contact layers has gas or liquid flow, conduction and convection is both assumed to be the modes of heat transfer.

In the actual calculations conducted with the mathematical model, the number of segments is specified by the user, and was varied from 1 to 60 segments for each layer for the outputs of this study.
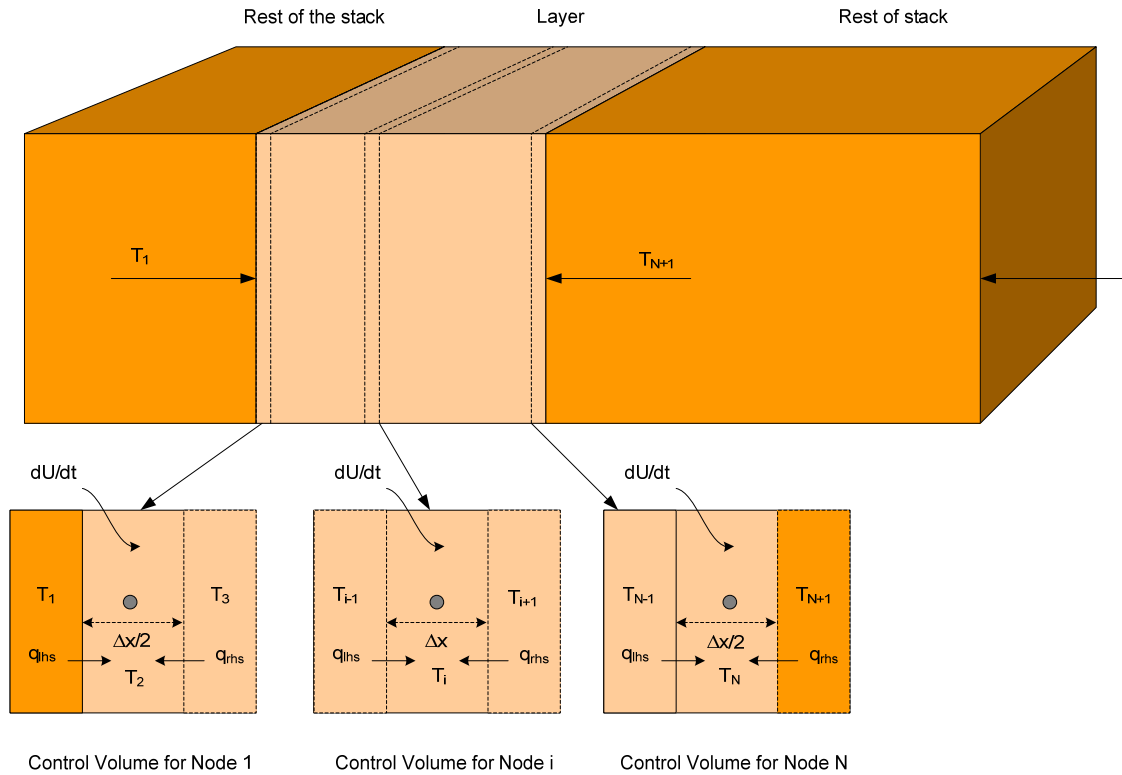
Figure 3.2. Schematic of the PEMFC stack and the nodes used for model development.

For the uniform distribution of nodes that is shown in Figure 3.2, the location of each node (x_i) is:

$$x_i = \frac{(i-1)}{(N-1)} L \quad \text{for } i = 1..N$$

(48)

where N is the number of nodes used for the simulation. The distance between adjacent

nodes (Δx) is:

$$\Delta x = \frac{L}{N-1}$$

(49)

Energy balances have been defined around each node (control volume). The

control volume for the first, last and an arbitrary, internal node is shown in Figure 3.2,

and explained in further detail in Appendix E.

3.2.1 Boundary Conditions

The next step in the analysis is to determine each layer, the hydrogen, air and

water temperatures. The initial conditions for this problem are that all of the temperatures

at t = 0 are equal to T_{in}.

$$T_{i,1} = T_{in} \quad \text{for } i = 1...N$$

(50)

Note that the variable T is a one-dimensional array.

3.2.2 Model Assumptions

The following assumptions were made for the stack thermal model.

1. The heat transfer in the stack is one-dimensional (x-direction).

2. All material thermal properties are constant over the temperature range considered (20° to 80 C).

3. For the MEA layers, only the active area was included in the model. The materials surrounding the MEA were not included in the model.

3.3 Energy Balances and Thermal Resistances for Each Fuel Cell Layer

This section illustrates the energy balances for each layer. Each fuel cell layer requires a unique energy balance because there are different thermal resistances, materials, and phases in each layer. Energy balances and thermal resistances are created for the end plate, contacts, flow field, gas diffusion, and catalyst and membrane layers in Sections 3.3.1 to 3.35.

3.3.1 End Plates, Contacts and Gasket Materials

The end plate is typically made of a metal or polymer material, and is used to uniformly transmit the compressive forces to the fuel cell stack. The end plate must be mechanically sturdy enough to support the fuel cell stack, and be able to uniformly distribute the compression forces to all of the major surfaces of each layer within the fuel cell stack. Depending upon the stack design, there also may be contact and gasket layers in the fuel cell stack. The gasket layers help to prevent gas leaks and improve stack

compression. The contact layers or current collectors are used to collect electrons from the flow field plate and gas diffusion layer (GDL) [4].

Depending upon the stack design, one or more of fuels may enter the end plates, and although the area of the fuel flow is small in these layers, both conduction and convection are both considered modes of heat transfer. Often one side of each of these layers is exposed to an insulating material (or the ambient environment), and the other side is exposed to a conductive current collector plate or insulating material. An illustration of the energy balance is shown in Figure 3.3 [4].
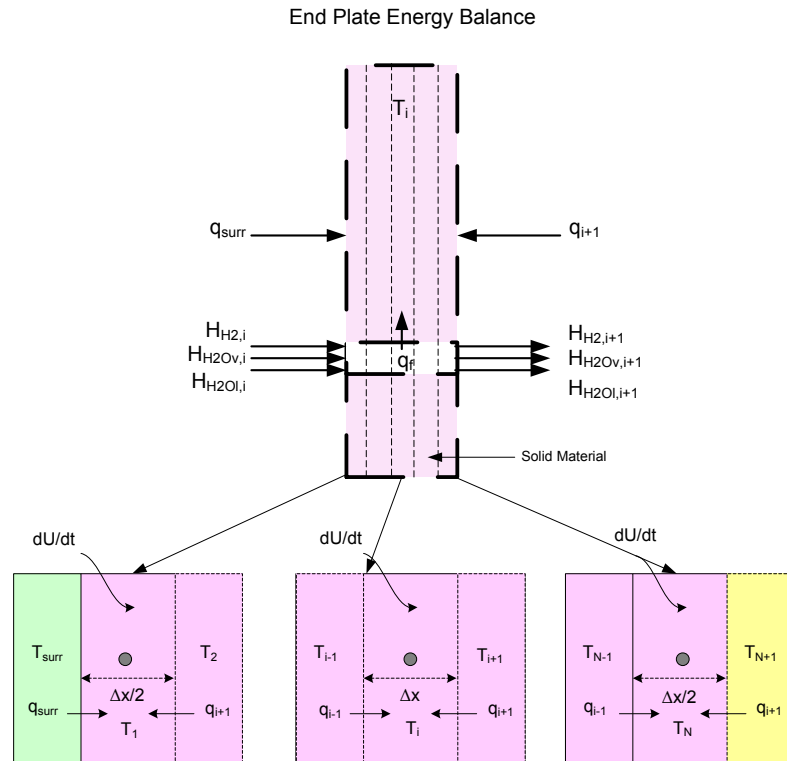
Figure 3.3. End plate energy balance

The general energy balance for the solid portion of the end plate, contact and gasket layers can be written as [59]:

$$(c_{p,mix} n_{tot} + \rho A_{i,s} \Delta x \ cp) \frac{dT_i}{dt} = \dot{q}_{i-1} + \dot{q}_{i+1} + H_{H2,i} + H_{H2Ov,i} + H_{H2Ol,i} -$$

$$H_{H2,i+1} - H_{H2Ov,i+1} - H_{H2Ol,i+1} - H_{H2\_out} - H_{H2Ov\_out} - H_{H2Ol\_out} \tag{51}$$

where ρ is the density, A is the area, Δx is the thickness of node i, cp is the specific heat capacity of the layer, $\dot{q}_{i-1}$ and $\dot{q}_{i+1}$ are the heat flows from the left and right nodes, and $\dot{q}_{i,f}$ is the heat flow from the gases/fluids. The derivative on the left side is the rate of change of control volume temperature (dT_i / dt).

3.3.1.1 Thermal Resistances

As shown in Figure 3-2, the heat flow for the first node takes into account the heat from the surrounding environment and the heat flow from the right node [59].

$$\dot{q}_{surr} = U_{surr} A_i (T_{surr} - T_i) \tag{52}$$

If the heat is coming from the surroundings, the overall heat transfer coefficient can be calculated by [60]:

$$U_{surr} = \frac{1}{\dfrac{\Delta x_i}{k_i} + \dfrac{1}{h_{surr}}} \tag{53}$$

where Δx is the thickness of node i, k is the thermal conductivity of node i and h_{surr} is the convective loss from the stack to the air.

The heat flow from the left node is:

$$\dot{q}_{i-1} = U_{i-1}(T_{i-1} - T_i) \tag{54}$$

where U_{i-1} is the overall heat transfer coefficient for the left node, A is the area of the layer and T is the temperature of the node. The overall heat transfer coefficient for the heat coming from Layer 1 is [60]:

$$U_{i-1} = \frac{1}{\dfrac{\Delta x_i}{k_i A_i} + \dfrac{\Delta x_{i-1}}{k_{i-1} A_{i-1}}} \tag{55}$$

The conduction from the adjacent node can be expressed as [59]:

$$\dot{q}_{i+1} = U_{i+1} A_{i+1}(T_{i+1} - T_i) \tag{56}$$

The overall heat transfer coefficient for the heat coming from node i+1 is [60]:

$$U_{i+1} = \frac{1}{\dfrac{\Delta x_{i+1}}{k_{i+1}} + \dfrac{\Delta x_i}{k_i}} \tag{57}$$

3.3.1.2 Heat Flow From Fluid/Gases in the Layer to the Solid

The conduction thermal resistance for the heat flow from the center of the gas channels to the center of the plate layer is a combination of two thermal resistances: the conduction resistance from the center of the gas channels to the interface, and the resistance from the interface to the plate surface. The heat flow from the fuel cell layers to the gases/fluids based upon the total conduction thermal resistance is given by [59]:

$$\dot{q}_{i,f} = U_{i,f}(T_i - T_{i,f})$$

(58)

where T_i is the temperature at node i, $T_{i,f}$ is the temperature of the gases/fluid at node i, and $U_{i,f}$ is the overall heat transfer coefficient, which can be expressed as:

$$U_{i,f} = \frac{1}{\dfrac{\Delta x_i}{k_i A_{i,s}} + \dfrac{1}{h_f A_{void}}}$$

(59)

where Δx_i is the thickness of the solid portion of the layer at node i, k_i is the thermal conductivities of the solid and gases respectively, h_f is the convective heat transfer coefficient and $A_{i,s}$ and A_{void} is the area of the solid and gases respectively.

The area of solid portion of the layer is:

$$A_{i,s} = A - A_{void}$$

(60)

And the channel area is calculated by:

$$A_{void} = w_{chan} \times L_{chan}$$

(61)

where w_{chan} is the width of the channel, and L_{chan} is the length of the channel.

3.3.2 Flow Field Plate

In the fuel cell stack, the flow field plates separate the reactant gases of adjacent cells, connect the cells electrically, and act as a support structure. The flow field plates have reactant flow channels on both sides, forming the anode and cathode compartments of the unit cells on the opposing sides of the flow field plate. Flow channel geometry affects the reactant flow velocities, mass transfer, and fuel cell performance. Flow field plate materials must have high conductivity and be impermeable to gases. The material should also be corrosion-resistant and chemically inert due to the presence of reactant gases and catalyst. An illustration of the energy balance is shown in Figure 3.4.

Anode Flow Field Energy Balance   Cathode Flow Field Energy Balance
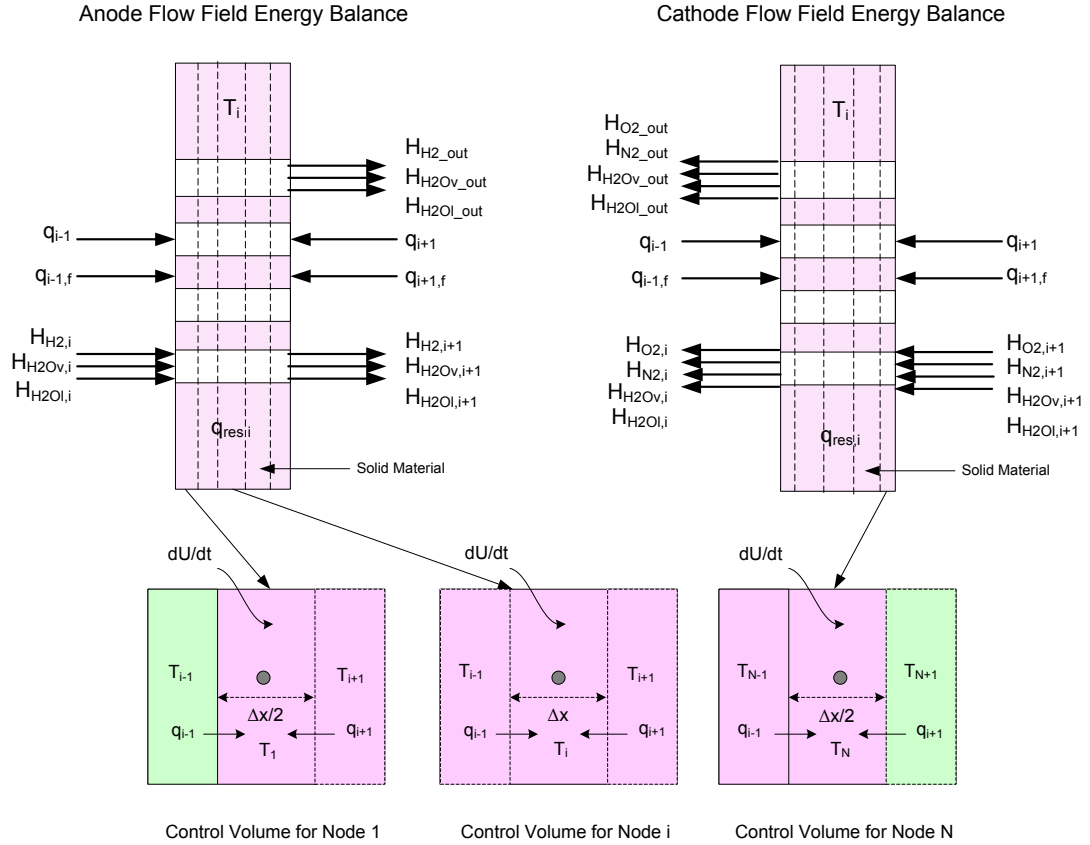
Figure 3.4. Anode and cathode flow field plate energy balance

The flow field plate has both conductive and convective heat transfer due to the gas channels in the plate. The total area of the flow field plate that has channels affects the heat transfer of the overall plate; therefore, this is accounted for by calculating the effective cross-sectional area for conduction heat transfer, A1R, which represent the area of the solid material in contact with the previous and next node. The equation for heat transfer in the anode flow field plate can be written as [59]:

$$(c_{p,mix}n_{tot} + \rho A_{i,s}\Delta x\ cp)\frac{dT_i}{dt} = \dot{q}_{i-1} + \dot{q}_{i+1} + \dot{q}_{i-1,f} + \dot{q}_{i+1,f} + \dot{q}_{i,f} + \dot{q}_{res,i} + H_{H2,i} + H_{H2Ov,i} +$$

$$H_{H2Ol,i} - H_{H2,i+1} - H_{H2Ov,i+1} - H_{H2Ol,i+1} - H_{H2\_out} - H_{H2Ov\_out} - H_{H2Ol\_out} \qquad (62)$$

where ρ is the density of the layer, A is the area of the layer, cp is the specific heat capacity of the layer, $\dot{q}_{i-1}$ is the gas heat flow from the previous node, $\dot{q}_{i-1,R}$ is the heat flow from the previous node to the solid material, $\dot{q}_{i+1}$ is the gas heat flow from the next node, $\dot{q}_{i+1,R}$ is the heat flow from the next node to the solid material, $\dot{q}_{res,i}$ is the heat generation in the layer due to electrical resistance, and H_i is the enthalpy of species i coming into or out of the current node. The derivative on the left side is the rate of change of control volume temperature (dT_i / dt). The heat flows coming from the right and left layer will transfer a different amount of heat from the layer to the solid and gas flow in the channels.

The area of the flow field layers for axial heat flow through the plate is given by the following equation:

$$A_{void} = w_{chan} \times L_{chan} \tag{63}$$

where w_{chan} is the width of the flow channel, and L_{chan} is the total length of the flow channel in the layer.

The heat flows are written similarly to Equations 52 through 57 both the anode and cathode flow field plates. For the anode shown in Figure 3.4, the heat flow from the previous layer to the channels is:

$$\dot{q}_{i-1} = U_{i-1} A_{i-1} (T_{i-1} - T_i) \tag{64}$$

where A_{i-1} is the area of the channels. The heat flow from the previous node to the solid material is:

$$\dot{q}_{i-1,f} = U_{i-1,f}(T_{i-1} - T_i)$$

<div align="right">(65)</div>

where $A_{i-1,R}$ is the area of the solid. The heat flow from the next node to the channels is:

$$\dot{q}_{i+1} = U_{i+1}A_{i+1}(T_{i+1} - T_i)$$

<div align="right">(66)</div>

The heat flow from the next node to the solid material is:

$$\dot{q}_{i+1,f} = U_{i+1,f}(T_{i+1,f} - T_i)$$

<div align="right">(67)</div>

where A_{void} is the area of the channels in the plate, and A_{1R} is the area of the solid material. The enthalpy of each gas or liquid flow into or out of the layer can be defined as:

$$H_i = n_i h_i T_i$$

<div align="right">(68)</div>

where H_i is the enthalpy of the stream entering or leaving the layer, n_i is the molar flow rate of species i, h_i is the enthalpy of species i at the temperature of the node (T_i).

The overall heat transfer coefficient term for the previous node can be calculated as [60]:

$$U_{i-1} = \frac{1}{\dfrac{\Delta x_i}{k_i A_{i,s}} + \dfrac{\Delta x_{i-1}}{k_{i-1} A_{i-1,s}}}$$

<div align="right">(69)</div>

The overall heat transfer coefficient term for the heat flow from fluid/gases in left node:

$$U_{i-1,f} = \frac{1}{\dfrac{\Delta x_i}{k_i A_{i,s}} + \dfrac{1}{h_{i-1,f} A_{i-1,void}}}$$

(70)

The overall heat transfer coefficient for the heat coming from node i+1 is [60]:

$$U_{i+1} = \frac{1}{\dfrac{\Delta x_{i+1}}{k_{i+1} A_{i+1,s}} + \dfrac{\Delta x_i}{k_i A_{i,s}}}$$

(71)

The overall heat transfer coefficient term for the heat flow from fluid/gases in right node:

$$U_{i+1,f} = \frac{1}{\dfrac{1}{h_{i+1,f} A_{i+1,void}} + \dfrac{\Delta x_i}{k_i A_{i,s}}}$$

(72)

3.3.3 Anode/Cathode Gas Diffusion Layer

The gas diffusion layer (GDL) is located between the flow field plate and the catalyst layer. This layer allows the gases and liquids to diffuse through it in order to reach the catalyst layer. The GDL has a much lower thermal conductivity than the flow field plates and other metal components in the fuel cell; therefore, it partially insulates the heat-generating catalyst layers. When modeling the heat transfer through this layer, the solid portion has conductive heat transfer, and the gas/liquid flow has advective heat transfer. An illustration of the energy balance is shown in Figure 3.5.
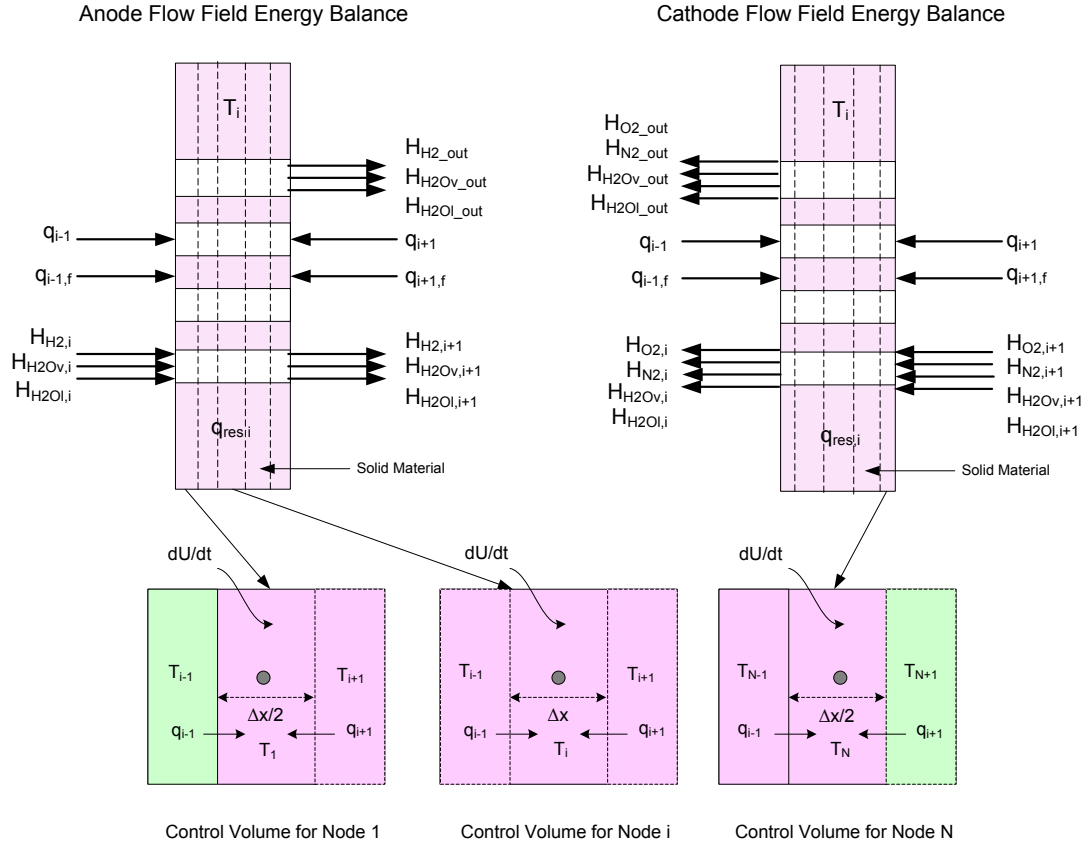
Figure 3.5. GDL energy balance

Heat is generated in the GDL due to ohmic heating. Since the GDL has high ionic conductivity, ohmic losses are negligible compared with the catalyst and membrane layers. The overall energy balance equation for the anode GDL can be written as:

$$(c_{p,mix}n_{tot} + \rho A \Delta x \ cp)\frac{dT_i}{dt} = \dot{q}_{i-1} + \dot{q}_{i-1,f} + \dot{q}_{i+1} + \dot{q}_{res,i} + H_{H2,i} + H_{H2Ov,i} + H_{H2Ol,i} -$$
$$H_{H2,i+1} - H_{H2Ov,i+1} - H_{H2Ol,i+1} \tag{73}$$

The overall energy balance equation for the cathode GDL can be written as:

$$(c_{p,mix}n_{tot} + \rho A \Delta x \ cp)\frac{dT_i}{dt} = \dot{q}_{i-1} + \dot{q}_{i+1} + \dot{q}_{i+1,f} + \dot{q}_{res,i} + H_{H2,i} + H_{H2Ov,i} + H_{H2Ol,i} -$$
$$H_{H2,i+1} - H_{H2Ov,i+1} - H_{H2Ol,i+1} \tag{74}$$

74

3.3.4 Anode/Cathode Catalyst Layer

The anode and cathode catalyst layer is a porous layer made of platinum and carbon. It is located on either side of the membrane layer. When modeling the heat transfer through this layer, the solid portion has conductive heat transfer, and the gas/liquid flow has advective heat transfer. Figure 3.6 shows the energy balance of the catalyst layer.
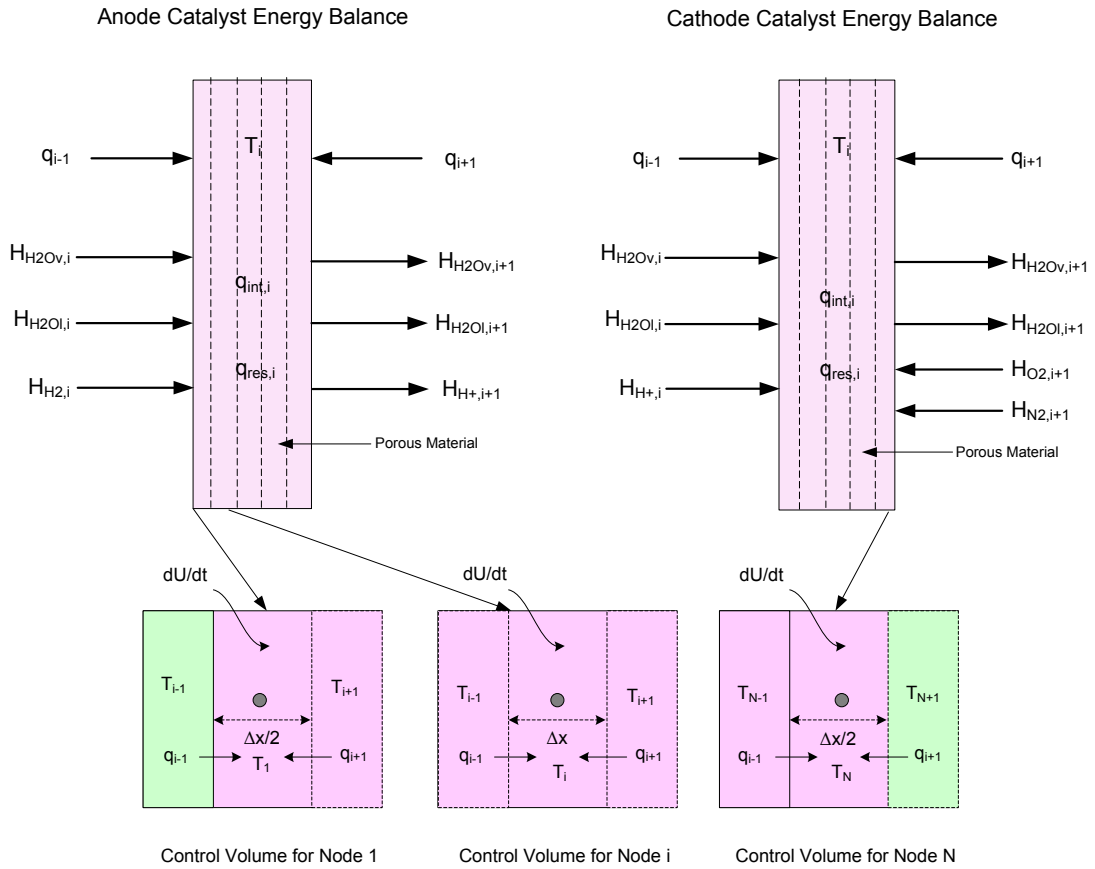
Figure 3.6. Catalyst energy balance

The overall energy balance equation for the anode and cathode energy balance can be written [4, 59]:

$$(c_{p,mix}n_{tot} + \rho A \Delta x \; cp)\frac{dT_i}{dt} = \dot{q}_{i-1} + \dot{q}_{i+1} + \dot{q}_{res,i} + \dot{q}_{int,i} + H_{H2,i} + H_{H2Ov,i} + H_{H2Ol,i} -$$
$$H_{H2,i+1} - H_{H2Ov,i+1} - H_{H2Ol,i+1} \tag{75}$$

The heat generation in the catalyst layer is due to the electrochemical reaction and voltage overpotential. The heat generation term in the catalyst layer can be written as [58]:

$$\dot{q}_{int,i} = \frac{i}{\Delta x_i}\frac{T_i \Delta S}{nF} + \upsilon_{act} \tag{76}$$

where T_i is the local catalyst temperature, i is the current density, Δx_i is the node thickness, n is the number of electrons, F is Faraday's constant, ΔS is the change in entropy and υ_{act} is the activation overpotential. The entropy change at standard state with platinum catalyst is taken as $\Delta S = 0.104$ J mol−1 K−1 for the anode, and

$\Delta S = -326.36$ J mol−1 K−1 for the cathode. The activation over-potential (υ_{act}) was calculated using the Butler-Volmer equation.

3.3.5 Membrane

The PEM fuel cell membrane layer is a persulfonic acid layer that conducts protons, and separates the anode and cathode compartments of a fuel cell. The most commonly used type is DuPont's Nafion® membranes. The dominant mode of heat transfer in the membrane is conduction. An illustration of the energy balance is shown in Figure 3.7.
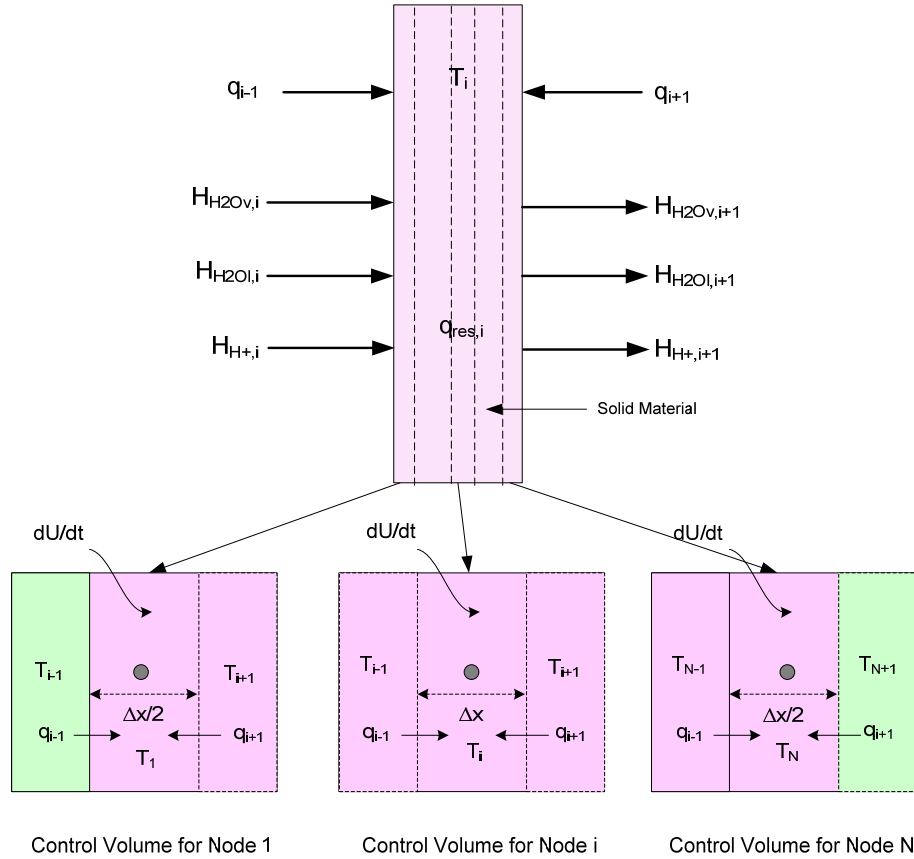
Figure 3.7. Membrane energy balance

The overall energy balance equation can be written as:

$$(c_{p,mix}n_{tot} + \rho A \Delta x \ cp)\frac{dT_i}{dt} = \dot{q}_{i-1} + \dot{q}_{i+1} + \dot{q}_{res,i} + \dot{q}_{int,i} + H_{H+,i} + H_{H2Ov,i} + H_{H2Ol,i} -$$
$$H_{H+,i+1} - H_{H2Ov,i+1} - H_{H2Ol,i+1} \tag{77}$$

Note that the heat generation term in the membrane consists of Joule heating only.

3.4 Heat Generated by Electrical Resistance

The rate at which energy is created by passing current, i, through a medium of electrical resistance is [43, 49]:

$$q_{res,i} = i^2 R \tag{78}$$

If the layer material is ohmic, the resistance can be found by [49]:

$$R = \frac{\rho_{res,i} \Delta x_i}{A_i} \tag{79}$$

If the layer conducts electricity (such as the contact layer), then there is an additional heat generation in node i ($q_{res,i}$) due to electrical resistance, which can be calculated as:

$$\dot{q}_{res,i} = i^2 \left(\frac{\rho_{res,i} \Delta x_i}{A_i} \right) \tag{80}$$

where i is the current density, A is the area of the layer, $\rho_{res,i}$ is the specific resistance of the material, Δx_i is the thickness of the layer and t is the amount of time that the current is flowing (sec). There is no heat generated in the end plate, contact or gasket layers. However, in some fuel cell stack designs, the end plate may be heated; therefore, an additional heat generation term would need to be added to the model formulation.

3.5 Heat Transfer to Gases

The conduction thermal resistance for the heat flow from the center of the plate layer to the center of the gas channels is a combination of two thermal resistances: the conduction resistance from the center of the plate surface to the interface, and the resistance from the interface to the center of the gas channels. The channel energy balance is shown in Figure 3.8.
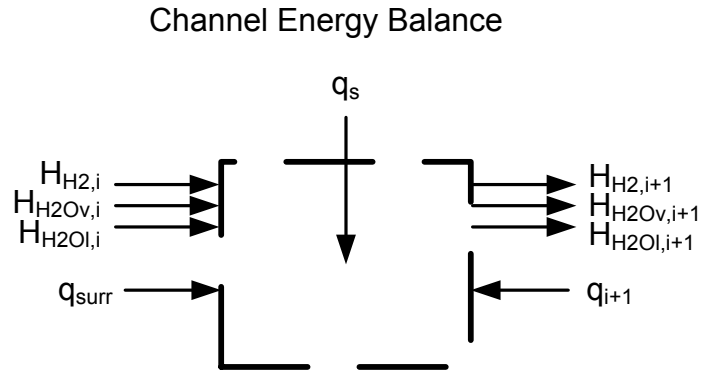
Figure 3.8. Energy balance for channels or void space in the fuel cell layers

The overall channel energy balance equation can be written as:

$$(c_{p,mix} n_{tot}) \frac{dT_{i,f}}{dt} = \dot{q}_{i-1} + \dot{q}_{i+1} + \dot{q}_{i,s} \; H_{H2,i} + H_{H2Ov,i} + H_{H2Ol,i} -$$

$$H_{H2,i+1} - H_{H2Ov,i+1} - H_{H2Ol,i+1} - H_{H2\_out} - H_{H2Ov\_out} - H_{H2Ol\_out} \qquad (81)$$

The heat flow from the fuel cell layer nodes to the center of the channel is based upon the total conduction thermal resistance is given by:

$$\dot{q}_{i,s} = U_{i,s}(T_{i,s} - T_i) \tag{82}$$

where T_i is the temperature at node i, $T_{i,s}$ is the temperature of the solid at node i, and $U_{i,s}$ is the overall heat transfer coefficient, which can be expressed as:

$$U_{i,s} = \cfrac{1}{\cfrac{\Delta x_i}{k_i A_{i,s}} + \cfrac{1}{h_f A_{void}}} \tag{83}$$

where Δx_i is the thickness of the solid portion of the layer at node i, k_i is the thermal conductivities of the solid and gases respectively, h_f is the convective heat transfer coefficient and $A_{i,s}$ and A_{void} is the area of the solid and gases respectively.

The area of solid portion of the layer is:

$$A_{i,s} = A - A_{void} \tag{84}$$

And the channel area is calculated by:

$$A_{void} = w_{chan} \times L_{chan} \tag{85}$$

where w_{chan} is the width of the channel, and L_{chan} is the length of the channel.

3.6 Convective Heat Transfer Coefficient

The calculation of the heat transfer coefficient is critical for obtaining a precise heat transfer model. In order to obtain the convective heat transfer coefficient, the procedure is as follows [61]:

1. Calculate the fluid properties including the viscosity and thermal conductivity.

2. Calculate the Reynold's number from the fluid properties and duct geometry.

3. Calculate the flow regime from the Reynold's number.

4. Calculation of the Nusselt number and convective heat transfer coefficient.

The properties of the gases are needed to evaluate the convective heat transfer coefficient at each wall. To calculate the dynamic viscosity of the components in a gas stream as a function of temperature, a fifth order polynomial is used with the constants in Table 3.1:

$$\mu = \sum_{n=1}^{6} a_{\mu,n} \left(\frac{T}{1000} \right)^n \tag{86}$$

Table 3.1

Polynomial coefficients for calculating dynamic viscosity

Constant	Hydrogen	Oxygen	Water
A	15.553	-169.18	-6.7541
B	299.78	889.75	244.93
C	-244.34	-892.79	419.50
D	249.41	905.98	-522.38
E	-167.51	-598.36	348.12
F	62.966	221.64	-126.96
G	-9.9892	-34.754	19.591

A similar expression is used for thermal conductivity with the constants in Table 3.2 [61]:

$$k = 0.01 \sum_{n=1}^{6} a_{k,n} \left(\frac{T}{1000} \right)^{n} \tag{87}$$

Table 3.2

Polynomial coefficients for calculating thermal conductivity

Constant	Hydrogen	Oxygen	Water
A	1.5040	-0.1857	2.0103
B	62.892	11.118	-7.9139
C	-47.190	-892.79	419.50
D	249.41	-7.3734	35.922
E	-31.939	-4.1797	35.993
F	11.972	1.4910	-18.974
G	-1.8954	-0.2278	4.1531

Since the model presented in this study predicts the temperatures and compositions locally, at each point in the cell, the evaluation of the heat transfer coefficients must include a dependence on position and composition inside the cell. The Nusselt number is typically calculated from correlations fitted to empirical data, and most of these studies give average values for Nu along the whole duct, and only a few of them are applicable to local studies [61].

$$Nu = \frac{(f/8)(\text{Re}-1000)\,\text{Pr}}{1+12.7\sqrt{(f/8)}(\text{Pr}^{2/3}-1)}\left(1+\left(\frac{D_h}{L}\right)^{2/3}\right) \tag{88}$$

$$f = \frac{1}{0.79\ln(\text{Re})-1.64} \tag{89}$$

Gnielinski's equation is used to evaluate Nu, and it is applicable to Re > 2300, 0.5 < Pr < 2000 and L > Dh. In the literature, simpler equations are often used such as Colburn's, which is valid for Re > 10,000, 0.7 < Pr < 160 and L > 10Dh. This correlation is easier to evaluate, but can lead to errors as high as 20% [59]. In addition, many of the flows within the cell are from 2300 to 10,000, and the values from this equation are significantly higher than when using Gnielinski's equation.

The convective heat transfer coefficient is evaluated directly from the value of Nu using the following equation [61]:

$$h = \frac{Nu \cdot k}{D_h} \tag{90}$$

where D_h is calculated at the axial position. The literature shows a slight underestimation

of Nu, however, the error is very small, and does not substantially increase the uncertainty in the value of the heat transfer coefficients.

Liquid or gas flow confined in channels can be laminar, turbulent, or transitional and is characterized by an important dimensionless number known as the Reynold's number (Re). This number is the ratio of the inertial forces to viscous forces and is given by [2, 46]:

$$\text{Re} = \frac{\rho v_m D_{ch}}{\mu} = \frac{v_m D_{ch}}{v}$$
(91)

where v_m is the characteristic velocity of the flow (m/s), Dch is the flow channel diameter or characteristic length (m), ρ is the fluid density (kg/m^3), μ is the fluid viscosity (kg/(m*s)), and v is the kinematic viscosity (m^2/s). When Re is small (< 2000), the flow is laminar. When Re greater than 4000, the flow is turbulent. When Re is between 2000 and 4000, it is know to be in the "transitional" range, where the flow is mostly laminar, with occasional bursts of irregular behavior. The flow in fuel cell channels usually falls in the laminar flow regime.

The velocity (m/s) in a fuel cell channel near the entrance of the cell is [59]:

$$v = \frac{v_{H2\_in}}{A_{ch}} \text{ where } A_{ch} = \frac{1}{2}\pi r^2$$
(92)

where r is the radius of the flow channel.

The specific heat capacity (J/molK) of hydrogen and oxygen were obtained from the shomate equations NIST chemistry webbook [62]:

$$c_p = A + B*t + C*t^2 + D*t^3 + E/t^2 \tag{93}$$

The enthalpy of each gas (J/mol) can be calculated by [62]:

$$h = At + \frac{Bt}{2} + \frac{Ct^2}{3} + \frac{Dt^3}{4} + \frac{E}{t} + F \tag{94}$$

where t is given by:

$$t = \frac{T_{f,i}}{1000} \tag{95}$$

where, A, B, C, D, and E can be obtained from Table 3.3, and t is T/1000.

Table 3.3

Polynomial coefficients for calculating specific heat capacity and formation enthalpies

Constant	Hydrogen (T=298-1000k)	Oxygen (T=298-6000K)	Water Vapor	Liquid Water
A	33.066178	29.659	30.09200	-203.6060
B	-11.363417	6.137261	6.832514	1523.290
C	11.432816	-1.186521	6.793435	3196.413
D	-2.772874	0.095780	-2.534480	2474.455
E	-0.158558	-0.219663	0.082139	3.855326
F	-9.980797	-9.861391	-250.8810	-256.5478

The specific heat capacity of the mixture can be calculated by [45]:

$$c_{p,mix} = x_i c_{p,i} + x_j c_{p,j} \tag{96}$$

4
MASS, CHARGE AND PRESSURE DROP MODEL

Mass, charge and pressure drop phenomena are all important when characterizing fuel cell performance. The fuel cell must be supplied continuously with fuel and oxidant, and product water must be removed continually to insure proper fuel and oxidant at the catalyst layers to maintain high fuel cell efficiency. High fuel and oxidant flow rates sometimes insure good distribution of reactants, but if the flow rate is too high, the fuel may move too fast to diffuse through the GDL and catalyst layers. If it is too low, the fuel cell will loose efficiency. Mass transport in the fuel cell GDL and catalyst layers are dominated by diffusion due to the tiny pore sizes of these layers (2 to 10 microns). In a flow channel, the velocity of the reactants is usually slower near the walls; therefore, this aids the flow change from convective to diffusive.

The pressure drop of the mixture gas in the fuel cell flow channels have rarely been considered in the fuel cell literature. However, in industrial design, it is a very important characteristic because it directly affects the efficiency of a fuel cell system, and is directly related to the selection of the system pump. In addition, since increased pressures within the fuel cell increase the overall fuel cell performance, it is very helpful to know the local pressures inside the fuel cell to better optimize the fuel cell design. A schematic of convective and diffusive mass transport in the fuel cell layers is shown in Figure 4.1.
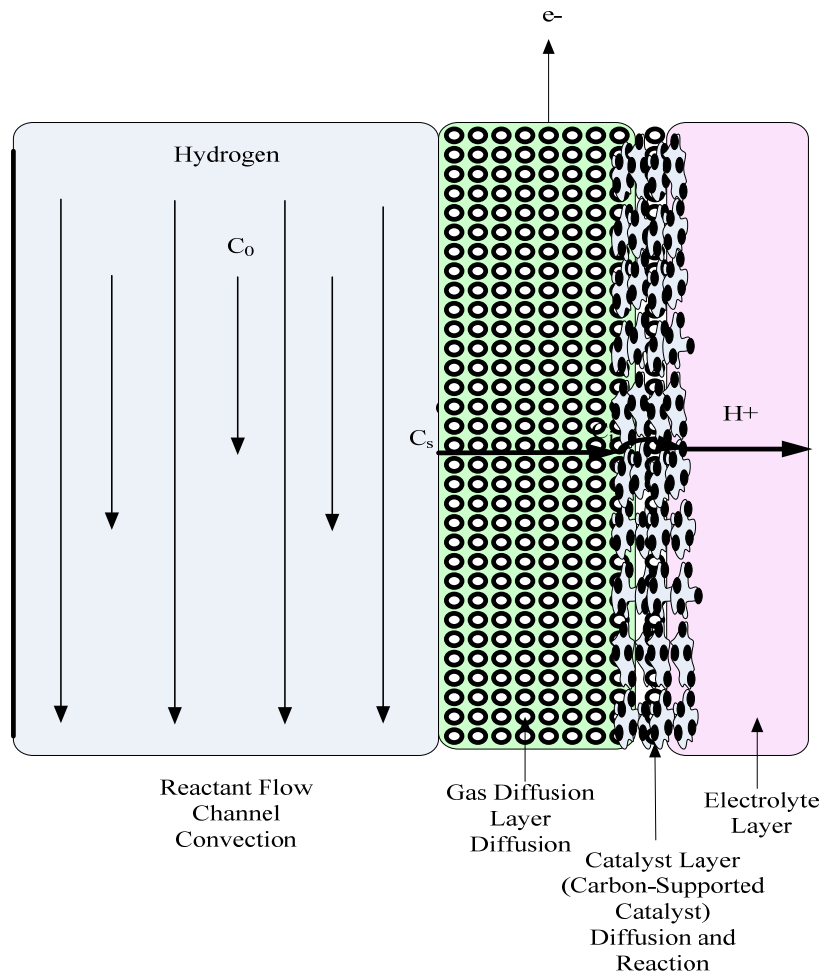
Figure 4.1. Fuel cell layers (flow field, gas diffusion layer, and catalyst layer) that have

convective and diffusive mass transport [4]

The transport of charges is also very important since efficient charge transport

ensures the highest possible electricity produced by the fuel cell stack. The two major

types of charged particles are electrons and ions, and both electronic and ionic losses

occur in the fuel cell. The electronic loss between the bipolar, cooling and contact plates

are due to the degree of contact that the plates make with each other due to the

compression of the fuel cell stack. The ionic losses occur in the membrane; therefore, ensuring optimal ionic transport is critical for good fuel cell performance. A charge balance only needs to be conducted on the layer if it conducts electrons.

The general mass balance equations presented in this chapter are used both for the outlet and inlet of each fuel cell stack layer. For the end plates, gaskets, contacts, and flow field plate layers, the mole fractions are determined using the saturation pressure equations. In the MEA layers (the GDL, catalyst and membrane layers), the same mass balance equations are used. However, more sophisticated methods of determining the mole fractions or concentrations are used due to diffusive transport in these layers. These are then substituted into the overall mass balance equation to obtain the rate of mass accumulation. An illustration of the mass, energy and charge balances in a layer are shown in Figure 4.2.
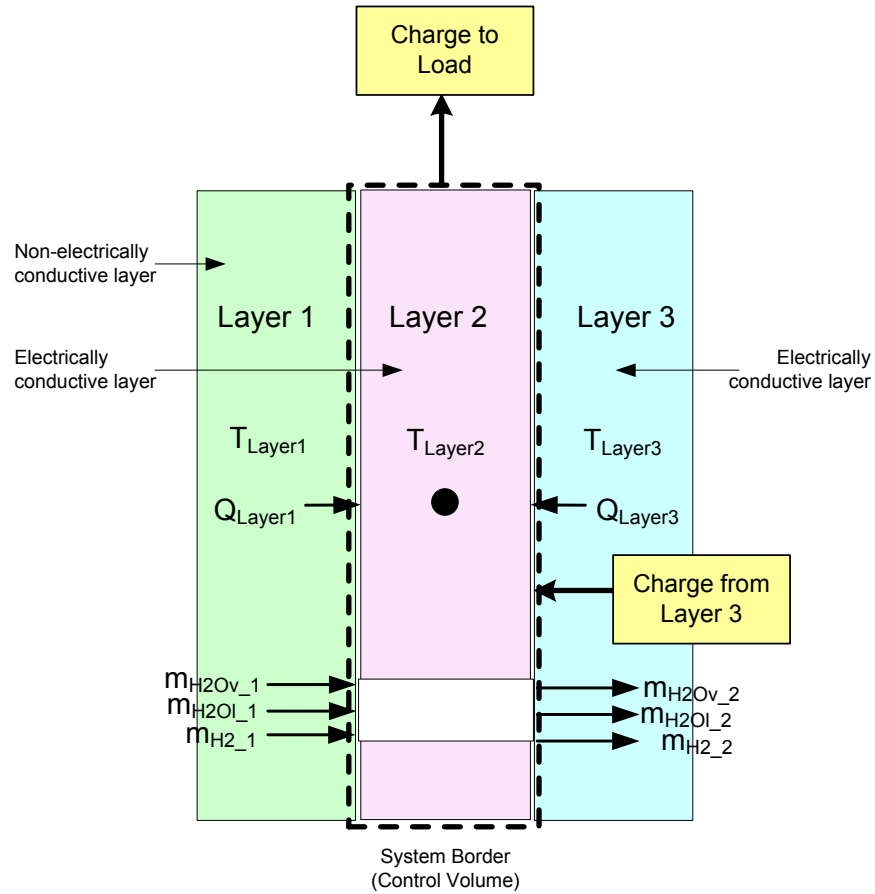
Figure 4.2. Mass, energy and charge balance around a layer

4.1 Methodology

In establishing the methodology for the mass and charge transfer, and pressure drop model, there are several important factors should be considered:

1. Mass and species conservation

2. Momentum and pressure across each layer

3. Pressure drop

Appendix H provides the detailed procedure employed for the mass, charge and pressure drop calculations discussed in this section. The five main steps in the analysis are:

1. Definition of the layers and nodes

2. Definition of the boundary conditions

3. A mass balance computation for each node.

4. A pressure drop calculation as a function of x.

5. Calculation of additional parameters such as concentration and relative humidity.

The following subsections describe each of the above steps in the nodal layer computation.

4.2 Definitions of Segments and Nodes

Figure 4.3 shows a schematic of the PEMFC stack, and the grid structure used in the fuel cell model. In the actual calculations conducted with the mathematical model, the number of segments is specified by the user, and was varied from 1 to 60 segments for the membrane layer for the outputs of this study.
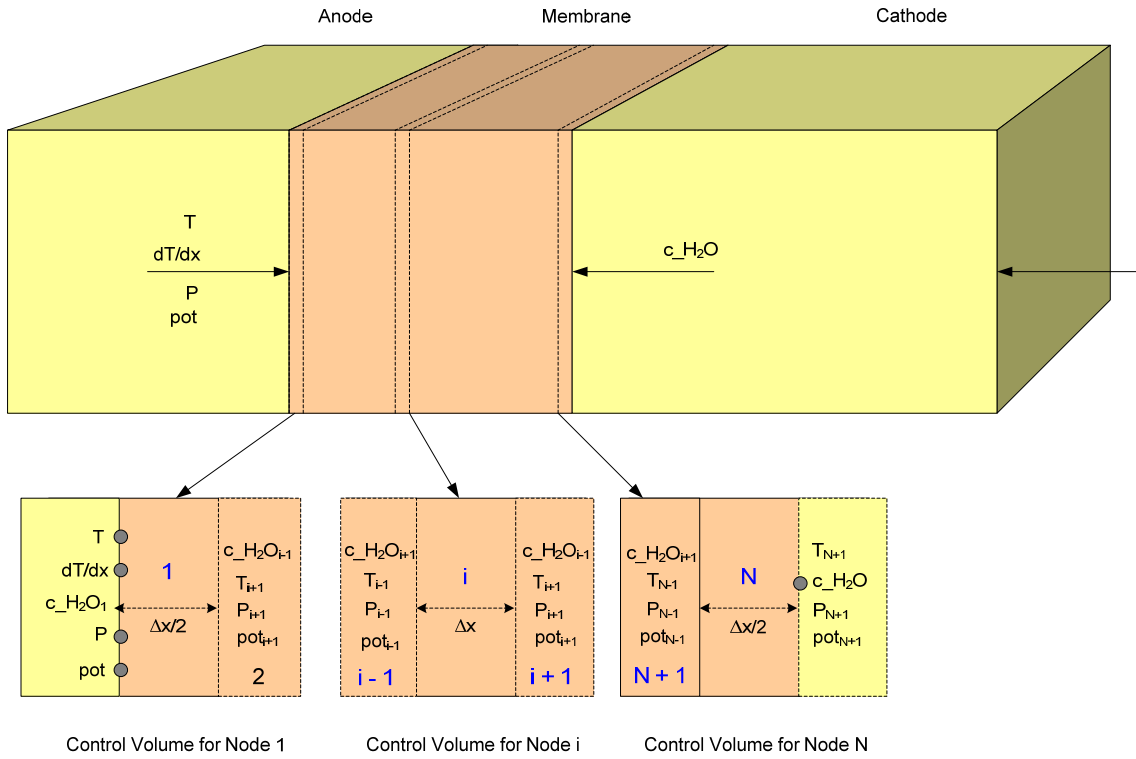
Figure 4.3. Slices created for mass, charge and pressure drop portion of the model

For the uniform distribution of nodes that is shown in Figure 4.3 the location of each node (x_i) is:

$$x_i = \frac{(i-1)}{(N-1)} L \quad \text{for } i = 1..N$$

(97)

where N is the number of nodes used for the simulation. The distance between adjacent nodes (Δx) is:

$$\Delta x = \frac{L}{N-1}$$

(98)

4.3 Boundary Conditions

The model solves for the concentration of water, potential, temperature and pressure simultaneously. In order to solve for these transient variables, initial and boundary conditions are required. At $x = 0$, four boundary conditions are necessary to fully specify the problem. These are:

For the left boundary:

$$c_{H2O,i}^m(x_i) = c_{H2O,i-1}^m(x_{i-1}) \tag{99}$$

$$T_i(x_i) = T_{i-1}(x_{i-1}) \tag{100}$$

$$\Phi_{m,i}(x_i) = \Phi_{m,i-1}(x_{i-1}) \tag{101}$$

$$P_{tot,i}(x_i) = P_{tot,i-1}(x_{i-1}) \tag{102}$$

For the right boundary:

$$c_{H2O,i}^m(x_i) = c_{H2O,i+1}^m(x_{i+1}) \tag{103}$$

$$T_i(x_i) = T_{i+1}(x_{i+1}) \tag{104}$$

$$\Phi_{m,i}(x_i) = \Phi_{m,i+1}(x_{i+1}) \tag{105}$$

$$P_{tot,i}(x_i) = P_{tot,i+1}(x_{i+1}) \tag{106}$$

4.4 Model Assumptions

The following assumptions were made for the mass, charge and pressure drop portion of the model:

1. All material thermal properties are constant over the temperature range considered.

2. The gases/fluid in each layer have ideal gas behavior.

3. The gas diffusion media is composed of void space and carbon fibers.

4. The catalyst layer is composed of carbon powder, platinum and void space, and its physcial structure is assumed to be composed of spherical agglomerates.

5. The electrochemical reaction occurs in the catalyst layer.

6. The transport of the reactants from the gas channels to the catalyst layer occurs only by diffusion to the agglomerate surface.

4.5 General Mass Balance Equations

In order to predict accurate hydrogen, oxygen and water mixture compositions throughout the fuel cell stack, accurate mass balances are required. Mass balance equations are used both for the outlet and inlet of each fuel cell stack layer. The mass balances for the end plate layer are shown in Figure 4.4.

Channel Mass Balance
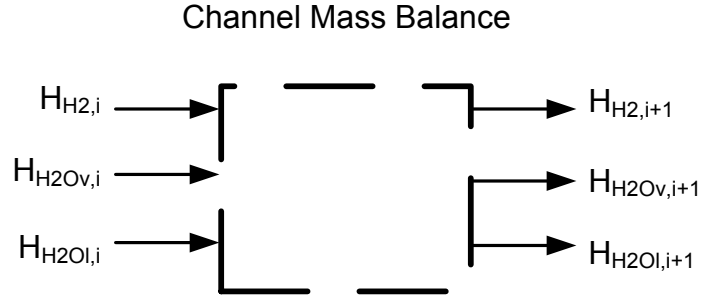
Figure 4.4. Mass balance illustration for the channels or void space in the fuel cell layers

Based upon the assumption that the mixture is regarded as an ideal gas, the volumetric flow rate is first converted to a molar flow rate using the ideal gas law [63]:

$$n_{tot\_in} = \frac{P_{in} \upsilon_{in}}{RT_{in}} \tag{107}$$

where n_{tot_in} inlet molar flow rate, P_{in} inlet pressure, υ_{in} inlet volumetric flow rate, T_{in} inlet temperature, and is the R ideal gas constant.

For transient mass balances, the total molar accumulation n_{tot} can be written as [63]:

$$\frac{dn_{tot}}{dt} = n_{tot,i} - n_{tot,i+1} \tag{108}$$

where $n_{tot,i}$ is the total molar flow rate of mixture into the control volume, and $n_{tot,i+1}$ is the total molar flow rate of mixture out of the control volume.

The rate of H_2 accumulation is:

$$\frac{d}{dt}(x_{H2}n_{tot}) = x_{H2,i}n_{tot,i} - x_{H2,i+1}n_{tot,i+1} \tag{109}$$

where $x_{H2,i}$ is the hydrogen mole fraction into the control volume, and $x_{H2,i+1}$ is the

hydrogen mole fraction out of the control volume.

The rate of O$_2$ accumulation is:

$$\frac{d}{dt}(x_{O2}n_{tot}) = x_{O2,i}n_{tot,i} - x_{O2,i+1}n_{tot,i+1} \tag{110}$$

where $x_{O2,i}$ is the oxygen mole fraction into the control volume, and $x_{O2,i+1}$ is the oxygen

mole fraction out of the control volume.

The rate of H$_2$O accumulation is:

$$\frac{d}{dt}(x_{H2O}n_{tot}) = x_{H2O,i}n_{tot,i} - x_{H2O,i+1}n_{tot,i+1} \tag{111}$$

where $x_{H2O,i}$ is the hydrogen mole fraction into the control volume, and $x_{H2O,i+1}$ is the

hydrogen mole fraction out of the control volume.

In order to calculate the mole fraction of the water vapor going into the fuel cell

stack, the first step is to calculate the vapor pressure of the inlet water vapor, $p_{H2O,i}$ [63]:

$$p_{H2O,i} = \phi_{in} P_{sat}(T_{i,f}) \tag{112}$$

where $P_{sat}(T_{i,f})$ is saturation pressure at the gas/fluid temperature at node i and ϕ_{in} is the

inlet humidity of the gas stream.

Humidity is the ratio of the mass of the vapor in one unit mass of vapor-free gas.

The humidity depends upon the partial pressure of the vapor in the mixture [64].

$$H = \frac{M_{H2O}\, p_{H2O,i}}{M_{H2}(P_{tot,i} - p_{H2O,i})} \tag{113}$$

where M_{H2O} molecular weight of water, M_{H2} molecular weight of hydrogen and $P_{tot,i}$

total pressure at node i.

The mole fraction of the water vapor is [64]:

$$x_{H2Ov,i} = \frac{\dfrac{H}{M_{H2O}}}{\dfrac{1}{M_{H2}} + \dfrac{H}{M_{H2O}}} \tag{114}$$

The molar flow rate of water vapor is:

$$n_{H2Ov,i} = x_{H2Ov,i} n_{tot,i} \tag{115}$$

The mole fraction of the liquid water in the fuel and oxidant streams entering the fuel cell stack is assumed to be zero:

$$x_{H2Ol,i} = 0 \tag{116}$$

Liquid water is included for all other nodes by calculating the molar flow rate for water condensation and evaporation using the following equation [53, 65]:

$$n_{H2Ol,i+1} = \left(\frac{k_c w_c d_c}{RT_{i,f}} \right) \frac{n_{H2Ov,i+1}}{n_{tot,i+1}} \left(P_{tot,i} - P_{sat}(T_{i,f}) \right) \tag{117}$$

where d_c channel depth (m), w_c is the channel width (m) and k_c is the evaporation and condensation rate constant (s^{-1}).

The total molar flow rate of water is:

$$n_{H2O,i} = n_{H2Ov,i} + n_{H2Ol,i} \tag{118}$$

The total mole fraction of water is:

$$x_{H2O,i} = \frac{n_{H2O,i}}{n_{tot,i}} \tag{119}$$

The mole fraction of hydrogen is:

$$x_{H2,i} = 1 - x_{H2O,i} \tag{120}$$

The molar flow rate of hydrogen is:

$$n_{H2,i} = x_{H2,i} n_{tot,i} \tag{121}$$

Total flow rate out of the layer is:

$$n_{tot,i+1} = n_{H2,i+1} + n_{H2O,i+1} \tag{122}$$

In order to present the state of water vapor and liquid water, the relative humidity (RH) and relative water content are defined as follows [53, 65]:

$$RH = \frac{n_{H2Ov,i+1}}{n_{tot,i+1}} \frac{P_{tot,i}}{P_{sat}(T_{i,f})} \tag{123}$$

Relative water content [53, 65]:

$$RW = \frac{n_{H2O,i+1}}{n_{tot,i+1}} \frac{P_{tot,i}}{P_{sat}(T_{i,f})} \tag{124}$$

4.6 Pressure Drop

The pressure drop of the gas mixture in the fuel cell literature has rarely been considered. However, in industrial design and practice, it is a significant parameter simply because it directly affects system efficiency.

In a typical flow channel, the gas moves from one end to the other at a certain mean velocity. The pressure difference between the inlet and outlet drives the fluid flow. By increasing the pressure drop between the outlet and inlet, the velocity is increased. The flow through bipolar plate channels is typically laminar, and proportional to the flow rate. The velocity (m/s) in a fuel cell channel near the entrance of the cell is [59]:

$$v_{chan} = \frac{\upsilon_{in}}{A_{ch}} \tag{125}$$

where A_{ch} is the cross-sectional area of the channel (m²), and υ_{in} inlet volumetric flow rate (m³/s).

The pressure drop can be approximated using the equations for incompressible flow in pipes [46]:

$$\frac{dP_{tot}}{dx} = f\frac{L_{chan}}{D_H}\rho\frac{\bar{v}^2}{2} + \sum K_L\rho\frac{\bar{v}^2}{2} \tag{126}$$

where f is the friction factor, L$_{chan}$ is the channel length, m, D$_H$ is the hydraulic diameter, m, ρ is the fluid density, kg/m³, $\bar{v}$ is the average velocity, m/s, and K$_L$ is the local resistance.

The hydraulic diameter for a circular flow field can be defined by [46, 59]:

$$D_{H,i} = \frac{4 \times A_c}{P_{cs}} \tag{127}$$

where A$_c$ is the cross-sectional area, and P$_{cs}$ is the perimeter. In this work, the flow field channels are rectangular, and the inlet channels through the plates are circular. For rectangular channels, the hydraulic diameter can be defined as [46, 59]:

$$D_{H,i} = \frac{2w_c d_c}{w_c + d_c} \tag{128}$$

where w$_c$ is the channel width, and d$_c$ is the depth.

The channel length can be defined as [2, 46]:

$$L_{chan} = \frac{A_{cell,i}}{N_{ch}(w_c + w_L)}$$

(129)

where A_{cell} is the cell active area, N_{ch} is the number of parallel channels, w_c is the channel

width, m, and w_L is the space between channels, m.

The friction factor can be defined by [46, 59]:

$$f_i = \frac{56}{Re}$$

(130)

Liquid or gas flow confined in channels can be laminar, turbulent, or transitional

and is characterized by an important dimensionless number known as the Reynold's

number (Re). This number is the ratio of the inertial forces to viscous forces and is given

by [46, 59]:

$$Re_i = \frac{\rho v_m D_{ch}}{\mu} = \frac{v_m D_{ch}}{v}$$

(131)

where v_m is the characteristic velocity of the flow (m/s), D_{ch} is the flow channel diameter

or characteristic length (m), ρ is the fluid density (kg/m^3), μ is the fluid viscosity

(kg/(m*s)), and v is the kinematic viscosity (m^2/s). When Re is small (< 2000), the flow

is laminar. When Re greater than 4000, the flow is turbulent, which means that it has

random fluctuations. When Re is between 2000 and 4000, it is know to be in the

"transitional" range, where the flow is mostly laminar, with occasional bursts of irregular

behavior. It is found that regardless of channel size or flow velocity, f * Re = 16 for

circular channels. The flow in fuel cell channels usually falls in the laminar flow regime with low reactant pressures.

The total outlet pressure (Pa) of each node is obtained by subtracting the pressure drop at the control volume inlet from the pressure at the inlet of the control volume [53, 65]:

$$P_{tot,i+1} = P_{tot,i} - \int_0^x \left[\frac{dP_{tot}}{dx} \right] dx \tag{132}$$

4.7 Charge Transport

Most models neglect conductivity calculations, since most metallic and carbon-based fuel cell layers have good conductivity. However, a rigorous model should include this calculation since it can become a limiting factor due to geometry or composition. Ohm's law can be used to take this into account [48]:

$$\frac{\partial \Phi_1}{\partial x} = -\frac{i}{\sigma_0} \tag{133}$$

where ε_1 and σ_0 are the volume fraction and electrical conductivity, respectively. All electrochemically conductive layers in the fuel cell (besides the MEA layers) will use Equation 133.

4.8 Flow Field Plate Layers

The transient mass balance equations, for the anode and cathode flow field plates, are similar to Equations 108 - 111, except that there is an additional term for the mass flows leaving the stack. The mass flows are illustrated in Figure 4.5.
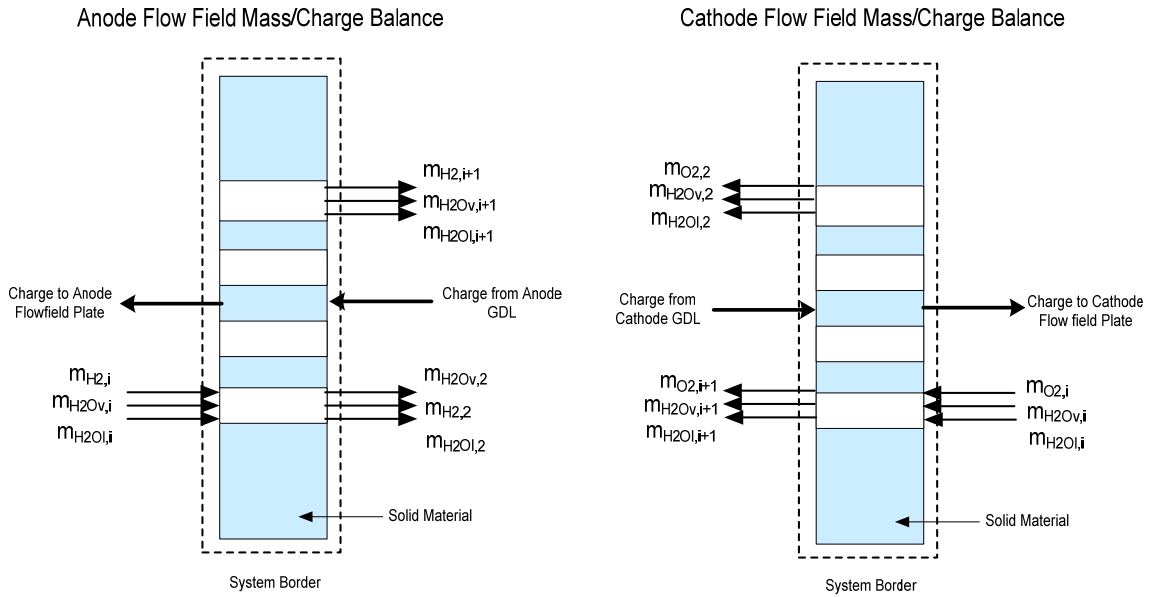
Figure 4.5. Cathode flow field plate mass/charge balance

For transient mass balances, the total molar accumulation can be written as [63]:

$$\frac{dn_{tot}}{dt} = n_{tot\_in} - n_{tot\_out} - n_{tot\_2} \tag{134}$$

The rate of H_2 accumulation is:

$$\frac{d}{dt}(x_{H2}n_{tot}) = x_{H2\_in}n_{tot\_in} - x_{H2\_out}n_{tot\_out} - x_{H2\_2}n_{tot\_2} \tag{135}$$

The rate of H_2O accumulation is:

$$\frac{d}{dt}(x_{H2O}n_{tot}) = x_{H2O\_in}n_{tot\_in} - x_{H2O\_out}n_{tot\_out} - x_{H2O\_2}n_{tot\_2} \tag{136}$$

The rate of O_2 accumulation is:

$$\frac{d}{dt}(x_{O2}n_{tot}) = x_{O2\_in}n_{tot\_in} - x_{O2\_out}n_{tot\_out} - x_{O2\_2}n_{tot\_2} \tag{137}$$

4.8.1 Diffusive Transport From the Flow Field Channels to the Gas Diffusion Layer

As shown in Figure 4.6, the reactant is supplied to the flow channel at a

concentration C_0, and it is transported from the flow channel to the concentration at the

electrode surface C_s through convection. The rate of mass transfer is then [1, 4]:

$$\dot{m} = A_i h_m (C_0 - C_s) \tag{138}$$

where A_i is the electrode surface area, and h_m is the mass transfer coefficient.
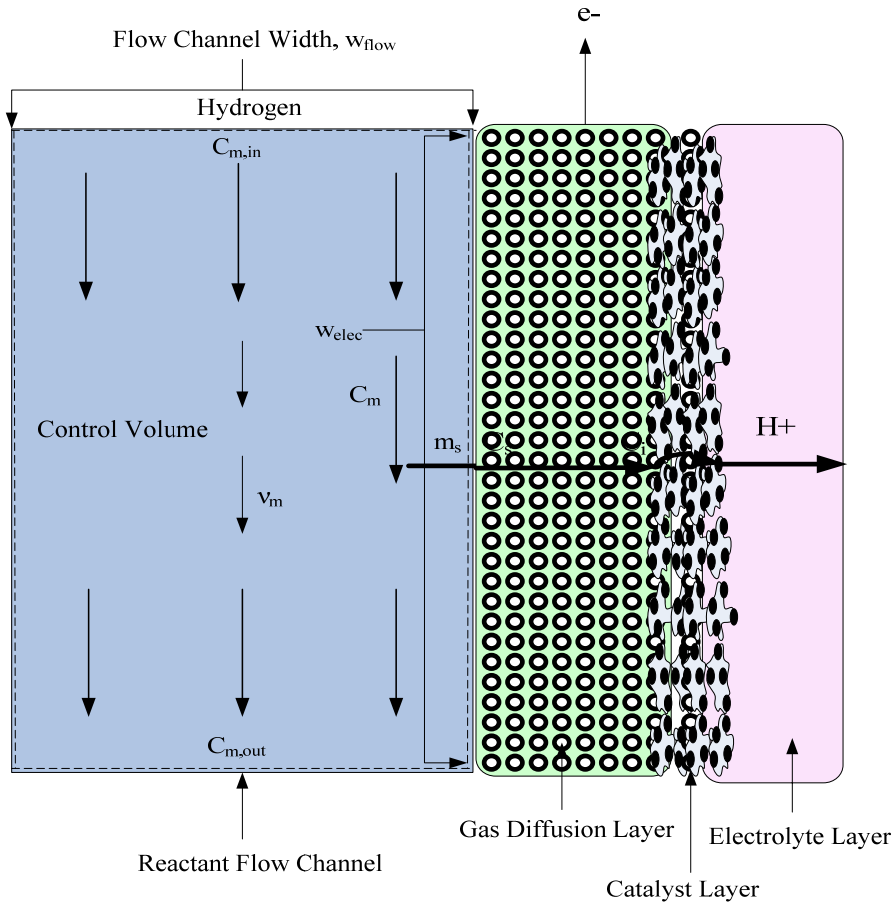
Figure 4.6. Entire channel as the control volume for reactant flow from the flow channel to the electrode layer [4]

The value of h_m is dependent upon the wall conditions, the channel geometry, and the physical properties of species i and j. The mass transfer coefficient, h_m, can be found from the Sherwood number [1, 4]:

$$h_m = Sh \frac{D_{i,j}}{D_h} \tag{139}$$

where Sh is the Sherwood number, D_h is the hydraulic diameter, and $D_{i,j}$ is the binary diffusion coefficient for species i and j given in Appendix B. The Sherwood number depends upon channel geometry, and can be expressed as [1, 4]:

$$Sh \equiv \frac{h_H D_h}{k} \tag{140}$$

where Sh = 5.39 for uniform surface mass flux ($\dot{m}$ = constant), and Sh = 4.86 for uniform surface concentration (Cs = constant).

The concentrations are calculated at the node inlet [59]:

$$C_{H2O,i} = x_{H2O,i} \left(\frac{P_{tot,i}}{RT_{i,f}} \right) \tag{141}$$

$$C_{H2,i} = x_{H2,i} \left(\frac{P_{tot,i}}{RT_{i,f}} \right) \tag{142}$$

The outlet average concentration [1, 4]:

$$C_{H2,i+1} = C_{H2,i} \exp\left(\frac{-h_m x_H}{b u_{m,i}} \right) \tag{143}$$

The average limiting current density is [1, 4]:

$$\bar{i}_L = nFh_m \left[\frac{C_{H2,i} - C_{H2,i+1}}{\ln\left(\dfrac{C_{H2,i}}{C_{H2,i+1}} \right)} \right] \tag{144}$$

4.8.2 Calculation of Pressure Drop

The flow through flow field plate channels, is typically laminar, and proportional to the flow rate. The pressure drop in the flow field and cooling layers are calculated using the same equations in addition to an equation for the increase/decrease in channel width.

The initial volumetric flow rate is first calculated for the number of inlet channels. The velocity (m/s) in the entrance of the flow field layer is [59]:

$$v_i = \frac{\left(\dfrac{n_{tot,i} * T_{f,i} * R}{P_{tot,i}} \right)}{N_{ch}} \tag{145}$$

The velocity is than calculated in each of the channel inlets using [63]:

$$v_{chan} = \frac{\upsilon_{in}}{A_{ch}} \tag{146}$$

where υ_{in} inlet volumetric flow rate (m³/s), and A_{ch} is the cross-sectional area of the channel (m²).

Often, after the reactant flow enters the entrance channel, the flow rate changes because the channel increases or decreases in cross-sectional area. The molar flow rate in each channel is calculated using the ideal gas law [63]:

$$n_{chan} = \frac{v_{chan} * P_{lay}}{T_{f,lay} * R} \tag{147}$$

In the anode and cathode flow field plates, there are two outlets: the outlet at the end of the flow channels that lead to the next layer and the outlet from the flow channels into the gas diffusion media. To calculate the flow rate from the channels to the GDL layer, the total channel length is calculated using the following equation [46]:

$$L_{chan} = \frac{A_{cell,i}}{N_{ch}(w_c + w_L)}$$ (148)

where A_{cell} is the cell active area, N_{ch} is the number of channels, w_c is the channel width, m, and w_L is the space between channels, m.

The hydraulic diameter for the rectangular flow channels is estimated using the hydraulic diameter equation for a rectangular flow field [46]:

$$D_{H,i} = \frac{2w_c d_c}{w_c + d_c}$$ (149)

where w_c is the channel width, and d_c is the depth. The Reynold's number at the channel exit can be written as [46, 59]:

$$\mathrm{Re}_i = \frac{\rho v_m D_{ch}}{\mu} = \frac{v_m D_{ch}}{v}$$ (150)

where v_m is the characteristic velocity of the flow (m/s), D_{ch} is the flow channel diameter or characteristic length (m), ρ is the fluid density (kg/m^3), μ is the fluid viscosity (kg/(m*s)), and v is the kinematic viscosity (m^2/s).

The friction factor is calculated using the formula for rectangular channels [46, 59]:

$$f_i = \frac{56}{\text{Re}}$$

(151)

The pressure drop can be approximated using the equations for incompressible flow in pipes [46]:

$$\frac{dP_{tot}}{dx} = f \frac{L_{chan}}{D_H} \rho \frac{\bar{v}^2}{2} + \sum K_L \rho \frac{\bar{v}^2}{2}$$

(152)

where f is the friction factor, L_{chan} is the channel length, m, D_H is the hydraulic diameter, m, ρ is the fluid density, kg/m3, $\bar{v}$ is the average velocity, m/s, and K_L is the local resistance.

The velocity going to the GDL layer is then calculated using the following equation [66, 67]:

$$u_{m,i} = \frac{k_i}{\mu_i \Delta x} \Delta P_{tot,i}$$

(153)

where k is the permeability (m^2), μ is the viscosity (Pa-s), Δx is the thickness of node i (m), and $\Delta P_{tot,i}$ is the change in total pressure (Pa).

4.9 Anode/Cathode Diffusion Layer

The same mass balance equations are used for the anode and cathode GDL layer, except the mass flow rates are obtained from the gas concentrations calculated using a

derivation based upon Fick's law that is shown in Appendix F. The overall mass and charge balances are illustrated in Figure 4.7.
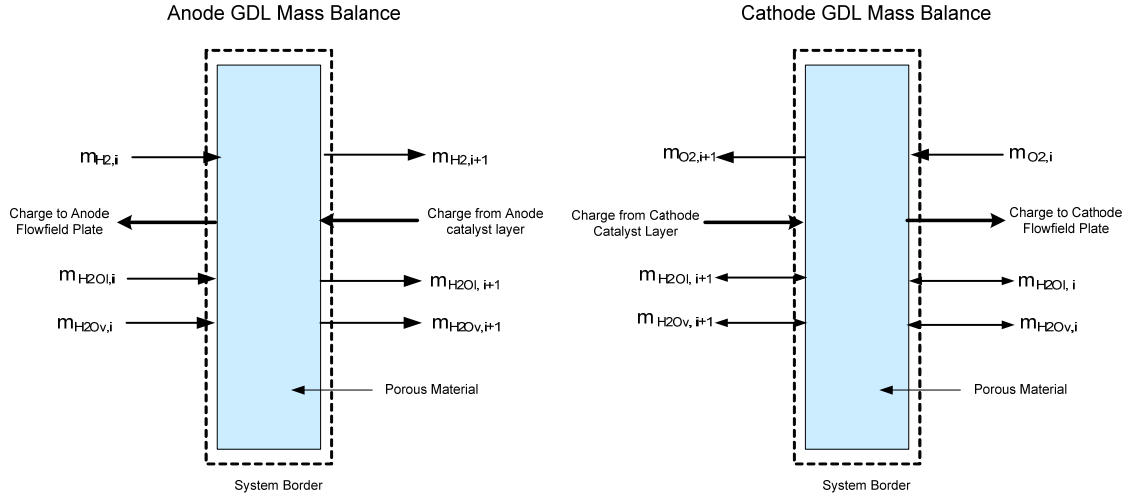
Figure 4.7. GDL mass/charge balance

The overall mass balances for the GDL layer are calculated in the same manner as described in Sections 4. 5 – 4.8. The pressure drop is calculated using Darcy's law:

$$\Delta P_{tot,i} = \frac{\mu_i \nu_i}{k_i A \varepsilon} \Delta x \tag{154}$$

where μ is the viscosity, ν is the volumetric flow rate, k is the permeability, A is the cross-sectional area (m^2), ε is the void space, and Δx thickness of node i (m).

The electrochemical reaction in the catalyst layer can lead to reactant depletion, which can affect fuel cell performance through concentration losses. In turn, the reactant depletion will also cause activation losses. The difference in the catalyst layer reactant

and product concentration from the bulk values determines the extent of the concentration loss.

The average outlet concentration can be calculated as shown in Equation 155 [1, 4]:

$$C_{H2,i+1} = C_{H2,i} \exp\left(\frac{-h_m x_H}{bu_{m,i}}\right) \qquad (155)$$

where x_H is the height of gas diffusion layer, $u_{m,i}$ is the velocity of mixture (m/s), b is the distance between flow channels and gas diffusion layer and $C_{H2,i}$ is the concentration of hydrogen at node i.

Using Fick's law, the diffusional transport through the gas diffusion layer at steady-state is [1, 4]:

$$n_{H2,i+1} = \frac{A_i D_{i,j}(C_{H2,i} - C_{H2,i+1})}{\Delta x_i} \qquad (156)$$

where C_i is the reactant concentration at the GDL/catalyst interface, and Δx_i is the gas diffusion layer thickness, and $D_{i,j}$ is the effective diffusion coefficient for the porous GDL, which is dependent upon the bulk diffusion coefficient D, and the pore structure. Assuming uniform pore size, and the gas diffusion layer is free from flooding of water, $D_{i,j}^{eff}$ can be defined as [66]:

$$D_{i,j}^{eff} = D_{i,j}\phi^{3/2} \qquad (157)$$

where ϕ is the electrode porosity.

Since the GDL layer is made of carbon, a charge transport relation is required. In order to account for porosity and tortuosity, the Bruggeman correction is used. Ohm's law is again used for charge transport [48]:

$$\frac{\partial \Phi_1}{\partial x} = -\frac{i}{\varepsilon_1^{1.5} \sigma_0} \tag{158}$$

where ε_1 and σ_0 are the volume fraction and electrical conductivity, respectively. The Bruggeman correction is used in Equation 158 to account for porosity and tortuosity. Since the GDL is often coated with Teflon to promote hydrophobicity, carbon is the conducting phase and the Teflon is insulating.

4.10 Anode/Cathode Catalyst Layer

The catalyst layer contains many phases: liquid, gas and different solids. Although various models have different equations, most of these are derived from the same governing equations, regardless of the effects being modeled. In most cases, the anode reaction can be described by a Butler-Volmer type expression, except for those which use a fuel other than pure hydrogen. In these cases, the platinum catalyst becomes "poisoned." The carbon monoxide adsorbs to the electrocatalytic sites and decreases the reaction rate. There are models in the literature that account for this by using a carbon monoxide site balance and examining the reaction steps involved. For the cathode, a Tafel-type expression is commonly used, due to the slow kinetics of the four-electron transfer reaction.

The mass and charge transport in the catalyst layer are interdependent, therefore, they are calculated together. Figure 4.8 shows the overall mass and charge balances for the anode and cathode catalyst layers.

Anode Catalyst Mass Balance

Charge to Anode Flowfield Plate

$m_{H2Ov,i}$ $m_{H2Ov,i+1}$

$m_{H2Ol,i}$ $m_{H2Ol,i+1}$

$m_{H2,i}$ $m_{H+,i+1}$

Porous Material

System Border

Cathode Catalyst Mass Balance

$m_{H+,i}$

$m_{O2,i}$

Charge to Cathode GDL layer

$m_{H2Ol,i}$ $m_{H2Ol,i+1}$

$m_{H2Ov,i}$ $m_{H2Ov,i+1}$

Porous Material

System Border
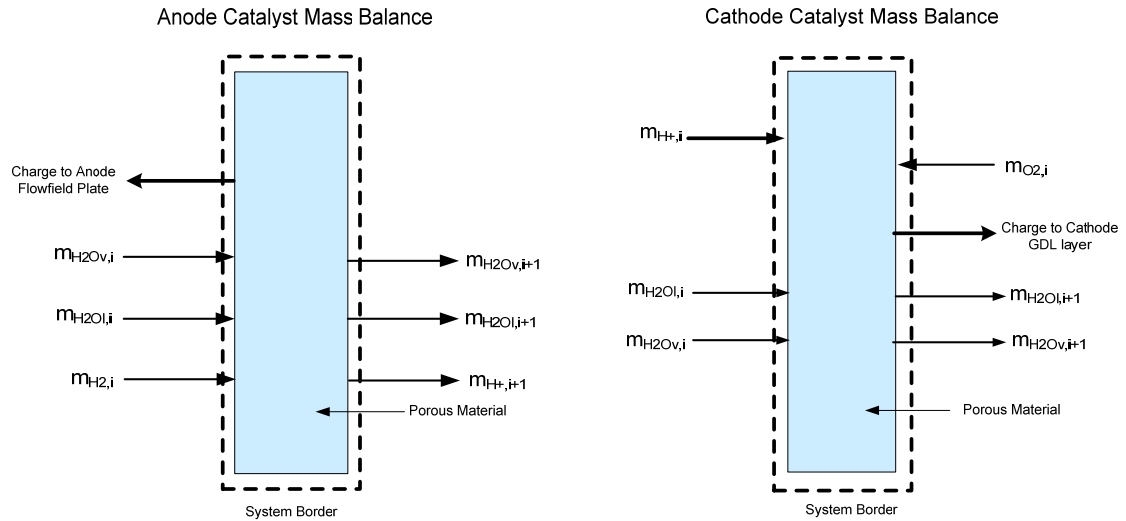
Figure 4.8. Catalyst layer mass/charge balances

The gaseous species in the anode catalyst layer are hydrogen and water. The gases are transported through the porous catalyst layer primarily through diffusion. The diffusive flux can be derived using Fick's law. The agglomerate structure for the catalyst layer was proposed by Ridge et al. [68], and has recently gained support through microscopy observations [68, 40]. Several models have assumed that the catalyst layer has a spherical agglomerate structure, and several studies have proved that this assumption provides a better fit with experimental results [68, 40, 69].

Since the cathode catalyst layer is modelled using an agglomerate approach, the kinetics expression for the total cathodic reaction rate per unit volume of electrode can be

111

written as [40, 69]:

$$\nabla \cdot i_{cath} = a_{1,2} i_{cathode} E \tag{159}$$

where $a_{1,2}$ is the specific interfacial area per unit volume of the catalyst layer, and $i_{cathode}$ is the transfer current for the oxidation reduction reaction. The solution of the mass conservation equation in spherical agglomerate yields an analytical expression for the effectiveness factor, which is the mass transfer and reaction within each agglomerate [70,71]:

$$E = \frac{1}{\phi_L} \left(\frac{1}{\tanh(3\phi_L)} - \frac{1}{3\phi_L} \right) \tag{160}$$

where ϕ_L is the Thiele modulus for the spherical agglomerate, and can be expressed as [70,71]:

$$\phi_L = \frac{r_{agg}}{3} \sqrt{\frac{k_c}{D_{O2,agg}^{eff}}} \tag{161}$$

where r_{agg} is the radius of the spherical agglomerate, which can be determined by [70,71]:

$$r_{agg} = 3 \frac{V_{agg}}{S_{agg}} \tag{162}$$

and k′ is a rate constant given by [70]:

$$k_c = \frac{a_{1,2} i_0^{ref}}{4F(1 - \varepsilon_v^{cl}) c_{O2}^{ref}} \exp\left(-\frac{\alpha_c F}{RT} (\eta_{ORR}) \right) \tag{163}$$

where a_{12} is the interfacial area between the electrically conducting and membrane phase with no flooding, i_0^{ref} is the exchange current density for the reaction, a_c is the cathodic transfer coefficient, η_{ORR} is the cathode overpotential, and the reference concentration is that concentration in the agglomerate that is in equilibrium with the reference pressure [70, 71]:

$$c_{O2}^{ref} = p_{O2}^{ref} H_{O2,agg}$$ (164)

where $H_{O2,agg}$ is Henry's constant for oxygen in the agglomerate. If external mass transfer limitations can be neglected, then the surface concentration can be set equal to the bulk concentration, which is assumed uniform throughout the catalyst layer in simple agglomerate models.

The local overpotential, η_{ORR}, can be defined as [70, 71]:

$$\eta_{ORR} = \phi_{el} - \phi_{ion}$$ (165)

The porosity of the catalyst layer, i.e. the space that is not occupied by the solid space, can be calculated using [70]:

$$\varepsilon_v^{cl} = 1 - \varepsilon_S^{cl}$$ (166)

This is the volume fraction of macro-pores for oxygen transport. The solid phase volume fraction can be calculated knowing the amounts of platinum and carbon in the catalyst layer [70, 71]:

$$\varepsilon_S^{cl} = \left(\frac{1}{\rho_{Pt}} + 1 - \frac{Pt/C}{Pt/C\rho_C} \right) \frac{m_{Pt}}{L}$$ (167)

where ρ_{Pt} and ρ_C are the platinum and carbon densities, Pt/C is the platinum to carbon ratio, m_{Pt} is the platinum loading and L is the catalyst layer thickness.

With the assumption that the catalyst layer is made of spherical agglomerates, the number of agglomerates per unit volume, n, can be written as [70]:

$$n = \frac{\hat{n}}{LH} = \frac{\varepsilon_S^{cl}}{4/3\pi r_{agg}^3} \tag{168}$$

Many models use catalyst loading, which is defined as the amount of catalyst in grams per geometric area of the fuel cell face. If a turnover frequency is desired, the reactive surface area of platinum can be used. This is related to the radius of the platinum particle, which assumes a roughness factor that is experimentally inferred using cyclic voltammetry measuring the hydrogen adsorption. These variables are used to calculate the specific interfacial area between the electrocatalyst and the electrolyte [40, 69, 70]:

$$a_{1,2} = \frac{m_{Pt} A_{Pt}}{L} \tag{169}$$

where L is the thickness of the catalyst layer. A_{Pt} is the active surface area of platinum in the catalyst layer, which can be determined with an empirical formula [70]:

$$A_{Pt} = 2.2779 \times 10^5 (Pt/C)^3 - 1.5857 \times 10^5 (Pt/C)^2 - 2.0153 \times 10^5 (Pt/C) + 1.5950 \times 10^5 \tag{170}$$

where Pt/C is the ratio of platinum catalyst and carbon powder.

The cell current versus the effectiveness factor is illustrated in Figure 4.9, and the superficial flux density of hydrogen is shown in Figure 4.10.
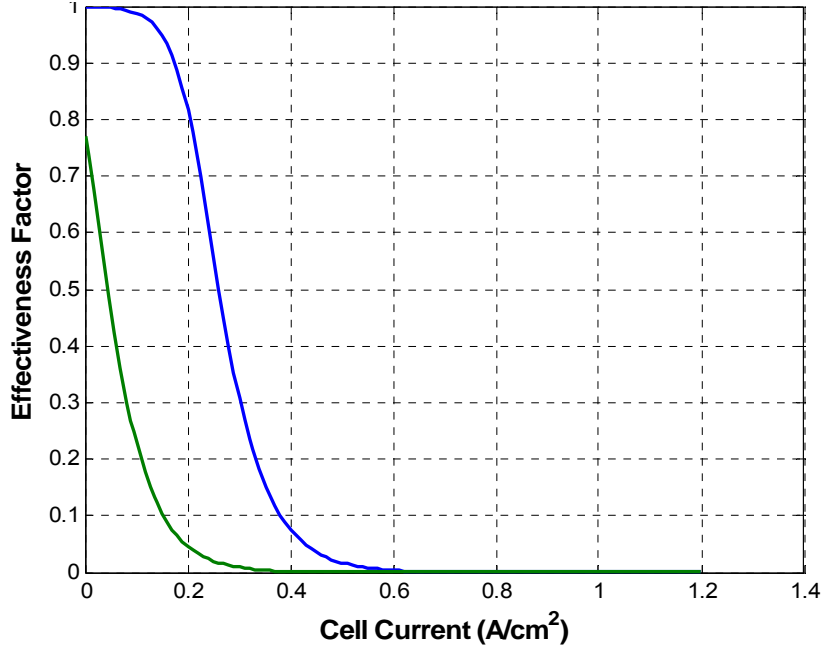
Figure 4.9. Cell current versus effectiveness factor

The hydrogen anode reaction can be written as [48, 64]:

$$\nabla \cdot i_2 = a_{1,2} i_{h,1-2} E \tag{171}$$

$$\nabla \cdot N_{H_2,G} = -\frac{1}{2F} a_{1,2}(1-S) i_{anode} E \tag{172}$$

$$i_{anode} = \left[\frac{p_{H2}}{p_{H2}^{ref}} \exp\left(\frac{\alpha_a F}{RT} \left(\upsilon_{act\_anode} \right) \right) - \exp\left(\frac{-\alpha_c F}{RT} \left(\upsilon_{act\_anode} \right) \right) \right] \tag{173}$$

The liquid water cathode catalyst reaction can be written as [48, 64]:

$$\nabla \cdot N_{H2O,L} = -\frac{1}{4F} a_{1,2}(1-S) i_{cathode} E \tag{174}$$

$$i_{cathode} = \left[\frac{p_{O2}}{p_{O2}^{ref}} \exp\left(\frac{-\alpha_c F}{RT} \left(\upsilon_{act\_cath} \right) \right) \right] \tag{175}$$

115
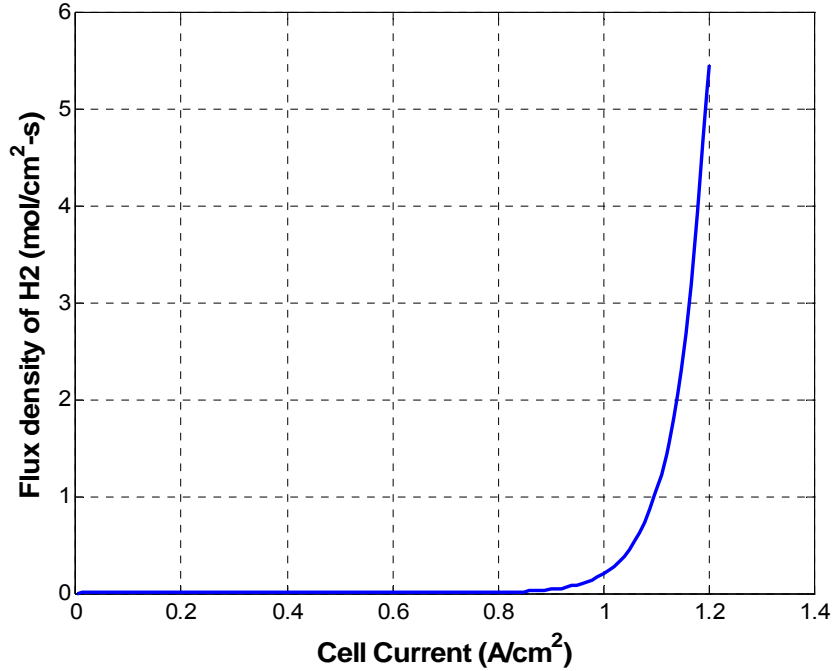
Figure 4.10. Superficial flux density of hydrogen [4]

The mass flow through the GDL layer is calculated in the same manner as described in Sections 4.5 – 4.8. However, the mass balances also need to include a term for the consumption of hydrogen or oxygen, and the water generated in the cathode catalyst layer [48, 64]:

$$n_{H2,i} = \frac{iA}{nF} \tag{176}$$

where i is the nominal cell current density, A is the cross-sectional area, F is Faraday's constant, and n is 2 for the anode and 4 for the cathode (for the number of protons and electrons transferred).

The pressure drop is calculated using Darcy's law:

$$\Delta P_{tot,i} = \frac{\mu_i v_i}{k_i A \varepsilon} \Delta x \tag{177}$$

116

where μ is the viscosity, ν is the volumetric flow rate, k is the permeability, A is the cross-sectional area (m^2), ε is the void space, and Δx thickness of node i (m).

As in the other layers, Ohm's law is used to calculate the potential [48]:

$$\frac{\partial \Phi_1}{\partial x} = -\frac{i}{\varepsilon_1^{1.5} \sigma_0} \tag{178}$$

where ε_1 and σ_0 are the volume fraction and electrical conductivity, respectively. The mass balances for the reactants should take into account the reaction and the mass transport.

5
POLYMER ELECTROLYTE MEMBRANE MODEL

In proton exchange membrane fuel cells (PEMFC), the fuel travels to the catalyst layer, and is decomposed into protons (H^+) and electrons. The electrons travel to the external circuit to power the load, and the hydrogen protons travel through the electrolyte until they reach the cathode to combine with oxygen to form water. The electrolyte layer is essential for a fuel cell to work properly. The PEMFC electrolyte must provide high ionic conductivity, present an adequate barrier to the reactants, be chemically and mechanically stable, have low electronic conductivity, be easily manufactured and preferably low-cost.

Ionic transport in polymer electrolytes follows the exponential relationship [42]:

$$\sigma T = \sigma_0 e^{-E_a / kT} \tag{179}$$

where σ_0 represents the conductivity at a reference state, and E_a is the activation energy (eV/mol). As seen in Equation 179, the conductivity increases exponentially with increasing temperature. The charged sites in the polymer have the opposite charge of the moving ions, and provide a temporary resting place for the ion. Ions are transported through the polymer membrane by hitching onto water molecules that move through the membrane. As mentioned previously, Nafion is a persulfonated polytetrafluoroethylene (PTFE)-based polymer which has high conductivity, and is currently the most popular membrane used for PEM fuel cells. Nafion has a similar structure to Teflon, but includes

sulfonic acid groups ($SO_3^-H^+$) that provide sites for proton transport. Figure 5.1 shows an illustration of the chemical structure of Nafion.
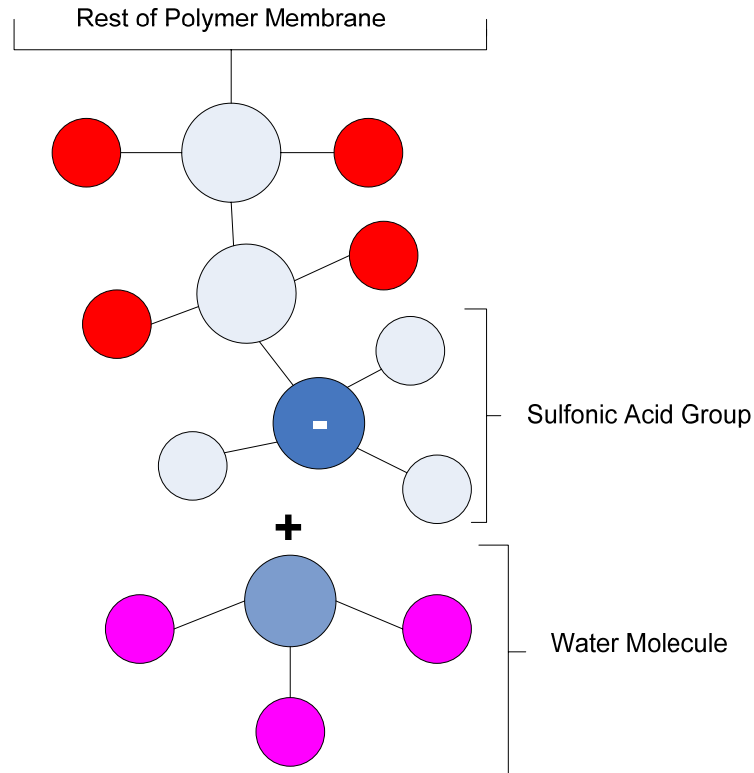
Figure 5.1. Illustration of the chemical structure of Nafion [4]

Nafion has to be fully hydrated with water in order to have high conductivity. Hydration can be achieved by humidifying the gases, or through fuel cell design to allow product water to hydrate the membrane. In the presence of water, the protons form hydronium complexes (H_3O^+), which transport the protons in the aqueous phase. When the Nafion is fully hydrated, the conductivity is similar to liquid electrolytes.

The polymer electrolyte membrane contains water and hydrogen protons, therefore, the transfer of the water and protons transfer are important phenomena to

investigate [6,7,8,72 - 75]. In addition to species transfer, the primary phenomena investigated inside the membrane are energy transfer and potential conservation [20]. For water transport, the principle driving forces modeled are a convective force, an osmotic force (i.e. diffusion), and an electric force [6,7,8,19,20,22]. The first of these results is from a pressure gradient, the second from a concentration gradient, and the third from the migration of protons from anode to cathode and their effect (drag) on the dipole water molecules. Proton transport is described as a protonic current and consists of this proton driven flux and a convective flux due to the pressure driven flow of water in the membrane [6,7,8,19,20,22]. Figure 5.2 illustrates the transport phenomena for the protons taking place within the membrane.
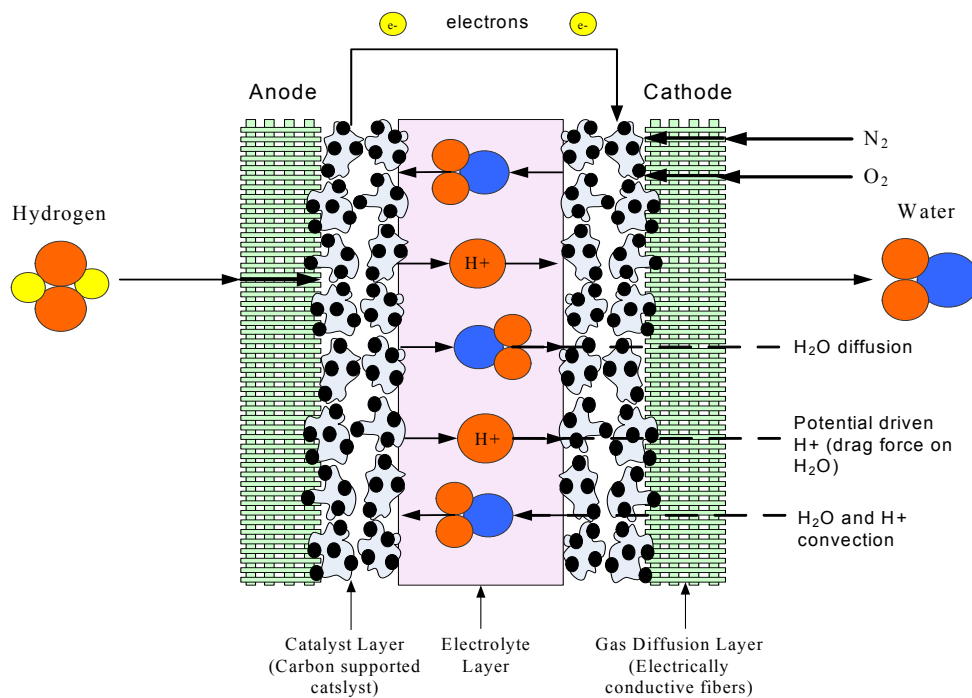
Figure 5.2. Membrane transport phenomena [4]

The dry membrane absorbs water in order to solvate the acid groups. The initial water content is associated strongly with the sites, and the addition of water causes the water to become less bound to the polymer and in turn, the water droplets to aggregate. The water clusters eventually grow and form interconnections with each other. These connections create "water channels," are transitory, and have hydrophobicities comparable to that of the matrix. A transport pathway forms when water clusters are close together and become linked. This percolation phenomenon occurs around $\lambda = 2$. The next stage occurs when a complete cluster-channel network has formed. In the last stage, the channels are now filled with liquid, and the uptake of the membrane has increased without a change in the chemical potential of water. This phenomenon is known as Schroeder's paradox. An illustration of the water uptake of the Nafion membrane is shown in Figure 5.3.
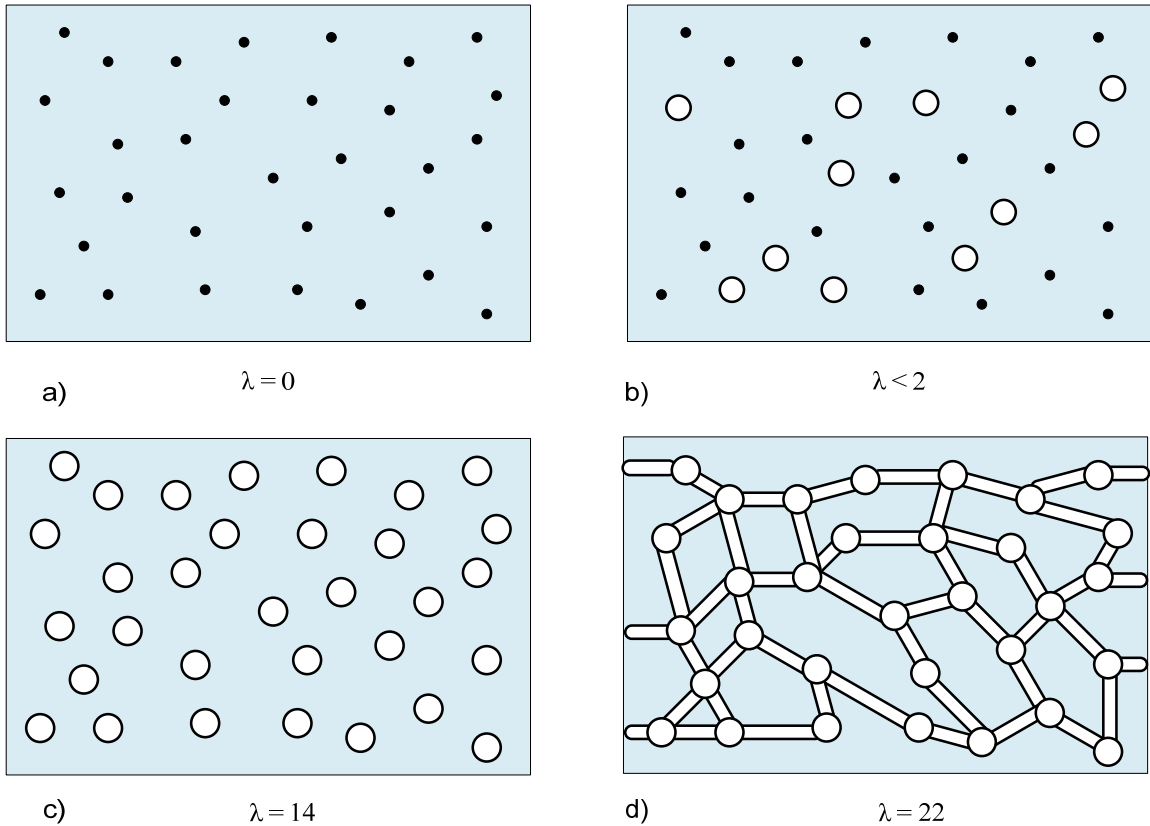
Figure 5.3. A pictorial illustration of the water uptake of Nafion [4]

5.1 Model Development

Proton exchange membrane fuel cell (PEMFC) models are necessary to predict fuel cell performance in order to optimize performance to help reduce development costs and time. Water management is critical for efficient fuel cells due to its large effect on ohmic and mass-transport overpotentials, operating conditions and membrane electrode assembly design.

Since the membrane is the key element in a fuel cell, a lot of attention has been focused on it in terms of modeling. In the literature, there are both macroscopic and microscopic models. The microscopic models focus on single ions and pore-level effects,

and the macroscopic models are typically more empirical and focus on the transport phenomena. Although the microscopic models reveal valuable information about what occurs in the membrane, they are generally too complex to use in an overall fuel cell model. The membrane system is assumed to consist of three main components: the membrane, protons and water.

The membrane model presented in this dissertation is a compact model that was integrated into the overall fuel cell stack model, and can simultaneously calculate the temperature, pressure, water concentration and potential at a user-specified number of positions through the membrane.

5.1.1 Background and Modeling Approaches

Most membrane models in the literature have been isothermal, and therefore, unsuitable for water and heat management studies. A relatively small number of models include noniosthermal effects [17, 18, 19, 77, 78], and typically, the ones that do focus on modeling multiple fuel cell layers, with simplifying assumptions for the membrane layer.

Transient models examine changes in potential and transport phenomena (flow rates, water production and current density). These models are aimed at examining different load requirements. Most models do not examine transients due to the computational cost and complexity. Some codes in the literature can take on the order of tens of minutes in certain circumstances [78]. One of the first models to examine transients in PEM fuel cells is a stack –level model by Amphlett et al. [79]. This is an empirical model that examines temperature and gas flow rates. There have been some more complex transient models that have examined the behavior of water content in the

membrane that have demonstrated the effects of the membrane drying out [22, 80]. Other transient models have either not included liquid water, do not report transient results or focuses mainly on water transport in the gas diffusion layers [15, 17, 27, 36, 77, 79, 81]. There are no results reported in the literature that simultaneously show the temperature, potential, water concentration and pressure profile in the membrane based upon varying current densities, temperatures and pressure gradients.

Verbrugge and Hill [72] and Bernardi and Verbrugge [6] developed a steady-state, isothermal, one-dimensional model for the electrochemical performance in a PEMFC. They claim that the liquid and gas pressure evolve separately in the GDL layer, which implies that they are not at equilibrium with each other. This model only applies to fully hydrated membranes, and the drag flux due on the water molecules is not taken into account.

Springer, Zawodzinski and Gottesfeld [7] presented a 1-D, steady-state isothermal model of a PEMFC with emphasis on water transport phenomena through a Nafion membrane. An improved model with a detailed treatment of ion transport and ionic conductivity in the catalyst and backing layer was developed in [8]. This model predicted the mass transport limitations at high current densities. In [73], Springer, Zawodzinski, Wilson and Gottesfeld provide experimental and theoretical results for unsteady-state effects in a 1-D isothermal PEMFC stack. They use a frequency diagram to quantify the specific influences of several sources of losses such as activity in the cathode and conductivity of the catalyst layer and the membrane.

Weisbrod, Grot, and Vanderborgh [74] developed a through the electrode model to predict fuel cell performance as a function of water balance in the channels, and across

the membrane. The model predicts the influence of both the catalyst layer thicknesses, and its Platinum catalyst loading.

Nyguyen and White [19] developed a 1-D, steady-state water and heat management model for PEMFCs. This model does not study the details of the membrane and the catalyst layers separately since it models that entire electrode as one unit. It does steady the effect of humidification levels and their effect on fuel cell performance. This model was enhanced in [75], with the addition of a linear model for the membrane, and then a 2-D, steady-state model for multispecies transport in the electrodes. This model studies the effect of an interdigitated gas distributor on PEMFC performance. However, it was unable to predict the effect of liquid water within the system. Thirumalai and White [20] used the model developed in [75] to predict the operating parameters, flow field design and gas manifold geometry on the performance of the fuel cell stack.

Van Bussel, Koene and Mallant [22] create a 2-D dynamic model, with a 1-D model through the membrane. The model is based upon the work of Springer et al. [7], but uses experimental data from Hinatsu, Mizhuta and Takenaka [82]. The model showed that current density can vary strongly along the gas channels, especially when operating with dry gases.

Gurau, Kakac, and Lui [76] developed a 2-D non-isothermal model. They considered the gas channel, and the diffuser-catalyst layer a single entity. The model shows a non-uniform, reactant distribution has an important impact on the current density distribution. This model is based upon an infinitely thin catalyst layer, which is unable to predict the voltage due to transport limitations in the catalyst layer.

125

Fuller and Newmann [18] and Weber and Newmann [83] developed a steady-state, 2-D model for the membrane electrode assembly. Unlike other models, concentration solution theory was used. They argued that water was produced in the gaseous phase at the catalyst surfaces. Their model is valid as long as there is no condensation within the catalyst layer. However, experimental evidence implies that liquid water forms as a result of the electrochemical reaction at the anode and cathode catalyst layers.

5.1.2 Methodology

In establishing the methodology for the membrane model, there are several important factors should be considered:

1. Mass and species conservation

2. Conservation of energy

3. Momentum and pressure across the membrane.

Proton and water transport is simultaneously coupled in the polymer membrane layer, and conjugate effects must be addressed. Appendix J provides the detailed procedure employed for the calculations discussed in this section. The five main steps in the proton exchange membrane analysis are:

1. Definition of the layers and nodes

2. Definition of the boundary conditions

3. A mass and energy balance computation for each node.

4. Calculation of additional parameters such as conductivity.

The following subsections describe each of the above steps in the nodal membrane computation.

5.2 Definitions of Segments and Nodes

Figure 5.4 shows a schematic of the PEMFC stack, and the grid structure used in the fuel cell membrane model. In the actual calculations conducted with the mathematical model, the number of segments is specified by the user, and was varied from 1 to 60 segments for the membrane layer for the outputs of this study.
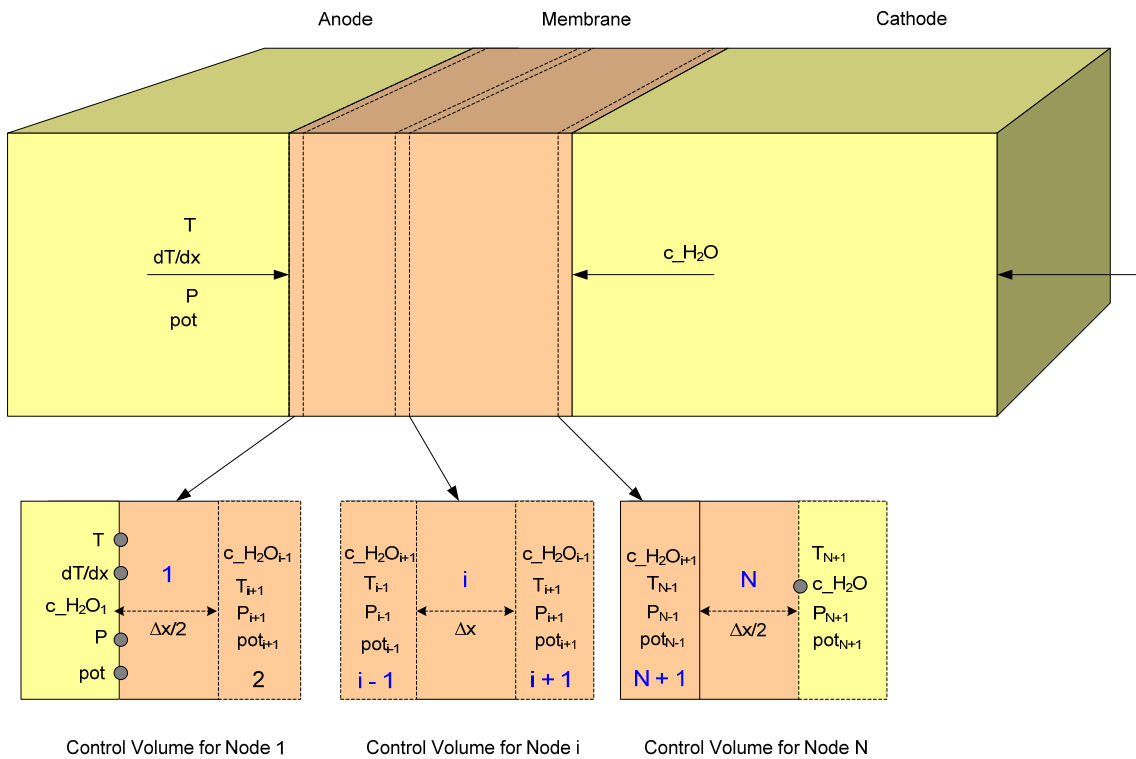
Figure 5.4. Slices created for 1-D membrane model

For the uniform distribution of nodes that is shown in Figure 5.4, the location of each node (x_i) is:

$$x_i = \frac{(i-1)}{(N-1)} L \quad \text{for } i = 1..N$$

(180)

where N is the number of nodes used for the simulation. The distance between adjacent nodes (Δx) is:

$$\Delta x = \frac{L}{N-1}$$

(181)

Energy balances have been defined around each node (control volume). The control volume for the first, last and an arbitrary, internal node is shown in Figure 5.4.

5.3 Boundary Conditions

The model solves for the concentration of water, potential, temperature and pressure simultaneously. In order to solve for these transient variables, initial and boundary conditions are required. At $x = 0$, four boundary conditions are necessary to fully specify the problem. These are:

For the left boundary:

$$c_{H2O,i}^m(x_i) = c_{H2O,i-1}^m(x_{i-1})$$

(182)

$$T_i(x_i) = T_{i-1}(x_{i-1})$$

(183)

$$\Phi_{m,i}(x_i) = \Phi_{m,i-1}(x_{i-1})$$

(184)

$$P_{tot,i}(x_i) = P_{tot,i-1}(x_{i-1})$$
(185)

For the right boundary:

$$c_{H2O,i}^{m}(x_i) = c_{H2O,i+1}^{m}(x_{i+1})$$
(186)

$$T_i(x_i) = T_{i+1}(x_{i+1})$$
(187)

$$\Phi_{m,i}(x_i) = \Phi_{m,i+1}(x_{i+1})$$
(188)

$$P_{tot,i}(x_i) = P_{tot,i+1}(x_{i+1})$$
(189)

5.3.1 Model Assumptions

The following assumptions were made for the membrane model:

1. Water diffusion perpendicular to the membrane surface (membrane thickness is much smaller than the channel length).
2. All material thermal properties are constant over the temperature range considered (20 to 80 °C).
3. For the MEA layers, only the active area was included in the model. The materials surrounding the MEA were not included in the model.
4. The gases/fluid in the membrane have ideal gas behavior.

5.4 Mass and Species Conservation

In polymer electrolyte membrane fuel cells, the two important fluxes or material balances are the proton flux and the water flux. The membrane needs to stay hydrated in

order to ionically conduct hydrogen; therefore, the water profile must be calculated in the electrolyte. One of the main reasons water content varies in Nafion is because the protons usually have one or more water molecules associated with them. This phenomenon is called the electroosmotic drag (n_{drag}), which is the number of water molecules accompanying the movement of each proton [7, 8, 73]:

$$n_{drag} = 2.5 \frac{\lambda_{H_2O/SO_3}}{22}$$

(190)

where n_{drag} is the electroosmotic drag (usually between 2.5 +/– 0.2), and λ is the water content (which ranges from 0 to 22 water molecules per sulfonate group, and when $\lambda =$ 22, Nafion is fully hydrated). The relationship between water activity on the faces of the membrane and water content can be described by [7, 8, 73, 81, 84]:

$$\lambda(a_w, T_{f,i}) = \begin{cases} 0.043 + 17.8a_w - 39.85(a_w)^2 + 36(a_w)^3 & \text{at } = 303\,\text{K} [7,8] \\ 0.3 + 10.8a_w - 16(a_w)^2 + 14.1(a_w)^3 & \text{at } = 353\,\text{K} [81,84] \end{cases}$$

(191)

Since in the study, the concept of non- isothermal conditions are of interest, the expression for membrane water content needs to be modified to take into account the temperature variation on the polymer membrane as proposed by Yi et al. [84]:

$$\lambda(a_w, T_{f,i}) = \lambda(a_w, 303) + (\lambda(a_w, 353) - \lambda(a_w, 303))\left(\frac{T_{f,i} - 303}{50}\right)$$

(192)

This concepts of water uptake (λ) and water activity (a_w), and the influence on cell potential and current density is demonstrated in Figures 5.5 and 5.6.
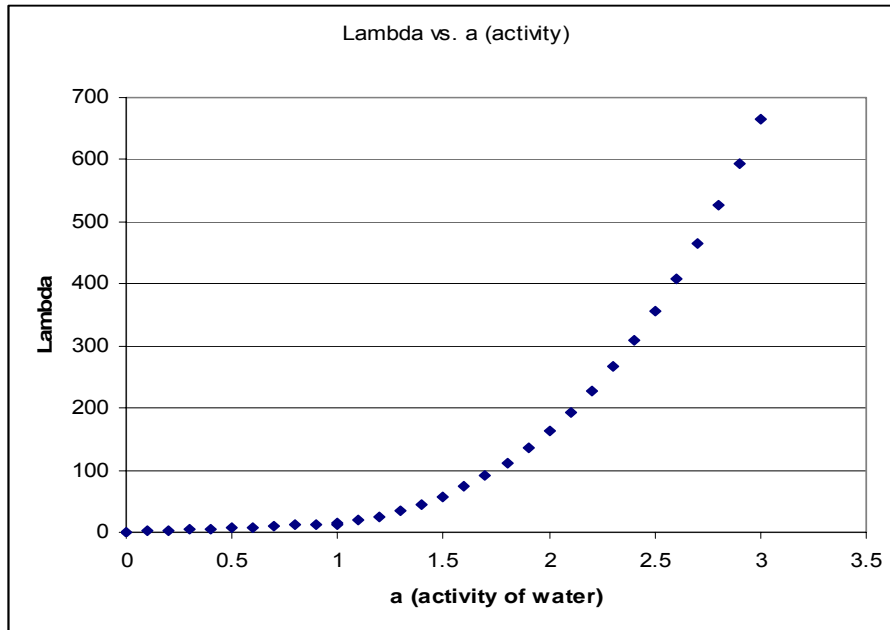
Figure 5.5. Lambda (λ) versus activity
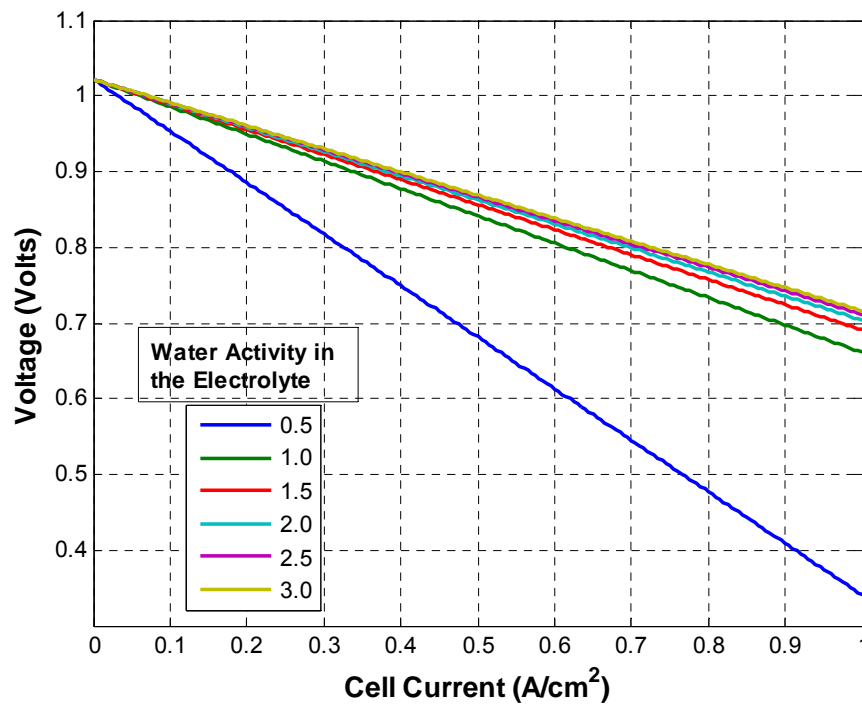
Figure 5.6. Cell voltage and current density based upon electrolyte RH

131

The relation for the water activity within the membrane is given by the reciprocal of the sorption curve. As with the water vapor activity at the interfaces, the results from Springer et al. [7] for water vapor activity in Nafion 117 at 30 °C is given by [7, 8, 73].

$$a = \begin{cases} \left[\left(\dfrac{c_1}{2160} + c_2 \lambda_{H_2O/SO_3} + 216\sqrt{c_3 - c_4 \lambda_{H_2O/SO_3} + c_5 \lambda^2_{H_2O/SO_3}} \right)^{1/3} \\ - \dfrac{134183}{2160} \left(c_1 + c_2 \lambda_{H_2O/SO_3} + 216\sqrt{c_3 - c_4 \lambda_{H_2O/SO_3} + c_5 \lambda_{H2O/SO3}}^2 \right)^{1/3} & \lambda_{H_2O/SO_3} \leq 14 \\ + \dfrac{797}{2160} \\ \\ 0.7143 \lambda_{H_2O/SO_3} - 9.0021 & 14 \leq \lambda_{H_2O/SO_3} \leq 16.8 \\ \\ 3 & 16.8 \leq \lambda_{H_2O/SO_3} \end{cases}$$
(193)

where c_1 is -41956×10^4, c_2 is 139968×10^3, c_3 is 382482×10^6, c_4 is 251739×10^3 and c_5 is 419904×10^6.

The water drag flux from the anode to the cathode with a net current i is [7, 8, 73]:

$$J_{H_2O,drag} = 2n_{drag} \frac{i}{2F}$$
(194)

where $J_{H_2O,drag}$ is the molar flux of water due to the electroosmotic drag (mol/scm^2), and j is the current density of the fuel cell (A/cm^2).

The electroosmotic drag moves water from the anode to the cathode, and when the water builds up at the cathode, some water travels back through the membrane. This is known as back diffusion, and it usually happens because the amount of water at thecathode is many times greater than at the anode. The water back-diffusion flux can be determined by [42]:

$$J_{H_2O,backdiffusion} = \frac{\rho_{dry}}{M_m} D_\lambda \frac{d\lambda}{dz}$$

(195)

where ρ_{dry} is the dry density (kg/m^3) of Nafion, M_n is the Nafion equivalent weight (kg/mol), D_λ is the water diffusivity and z is the direction through the membrane thickness.

The total amount of water in the membrane is a combination of the electroosmotic drag and back diffusion, and can account for by the following equation [42]:

$$J_{H_2O}^M = -D_{cH_2O,T} \frac{\partial c_{H_2O}^m}{\partial x} + n_{drag} \frac{i_x}{F}$$

(196)

where n_{drag} is the measured drag coefficient, i_x is the protonic current in the x direction, F is Faradays constant, λ_{H_2O/SO_3} is the water content (molH2O/molSO3-), ρ_{dry}^m is the dry membrane density (kg/m3), $D_{cH_2O,T}$ is the diffusion coefficient and M^m is the membrane molecular mass (kg/mol).

Many different values for the diffusion coefficients have been reported in the literature. $D_{cH_2O,T}$ is the diffusion coefficient which includes a correction for the temperature and for the water content it is expressed in a fixed coordinate system with the dry membrane by [7, 8]:

$$D_{cH_2O,I} = D'e^{2416\left(\frac{1}{303} - \frac{1}{T}\right)} \frac{\lambda_{H_2O/SO_3}}{a\left(17.81 - 78.9a + 108a^2\right)}$$

(197)

where a is the activity of water, and D' (m^2/s) is the diffusion coefficient measured at constant temperature and in coordinates moving with the swelling of the membrane. D'

133

has been added to the above equation to ensure that water contents below 1.23 do not result in negative diffusion coefficients. D' at 30 °C is written as [7, 8]:

$$D = \begin{cases} 2.642276 \times 10^{-13} \lambda_{H_2O/SO_3} & \lambda_{H_2O/SO_3} \leq 1.23 \\ 7.75 \times 10^{-11} \lambda_{H_2O/SO_3} - 9.5 \times 10^{-11} & 1.23 < \lambda_{H_2O/SO_3} \leq 6 \\ 2.5625 \times 10^{-11} \lambda_{H_2O/SO_3} - 2.1625 \times 10^{-10} & 6 < \lambda_{H_2O/SO_3} \leq 14 \end{cases} \qquad (198)$$

When modeling the polymer electrolyte membrane, a typical assumption is that the concentration of positive ions is fixed by electroneutrality, which means that a proton occupies every fixed SO3- charge site. The charge sites are assumed to be distributed homogeneously throughout the membrane, which results in a constant proton concentration in the membrane. A flux of protons, thus, results from a potential gradient and not a concentration gradient. In addition, the number of protons that can be transported is only one, which helps to simplify the governing transport equations. Now, due to the assumption of electroneutrality and the homogeneous distribution of charge sites, the mass conservation of protons simplifies to:

$$\frac{\partial c_{H+}}{\partial x} = 0 \qquad (199)$$

$$\frac{\partial c_{H+}}{\partial t} = 0 \qquad (200)$$

Thus, as soon as a current exists, the membrane is charged; and the concentration of protons remains constant. The charge of the protons equals that of the fixed charges. The diffusive molar flux for the protons, J_{H+}, can, therefore, be written as [7,8]:

$$J_{H+} = -\frac{F}{RT} D_{H+} c_{H+} \frac{\partial \Phi_m}{\partial x} \qquad (201)$$

Combining this diffusive flux with the convective flux results in the total molar flux for the hydrogen protons, i.e.:

$$N_{H+} = J_{H+} + c_{H+}u^m \tag{202}$$

5.5 Charge Transport

The equation for the proton potential is derived from Ohm's law. The electroneutrality assumption allows the total molar proton flux to be related directly to current density and results in the first term. The second term containing u^m represents the convective flux of protons. Combined they result in the following equation [7,8]:

$$\frac{\partial \Phi_m}{\partial x} = -\frac{i}{\sigma_m} + \frac{F}{\sigma_m}c_{H+}u^m \tag{203}$$

where is the conductivity of the membrane. The conductivity of a membrane is highly dependent upon the structure and water content of the membrane. The amount of water uptake in the membrane also depends upon the membrane pre-treatment. For example, at high temperatures, the water uptake by the Nafion membrane is much less, due to changes in the polymer at high temperatures. Springer et al. [7,8,73] correlated the ionic conductivity (σ)(in S/cm) to water content and temperature with the following relation [7, 8]:

$$\sigma_m = \sigma_{m303}e^{1268\left(\frac{1}{303}-\frac{1}{T}\right)} \tag{204}$$

with σ_{m303}, the conductivity of the membrane at 303 K given by [7, 8]:

$$\sigma_{m303} = 0.5139\lambda_{H_2O/SO_3} - 0.326 \quad for \quad \lambda_{H_2O/SO_3} > 1 \tag{205}$$

135

Since the conductivity of Nafion can change depending upon water content, the resistance of the membrane changes with water saturation. The total resistance of a membrane (Rm) is found by integrating the local resistance over the membrane thickness [7, 8]:

$$R_m = \int_0^{t_m} \frac{dz}{\sigma[\lambda(z)]}$$

(206)

where t_m is the membrane thickness, λ is the water content of membrane, σ is the conductivity (S/cm) of the membrane. Figures 5.7 and 5.8 show the correlation between membrane thickness and water content, and membrane thickness and local conductivity.
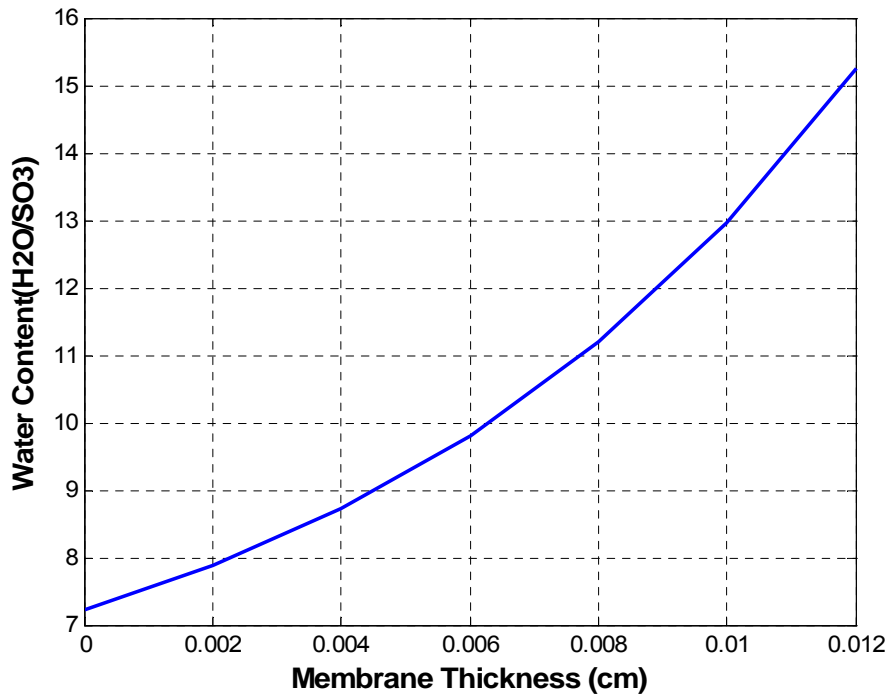
Figure 5.7. Membrane thickness and water content
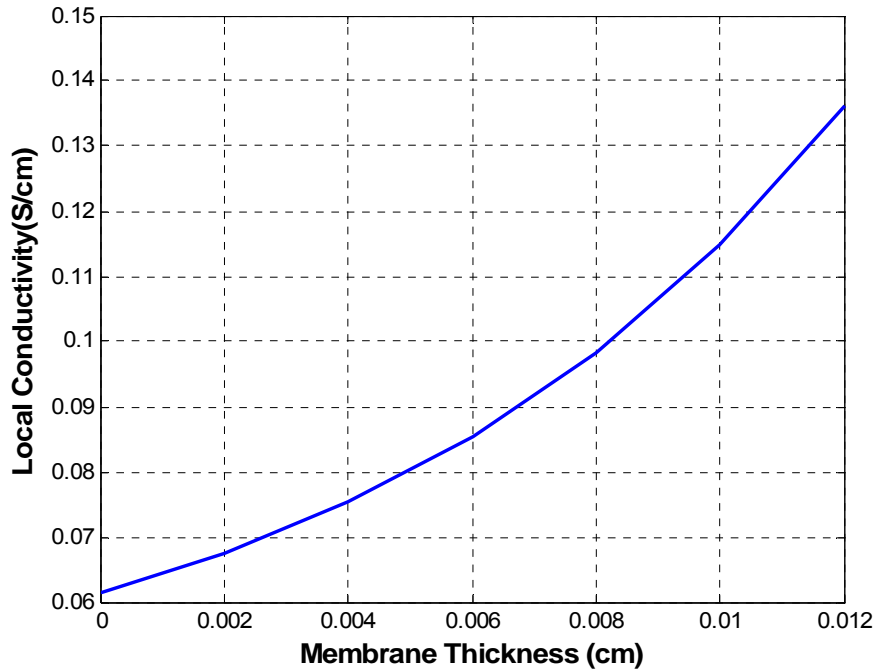
Figure 5.8. Membrane thickness and local conductivity

5.6 Pressure in the Polymer Membrane

Most models in the literature assume only concentration gradients, and not pressure gradients [7]. A pressure drop can occur if the anode and cathode pressure are different. The pressure in the membrane layer was calculated based upon the pressures and concentrations on the feed and permeate side as shown in Figure 5.9. The average membrane pressure was obtained by subtracting the pressure on the anode minus the cathode side.
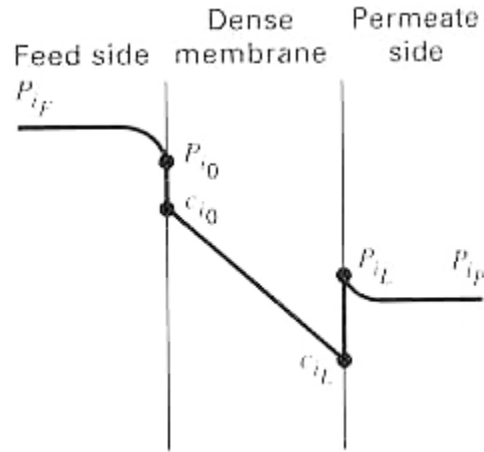
Figure 5.9. Pressure profile for transport through polymer membrane

The mixture pressure gradient is assumed to behave linearly between the anode and cathode interfaces so that the total pressure at node i $P_{tot,i}$ (Pa) is [6]:

$$P_{tot,i} = \frac{P_{tot,i+1} - P_{tot,i-1}}{\Delta x_i} \tag{207}$$

where Δx is the thickness of node i (m), $P_{tot,i+1}$ and $P_{tot,i-1}$ are the pressures at the anode/membrane and cathode/membrane interface. At the interface with the anode catalyst layer, the mixture pressure is assumed equal to that of the gas pressure under the assumption that no liquid is present. At the cathode catalyst interface, it is assumed that the mixture pressure can be approximated by a linear relation and the liquid pressure, weighted by the saturation ratios (the volume ratio of liquid water to gaseous water in the pores of the catalyst layer). For the results generated, the saturation ratio was set to zero; therefore there was no effect of liquid pressure on the pressure gradient.

5.7 Momentum Equation

For the water, protons and gases mixture, the momentum equation takes the form of the generalized Darcy relation [66, 67]:

$$u_{m,i} = \frac{k_i}{\mu_i \Delta x} \Delta P_{tot,i} \tag{208}$$

where k is the permeability (m^2), μ is the viscosity (Pa-s), Δx is the thickness of node i (m) and $\Delta P_{tot,i}$ is the change in total pressure (Pa) with respect to x.

5.8 Gas Permeation

The membrane should theoretically be impermeable to reactant species in order to prevent mixing. However, due to the membrane's porous structure, its water content and solubility of hydrogen and oxygen in water, some gas does permeate through the membrane. Permeability is a product of diffusivity and solubility [46, 85]:

$$P_{H2} = D_{H2} \times S_{H2} \tag{209}$$

$$P_{O2} = D_{O2} \times S_{O2} \tag{210}$$

The solubility of hydrogen in Nafion was shown to be SH$_2$ = 2.2 x 10-10 mol-cm-3 Pa-1, and is independent of temperature and diffusivity. The hydrogen diffusivity can be calculated as follows [46, 85]:

$$D_{H2} = 0.0041 \exp\left(-\frac{2602}{T_{f,i}}\right) \tag{211}$$

where $T_{f,i}$ is the temperature of gas/fluid mixture in the membrane. The oxygen solubility is a function of temperature, and is given by the following expression [46, 85]:

$$S_{O2} = 7.43 \times 10^{-12} \exp\left(\frac{666}{T_{f,i}}\right) \tag{212}$$

The oxygen diffusivity (cm2 s-1) can be calculated from [46, 85]:

$$D_{O2} = 0.0031 \exp\left(-\frac{2768}{T_{f,i}}\right) \tag{213}$$

Hydrogen has an order of magnitude higher permeability than oxygen in Nafion. The oxygen and hydrogen permeability can then be used to calculate the hydrogen and oxygen permeation rates [46, 85]:

$$n_{H2,i} = \frac{P_{H2} A_i P_{tot,i}}{\Delta x_i} \tag{214}$$

$$n_{O2,i} = \frac{P_{O2} A_i P_{tot,i}}{\Delta x_i} \tag{215}$$

6
BOLT TORQUE MODEL

There are many steps involved in the manufacturing of a fuel cell stack. One of

these steps is the hot pressing of the polymer electrolyte membrane to the two gas

diffusion layers (GDLs). This creates a three layer laminate membrane electrode

assembly (MEA). Other steps involve the machining or etching of the end plates, bipolar

plates and cooling plates, and the sizing of the gaskets, contacts and MEA surrounds.

After all of the fuel cell components have been manufactured, they are stacked together

and clamped using a clamping mechanism such as bolts. The contact resistance, mass and

charge transfer between the electrolyte membrane and the GDL is very good due to the

fusion of the three layers [86]. In contrast, the remaining layers are separated until they

are clamped together using bolts or some other type of clamping device. Therefore, the

interfacial resistances between the remaining layers are significant. The contact, cooling

and bipolar plates are clamped together, and since the Poisson's ratio and Young's

Modulus of the bipolar, cooling and contact layers are similar, and the surface roughness

can be considered negligible, the contact resistance between these layers is small when

the stack is clamped together. The interface that is most affected by the clamping

pressure is the GDL and bipolar plate interface. The material properties of these adjoining

layers are extremely different, and since the GDL layer is porous, it is highly sensitive to

the clamping pressure. Not only does the GDL thickness change with clamping pressure,

but the change in thickness also affects the porosity and permeability of the GDL. The bolt torque, clamping force, contact resistance and permeability of the GDL all affect the electrochemical performance of a PEM fuel cell by influencing the ohmic and mass-transport polarizations inside of the fuel cell [86].

In order to predict the optimal clamping pressure, and ultimately, the ideal bolt torque, a MATLAB program was created to calculate the force required for optimal GDL compression and assembly force of the stack. The program is illustrated in Figure 6.1.

Parameters
These parameters are specified for each layer:

(1) Thickness (mm)
(2) Modulus of elasticity in Tension (MPa)
(3) Young's Modulus (N/mm2)
(4) Poisson's ratio

Constants

(5) No. of Bolts
(6) Bolt diameter (mm)
(7) Bolt hread root diameter (mm)
(8) Thread Pitch
(9) Pitch diameter (mm)
(10) Bolt head diameter (mm)
(11) Thickness of Bolt Head (mm)
(12) Bolt length (between bolt head & nut) (mm)
(13) Outer diameter of annulus seating face (mm)
(14) Inner diameter of annulus seating face (mm)
(15) Nut thickness (mm)
(16) Bolt clearance hole (mm)
(17) Modulus of elasticity in tension of bolt material (MPa)
(18) Force for optimal GDL compression (N)
(19) Diameter of active area of material (mm)
(20) Total elastic compression (microns)
(21) friction coefficient in seating face of head (nut) of the bolt
(22) Coefficient of tightness
(23) friction coefficient in he thread
(24) Interface area (mm)

Inputs: 1, 2, 16

Inputs: 6, 7, 9, 10, 11, 12, 15, 17

Inputs: 3, 4, 18, 19, 20

Inputs: 5

Calculate he stiffness of each fuel cell layer

Calculate total stiffness of clamped fuel cell layers

Calculate the bolt, head, shaft & nut stiffness

Calculate the force required for optimal GDL compression

Part of force relieving he clamped parts

Calculate stiffness of the group of surcharged parts of the stack

Bolt seating coefficent

Inputs: 13, 14, 16, 21

Calculate the stiffness of the relieved parts

Assembly force of the stack

Inputs: 22

Tightening torque

Inputs: 8, 9, 23

Average interface contact pressure

Inputs: 5, 24

Figure 6.1. Flow chart of bolt torque model

142

6.1 The Mechanics of Bolted Joints

Materials bolted together withstand moment loads by clamping the surfaces together, where the edge of the part acts as a fulcrum, and the bolt acts as a force to resist the moment created by an external force or moment. Figure 6.2 shows forces exerted by the clamped materials (fuel cell layers) on a clamping bolt and nut. The forces exerted by the tightening bolts are due to the bolt material properties, the properties of the materials being clamped together and the torque applied to the bolts.
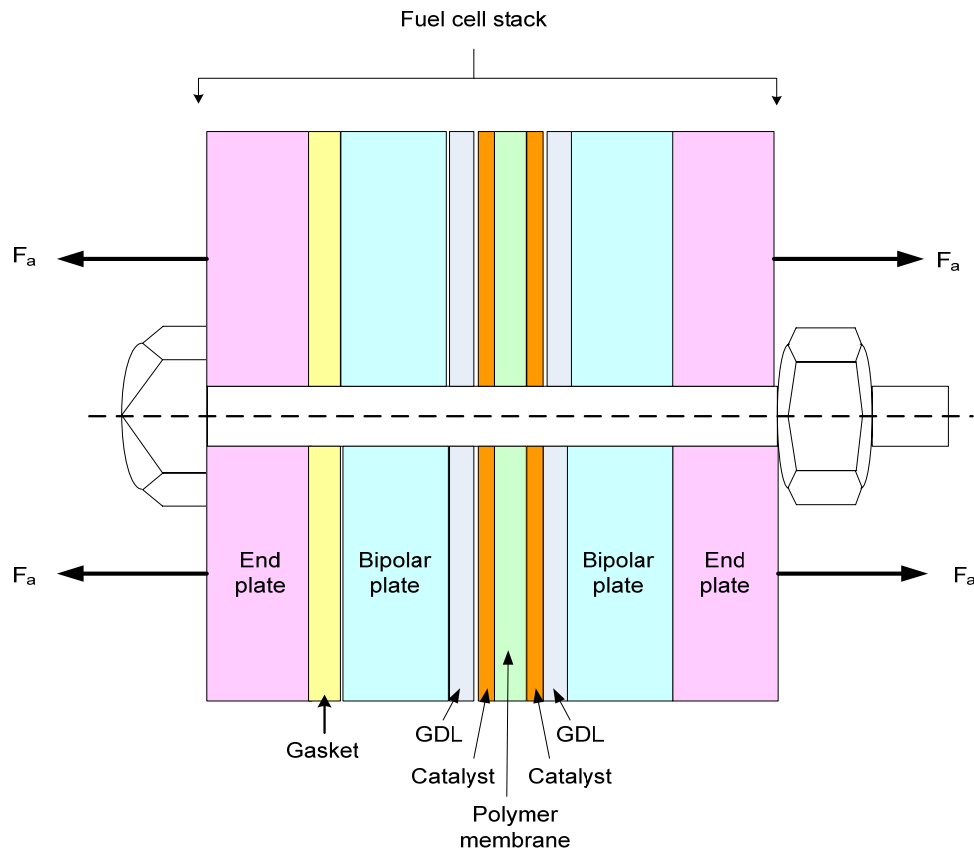
Figure 6.2. The forces exerted by the clamped materials (fuel cell layers) on the bolt and nut

143

Materials that are held together by a bolt are subjected to a force a distance away from the center of stiffness of a bolt pattern. In order to determine the optimal torque for a bolt, a maximum bolt force is typically calculated based upon the maximum amount of stress and force that can be applied to the bolt, and the "joint" which is the fuel cell stack in this case. The optimal torque is found by calculating the force that can be applied to joint until the force on the joint is lost. When the joint starts to leak, at which the bolts break, the total stress in a bolt when the joint begins to leak, and the percent of maximum stress that can be used by the bolt head. Assuming each of N bolts is a distance from the bolt pattern's center of stiffness, each bolt has the same force and there is a coefficient of friction between the bolted members [87, 88].

Tightening the bolts stretches the bolts and compresses the stack materials. If an external force is applied to the stack, the optimal torque usually means that the stack stays compressed. This ensures proper stiffness and fatigue life of the stack. Figure 6.3 shows how the region under a bolt head acts like a spring.
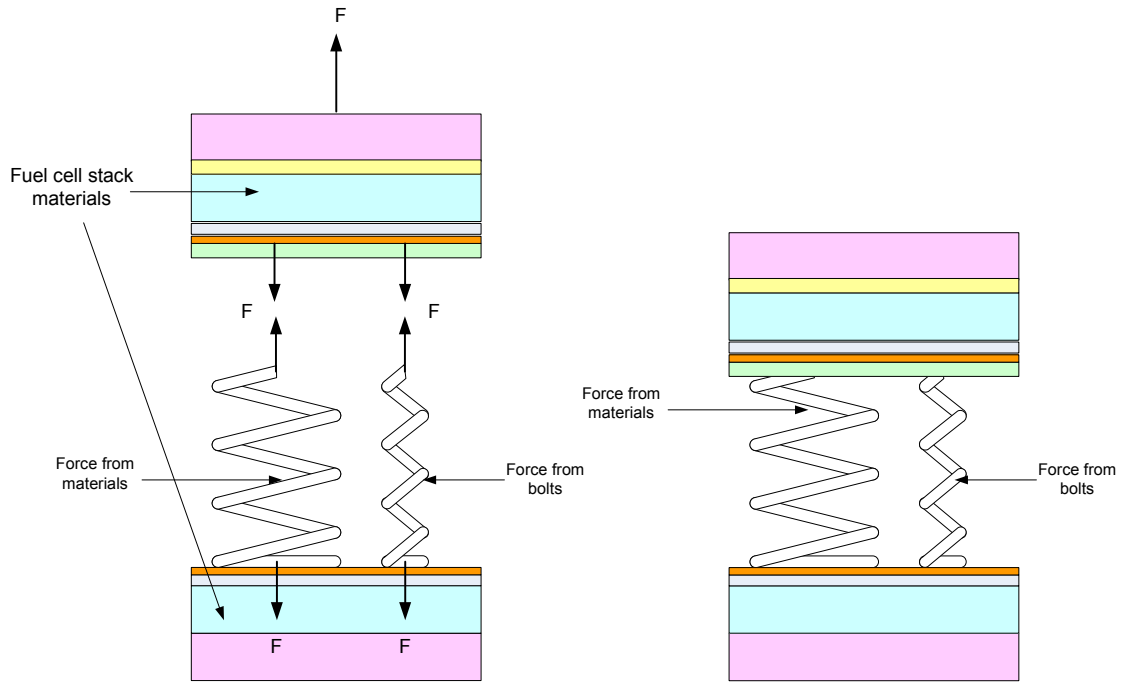
Figure 6.3. The forces exerted by the clamped materials and bolt

Of the energy created by the bolt force, about 50% of the energy goes to friction under the bolt head, 40% goes to friction in the threads and about 10% goes to create tension in the threads [88, 89]. The rotation of the bolt head relative to the parts being bolted together is a good measure of tension in the bolt. As shown in Figure 6.4, there is a strain or stress cone under the bolt head that project from 30 to 45 degrees from the vertical, and 45º is most commonly used for bolt torque calculations [88, 89].
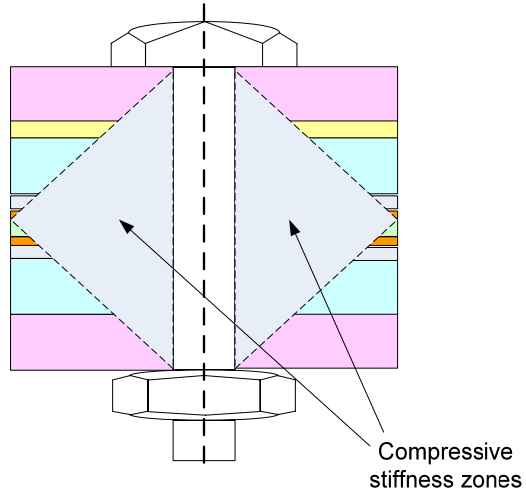
Figure 6.4. Compressive stiffness zones underneath a bolt head in a fuel cell stack

When determining a fuel cell stack design and the optimal clamping pressure, two questions need to be answered:

1. How much tension does the clamping device (a bolt in this case) actually create?

2. What is the optimal tightness for ideal permeability through the MEA layers?

3. What is the ideal tightness to minimize contact resistance?

4. What effect do all the fuel cell layers have on ideal tightness?

All of these properties need to be considered when trying to determine the optimal clamping pressure for a stack. The traditional method of determining the ideal clamping pressure is to just take the fuel cell prototype into the lab, and obtain I-V curves for the fuel cell stack to determine the optimal clamping pressure. However, this can be very time-consuming and unrealistic for real world applications since the stacks can be

146

extremely large with greater than 200 cells, and often multiple stacks with varying number of cells are rapidly being prototyped. In addition, new stack configurations from very large to very small scale, and clamping methods are being created where it may be more convient to calculate the ideal clamping pressure and bolt torque.

In bolt science, the optimal torque can be found by calculating the forces that the bolt can withstand, along with the stiffness of the materials being clamped, and the desired tightness that the clamped materials require. The numerical model of the ideal tightening torque originally proceeded in this direction, but these forces overestimated the required torque for a fuel cell stack because they were based upon the amount of stress that the bolt material could handle. For a fuel cell stack, the bolt material can handle more force than the fuel cell stack needs for optimal performance. Therefore, in order to calculate the ideal torque for a fuel cell stack, the effects of compression of the GDL and the channel land area had to be added to the existing model.

6.2 Calculating the Force Required on the Stack for Optimal Compression of the GDL

The contact resistance and GDL permeability is governed by the material properties of the contacting GDL and bipolar plate layers. The contact resistance is most reliant on the contact between these layers. The contact resistance between the catalyst, gas diffusion and membrane layers is low because they are fused together. The contact resistance between the bipolar plates and the gas diffusion media can vary depending upon the land to channel area, the GDL porosity after compression. The important aspects for calculating the optimal bolt torque and clamping pressure are as follows:

147

1. The Poissons' ratios and Young's Moduli have large differences (a hard material with a soft material)

2. The GDL layer is porous, and the permeability has been reduced due to the reduction in pore volume or porosity, and

3. Part of the GDL layer blocks the flow channels that are in the bipolar plate creating less permeability through the GDL as the compression increases.

The original clamping pressure model did not take this into effect, and only calculated the optimal torque on the bolts based upon the forces that the bolt could withstand, and the stiffness of the materials. The tightening torque calculations predicted the optimal torque for the tightness of the bolts due to the stiffness of the bolt and materials being clamped together. However, it did not take into account the optimal tightness of the bolt (pressure on the stack) for optimal compression of the GDL. If the GDL is not adequately compressed, the fuel cell gases may leak, and therefore, will not be able to react inside the fuel cell. In addition, the contact resistance will be high due to inadequate contact between the GDL and the other fuel cell layers. Therefore, a relation had to be included for the ideal GDL compression thickness.

Herzian compression effects are used to determine the compression of the GDL and bipolar plate materials. The calculations assume that the surfaces in contact are not perfectly smooth (which is not the case as presented in [90, 91]), that the elastic limits of the materials are not exceeded, that the materials are homogenous and that there are no frictional forces within the contact area. The actual variation due to the frictional effects from non-smooth surfaces lead to compression effects differing from these calculations by 5%. These formulas are sufficiently precise for use with this tightening torque model.

148

The compression formula for two spheres in contact is [92]:

$$h(x) = \frac{(3\pi)^{2/3}}{2} \cdot F^{2/3} \cdot (V_1 + V_2)^{2/3} \cdot \left(\frac{1}{D_1} + \frac{1}{D_2} \right)^{1/3} \tag{216}$$

where $h(x)$ is the total elastic compression at the point of contact of two bodies (μm), measured along the line of applied force, F is the total applied force, D is the diameter of the active area of the material (width of MEA), and [92]

$$V = \frac{(1 - v^2)}{\pi E} \tag{217}$$

where v is Poisson's ratio, and E is the Young's modulus.

As noted by Nitta et al. [93], the change in thickness of the GDL caused by compression is mainly attributed to the loss of pore volume, which affects the mass and charge transport through the GDL. The gas permeability decreased non-linearly when the thickness of the GDL was decreased by compression. The permeability was reduced by one order of magnitude when the GDL was compressed to 250 μm from the initial thickness of 380 μm. These results agree with Mathias et al [94], who determined the in-plane permeability to be in the range from 5 x 10^{-12} when Toray paper was compressed to 75% of the initial thickness. The compression of the GDL leads to loss of pore volume; therefore, porosity can be correlated directly with compressed GDL thickness.

As shown in Figure 6.5 which was adapted from [93], both the in-plane and through-plane conductivities increase as the compressed thickness of the GDL was decreased. The conductivities have a linear dependence on the GDL compressed thickness. This may be due to the reduced porosity of the GDL, which leads to shorter distances between conductive carbon fibers and better contacts between the fibers.
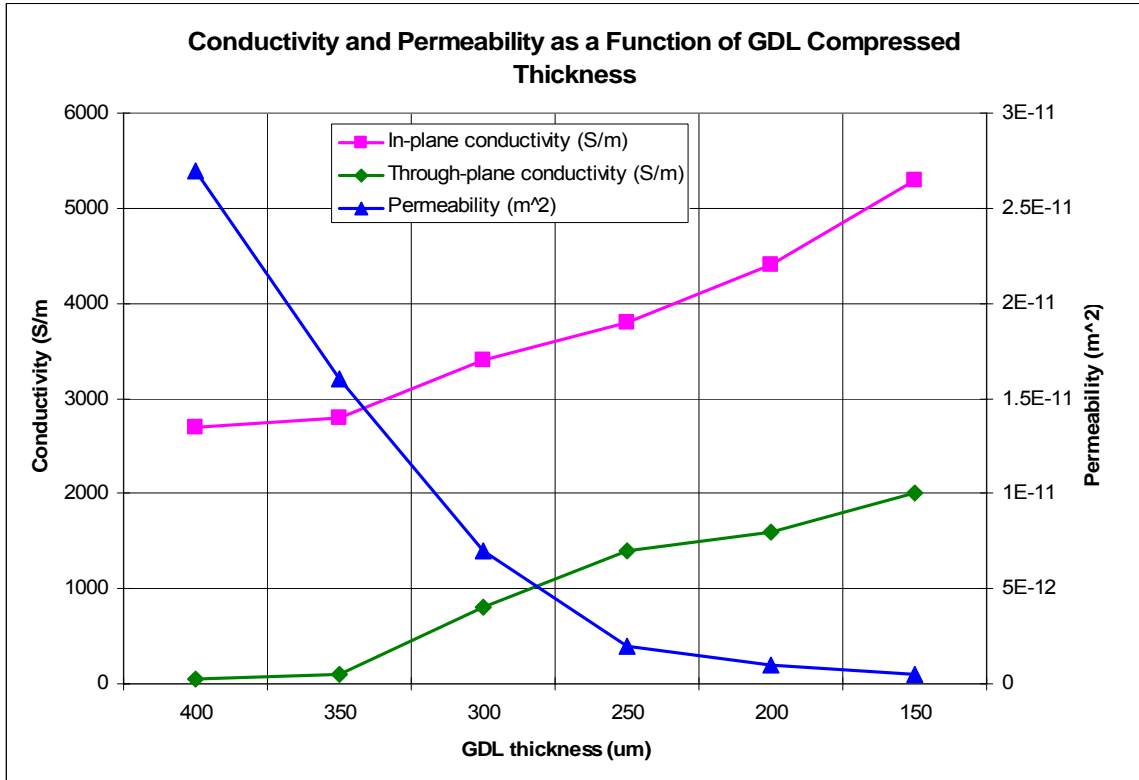
Figure 6.5. Conductivity and permeability as a function of GDL compressed thickness

[93]

Using the intersection of the in-plane, through-plane and gas permeability from Figure 6.5, a compressive GDL thickness of 325 μm was assumed to be an ideal compression for optimal GDL conductivity and permeability. The force in equation 216 was calculated based upon a compression of 75 μm (assuming that the GDL has a 400 μm thickness), the diameter of the MEA and the part of the bipolar plate contacting the GDL (the channel area), and the properties of the bipolar plate and GDL materials. This force was used as part of the ideal compression force for the bolt-torque model.

From the data from Figure 6.5, a third degree polynomial fit was made with the least square sum method to the permeability data, and the following function results [93]:

150

$$k(x) = -1.700 \times 10^{-11} + 2.760 \times 10^{-7} h(x) - 1.484 \times 10^{-3} h(x)^2 + 2.754 h(x)^3 \quad (218)$$

The GDL in and through plane conductivities were modeled as a linear fits from the experimental data, and can be written as [93]:

$$\sigma_{GDL,x}(x) = 6896 - 1.159 \times 10^7 h(x) \quad (219)$$

$$\sigma_{GDL,y}(x) = 3285 - 8.385 \times 10^6 h(x) \quad (220)$$

6.3 The Stiffness of Bolted Joints

In order to accurately determine the ideal clamping pressure (tightening torque) for a fuel cell stack, the stiffness of the materials between the bolts has to be estimated. The stiffness of the materials includes the compressive stiffness of the materials under the bolt head in series with the stiffness of the physical interface, which increases with pressure, and the stiffness of the threaded material. Some of the dimensions used in the bolt and layer stiffness calculations are shown in Figure 6.6.
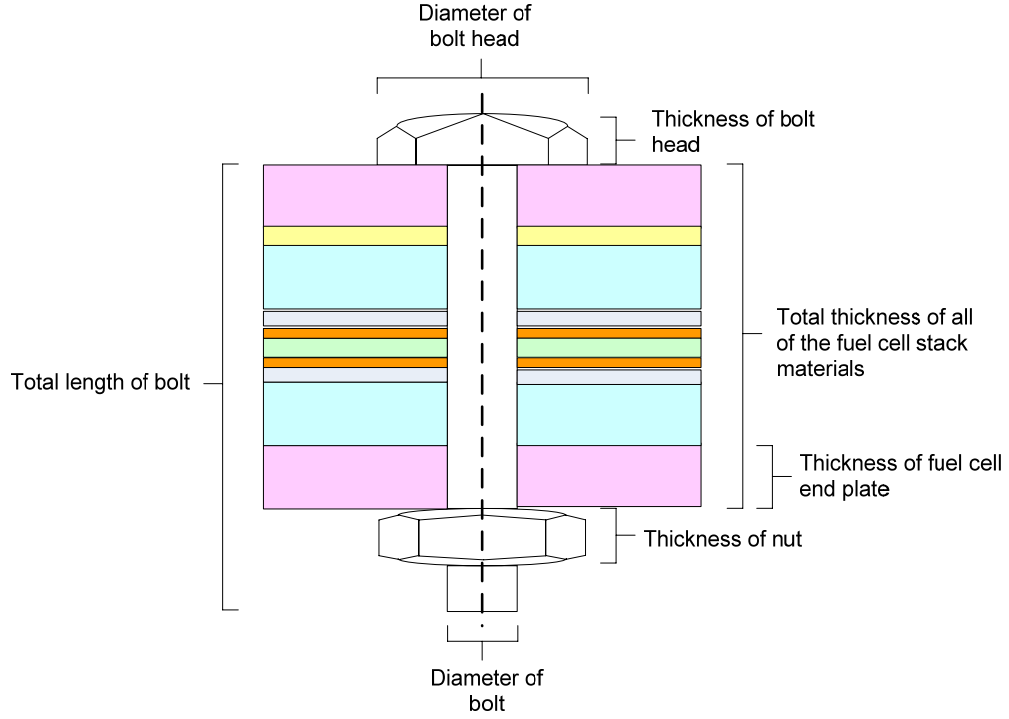
Figure 6.6. Dimensions used in the bolt and layer stiffness calculations

In order to determine the stiffness of the cone-like section under the bolt head, the first step is to calculate the stiffness of each layer of the fuel cell stack [94]:

$$k_{layer} = \frac{4 * h_{layer}}{\pi E_{layer} \left(d_{bolthead} * \left(d_{bolthead} + 2h_{layer} * \cos \alpha \right) - d_{bore}^2 \right)} \quad (221)$$

where k_{layer} is the stiffness of the fuel cell layer (such the end plate or bipolar plate), h_{layer} is the thickness of that particular layer, E_{layer} is the modulus of elasticity in tension (MPa) of the material, $d_{bolthead}$ is the diameter of the bolt head, α is the effective cone angle and d_{bore} is the clearance hole diameter.

The stiffness of the bolt, head, shaft and nut are all calculated in a similar fashion. The tensile stiffness of the bolt shaft is [94]:

$$k_{boltshaft} = \frac{\pi \left(\dfrac{d_{bolt\_dia}}{2} \right)^2 E_{bolt}}{L_{bolt}} \qquad (222)$$

where d_{bolt_dia} is the bolt diameter, E_{bolt} is the Young's Modulus of the bolt, and L_{bolt} is

the bolt length. The shear stiffness of the bolt head is [94]:

$$k_{bolthead} = \frac{h_{bolthead} \pi E_{bolt}}{(1 + v_{bolt}) * \ln(2)} \qquad (223)$$

where $h_{bolthead}$ is the thickness of the bolt head, E_{bolt} is the Young's Modulus of the bolt,

and v_{bolt} is the Poisson's ratio of the bolt. The shear stiffness in the nut is [94]:

$$k_{nut} = \frac{h_{nut} \pi E_{bolt}}{(1 + v_{bolt}) * \ln(2)} \qquad (224)$$

The total stiffness of the stack is [94, 95]:

$$k_{stack} = \frac{N}{\displaystyle\sum_{1}^{i} \frac{1}{k_{layer,i}}} \qquad (225)$$

where N is the number of bolts in the stack. The stiffness of the bolt shaft in tension, and

the head and nut (if a nut is used) in shear, all act in series, so their stiffness combine to

give the total stiffness of the bolt [94, 95]:

$$k_{bolt} = \frac{N}{\dfrac{1}{k_{boltshaft}} + \dfrac{1}{k_{bolthead}} + \dfrac{1}{k_{nut}}} \qquad (226)$$

As the stack thickness increases, the length of the bolt to pass through the stack

thickness also increases, so the bolt stiffness decreases in a linear fashion. On the other

hand, the diameter of the strain cone increases, which offsets much of the height increase,

and the stack stiffness decreases far more slowly than that of the bolt.

153

The ratio of flange to bolt stiffness is [94, 95]:

$$k_{s-b} = \frac{k_{stack}}{k_{bolt}} \tag{227}$$

The total stiffness can be expressed by [94, 95]:

$$k_{tot} = k_{bolt} + k_{stack} \tag{228}$$

6.4 Calculating the Tightening Torque

The stiffness of the group of surcharged parts of the stack is [96]:

$$c_1 = \frac{1}{k_{bolt}} + \frac{(1-n)}{k_{stack}} \tag{229}$$

where n is the coefficient of implementation of the operational force (0.5). The resulting stiffness of the group of relieved parts of the stack is [96]:

$$c_2 = \frac{k_{stack}}{n} \tag{230}$$

The part of the operational force relieving the clamped parts is [96]:

$$F_2 = \frac{F * c_2}{(c_1 + c_2)} \tag{231}$$

where F is the force required for the ideal compression of the GDL by 75 microns. The bolt seating coefficient is calculated by [96]:

$$m_{seat1} = m_c * \frac{(De_{seat} + Di_{seat})}{2} \tag{232}$$

where De_{seat} is the outer diameter of the seating face, and Di_{seat} is the inner diameter of the seating face and m_c is the friction coefficient in seating face of head (nut) of the bolt. The assembly force of the stack can be calculated by [96]:

154

$$F_0 = q_a * F * F_2 + F_{0T} + 0.05 \qquad (233)$$

where q_a is the desired coefficient of tightness, and F_{0T} is the change of force required

due to the heating of the connection. F_{0T} was assumed to be zero for all of the

calculations since the stacks used for validating the model were all air-breathing fuel cell

stacks tested at room temperature. The bolt seating is calculated by [96]:

$$M_{seat} = m_{seat1} * F_0 \qquad (234)$$

The tightening torque is then [96]:

$$M = F_0 * d_{pitch} * M_{seat} * \frac{thr_{pitch} * \pi * d_{pitch} * m_i}{\pi * d_{pitch} - thr_{pitch} * m_i} \qquad (235)$$

where F_0 is the assembly force of the stack, d_{pitch} is the pitch diameter, thr_{pitch} is the

thread pitch, m_i is the friction coefficient in thread (0.15).

6.5 Relating Torque to the Total Clamping Pressure Applied to the Stack

The average interface contact pressure, P_{avg}, can be calculated by dividing the total

clamp force (product of the number of bolts, and the individual bolt clamp force) with the

interface contact area, A_{int} [97]:

$$P_{avg} = \frac{N * F_0}{A_{int}} \qquad (236)$$

where A_{int} is the land area of the flow field plate. The average contact pressure is a linear

function of bolt torque.

6.6 Torque Tightening Parameters

Many simulations were performed in order to estimate the tightening torque for several fuel cell stacks. In order to calculate the stiffness of each fuel cell layer and the total stack stiffness, the materials and their applicable properties are listed in Tables 6.1 to 6.3 for each fuel cell stack. Fuel cell stack #1 has an active area of 16 cm^2, had stainless steel bipolar plates and had end plates of 10 mm in thickness. Fuel cell stack #2 is similar in construction, with an active area of 4 cm^2. The end plates were 8 mm in thickness, and the flow fields were made of 2 separate layers: one Nylon mesh and one stainless steel mesh. Stack #3 had a slightly different construction than the other two stacks with aluminum end plates and Delrin bipolar plates.

Table 6.1

Material properties used for material stiffness and compression calculations for stack #1

Fuel Cell Layer/ Material	Thickness (mm)	Modulus of elasticity in Tension (MPa)	Young's Modulus (N/mm²)	Poisson's ratio
Polycarbonate end plate	10	2,896	2,200	0.37
Gasket: Black Conductive Rubber	1	2	100	0.48
SS Flow field plate	0.5	206,000	200,000	0.31
Carbon Cloth	0.4	2	300	0.4
Nafion	0.05	2	236	0.487
Carbon Cloth	0.4	2	300	0.4
SS Flow field plate	0.5	206,000	200,000	0.31
Gasket: Black Conductive Rubber	1	2	100	0.48
Polycarbonate end plate	10	2,896	2,200	0.37

Table 6.2

Material properties used for material stiffness and compression calculations for stack #2

Fuel Cell Layer/Material	Thickness (mm)	Modulus of elasticity in Tension (MPa)	Young's Modulus (N/mm^2)	Poisson's ratio
Polycarbonate end plate	8	2,896	2,200	0.37
Gasket: Black Conductive Rubber	1	2	100	0.48
Nylon Flow field plate	0.2	4,067	7,000	0.41
SS Flow field plate	0.1	206,000	200,000	0.31
Carbon Cloth	0.4	2	300	0.4
Nafion	0.05	2	236	0.487
Carbon Cloth	0.4	2	300	0.4
SS Flow field plate	0.1	206,000	200,000	0.31
Nylon Flow field plate	0.2	4067	7,000	0.41
Gasket: Black Conductive Rubber	1	2	100	0.48
Polycarbonate end plate	8	2,896	2,200	0.37

Table 6.3

Material properties used for material stiffness and compression calculations for stack #3

Fuel Cell Layer/Material	Thickness (mm)	Modulus of elasticity in Tension (MPa)	Young's Modulus (N/mm^2)	Poisson's ratio
Aluminum end plate	6	70,000	0.35	62,052.8
Gasket: Silicon Rubber	1	320,000	0.48	2
Delrin Flow field plate	1	3,100	0.35	3,300
Carbon Cloth	0.4	300	0.4	2
Nafion	0.05	236	0.487	2
Carbon Cloth	0.4	300	0.4	2
Delrin Flow field plate	1	3,100	0.35	3,300
Aluminum end plate	6	70,000	0.35	620,52.8

In order to calculate the bolt stiffness, the bolt parameters for each stack are listed in Table 6.1. Each stack used different bolts. Stack #1 and #2 used stainless steel bolts, and stack #3 used Nylon. The lengths, diameters and other characteristics of the bolts varied, as shown in Table 6.4.

Table 6.4

Bolt properties used for bolt stiffness and torque calculations

Property	Stack 1 Bolts	Stack 2 Bolts	Stack 3 Bolts
Number	4	4	4
Material	SS316	SS316	Nylon
Hex Key Size	5/32"	3/32"	3/32"
Bolt Diameter mm	4.826	2.18	2.18
Bolt Thread Root	3.451	1.60	1.60
Thread Pitch	1.058	0.45	0.45
Pitch Diameter mm	4.139	1.89	1.89
Bolt Head Diameter	8	5	2.5
Thickness of Head	5	2.5	2
Bolt Length	25	23	25
Outer Diameter-Annulus Seating	7.925	5	3.175
Inner Diameter-Annulus Seating	5.232	3	2.3876
Nut Thickness	3	2	1.59
Bolt Clearance	5.232	4	2.38

6.7 Electrochemical Performance of PEM Fuel Cell Stacks

Three single cell, air breathing fuel cell stacks were assembled for fuel cell I-V tests with different tightening torques. Five-layered MEAs are used, which are composed of Nafion 112, GDL of carbon cloth material and 1 mg/cm^2 of Pt loading on both anode and cathode. The active fuel cell area for stack #1 is 16 cm^2, 4 cm^2 for stack #2 and 1 cm^2 for stack #3. Each stack was constructed differently, with different fuel cell layers, thickness and used different types of clamping bolts. The torque was measured using a Precision Instruments Dial Indicating ¼" torque driver with a range of 0 - 48 oz/in with

hex head adapters to fit the fuel cell stack bolts. The single cell fuel cell stacks are shown in Figure 6.7.
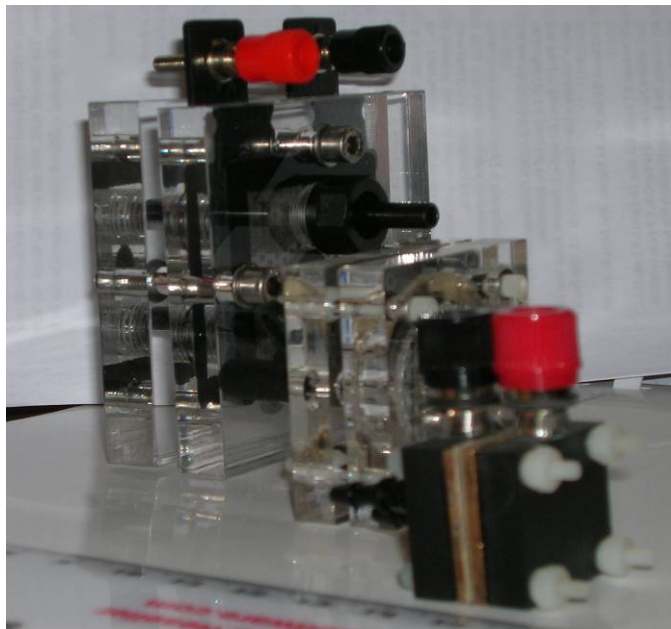
Figure 6.7. Fuel cell stack sizes that were tested (a) 16 cm^2, (b) 4 cm^2, and (c) 1 cm^2 active areas

Cell performance tests are conducted with 0.5 to 1.0 standard cubic centimeter per minute (SCCM) of hydrogen from an electrolyzer, with no additional humidification. All tests are taken at 25º C and ambient pressure. I–V curves of these cell performance tests with various tightening torques are plotted in Figures 6.8 through 6.10.

Figure 6.8 shows the polarization curves of the current of the PEM fuel cell under five different clamping pressures. The current is dynamically stable for four of the five clamping pressures. The lowest clamping pressure of 28 oz-in displayed the worst I-V

performance, due to mass transfer limitations and higher contact resistance. The

polarization curves continuously increase until a torque of 36 oz-in is reached. As the

torque continues to increase to 44 oz-in, the polarization curves again begin to decrease.
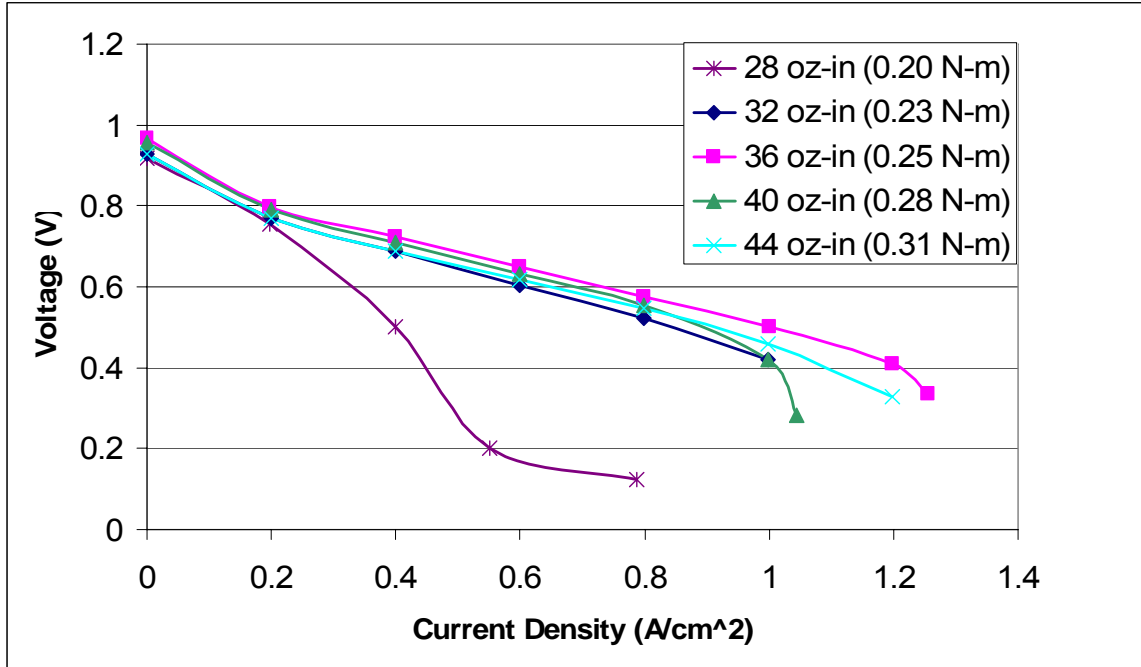
Figure 6.8. Polarization curves with tightening torques of 28 oz-in to 44 oz-in for stack

#1

The material and bolt properties from Tables 1 and 2 were entered into the

numerical model for stack #1, and the optimal force, pressure and tightening torque was

calculated. The results are shown in Table 6.5.

Table 6.5

Calculated force, tightening torque, and contact pressure for stack #1

Parameter	Value
Total Force on the Stack	310.8 N
Tightening Torque	36.35 oz-in (0.257 N-m)
Average Interface Contact Pressure	0.194 MPa (1.94 bar)

The values in Table 6.5 show that the calculated optimal tightening torque matches the tightening torque associated with the best fuel cell I-V curve in Figure 6.9.

Figure 6.9 displays the performance curves for fuel cell stack #2 with five different clamping pressures. Again, the polarization curves reflect the effect of the interfacial electrical resistance, mass transfer and optimal clamping pressure on the fuel cell stack. As seen in Figure 34, the fuel cell performance appears to be the poorest with the 6 oz-in clamping pressure. Compression with a torque of 10 oz-in shows the best performance curve. As the torque increased from 10 to 14 oz-in, the fuel cell performance decreased as the mass transfer is hindered due to the decreased porosity of the GDL layer.
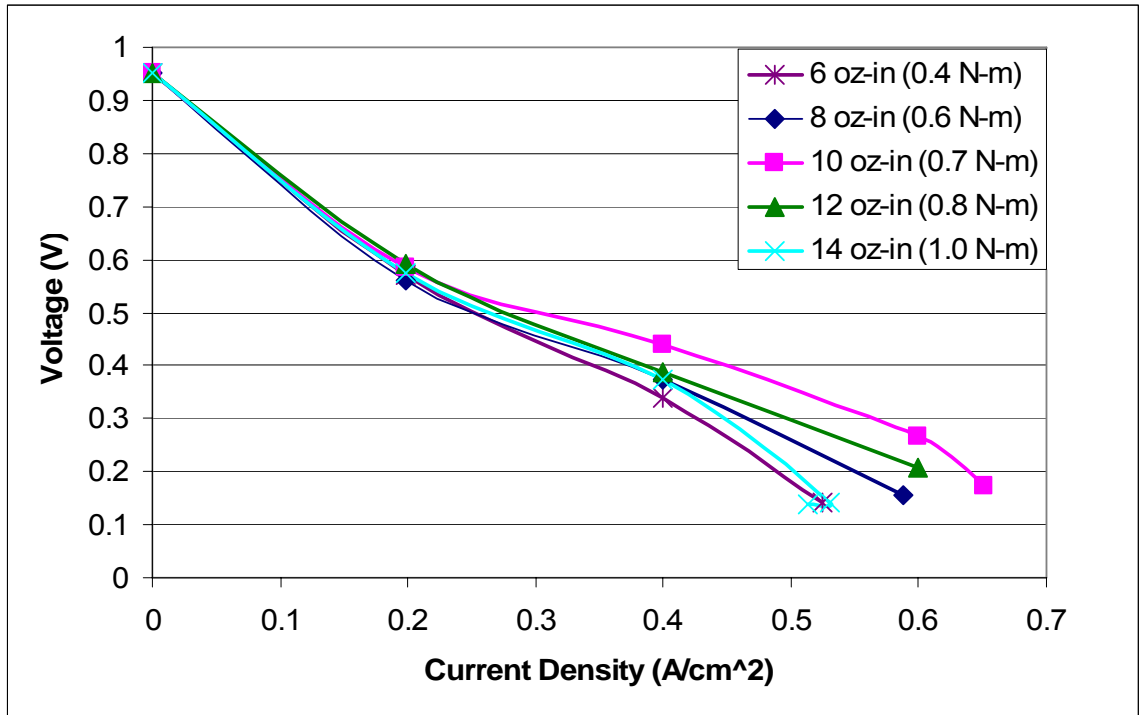
Figure 6.9. Polarization curves with tightening torques of 6 oz-in to 14 oz-in for stack #2

The numerical model for tightening torque was run for stack #2, and the optimal force, pressure and torque calculations are shown in Table 6.6. Like fuel cell stack #1, the calculated optimal tightening torque matches the torque associated with the best fuel cell performance.

Table 6.6

Calculated force, tightening torque, and contact pressure for stack #2

Parameter	Value
Total Force on the Stack	205.9 N
Tightening Torque	10.6 oz-in (0.7 N-m)
Average Interface Contact Pressure	0.129 MPa (1.29 bar)

As shown in Figure 6.10, the case of 4 oz-in compression showed the best polarization curve. As with the previous polarization curves for the other fuel cell stacks, the lowest torque showed a poor polarization curve in comparison with the polarization curve obtained with the optimal torque. It seems to be difficult to achieve more than 40 mA cm−2 of current density with a compression of 6 oz-in due to the mass-transfer limitation.
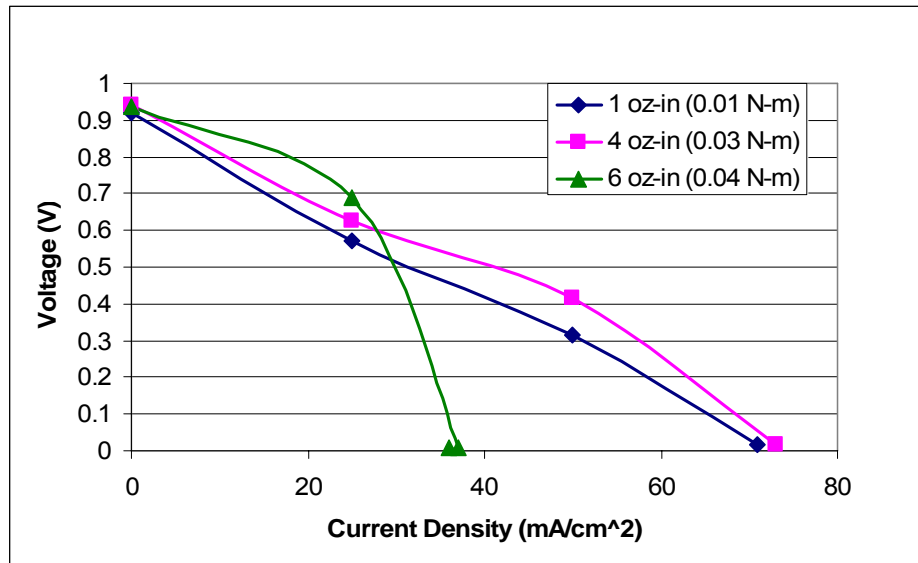
Figure 6.10. Polarization curves with tightening torques of 1 oz-in to 6 oz-in for stack #3

The numerical model was again run to obtain the tightening torque for stack #3, and the optimal force, pressure and torque calculations are shown in Table 6.7. Once again, the calculated optimal tightening torque matches the torque associated with the best fuel cell performance in Figure 6.10.

Table 6.7

Calculated force, tightening torque, and contact pressure for stack #3

Parameter	Value
Total Force on the Stack	126.4 N
Tightening Torque	4.8 oz-in (0.3 N-m)
Average Interface Contact Pressure	0.079 MPa (0.79 bar)

Therefore, it can be concluded that the numerical model does a good job of estimating the tightening torque for a fuel cell stack using clamping bolts ($\pm$ 2%). When polarization curves are obtained with the tightening torque values lower than the predicted value, the poor performance in comparison with the performance obtained with the optimal torque can be attributed to mostly high contact resistance. Since the polarizations curves generally have the same shape at slightly lower tightening torques, the ohmic polarization seems to be dominating the losses. If the torque is well below the calculated value, concentration (mass transport) losses are also seen in the polarization curve as with the 28 oz-in in Figure 6.8. When polarization curves are obtained with the tightening torque values higher than the predicted value, the poor performance in

166

comparison with the performance obtained with the optimal torque can be attributed to mostly high mass transfer resistance. This is very obvious in Figure 6.10 with 6 oz-in where the fuel cell I-V curve drops abruptly after the activation polarization part of the polarization curve.

The effect of changing the clamping pressure on the performance of a PEM fuel cell has been investigated numerically and experimentally. A numerical model was developed with four major parts: the stiffness of the stack materials, stiffness of the bolts, ideal compression of the GDL, and finally the tightening torque. The compression of the GDL, and the effects of contact electrical resistance and limited mass transfer affects is estimated and taken into consideration in the numerical model. A Herzian equation is used for predicting the optimal force on the GDL layer based upon ideal gas permeability and GDL contact resistance. The torque is used as an indirect means of measuring the stack clamping pressure, and has a direct effect on fuel cell stack performance. The experimental validation consisted of experimentally examining the effect of the clamping pressure on the electro-physical properties on three different free-convection PEM fuel cell stacks. As the stack material stiffness, bolt material, or GDL compression changed, the resulting fuel cell polarization curve changed. Results show that the numerical calculations agree well (± 2%) with the fuel cell stack torque tests. It is further shown that low tightening torque results in a high interfacial resistance between the bipolar plate and the gas diffusion layer that reduces the electrochemical performance of a PEM fuel cell. In contrast, high tightening torque reduces the contact resistance between the graphite plate and the gas diffusion layer, but meanwhile narrows down the diffusion path for mass transfer from gas channels to the catalyst layers. The model and experimental

167

validation verified the correct balance of obtaining a tightening torque based upon stack

and bolt stiffness, contact resistance and mass transfer limitations within a fuel cell stack.

7
DESIGN AND FABRICATION OF MICRO FUEL CELL STACKS

An understanding of how the design and manufacturing processes influence

performance variables is critical in order to successfully design new fuel cells. There

have been numerous design variables examined in this dissertation, and some of the most

important ones include flow channel geometry, catalyst particle size and shape, and

electrolyte thickness. Studying the fuel cell microstructure is very important for

optimizing fuel cell electrical behavior, however, it is even more important for micro fuel

cells since surface characteristics begin to dominate over bulk effects [98, 99].

The flow field plates are one of the most important components of the fuel cell

stack. The flow field plates distribute the fuel across the electrode surface, remove liquid

water, conduct electricity and mechanically stabilize the fuel cell membrane electrode

assembly (MEA). The traditional materials used for these plates include stainless steel or

graphite, aluminum or nickel. The processes commonly used to produce the flow field

design are CNC (computer numerical control) machining, injection molding and

stamping. These materials and processes are not suitable for MEMS-based (microelectro

mechanical) fuel cell systems. Typical materials that have been used for MEMS fuel

cells, in the literature, are silicon wafers, carbon paper, PDMS (polydimethylsiloxane),

SU-8 (EPON SU-8 epoxy resin from Shell Chemical), copper and stainless-steel metal

foils [98].

169

7.1 Background and Approaches

Several studies have investigated the creation of microchannels using MEMS techniques in the literature. Flow channel depths ranging from 50 to 200 μm were created in a silicon wafer in Lee et al. [100]. The micro fuel cell produced a current density of 50 mA/cm2, which is typical performance for a micro fuel cell. However, the fuel cell performance could have been improved if a non-corrosive metallic layer was applied to the silicon flow field plate to increase the conductivity. Yu et al. [101] had developed a reactive ion etching (RIE) process on silicon wafers with a 200 μm flow channel depth. A conductive metal (0.5–1.5 μm Au, Cu or Ti) was sputtered on the surface of the silicon wafer. The results showed that the micfeatures created on the silicon-based flow field plates would provide more uniform distribution of fuels under the same operating conditions of gas pressure and flow rate over traditional flow field plates. Schmitz et al. [102] applied MEMS fabrication processes to create the flow field plates. The current density could have been higher if the copper flow channels (35 μm) were deeper, and the glass fiber substrate was more conductive. O'Hayre et al. [103] designed a 16-cell PEM fuel cell in a 3.5 in.2 glass fiber composite plate, which had an open circuit voltage of 12 V for a 3C battery. However, there was still a large contact resistance, and the glass fiber substrate did not have the required stacking pressure, and there was large contact resistance.

The feature sizes for flow channels in the literature range from 100 μm x 200 μm x 20 μm to 500 μm x 500 μm to 750 mm x 750 mm x 12.75 mm, with many lengths, widths and depths in between with various rib widths [98, 104, 105, 106, 107, 108, 109, 110, 111, 112, 113]. Intuitively, it seems that fuel cell performance should improve as the

channel feature size decreases and gas flow velocity increases, since the increased flow velocity enhances mass transport. Yet, one of the disadvantages of the smaller feature size is the increased pressure drop in the flow channels. Although there has been a lot of speculation in the literature regarding the dimensions that should give the best performance, the entire range of channel width and depth dimensions has not been experimentally compared. The viewpoints regarding the performance of microchannels conflict mainly in the 20 μm to 500 μm range. For example, in [104] it mentions that better performance is gained between feature sizes of 483 μm – 99 μm, but the pressure losses under 200 μm are so large that it negates the effect of down-scaling [104]. In [105], when the channel depth was decreased from 1 mm to 300 μm, the power density performance increased by 71.9%. When the flow field channel depth was further reduced to 100 μm, the performance decreased by 8.6% [98, 105].

7.2 Design and Production of the Micro Fuel Cell Stack

Two micro fuel cell stacks were designed for this study, and are illustrated in Figure 7.2. Each stack was 25.4 mm x 25.4 mm x 14.7 mm, and the dimensions of the fuel cell components are given in Table 7.1. One stack used polyvinyl chloride (PVC) end plates, and the other used Delrin end plates, due to the low-cost, and commercial availability of the materials. Thin silicon gaskets were used to prevent gas leakage, and a contact layer was created by depositing a gold layer on the sides of the end plates that were in contact with the flow field plates. Six different 1 cm^2 flow field patterns were fabricated with various serpentine channel sizes ranging from 1000 μm to 20 μm in width and depth. The channel dimensions are shown in Table 7.2, and were chosen to give a

171

comparison of the range of micro to MEMS-sized channels in order to compare the effect

of the overall performance due to the change in flow field dimensions.

Table 7.1

Prototype stack dimensions

Stack Dimensions	Inches	Millimeters
End Plate	0.250	6.350
Gasket	0.004	0.102
Silicon Flow Channel Plate	0.016	0.400
Gasket	0.004	0.102
MEA (Fuel Cell)	0.040	1.016
Silicon Flow Channel Plate	0.016	0.400
End Plate	0.250	6.350
Total Thickness	0.58	14.72

The flow field plates were made from 400 μm thick, 4″ silicon wafers. Two flow

field plates for a single cell had a total cell area of 6.45 cm^2 and a reaction area of 1 cm^2.

A deep reactive-ion etching (DRIE) fabrication process was used for the fabrication of

micro flow fields in the silicon wafer for the 200 μm – 20 μm depth. In order to compare

the silicon DRIE fabricated flow field plates with conventional machining and

dimensions, four additional plates made of Delrin were made using traditional CNC

machining process. The micro-sized flow fields had channel dimensions of 500 μm and

1000 μm. As shown in Table 7.2, the width and depth of the flow channels ranged from

1000 μm – 20 μm, and the channel length range was from 7.8 – 8.0 mm. The width of the

ribs also ranged from 1000 μm – 20 μm, with a consistent channel area of 50% (channel to rib ratio of 1:1) [98].

Table 7.2

Flow field plate channel dimensions

No.	Channel Width (microns)	Channel Depth (microns)	Rib (Gap) Width (microns)	% of Active Area that is Channels	No. of Channels & Ribs	Channel Length
1	1000	1000	1000	50.0%	4	7
2	500	500	500	50.0%	8	7.5
3	200	200	200	50.0%	20	7.8
4	100	100	100	50.0%	40	7.9
5	50	50	50	50.0%	80	8.0
6	20	20	20	50.0%	200	8.0

The serpentine flow field design was chosen because it has been shown to perform the best in several MEMS fuel cell studies [104, 105], and it had to be easily compared with other micro-sized channel studies in the literature. One advantage of the serpentine flow path is that it reaches a large portion of the active area of the electrode by eliminating areas of stagnant flow.

The flow field plates were coated with gold in order to promote conductivity and reduce contact resistance. The openings in the inlet and outlet of the gas channel and end plates were made much larger than the flow field channel dimensions in order to fit standard connectors for gas flow into the stack. Figure 7.1 illustrates the single cell stack assembly. The flow chart of research methodology is presented in Figure 7.2.
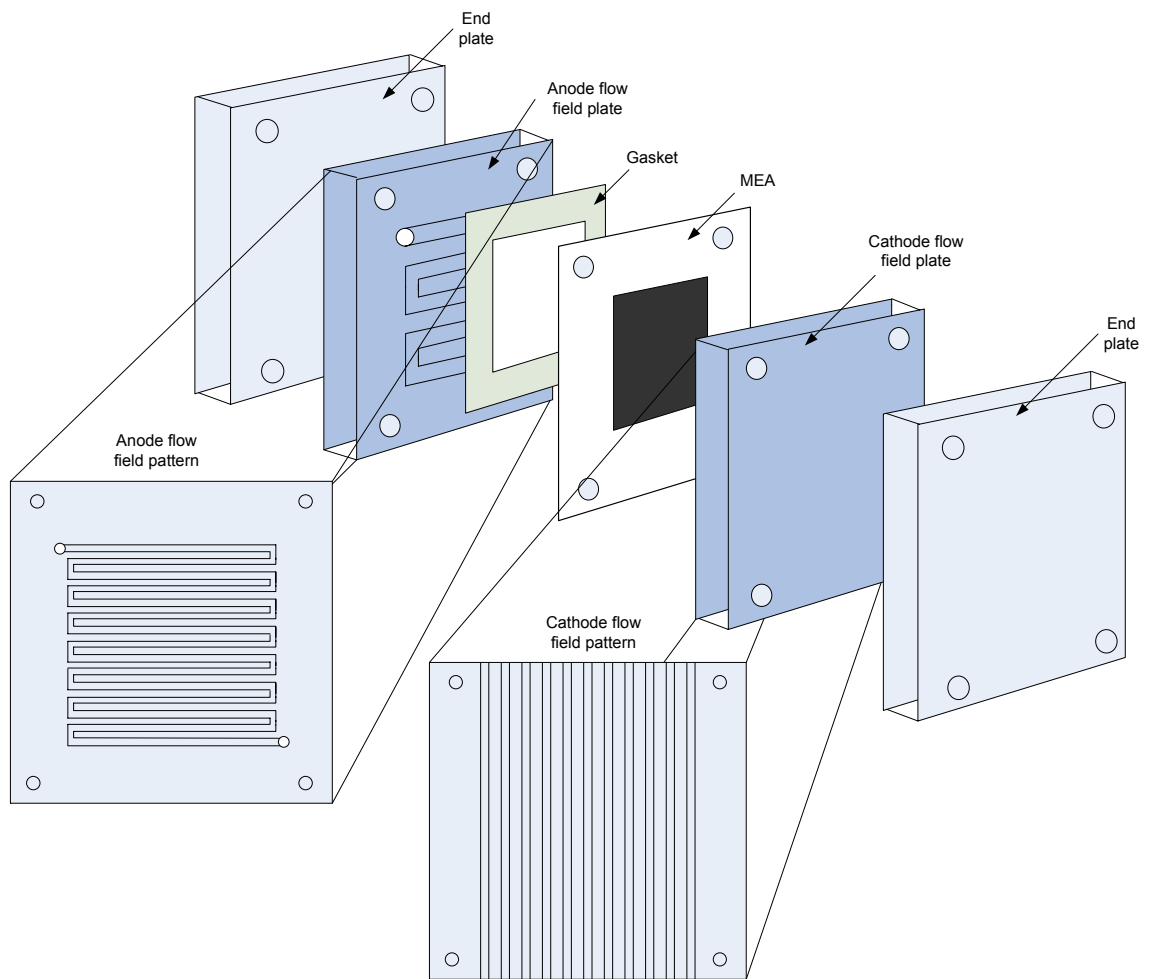
Figure 7.1. Single cell design and its components [98]
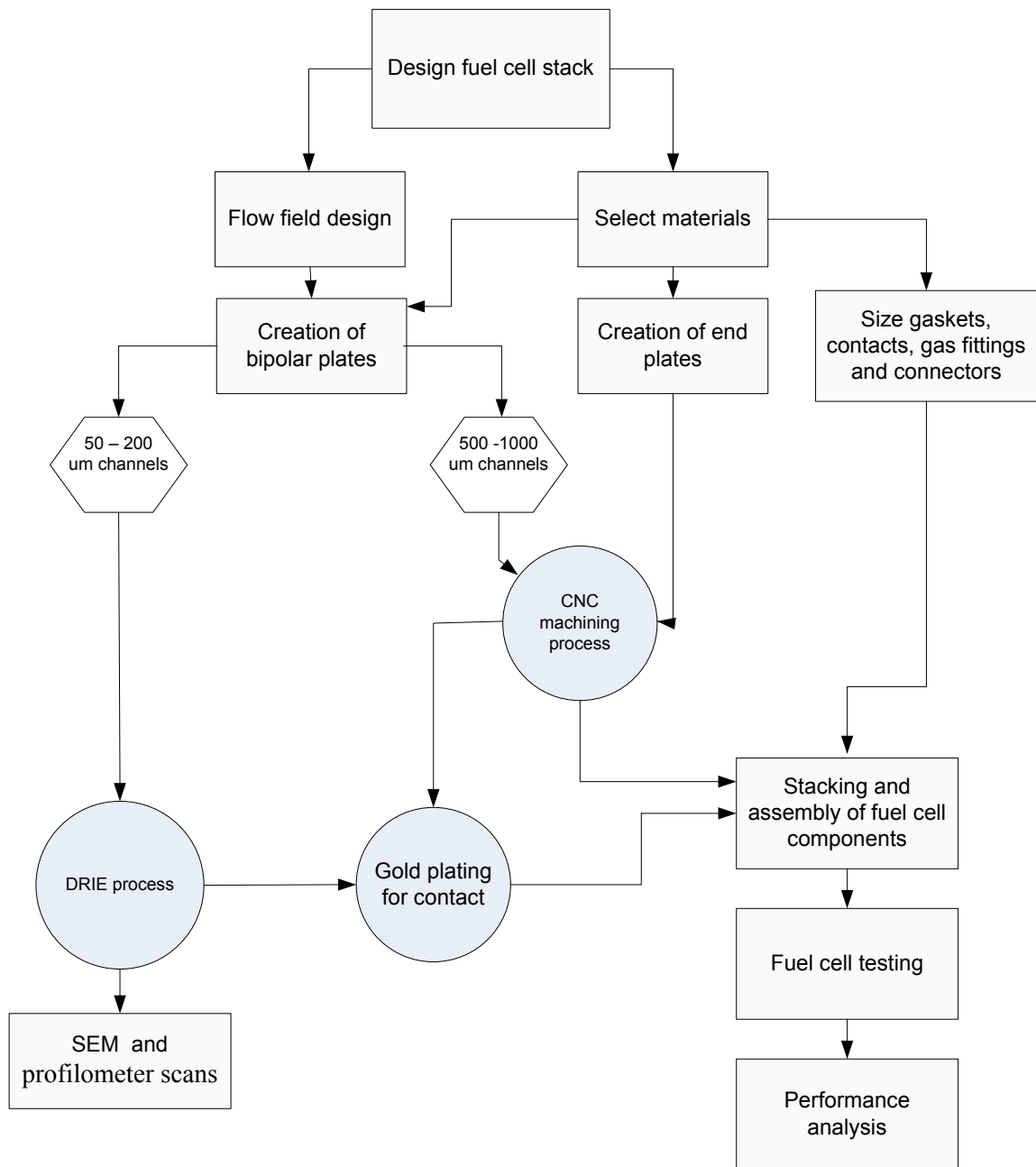
Figure 7.2. Flow chart of research methodology [98]

7.3 Microchannel Fabrication Process

The first step in the microchannel fabrication process is depositing a 2 μm thick

PECVD SiO_2 layer on both sides of the Si wafer. The front side was patterned using the

channel mask and Futurex PR2000 photoresist. The exposed SiO_2 was partially etched by

RIE for 10 minutes. Next, Shipley 1813 photoresist was manually placed over the

alignment marks, and then baked for 1 minute at 90°C. The remaining SiO_2 was etched

off by RIE for 60 minutes. The photoresist was then stripped off using acetone/methanol.

The wafer was then put into DRIE, and etched (~ 1μm/min) to the desired depth of the

channels [98].

After the microchannels were created, through-holes were then made in the same

silicon wafer in order for the silicon flow field plate to be placed into the fuel cell stack.

PR2000 was spun onto the back side of the wafer, and then RIE of SiO_2 was performed

for 70 minutes. The through-holes were created with a through-wafer DRIE process. The

last step for creating the through holes was stripping off the oxide layer using BOE. A

layer of Ti/Au 300nm/1μm was then sputtered on the wafer from the channel side (front

side) to prevent corrosion and improve conductivity [98]. The processes used to create

the flow field pattern are presented in Figure 7.3, and further details of the fabrication

process can be found in [114].

The following labels appear alongside the process flow diagram, top to bottom:

Start with a 4" DSP wafer

Deposit 2microns PECVD oxide on both sides

Pattern the front side using channel mask. Do the partial etch of Oxide using photoresist as masking layer.

Manually protect the alignment marks using photoresist. Etch the remaining oxide off using RIE.

Strip off the photoresist and perform DRIE for channels.

Pattern the back side using through hole mask. Etch off the oxide using RIE

Strip the photoresist from the back side

Perform through wafer DRIE

Strip the oxide from the wafer using BOE clean.

Figure 7.3. Flow chart of the RIE process used for the creation of the flow field plates

[98]

177

7.3.1 The Two Stage DRIE Process

      Two iterations of the etching process are conducted in order to create the micro flow fields and through holes in the silicon flow field plates. The first iteration of the etching process created the main flow field channel pattern, and the second iteration created the through holes for the gas inlet, outlet and through bolts. Figure 7.4 shows the main flow channels. Figure 7.5 shows the through hole with the micro flow channels.
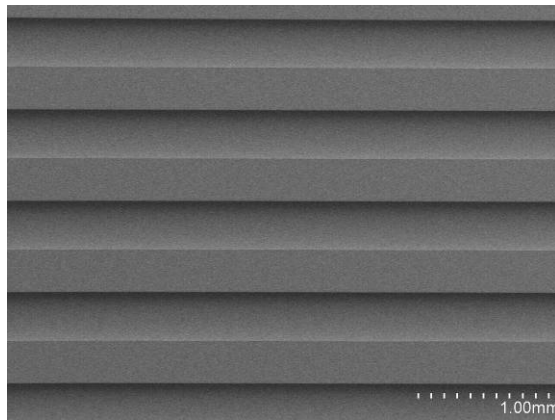
Figure 7.4. Micro flow field channels in silicon flow field plate
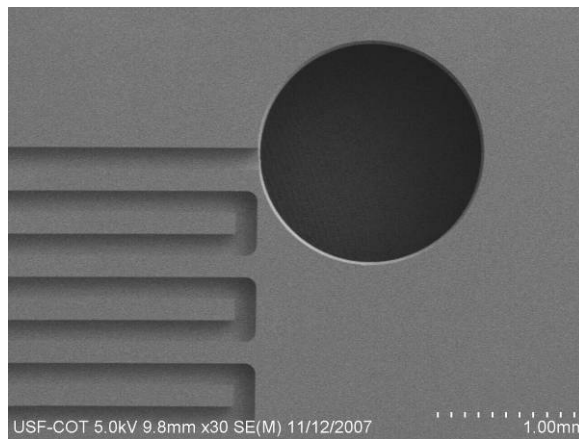
Figure 7.5. Through-hole added to micro flow field channels in silicon flow field plate

The surface profile and depth of the flow channel were obtained using scanning electron microscopy (SEM) and profiler scans. Figure 7.6 compares the micro flow field channels at 20 μm, 50 μm and 200 μm. The SEM photos demonstrate the precision of the micro channel structure created by the DRIE process [98].
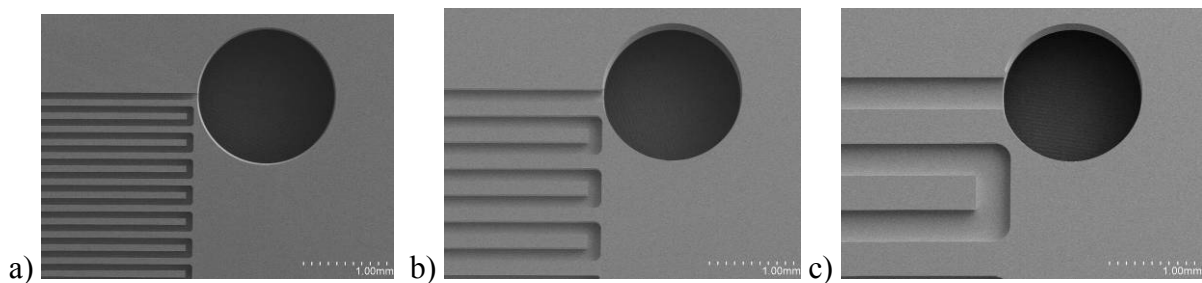
Figure 7.6. SEM images of micro flow field channels and through holes, (a) 20 μm, (b) 50 μm, and (c) 200 μm width channels

7.3.2 Single Cell Fuel Cell Stack Performance Tests

The two single cell, air breathing fuel cell stacks had an active fuel cell area of 1 cm × 1 cm, and was comprised of a 5-layered MEA made of Nafion 112, carbon cloth and 1 mg/cm^2 of Pt loading on both the anode and cathode. The same MEA and stack is used with the different micro flow field plates (20 μm – 200 μm flow channels). A second stack was assembled for the 500 μm and 1000 μm channel flow field plates [98]. The single cell fuel cell stacks are shown in Figure 7.7.

Figure 7.7. Prototypes of the single cell fuel cell stacks [98]

Cell performance tests are taken at 25º C and ambient pressure with 0.5 standard cubic centimeter per minute (SCCM) of hydrogen from an electrolyzer, with no additional humidification. *I–V* curves of these cell performance tests are plotted in Figures 7.8 and 7.9. The 1000 µm and 500 µm flow channels had the worst cell performance characterized by low current densities, high contact resistance and poor mass transfer [98].
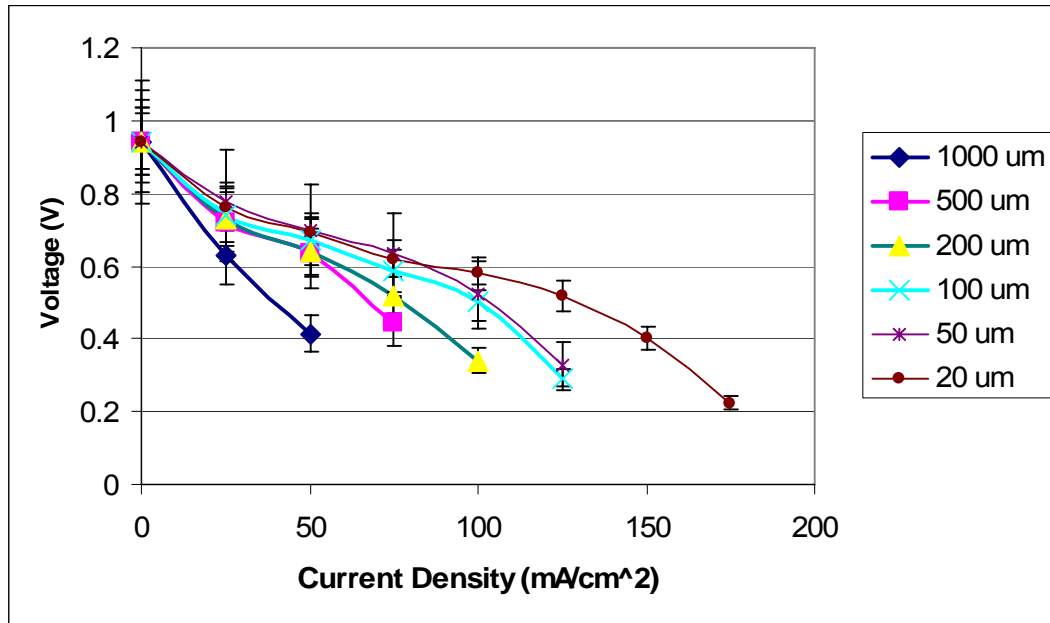
Figure 7.8. I–V curve of the cell performance tests [98]
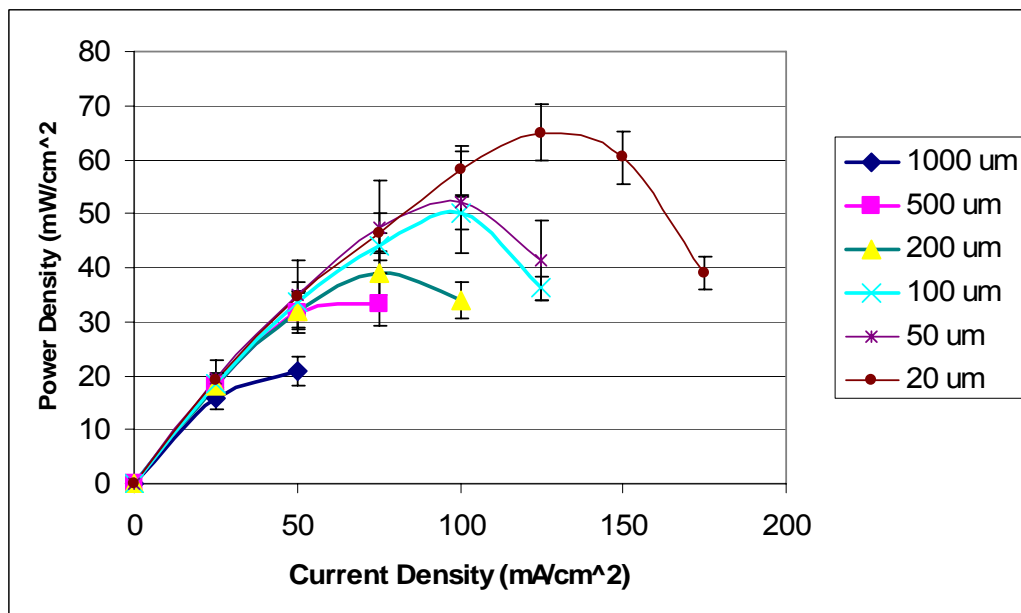
Figure 7.9. Fuel cell power density curves for 20 - 1000 μm channel widths and depths

[98]

181

The single fuel cell stack was designed as a smaller version of a traditional fuel cell to enable comparison with both larger commercial fuel cells, and with other MEMS fuel cells in the literature. The channel and rib dimensions selected for this study were used to determine the optimal flow channel dimensions for a MEMS fuel cell. Some of the benefits of the MEMS flow regime include laminar flow, higher velocities, rapid diffusion, low leakage, surface effects, good flow control and very small dead volumes. A major advantage for MEMS fuel cells is that many of the layers can be applied through sputtering (or some other MEMS-based process). The layers can be extremely thin, which will make the future stacks lighter and less costly, but will allow the fuel cell to maintain high current densities. When designing MEMS fuel cells, some of the issues that may be encountered are surface roughness, uneven topography, bubbles and flooding in flow channels [98].

The flow field channels increase in performance with the decrease in channel width, depth and rib size, which is the space between flow channels. The 20 μm flow channel width, depth and rib size outperformed all other channel sizes in terms of power density and current density. In the activation polarization dominated region ($\sim 0.8 - 1.0$ V), all of the activation voltage losses were about the same for all of the fuel cell tests conducted. Since the same fuel cell MEA was used, the electrode kinetics should be similar, and therefore, the activation voltage losses should be similar [98].

In the ohmic polarization dominated region ($\sim 0.5 - 0.8$ V), the 20 μm flow channel width, depth and rib size had superior performance in terms of voltage and current density. Since the majority of the ohmic resistance in fuel cells is the electrolyte, and the same MEA was used, the difference in ohmic resistance is due to the difference

in width, depth, rib size, the number of channels and the percent channel area. As shown in Table 7.2, the percent area of channel and rib space (50 %) is consistent for all of the flow field plates. The decreased contact resistance for the flow field plates with the 20 μm dimensions may be due to the gas diffusion media protruding into the flow channel. This provides greater surface area of the GDL layer in contact with the flow field plates.

The concentration polarization dominated region (~ 0 – 0.5 V) displays the most notable difference between polarization curves for the dimensions of the flow field plates. As the channel width and depth decreases from 1000 to 20 μm, the velocity and pressure drop increase rapidly. The large increase in pressure drop is counteracted by the rapid increase in velocity. Although the channel to rib ratio is identical for all of the flow field plates created (1:1), the decrease in rib size may aid in better overall reactant flow through the gas diffusion media since the "void space" between channels is decreased. In addition, since the depth of the 20 μm is substantially less than the other depths, the stagnant flow region at the interface between the channel and gas diffusion media encompasses a larger portion of the flow channel. Also, if the gas diffusion media is protruding into the channels, this stagnant flow region may encompass a large portion of the channel, and therefore, the flow in the channel enters the diffusive regime with greater ease than in larger channels where the flow has to convert from convective to diffusive [98].

Although the performance of the MEMS fuels cells presented in this dissertation performed better than most other MEMS fuel cells currently in the literature, the performance is still poor in comparison to convectional fuel cells where the current density typically reaches $1 – 1.5$ A/cm^2 ($0.5 – 8.0$ A/cm^2 for free-convection fuel cells).

One of the issues with MEMS fuel cells is that liquid water droplets generated at the cathode can block a flow channel entirely. These blockages can lead to reactant starvation at the cathode, which not only affects the concentration polarization region of the polarization curve, but also affects the fuel cell performance through reaction kinetics (the activation polarization region) due to the dependence upon the reactant and product concentrations at the reaction sites. In addition, when the reactants are deficient at the reactant sites, this generates less charge, therefore, the amount of charge that is transported through the cell is reduced, which contributes to the ohmic polarization dominated region. The combination of these voltage losses creates a total polarization curve with poor performance in comparison to traditional fuel cells [98].

8
FUEL CELL MODEL RESULTS

A mathematical model can help the fuel cell engineer to design a better fuel cell through an understanding of the physical phenomena occurring within the PEM MEA layers. This is important because the direct measurement of concentrations and velocities within a fuel cell is currently unavailable due to the thinness of, and the bonding between, the MEA layers. Therefore, a transient 1-D mass, heat, pressure and membrane model was created in MATLAB to study the transport phenomena, and this chapter highlights some of the processes that the current model illustrates.

In order to examine these processes occurring within the PEM fuel cell, design parameters were taken from several actual PEM fuel cell stacks, and necessary constants were taken from the literature, and are noted in Appendix A. The model considers mass and energy balances, heat generation equations at the anode and cathode catalyst layer, and pressure losses throughout the fuel cell stack. The model was coded to allow the user to divide each fuel cell layer into smaller nodes along the x-axis, if specified. Unlike most published models, this model includes all of the layers in the fuel cell stack, including the end, flow field and cooling plates, terminals, the gas diffusion layers (GDL), catalyst layers and membrane. Many of the variables in the model were put into arrays to make the code cleaner, and to reduce the number of lines in the code. The numerical code allows the discretization of each of the layer into smaller control volumes. The temperatures were assumed to be at the center of each node, and the mass flow rates,

pressure drop, velocity and charge transport was defined at the boundaries of each control volume as illustrated in Figure 8.1. The set of equations were put into matrix form, and solved simultaneously using MATLAB's ode45 ordinary differential equation solver. ode45 is based on an explicit Runge-Kutta (4,5) formula, the Dormand-Prince pair. It computes $y(t_n)$ in one step, and needs only the solution at the immediately preceding time point, $y(t_{n-1})$.
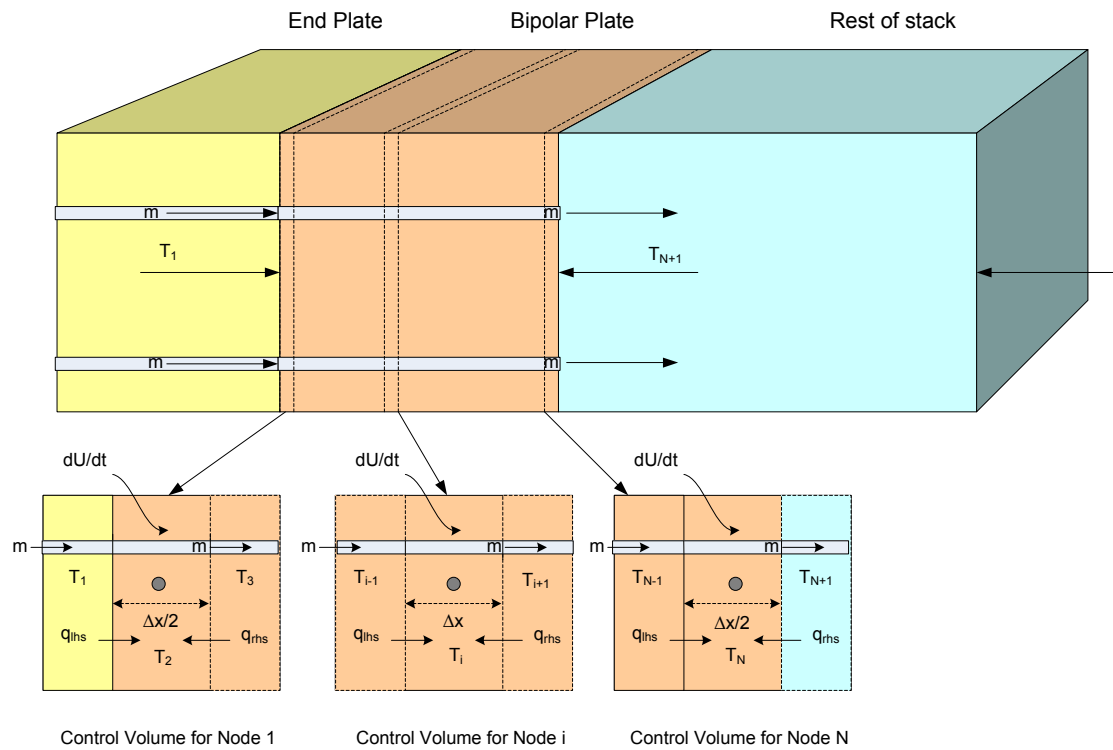
Figure 8.1. Schematic of the PEMFC stack and its components for model development

The numerical code that was developed for this study has approximately 3500 lines. Lines 11 – 117 initialize all of the constants used in the model, and the lines 118 – 225 initialize all of the parameters in form of vectors, which are listed in Appendix A. Lines 235 – 253 assign the layer numbers, and the number of user-specified nodes in each layer. The x coordinates for each node are then calculated assuming a uniform distribution. Lines 235 – 253 include code that specifies skipping the layers that do not repeat in each cell (such as the end plates), and assign coordinates to all of the nodes for each layer in the fuel cell stack. Lines 256 - 318 calculate or specify the initial pressures, temperatures, velocities, molar flow rates and potentials for the simulation program. The state variable matrix is formed in lines 324 – 341, and this is passed to the *fuel cell* function, which calculates the change in temperature, pressure, velocity, molar flow rates, and potentials with respect to time using the MATLAB's ode45 solver.

In the *fuel cell* function, the components of state vector are separated on lines 349 – 355. The vectors are initialized for all of the outputs on lines 362 – 389 and 434 – 500. The Prandtl numbers are calculated on lines 508 – 518 to obtain the heat transfer coefficients. The mass transfer section ranges from lines 520 – 1593, the pressure drop section is in lines 1595 -2317, the temperature section spans lines 2319 – 2762 and the potential section makes up lines 2764 – 2997. The rate change equations for the molar flow rates, pressures, velocities, potentials, and temperatures are on lines 2999 – 3089. The remainder of the code creates the plots that are automatically generated while the program is running. The mass flow, pressure, temperature portions of the model will be discussed in more detail throughout this chapter. An overall diagram of the MATLAB simulation program is illustrated in Figure 8.2.

Parameter Vectors
These parameters are specified for each layer:

(1) Number of slices
(2) Density (kg/m3)
(3) Area (m)
(4) Area of void (m2)
(5) Channel Area (m2)
(6) Thickness (m)
(7) Thermal Conductivity (W/m-K)
(8) Specific Resistance (ohm-m)
(9) Specific heat capacity (J/kg-K)
(10) Channel radius (m)
(11) Channel width (m)
(12) Channel depth (m)
(13) Channel length (m)
(14) No. of Bends
(15) No. of Channels

Constants

(16) Initial stack temperature (K)
(17) Hydrogen temperature (K)
(18) Air temperature (K)
(19) Convective loss to air from the stack
(20) Ambient temperature (K)
(21) Current (A)
(22) Humidity
(23) Activation overpotential (V)
(24) Entropy change for anode
(25) Entropy change for cathode
(26) Volumetric flow rate of hydrogen (m3/s)
(27) Volumetric flow rate of air (m3/s)
(28) Viscosity of hydrogen (Pa-s)
(29) Viscosity of air (Pa-s)
(30) Hydrogen pressure (Pa)
(31) Air pressure (Pa)
(32) Density of hydrogen (kg/m3)
(33) Density of air (kg/m3)

Inputs: 1, 6

Inputs: 7, 19

Inputs: 16, 20, 26, 27, 30, 31

Assign layer numbers, and slices to each layer, specify x coordinates based upon the uniform distribution of nodes

Compute heat transfer coefficients for the left and right sides of each layer U(layer)

Initialize temperature, total mass flow, pressure and velocity vectors, and specify the initial values T(layer), n_tot(layer), P(layer) and u_m(layer)

Calculate Slice Thicknesses: Get derivative's between x's dx(layer)

Calculate the change in T, n_tot and P using ode45 (ODE solver based upon Runge-Kutta (4,5) formula)

Form state variable matrix

Call fuel cell function to calculate dTdt, dndt and dPdt

Separate components of state vector

Inputs: 2, 3, 4, 8, 9, 21, 23, 24, 25

Inputs: 5, 6, 10, 11, 12, 13, 14, 15, 17, 18, 28, 29, 30, 31

Inputs: 17, 18, 22, 30, 31, 32, 33

Calculate the right and left heat flows for each layer (Q_left + Q_right), energy mass terms (mass), thermal mass (thmass), layer-specific heat flows (Q2) and enthalpies (H)

Calculate velocity

Calculate pressure drop

Calculate inlet and outlet molar flows

Calculate molar flows of protons, oxygen and water in the catalyst layers

Combine into rate change of T, n_tot and P:

dTdt = (Q_left + Q_right + Q2 + H) ./ (mass + thmass)
dndt(outlet(i)) = dndt(outlet(i)) + n_outlet(i) - n_tot(outlet(i))
dPdt(outlet(i)) = dPdt(outlet(i)) + P_outlet(i) - P(outlet(i))

Use calculated T, P and mole fractions of H2 and O2 to calulate charge generated in catalyst layers

Polarization curve

Figure 8.2. Overall diagram of MATLAB code created

Since the hydrogen flow rate into the fuel cell enters the stack from one end, and the oxygen enters from the other end, this creates a challenge when creating an overall fuel cell stack model. Figure 8.3 shows a diagram of the order of fuel cell layers in the stack, the directions of the flow into each layer, and the associated layer numbers used for the model. To better understand the outputs discussed in this chapter, the layer and flow numbering are shown in Figures 8.3 and 8.4. Both the layer and the flows into each layer are numbered from left to right.
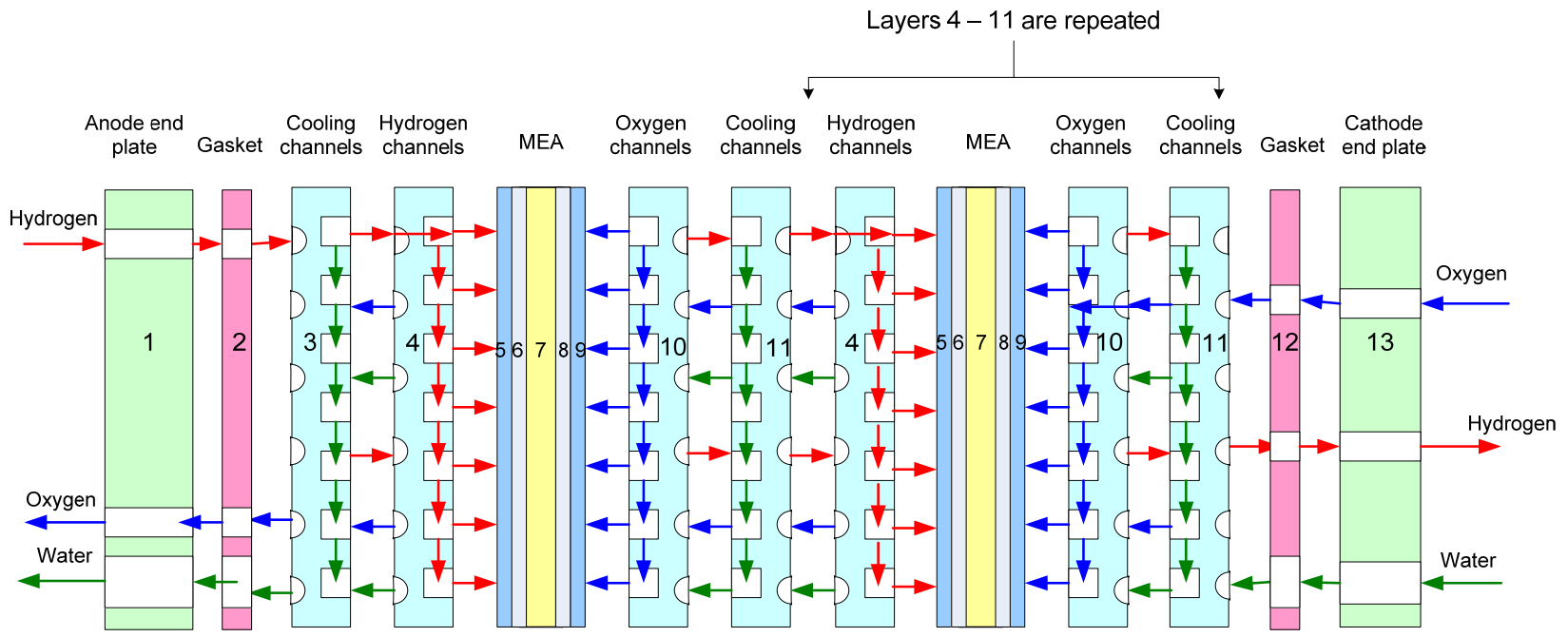
Figure 8.3. Illustration of fuel cell stack layer numbering
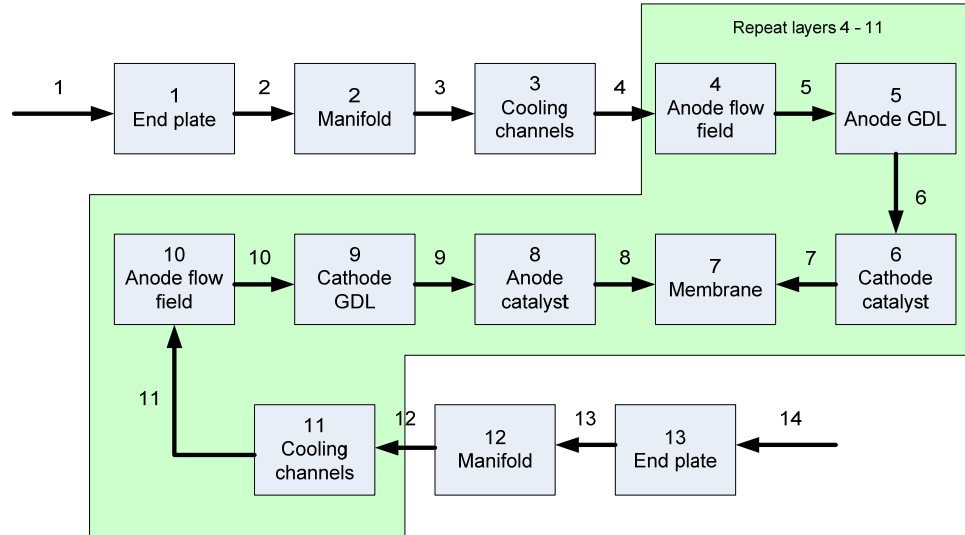
Figure 8.4. Schematic of the numbering of layers and flows for the PEMFC model

8.1 Heat Transfer Portion of the Overall Fuel Cell Stack Model

A numerical code was developed to investigate the effect of various stack materials and operating parameters on fuel cell heat transfer behavior. The energy balances and thermal resistance equations for each layer are integrated simultaneously using MATLAB's ode45 function. Arrays were created for the node temperatures, thermal resistances, heat transfer coefficients, heat flows, Nusselt numbers, specific heats, thermal conductivities and enthalpies of each node or layer. The stack dimensions and other parameters used in the simulations are summarized in Appendix G.

As mentioned previously, the initiation of the variables, and initial temperature parameters are given in lines 267 – 279, 313 – 319, 366 -382, 403 – 428, 456 – 482, 508 – 518 in the overall model code. Beginning with line 2319, the ohmic heating, thermal resistance, enthalpies, specific heats, viscosities, and thermal conductivities for the nodes in each layer are calculated. In addition, the thermal resistances for the solid portion of

the layer to the gas/liquid portion of each layer are computed. A summary of the thermal

portion of the code in shown in Figure 8.5.

Parameter Vectors
These parameters are specified for each layer:

(1) Number of slices
(2) Density (kg/m3)
(3) Area (m)
(4) Area of void (m2)
(5) Thickness (m)
(6) Thermal Conductivity (W/m-K)
(7) Specific Resistance (ohm-m)
(8) Specific heat capacity (J/kg-K)

Constants

(9) Initial stack temperature (K)
(10) Hydrogen temperature (K)
(11) Air temperature (K)
(12) Convective loss to air from the stack
(13) Ambient temperature (K)
(14) Current (A)
(15) Humidity
(16) Activation overpotential (V)
(17) Entropy change for anode
(18) Entropy change for cathode
(19) Volumetric flow rate of hydrogen (m3/s)
(20) Volumetric flow rate of air (m3/s)
(21) Hydrogen pressure (Pa)
(22) Air pressure (Pa)

Inputs: 1, 5
Inputs: 6, 12
Inputs: 9, 13

Assign layer numbers, and slices to each layer, specify x coordinates based upon the uniform distribution of nodes

Compute heat transfer coefficients for the left and right sides of each layer U(layer)

Initialize temperature vector, and specify the initial layer temperatures T(layer)

Calculate Slice Thicknesses: Get derivative's between x's dx(layer)

Calculate the change in T using ode45 (ODE solver based upon Runge–Kutta (4,5) formula)

Call heat function to calculate dTdt

Inputs: 2, 3, 8

Calculate the right and left heat flows for each layer (Q_left + Q_right) & energy mass terms (mass)

Initialize heat flow (Q2), enthalpy (H) and thermal mass (thmass) vectors

Inputs: 3, 4, 7, 14, 16, 17, 18

Calculate additional layer-specific heat flows (Q2)

Inputs: 10, 11, 15, 19, 20, 21, 22

Calculate molar flow rates (n)

Enthalpy (h)

Enthalpy portion of energy balance (H)

Combine into rate change of T:
dTdt = (Q_left + Q_right + Q2 + H) ./ (mass + thmass)

Figure 8.5. Temperature portion of overall model

The heat distribution in stacks with at least 20 cells shows an almost identical

distribution with stacks of larger size. Therefore, it was found that stacks with at least 20

cells were adequate in simulating stacks of 100 cells or more. Since the minimum number

of cells is a strong function of end plate and stack design, the results presented in this

section is for a generic stack, and will not be applicable for all stack configurations.

Figures 8.6 and 8.7 shows a typical temperature distribution through a 20 cell and 250

cell stack with an initial heating of the stack to 333 K, a current density of 0.6 A/cm2,

and reactant gas pressure of 3 atm.
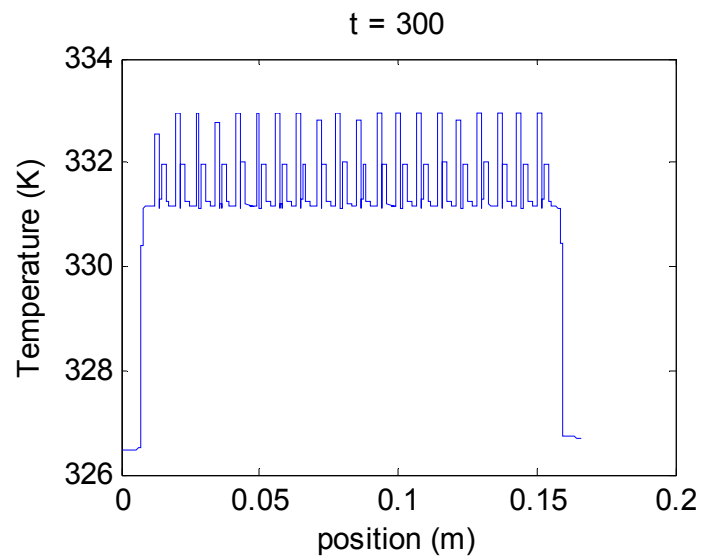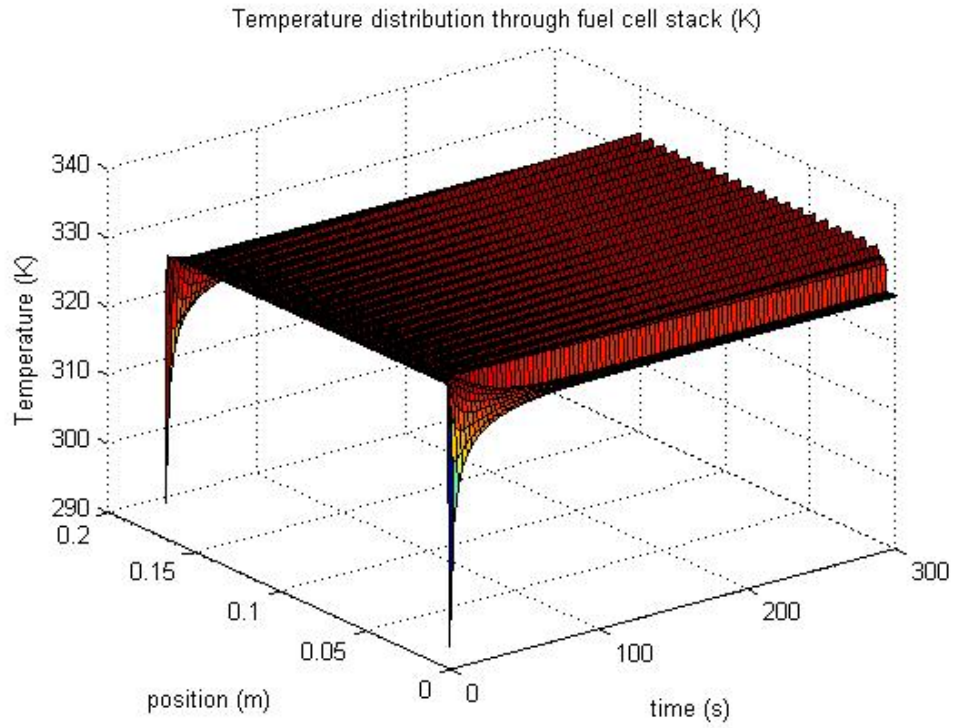
Figure 8.6. Temperature distribution in a 20 cell fuel cell stack, a) surface plot of the

temperature distribution as a function of position and time, (b) temperature distribution at
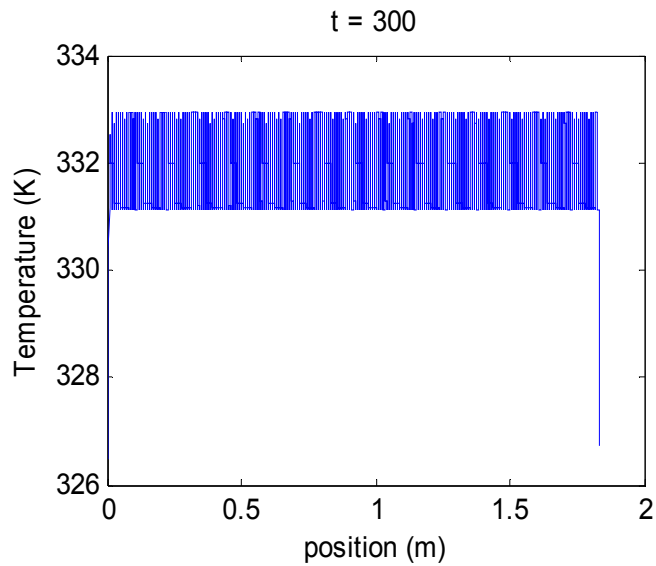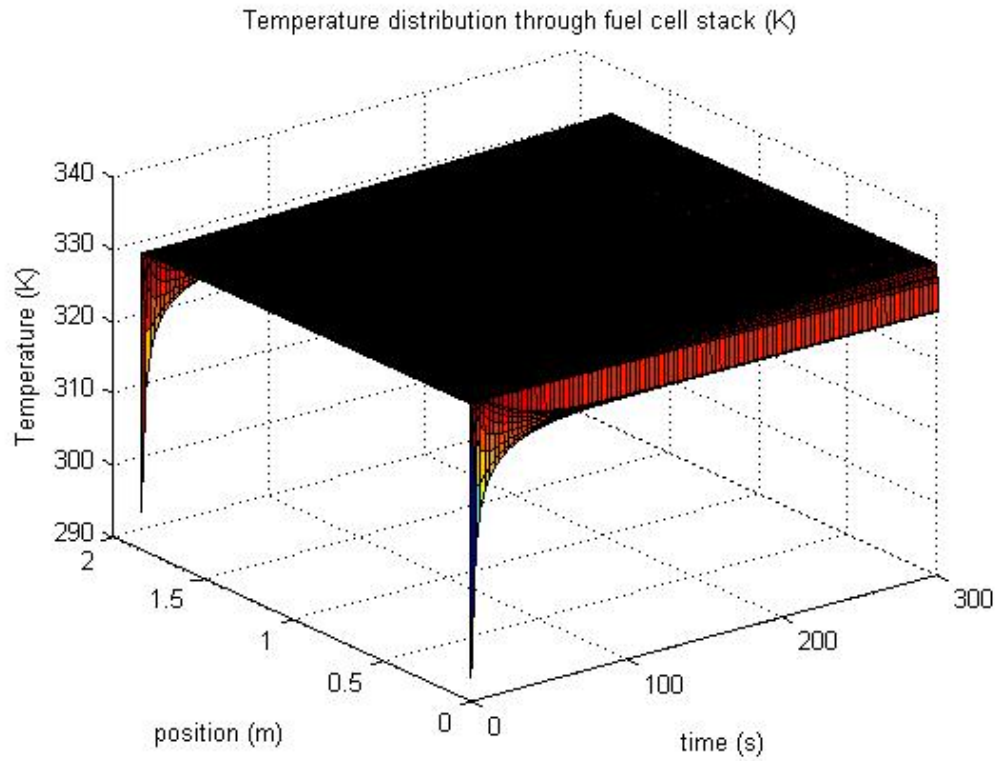
t = 300s

Figure 8.7. Temperature distribution in a 250 cell fuel cell stack, (a) surface plot of the

temperature distribution as a function of position and time, (b) temperature distribution at

t = 300 s

8.1.1 Temperature Distribution of Various Stack Sizes

The minimum number of cells that can be used to simulate a larger stack is influenced by the stack and end plate design. Figure 8.8 illustrates a comparison of the temperature distribution of a 5, 10, 20, 50 and 100 cell stacks. Due to the number of cells in the 20, 50 and 100 cell stacks, the temperature distribution in the center cells for the 20 and 50 cell stacks were almost identical at varying times for the heating in the cell layers, which indicates that the 20 cell stack is adequate for studying the temperature distribution and other stack transport phenomena.
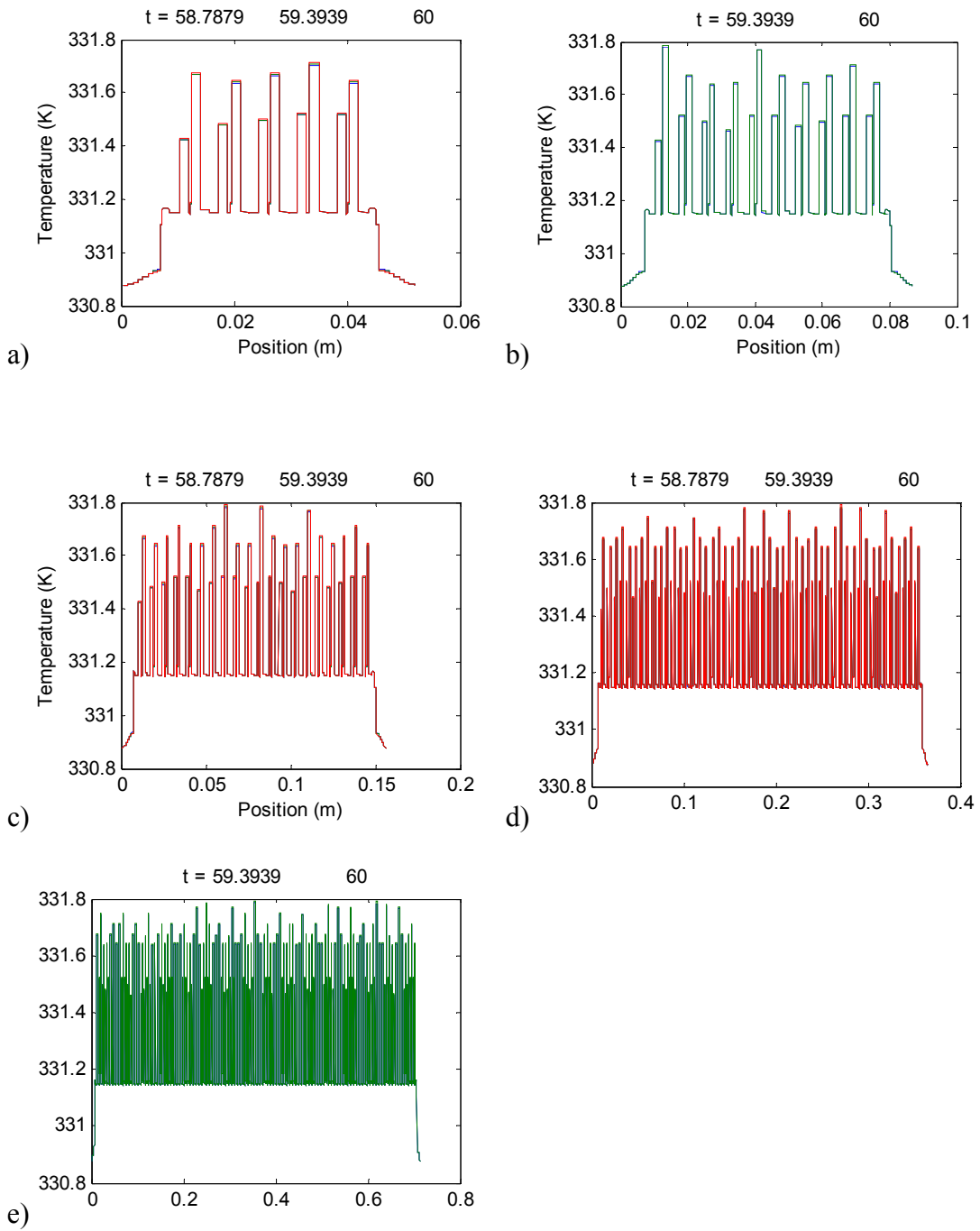
Figure 8.8. Temperature distribution at the end of 60 seconds for (a) 5 (b) 10 (c) 20 (d)

50 and (e) 100 cell stacks

8.1.2 Stack Temperature Distribution Over Time

Figure 8.9 shows the effect of time on the stack temperature distribution. As expected, as the time increased, the catalyst layers become hotter, and the entire stack heats up due to catalytic heating. There is a significant increase in heating from t = 10 s to t = 600 sec. The local heating in the anode and cathode catalyst layers increases from 331.3 K to 331.3 K after 10 s. By 60 s, the local heating of the catalyst layers ranges from 331.6 to 331.8 K, and at 600 s, the local heating in these layers has increased approximately 7 K. The catalytic heating in the cells of the fuel cell stack can present a challenge for fuel cell designers. However, these local temperatures are unable to be accurately measured within the fuel cell stack. The fuel cell researcher is able to measure the temperature of the bipolar plates instead in order to obtain an idea of the heat generated by the catalytic heating.
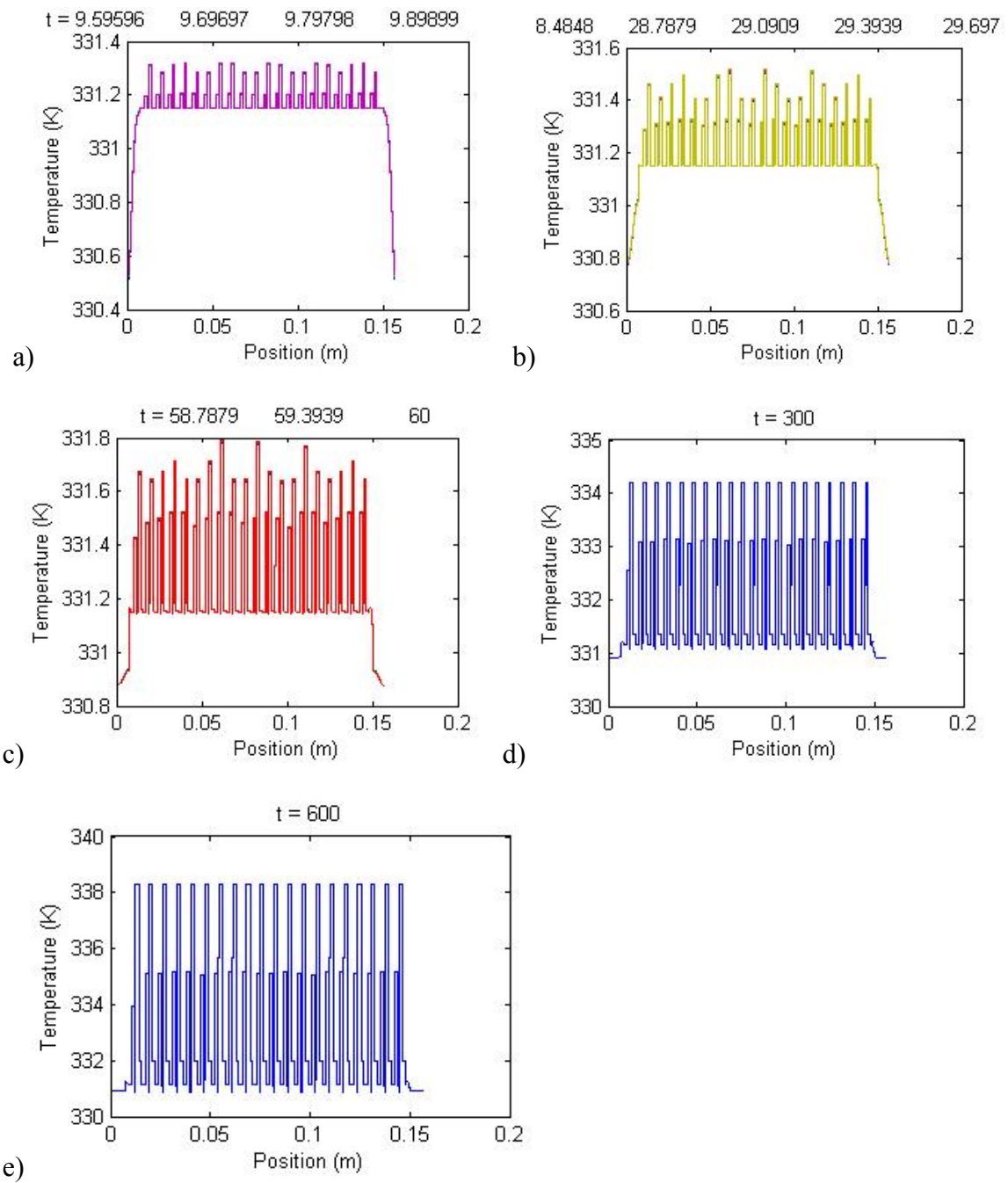
Figure 8.9. Temperature distribution at different times (a) 10 (b) 30 (c) 60 (d) 300 and (e)

600 seconds

8.1.3 Temperature Distribution in a Single Cell

When the number of nodes are increased significantly for each layer, the temperature variation in the graphs become minimized because the heat is transferred to the previous and next nodes, and the effect of the heat/cooling is shown in the overall cell or stack temperature distribution. However, the local heating from the catalyst layers are still very obvious in the graphs, and there is little change in the magnitude of the heating of the catalyst layers. Increasing the number of nodes per layer is very important as the layer thickness increases. This enables the heat to diffuse through each node more quickly, and be transferred to the next node faster, which crates a realistic result. Figure 8.10 illustrates the temperature distribution in a single fuel cell with 1, 10, 32 and 64 nodes per layer.
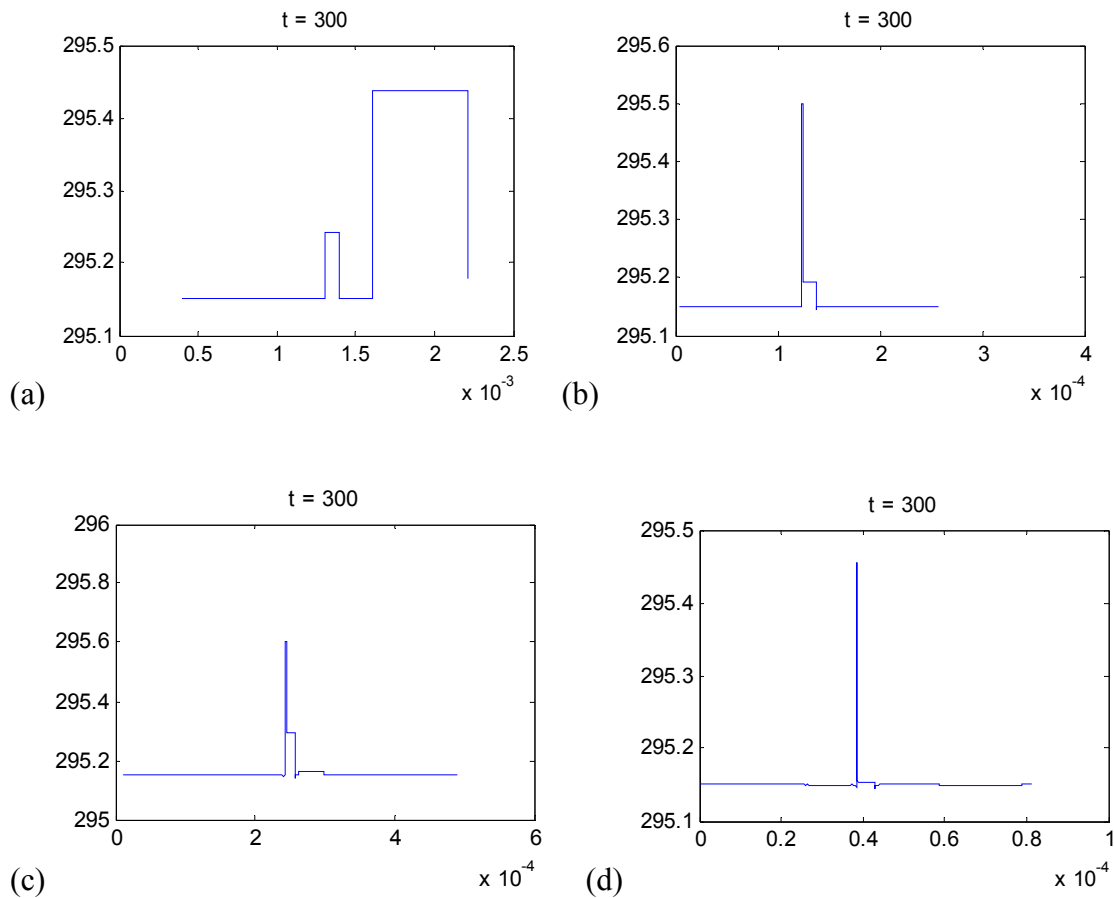
Figure 8.10. Temperature distribution through a single fuel cell, with using a (a) 1, (b) 10, (c) 32 and (d) 64 nodes per layer

8.1.4 Variation of Operating Current Density

Figure 8.11 shows the stack temperature distribution for current densities i = 0.1, 0.6 and 1.0 A/cm^2 respectively. After 300 seconds, the temperature increased from 334 K to 336 K for a current density of 0.1 A/cm^2, it increased an extra degree for a current density of 0.6 A/cm^2 and it increased to 342 K for a current density of 1.0 A/cm^2. The asymmetric stack distribution can be attributed to the different heat source term on the

anode and cathode sides [115]. Similar stack temperature distributions were also achieved

by Khandelwal et al. [115] and Shan and Choe [116]. In certain stack designs, it may be

advantageous to use the fact that there is rapid catalytic heating at current densities of 1.0

A/cm2. Some of the heat generated by the catalyst layers can be removed by the reactant

gases or by the coolant. The effect of inlet gas temperature and coolant temperature is

explained in Sections 8.1.5.

b)

c)
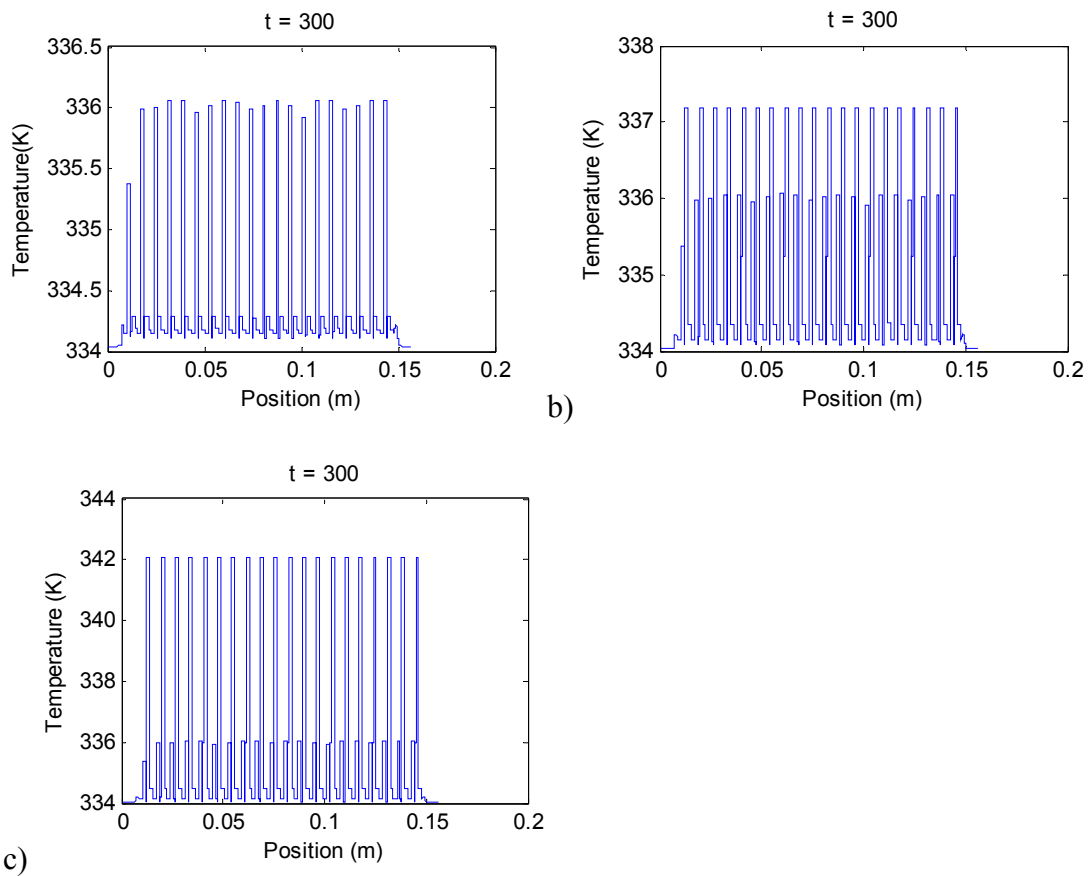
Figure 8.11. Stack temperature profile for base conditions at various time for (a)

$i = 0.1$ A/cm^2 (b) $i = 0.6$ A/cm^2 (c) $i = 1.0$ A/cm^2

8.1.5 Effect of the Inlet Gas and Coolant Temperatures

The effect of inlet gas temperature on the solid portion of each layer of the fuel cell stack is shown in Figure 8.12. Heating the anode gas will help to reduce the temperature difference between the anode and cathode side due to the unbalanced heat generation in the electrodes. Heating the cathode gas may also be useful to enhance product water uptake to help minimize the water flooding in the cathode, and to help enhance mass transport. Heat loss to the reactant gas or coolant can be reduced by either increasing the inlet gas flow temperature or reducing the gas flow rate. As expected, the gas temperature profile is similar to the stack temperature profile. The temperature of the gases rises very slowly in comparison with the temperature of the stack due to the heat capacity and thermal conductivity of the gases.
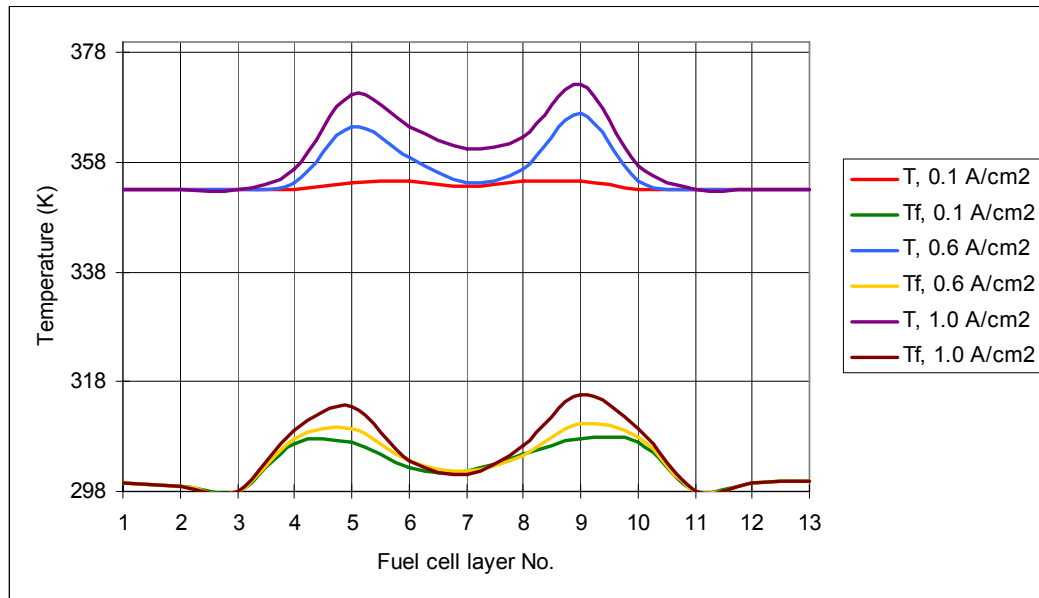
Figure 8.12. Stack gas temperature profile for base conditions at 1200 s for (a)
$i = 0.1$ A/cm^2 (b) $i = 0.6$ A/cm^2, and (c) $i = 1.0$ A/cm^2

Figure 8.13 shows the effect of heating the fuel cell stack layers on the inlet gas temperature from 60 s to 1200 s. As the stack heats up due to catalytic heating, the gas/fluid temperature also heats up. The gas/fluid temperature enters the stack at 298 K, and the stack is heated and maintained at 353 K.
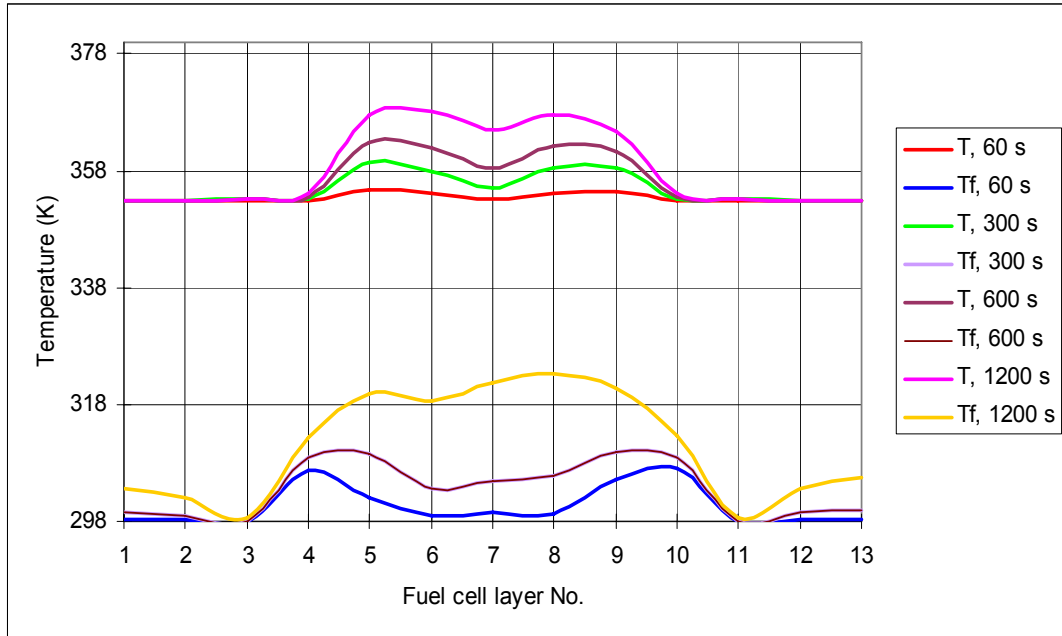
Figure 8.13. Effect of heating the fuel cell stack layers on the inlet gas temperature

Figure 8.14 illustrates the effect of heating the inlet gases to 353 K, and the effect on the stack temperature initially at 298 K. Of course, this is highly dependent on stack design, and Figure 8.14 illustrates a single cell stack, therefore, it is more difficult to heat the stack with the gases due to the large amount of stack volume that is solid.
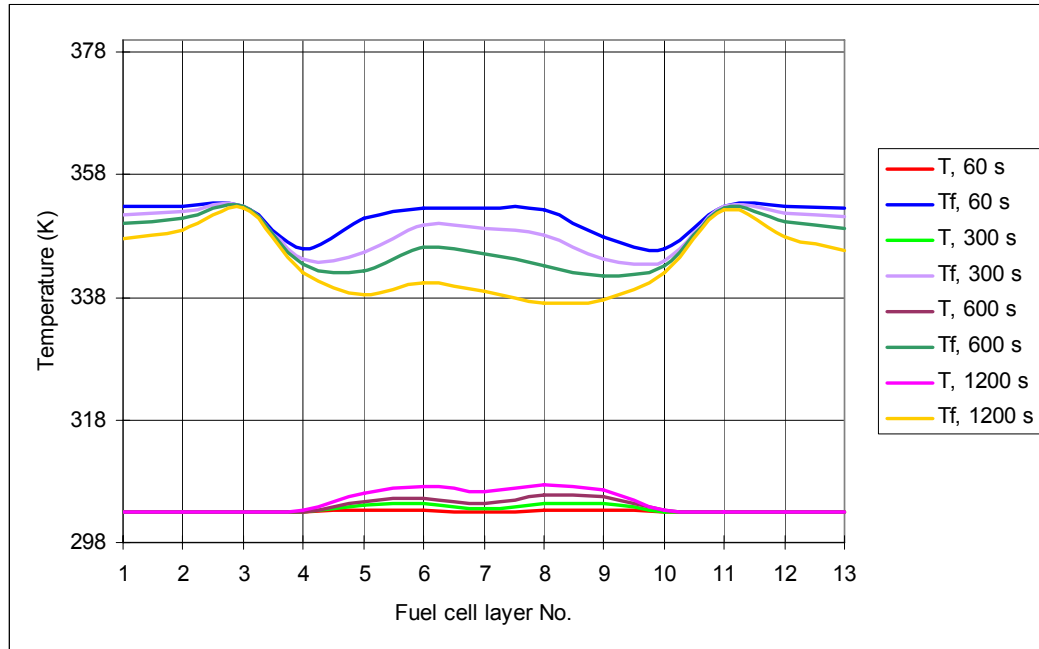
Figure 8.14. Effect of heating the inlet gas temperature on the temperature of the fuel cell

stack

Figure 8.15 illustrates the comparison of the stack temperature with inlet gas and coolant temperature of 298 K and 288 K respectively. As the coolant temperature, in layers 3 and 11, is lowered from 298 K to 288 K, the effect of the coolant temperature on the inlet gases is minimal. However, the effect on maintaining a more uniform stack temperature is very obvious. The heating by the catalyst in layers 6 and 8 is minimized after 1200 s by the coolant in layers 3 and 11.
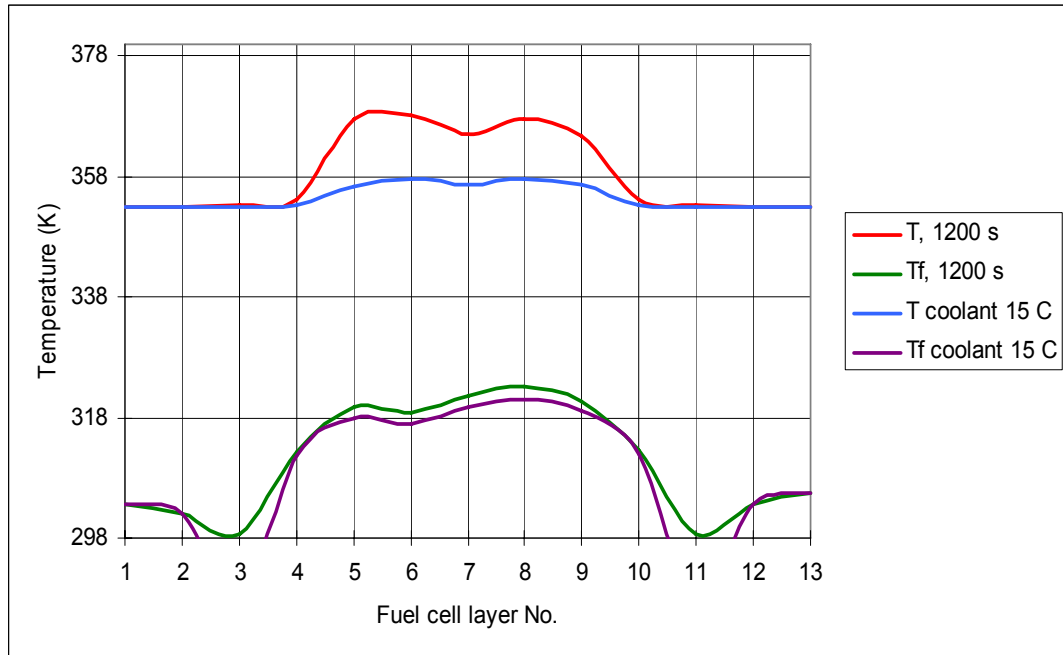
Figure 8.15. Comparison of the effect of coolant on the stack temperature

Figure 8.16 illustrates the effect of temperature on relative humidity on the single fuel cell stack for the temperature results presented by Figure 8.13. The anode side relative humidity is beginning to decrease due to the electrochemical reaction, since for every mole of hydrogen that is removed: two moles of water are also removed. In the cathode channel, the relative humidity of stream is equal to 1.0. This is due to the fact that the water is produced continually, therefore, the water content continually increases. The mass flow rates and mole fractions of water, hydrogen and oxygen will be discussed in more detail in section 8.2.
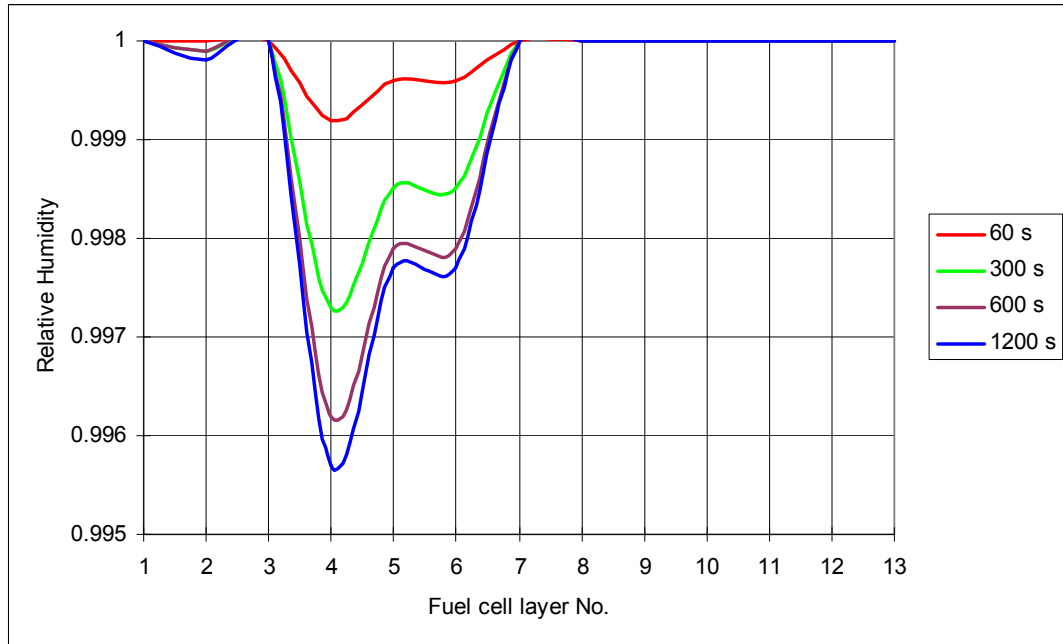
Figure 8.16. Relative humidity of the gas streams in the fuel cell stack

8.2 Mass and Charge Transfer and Pressure Drop Portion of the Overall Fuel Cell Stack Model

The numerical code was further developed to incorporate the effects of mass and charge transfer and pressure drop in order to study the fuel cell behavior. The mass and charge balances, and pressure drop mathematical equations for each layer are solved simultaneously in MATLAB. An array was created for the molar flow rates, mole fractions, concentrations, humidities, pressure drops, resulting pressures, hydraulic diameters, Reynold's numbers and potentials for each node or layer. The stack dimensions and other parameters used in the simulations are summarized in Appendix A.

In the code, lines 430 - 1592, the mole fractions, molar flow rates, concentrations and humidity's are calculated for the nodes for each fuel cell layer. The pressure drops for each layer are calculated on lines 1595 to 2316. The velocities, hydraulic diameters,

Reynold's numbers, friction factors and the change in pressure with respect to x are calculated for each node. The charge transfer portion begins on line 2769, and includes the calculation of current densities in the anode and cathode catalyst layer, the potential losses due to activation polarization, ohmic polarization and concentration losses. A charge balance is also included for each layer. A summary of the mass and pressure portion of the code is shown in Figure 8.17.
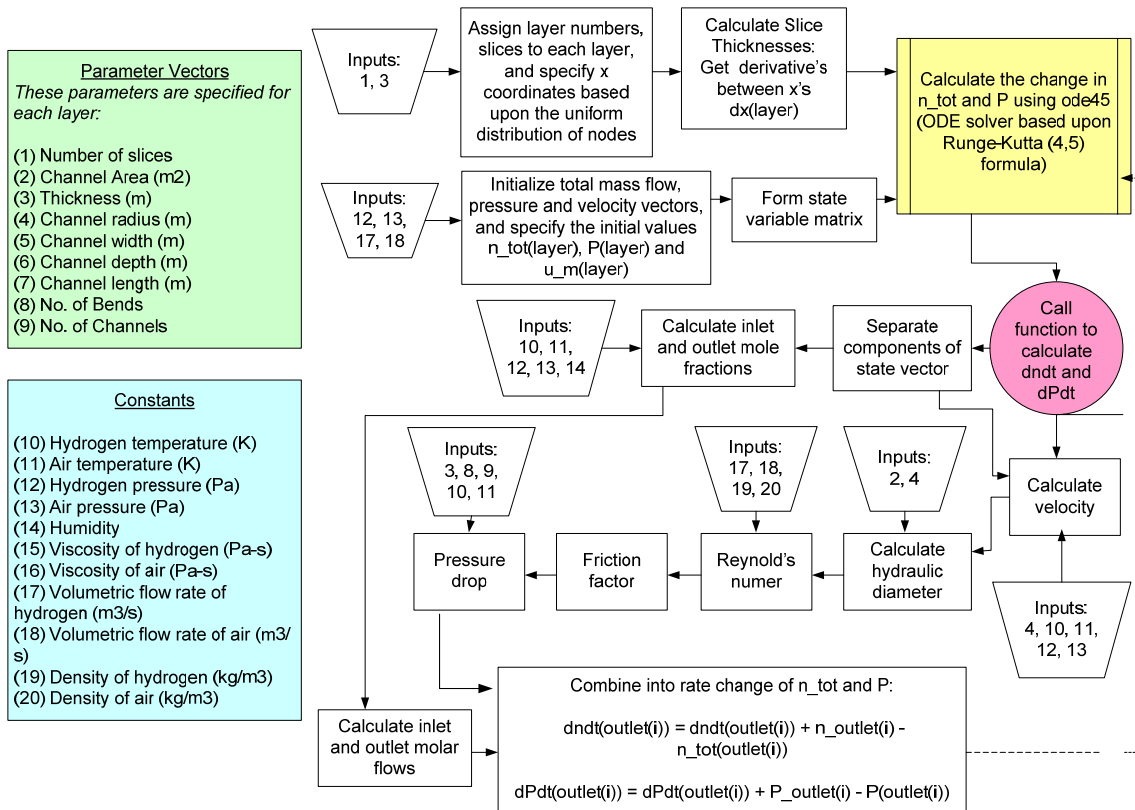
Figure 8.17. Mass transfer and pressure drop portion of the model

8.2.1 Total Mass Flow Rates

The molar flow rate of hydrogen and oxygen through the end plates, terminals and gasket layers are the largest due to the large pipe diameter. The hydrogen and oxygen

flow rate decreases through the flow channels due to the branching of the inlet channel into several channels. The hydrogen and oxygen flowrate changes as it goes through the GDL, and catalyst layers due to the pore sizes. The flow through the membrane in the base case is just due to permeability and water concentration. The total mass flow rates, for a 20 cell fuel cell stack, are shown in Figure 8.18.
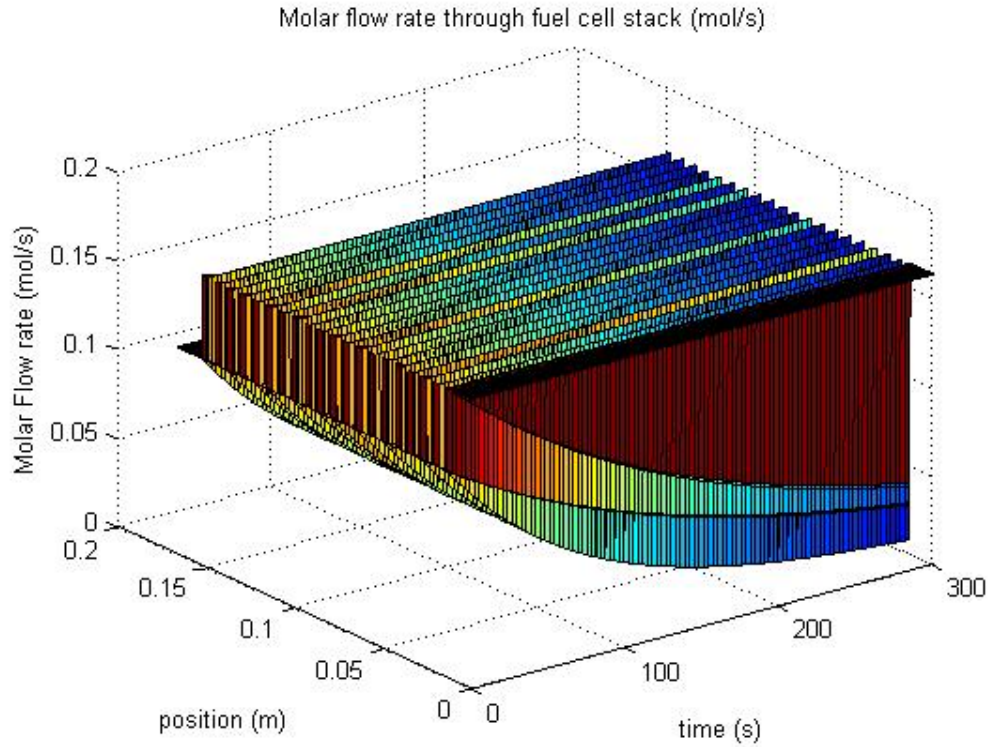
(a)
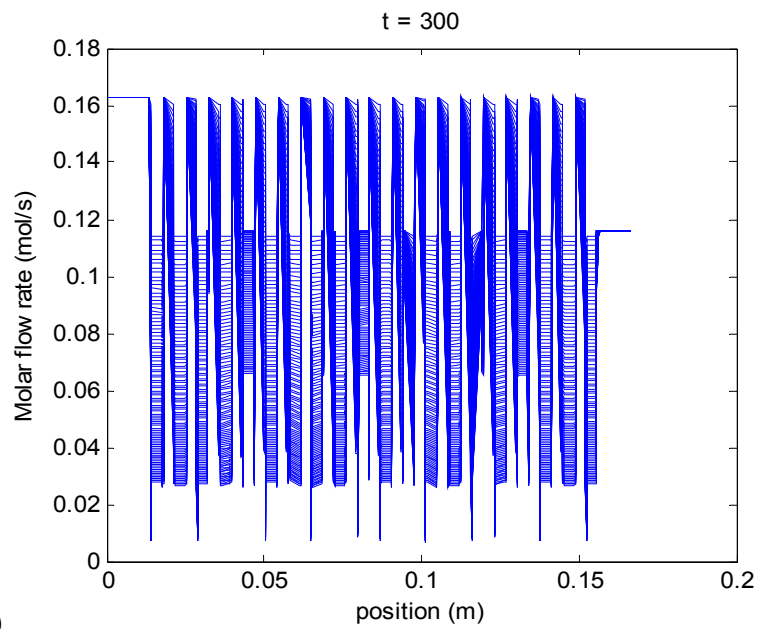
(b)

Figure 8.18. Mass flow rates through a 20 cell fuel cell stack, (a) surface plot of the mass

flow rate distribution as a function of position and time, (b) mass flow distribution at t

=300 s

Figure 8.19 compares the mass flow rates of the fuel cell layers at 1, 2 and 3 atm. The flow rate decreases from the flow field layers (1 and 7) because only a small fraction of the total flow rate enters the GDL layers. The remainder of the flow rate exits the flow field plates to the manifold. As mentioned previously, the decrease and increase of the mass flow rates in the GDL, catalyst and membrane layers is due to the changes in pore sizes of each layer.
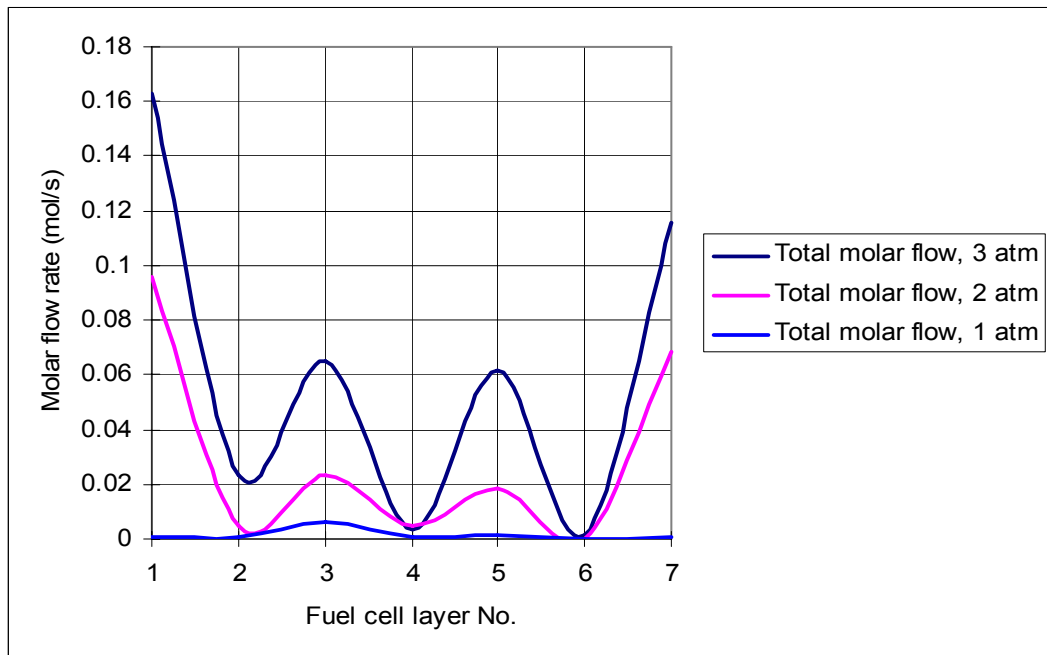
Figure 8.19. Comparison of total mass flow rates with pressures of 1, 2 and 3 atm

8.2.2 Pressures Through Fuel Cell Stack

The pressures of hydrogen and oxygen through the layers of a 20 cell fuel cell stack, and a single cell fuel cell stack for the base case shown in Appendix L, are shown in Figures 8.20 and 8.21 for T = 298 K, P = 3 atm with a current density of 1.0 A/cm^2.

The pressure drop of hydrogen and oxygen through the end plates, terminals, and gasket layers is minimal due to the short pipe length. The hydrogen and oxygen pressure drop is substantial through the flow channels due to the small channel diameter, channel length, number of bends, and number of channels. The hydrogen and oxygen pressure decreases even further as the gases pass through the GDL and catalyst layers due to the small pore sizes. The pressure in the membrane is dependent upon the pressure at the anode catalyst/membrane and cathode catalyst/membrane interfaces, and displays a similar distribution as previously shown in Figure 5.9.
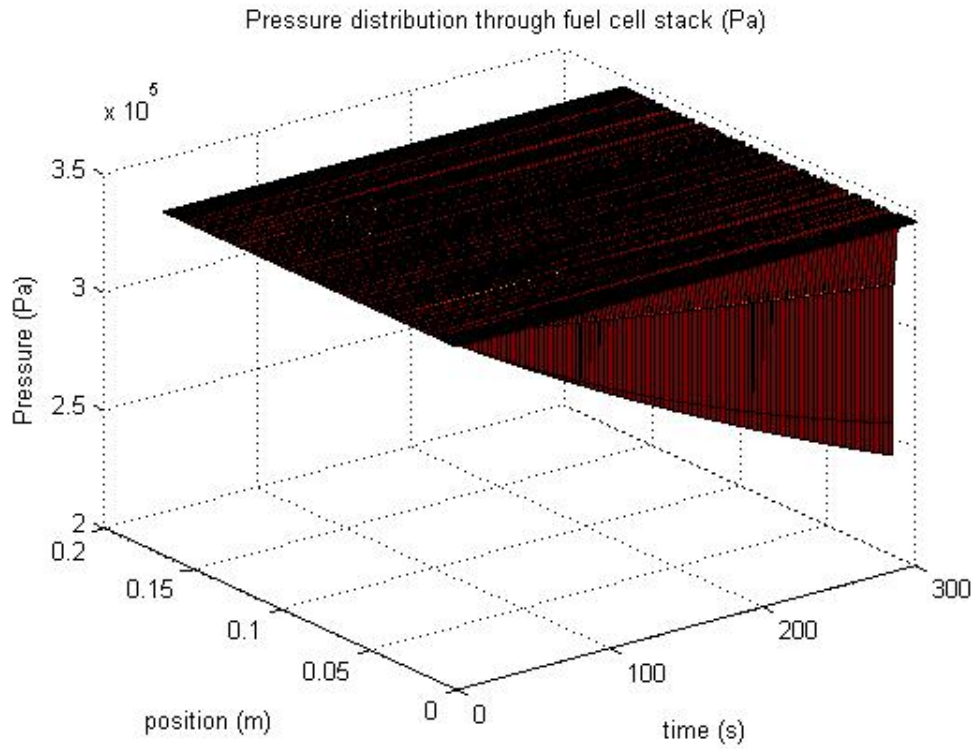
(a)
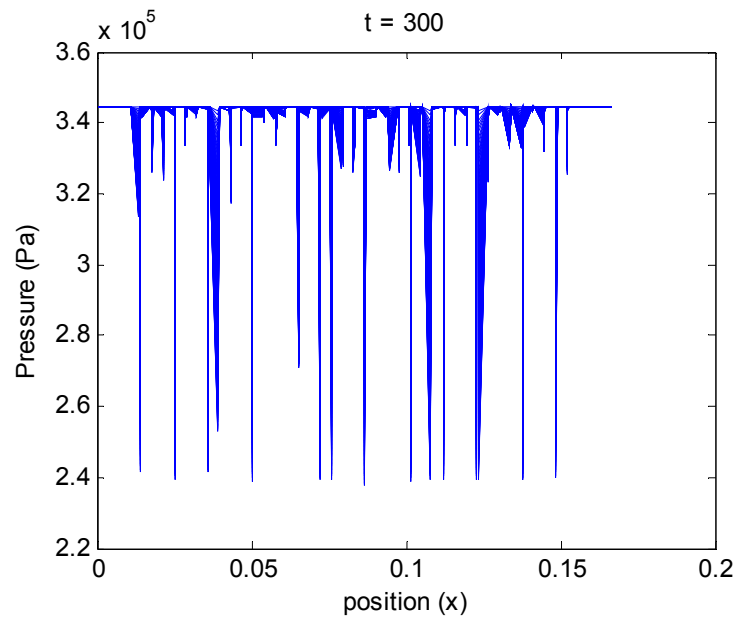
(b)

Figure 8.20. Pressure distribution through a 20 cell fuel cell stack, (a) surface plot of

the pressure distribution through a 20 cell stack as a function of position and time, (b)

pressure distribution at t = 300 s

Pressure distribution through fuel cell stack (Pa)

(a)

t = 296.9697
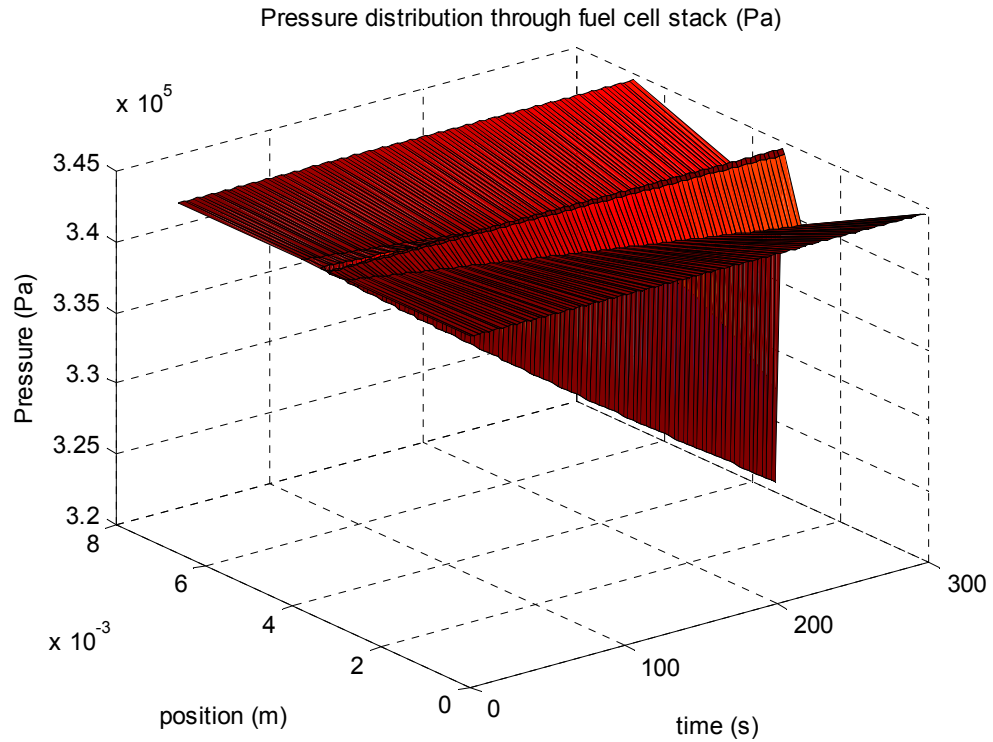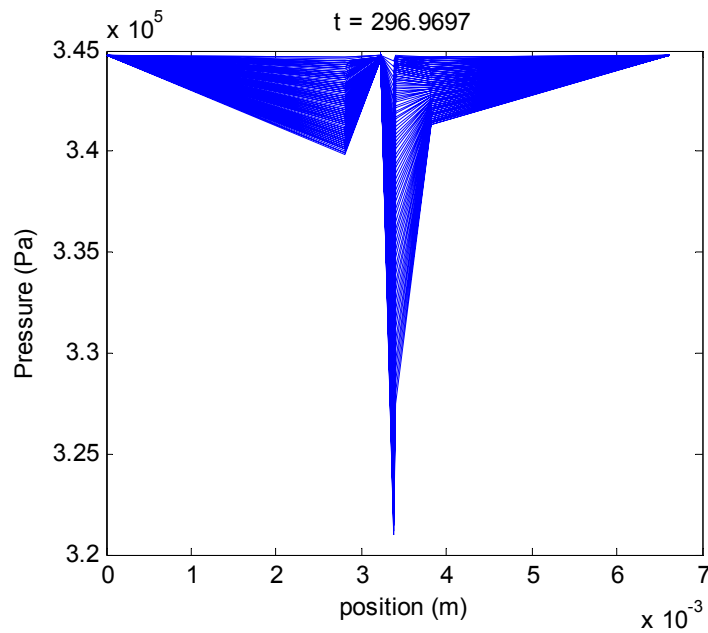
Figure 8.21. Pressure distribution through a single cell fuel cell stack, (a) surface plot

of the pressure distribution through a single cell stack as a function of position and

time, (b) pressure distribution at t = 300 s

Figures 8.22 and 8.23 compare the pressure drop for the base case fuel cell stack at pressures of 1, 2 and 3 atm. It is well-known that higher pressures lead to higher fuel cell performance. However, there is a greater effect on fuel cell performance between 1 and 2 atm than between 2 and 3 atm. This effect becomes more obvious at higher current densities because the higher pressures of the reactants will bring more water into the channel. As a result, the membrane is better hydrated and the speed of chemical reaction increases. Therefore, the fuel cell can generate more power under the high flow pressure. However, whether to use the high pressure in a fuel cell system depends on the tradeoff between fuel cell performance improvement, and cost to store and distribute the compressed gas.
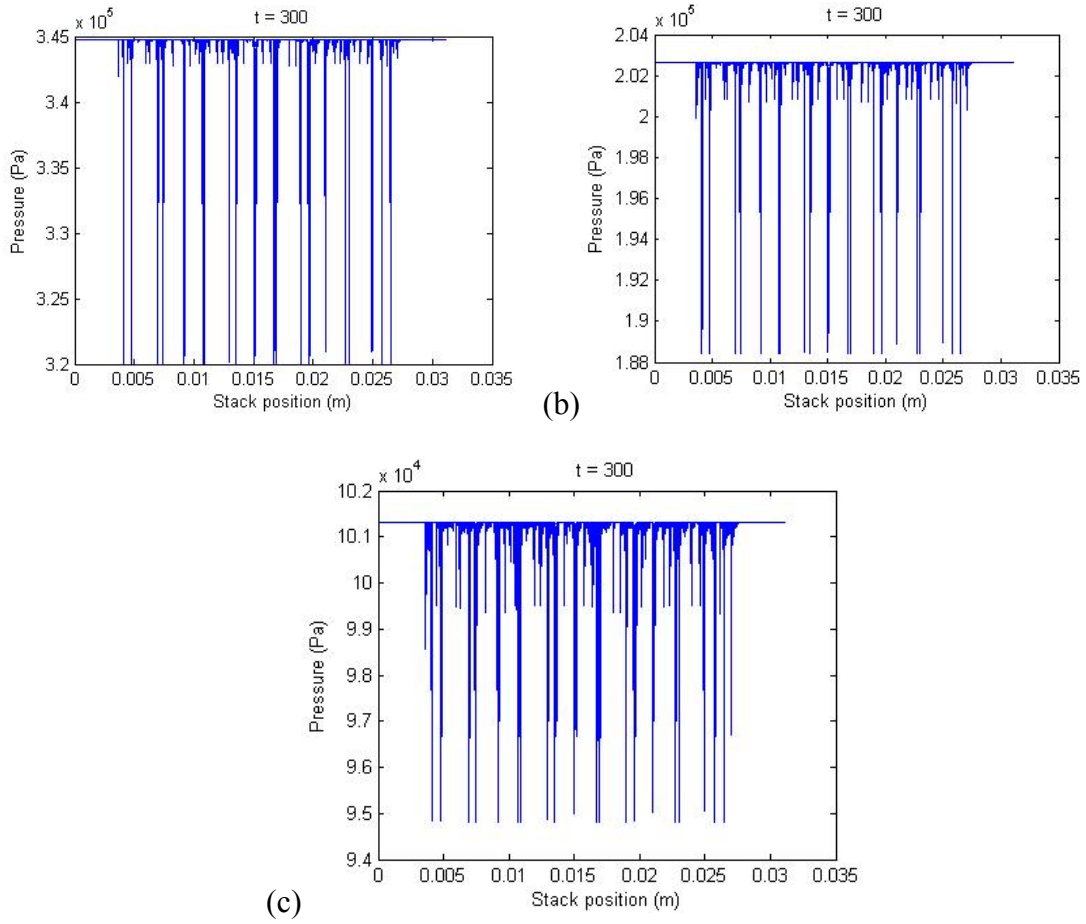
Figure 8.22. Pressure distribution for a 20 cell fuel cell stack with initial pressure of

(a) 3 atm, (b) 2 atm, and (c) 1 atm
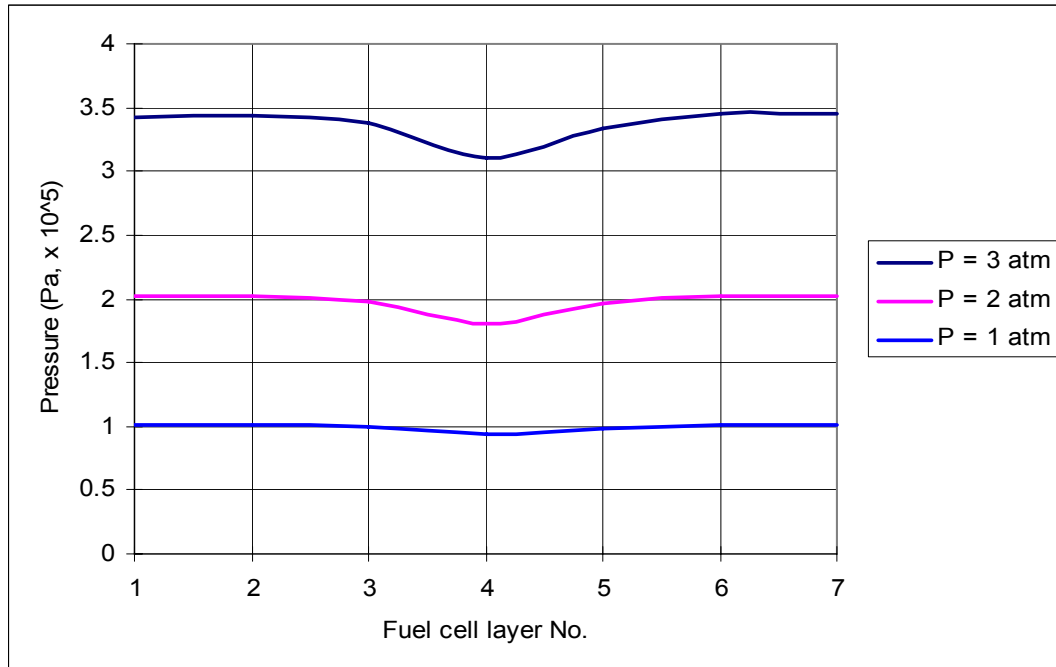
Figure 8.23. Pressure distribution through a single cell fuel cell stack

8.2.3 Velocity Distribution Through the Fuel Cell Stack

The velocities of hydrogen and oxygen in the end plate layers are the largest due to the pressure and pipe diameter. The hydrogen and oxygen velocity increases in the flow channels due to the decrease in flow diameter. When the molar flow reaches the outlet of the flow channels, the velocity then decreases because the outlet channel of the flow field plate widens. The hydrogen and oxygen velocity is slightly higher as it goes into the GDL. The velocity leaving the GDL and catalyst layers increase again due to the small pore diameters in these layers. The velocity through the membrane varies based upon the pressure differential and flow rate. Figure 8.24 illustrates the velocity profile of a 20 cell stack, and Figure 8.25 shows a surface plot of the velocity profile in the flow field, gas diffusion, catalyst and membrane layers of a single fuel cell.

215
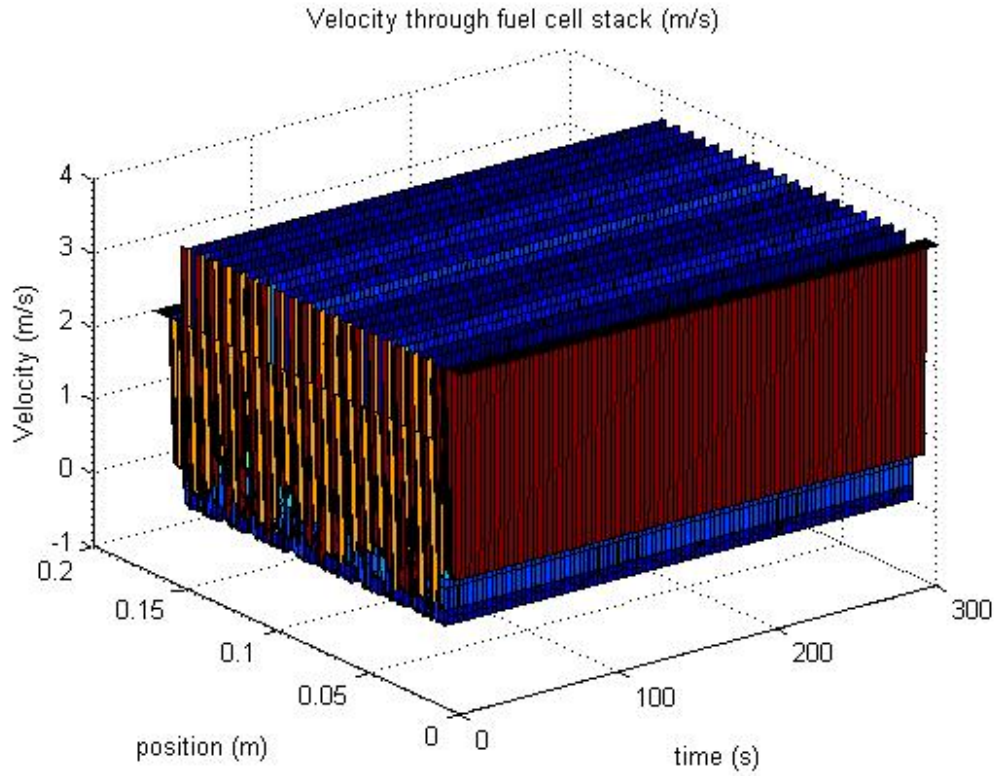
(a)
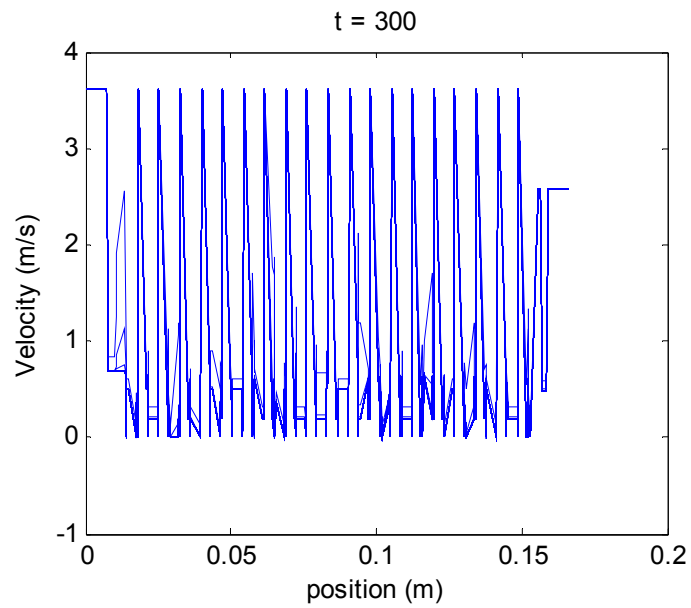
(b)

Figure 8.24. Velocity distribution through a 20 cell fuel cell stack, (a) surface plot of

the velocity distribution through a 20 cell stack as a function of position and time, (b)

velocity distribution at t = 300 s

216

Velocity through fuel cell stack (m/s)

(a)
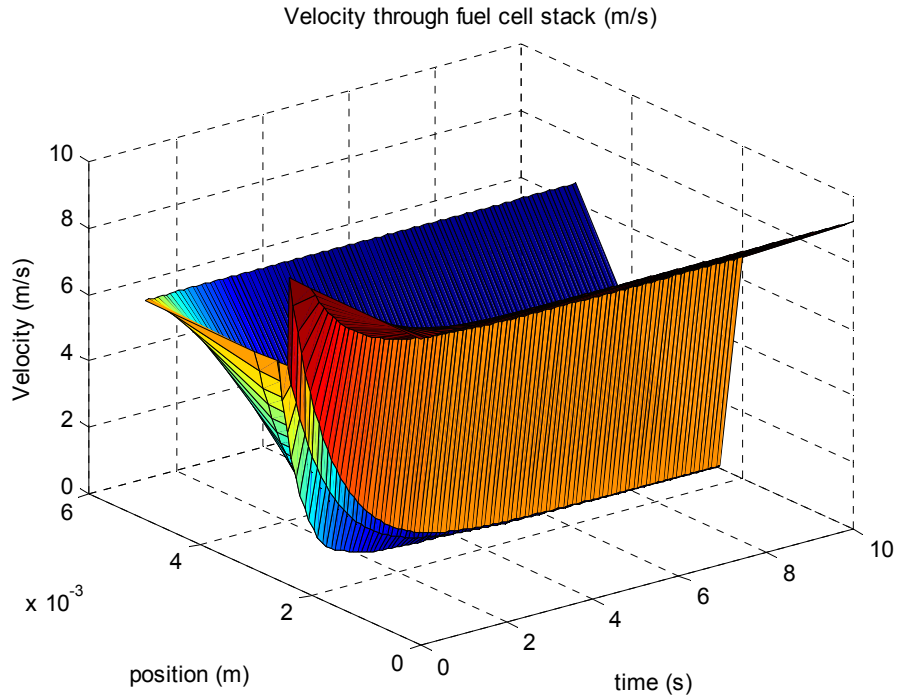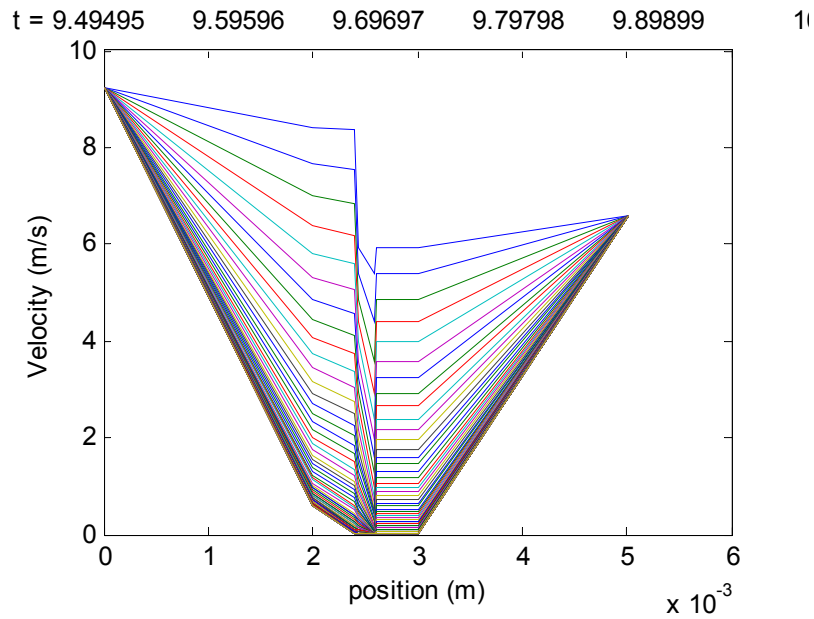
Figure 8.25. Velocity profile in the flow field, gas diffusion, catalyst and membrane

layers of a single fuel cell, (a) surface plot as a function of position and time, (b) velocity

distribution at t = 10 s

The velocity in the gas diffusion layers is approximately two orders of magnitude smaller than in the gas flow channels. The velocity in the diffusion media is smaller than in the flow channels because it has a much higher resistance to flow due to the small pores in this layer. The change in porosity from the GDL (0.55) to the catalyst layer (3.0) results in an increase in velocity. If the density of the gas phase is constant across the interface between the two layers, the velocities can be related by [117]:

$$\frac{\text{Velocity magnitude in the catalyst layer}}{\text{Velocity magnitude in the GDL layer}} = \frac{\varepsilon_{GDL}}{\varepsilon_{catalyst}} \tag{237}$$

Therefore, the magnitude of velocity in the catalyst layer should be about twice the value of that in the electrode backing layer. This is in agreement with the results shown in Figures 8.26 and 8.27.
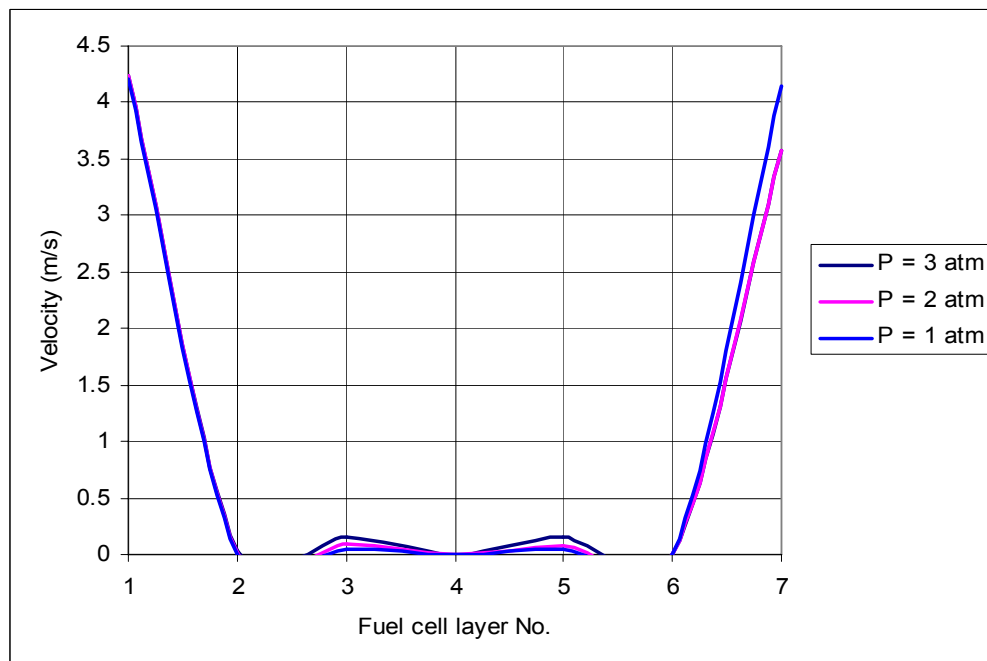
Figure 8.26. Velocity of a single cell
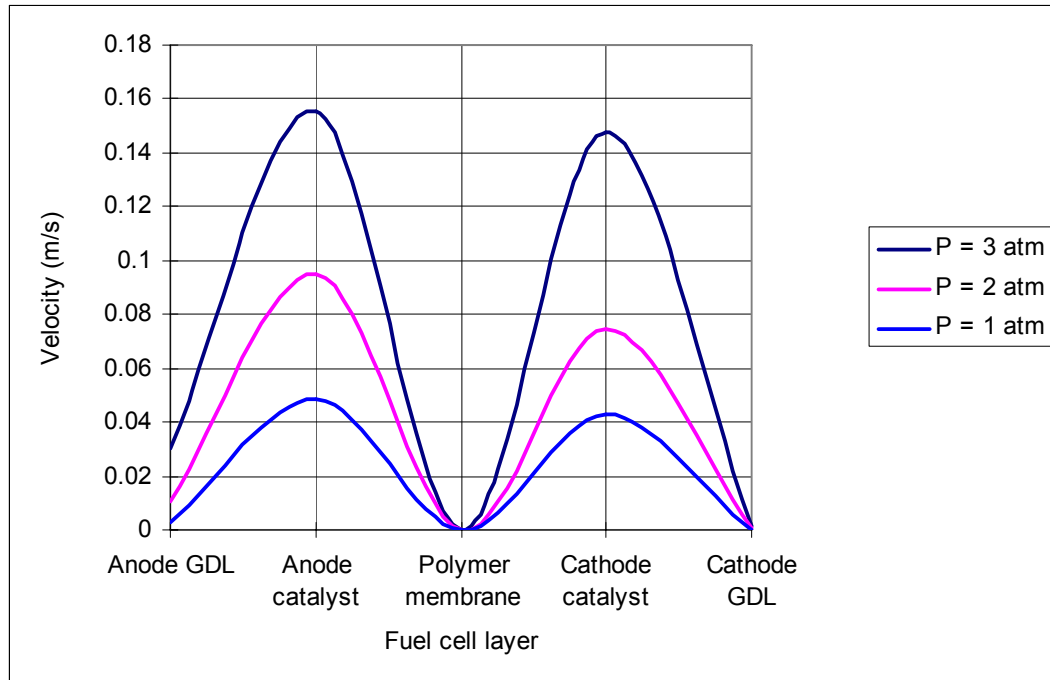
Figure 8.27. Velocity of the MEA layers at different pressures

8.2.4 Hydrogen Transport

For the gas phase species, it is assumed that convection is the dominant mode of mass transport in the end plate, terminal, gasket and flow field layers, and diffusion is the dominant mode of transport in the GDL, catalyst and membrane layers. The direction of diffusional flux generally moves from the anode flow field to the anode catalyst layer, where the hydrogen is consumed. However, some of the hydrogen diffusional flux also flows in the opposite direction than the total hydrogen mass flux, and the convective velocity. Since the electrochemical reaction requires hydrogen to be supplied to the anode catalyst layer, diffusion hinders the electro-chemical reactions. At low pressures, such as 1 atm, the mole fractions of hydrogen begin to decrease in the anode GDL due to hydrogen consumption in the anode catalyst layer. Therefore, it seems as though the

219

amount of hydrogen diffusing into the catalyst layer could be limiting the electrochemical reactions. As the pressure is increased to 3 atm, the hydrogen mole fraction in the anode flow field, GDL and catalyst layer is consistent, which indicates that enough hydrogen is being supplied to the anode catalyst layer. Figure 8.28 illustrates the increase in mole fraction from the gas flow channels to the anode catalyst layer.
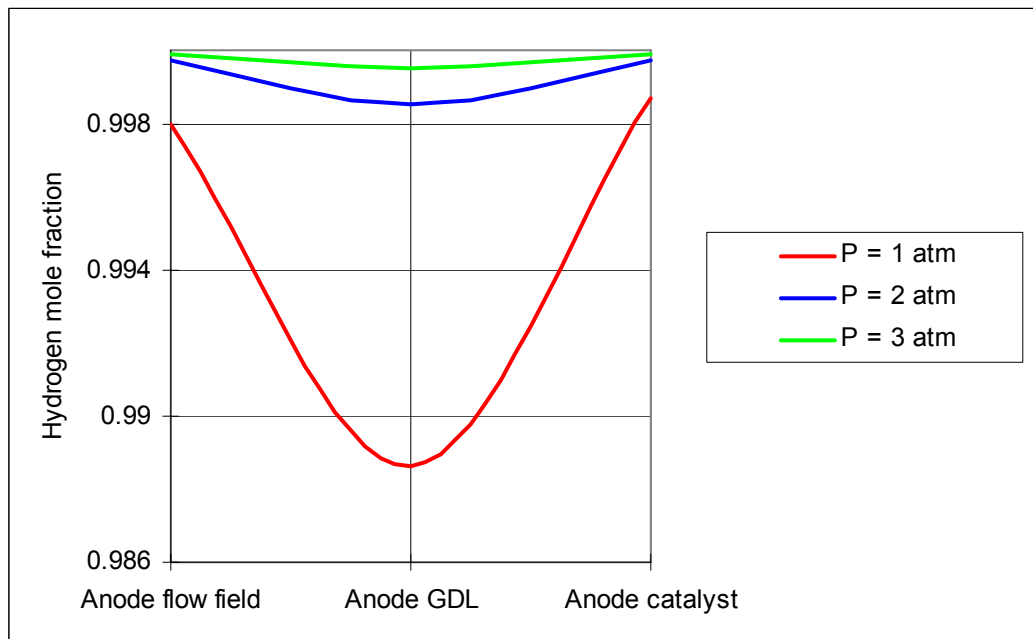
Figure 8.28. Hydrogen mole fraction in the anode gas flow channel, electrode backing layer and catalyst layer

Figure 8.29 again shows that there is a significant decrease of hydrogen mole fraction in the anode catalyst layer to the anode gas flow channel at $P = 1$ atm. The mole fraction in the anode gas flow channels stays nearly constant, and increases at the GDL/ flow channel interface. As the current density increases, there was no noticeable change in hydrogen mole fraction as shown by Figure 8.29.
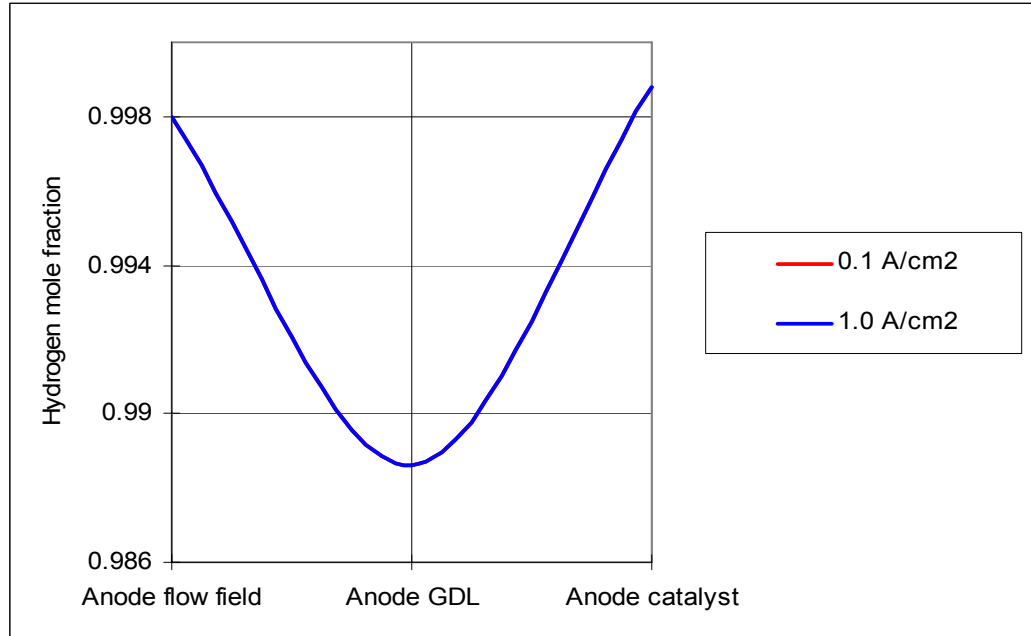
Figure 8.29. Hydrogen mole fraction due to the varying current density in the anode gas flow channel, GDL layer and catalyst layer

The concentration of hydrogen also increases as shown in Figures 8.30 and 8.31. Although hydrogen is consumed, the mole fraction increases. This increase is due to the electrochemical reactions since for every mole of hydrogen that is removed; two moles of water are also removed. The hydrogen mole fraction (x_{H2}) will be positive if it is greater than 0.053 according to the following equation:

$$x_{H2} = \frac{M_{H2}}{M_{H2} + 2M_{H2O}} \tag{238}$$
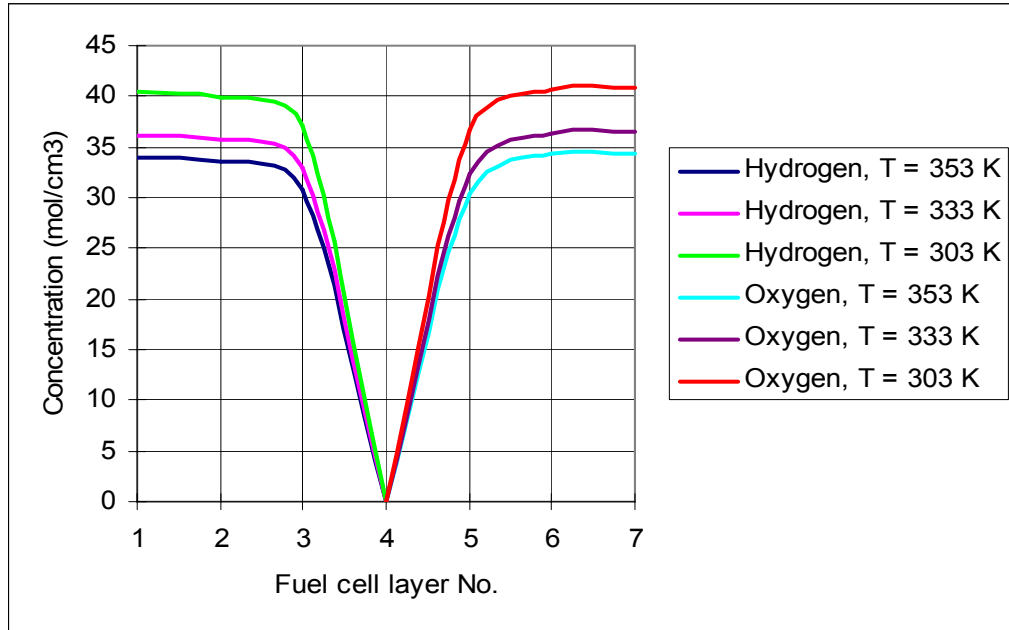
Figure 8.30. The concentration of hydrogen in the anode gas flow channel, electrode

backing layer and catalyst layer
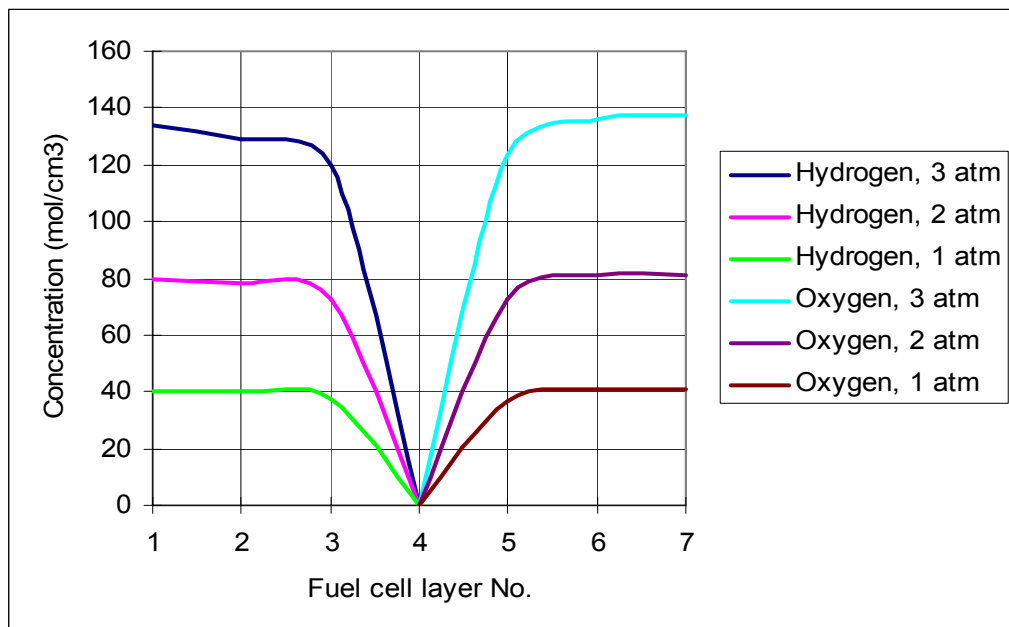
Figure 8.31. Hydrogen and oxygen concentration in the MEA fuel cell layers

8.2.5 Oxygen Transport

In the cathode catalyst layer, water is produced, and oxygen is consumed. The oxygen travels from the flow channel to the cathode catalyst layer. It is assumed that the transport of oxygen from the gas flow channels to the reaction sites in the cathode catalyst layer is by diffusion. The oxygen mole fraction at a pressure of 1 atm is lower in the flow field and cathode catalyst layers as shown in Figure 8.32. As the pressure increases to 2 and 3 atm, the oxygen mole fraction begins to become more uniform in the cathode flow field layer, GDL and catalyst layers. This again illustrates that with lower pressure, the decrease in oxygen concentration hinders the electrochemical reaction -- which is proportional to oxygen concentration.
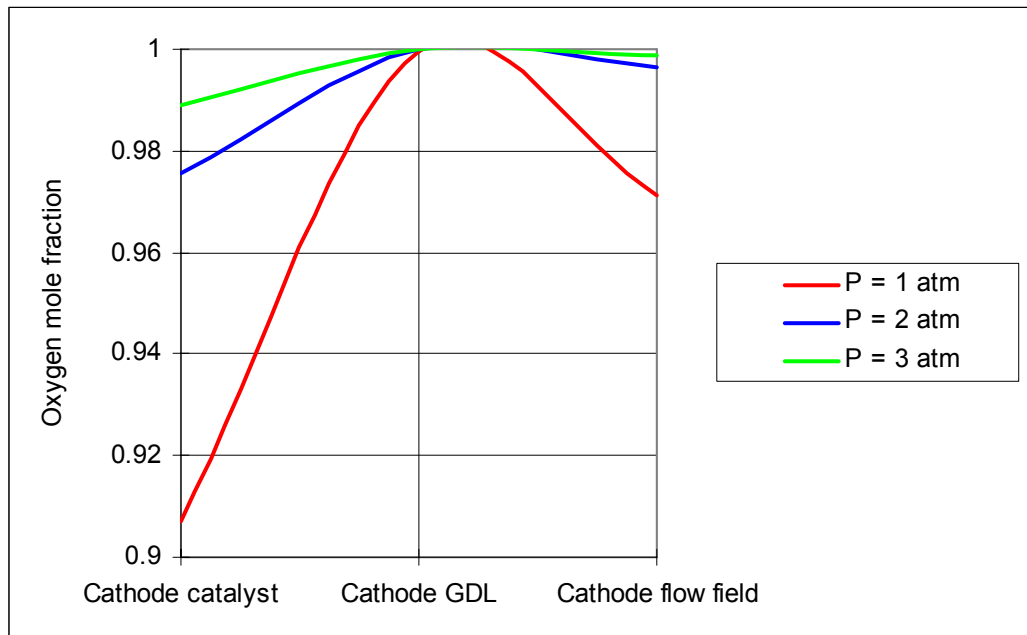
Figure 8.32. The mole fraction of oxygen in the anode gas flow channel, gas diffusion layer and catalyst layer

Figure 8.33 illustrates the mole fraction of oxygen with varying current density with P = 1 atm and T = 298 K. As expected, the lowest current density of 0.1 A/cm^2 has the highest oxygen concentration in the cathode catalyst layer, and the highest current density of 1.0 A/cm^2 has the lowest oxygen mole fraction in the cathode catalyst layer due to the greater consumption of oxygen.
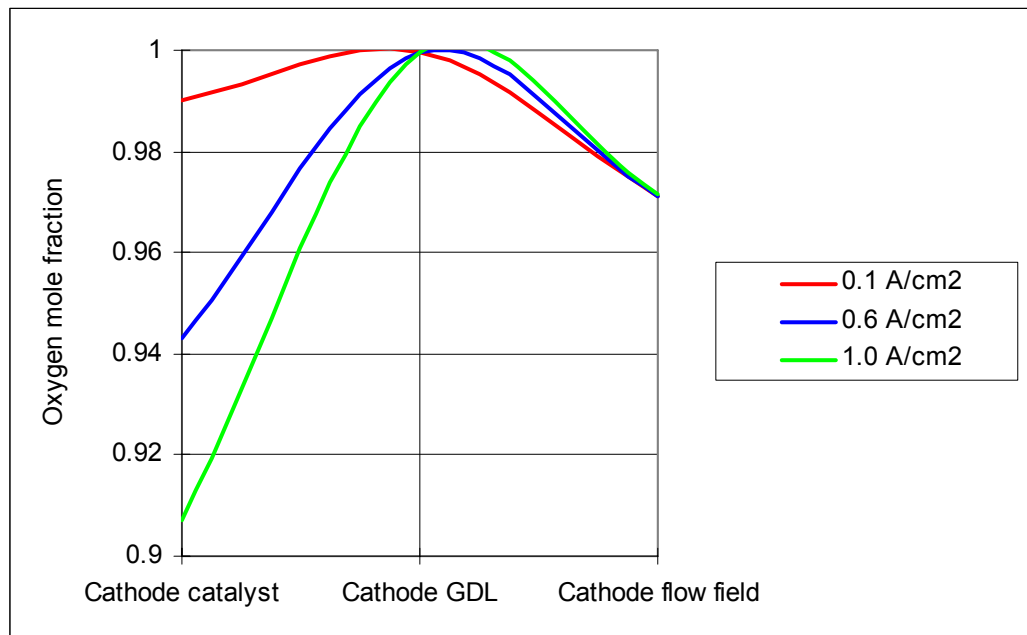
Figure 8.33. The mole fraction of oxygen in the cathode gas flow channel, gas diffusion layer and catalyst layer

8.2.6 Water Transport

Water exists in both the gas and liquid phase throughout the fuel cell stack. Due to the electrochemical reactions, water is consumed in the anode catalyst layer and produced in the cathode catalyst layer. The water in the anode catalyst layer is primarily from the

humidity in the hydrogen inlet stream. The water flux in the polymer membrane is primarily due to water generated by the cathode catalyst layer.

Figure 8.34 shows the mole fraction of water for the flow field and MEA layers with varying current densities at T = 298 K and P = 1 atm. As seen experimentally, the largest amount of water (mole fraction of 0.092) is with the highest current density of 1.0 A/cm^2, and the mole fraction of water decreases with the decrease in current density. This is due to the fact that a greater amount of water is generated with a higher current density according to Faraday's law (equation 133).
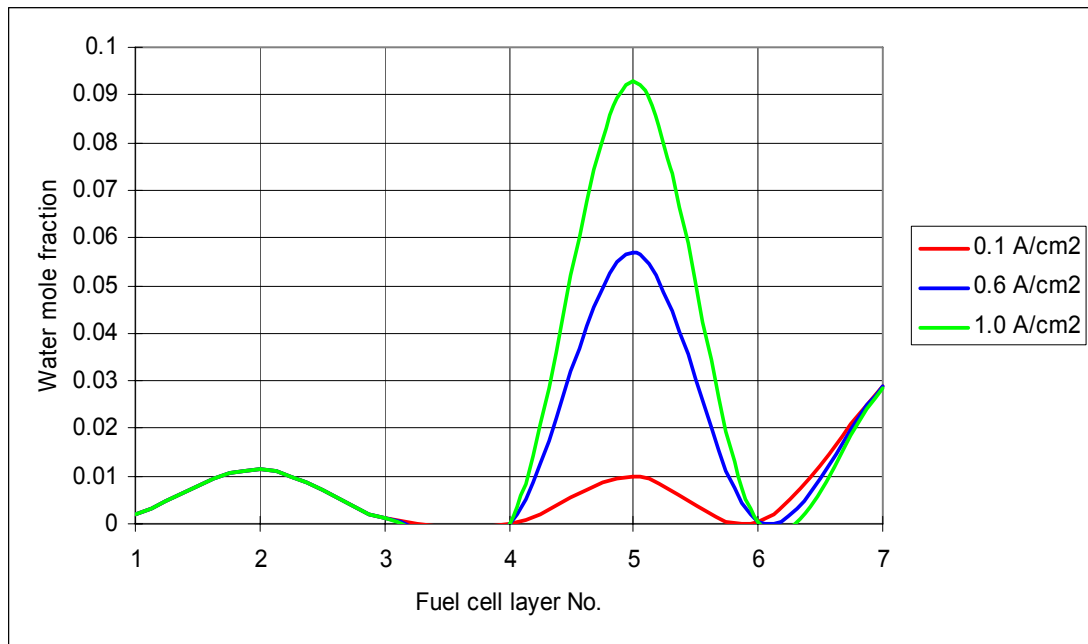
Figure 8.34. Effect of current density on water mole fraction

Figure 8.35 shows the water mole fraction over a total time of 1200 s with a current density of 1.0 A.cm^2, T = 303 K and P = 3 atm. At time = 10 s, the water mole fraction is 0.011, and the mole fraction increases to 0.019 at t = 1200 s. The water mole

fraction is also increasing in the anode flow field and GDL, and the cathode flow field layers. This is due to the water traveling from the cathode catalsyt layer and accumulating in the flow field and GDL layers.
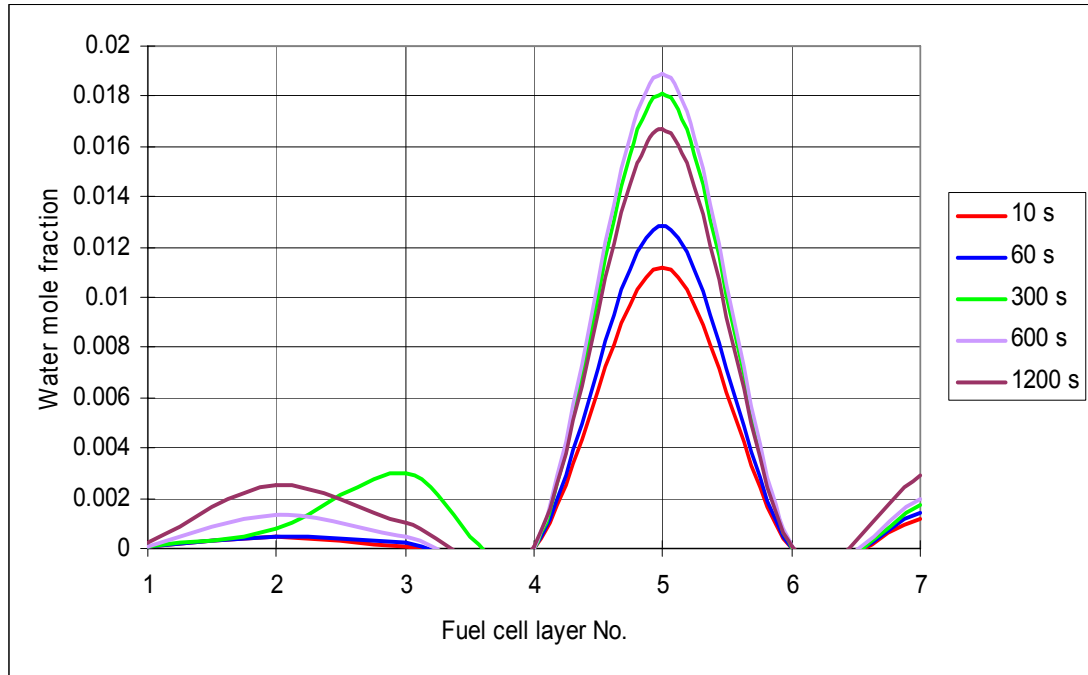
Figure 8.35. **E**ffect of time on water mole fraction

Approximately 25% of the water consumed by the anode catalyst layer reaction comes from the cathode catalyst layer. Ideally, the water produced in the cathode catalyst layer should provide 100% of the water needed by the anode catalyst layer since this would eliminate the need to have fully hydrated reactants. However, in practice, the reactants must be fully humidified in order to adequately hydrate the membrane. Water concentration as a function of time is illustrated in Figure 8.36.
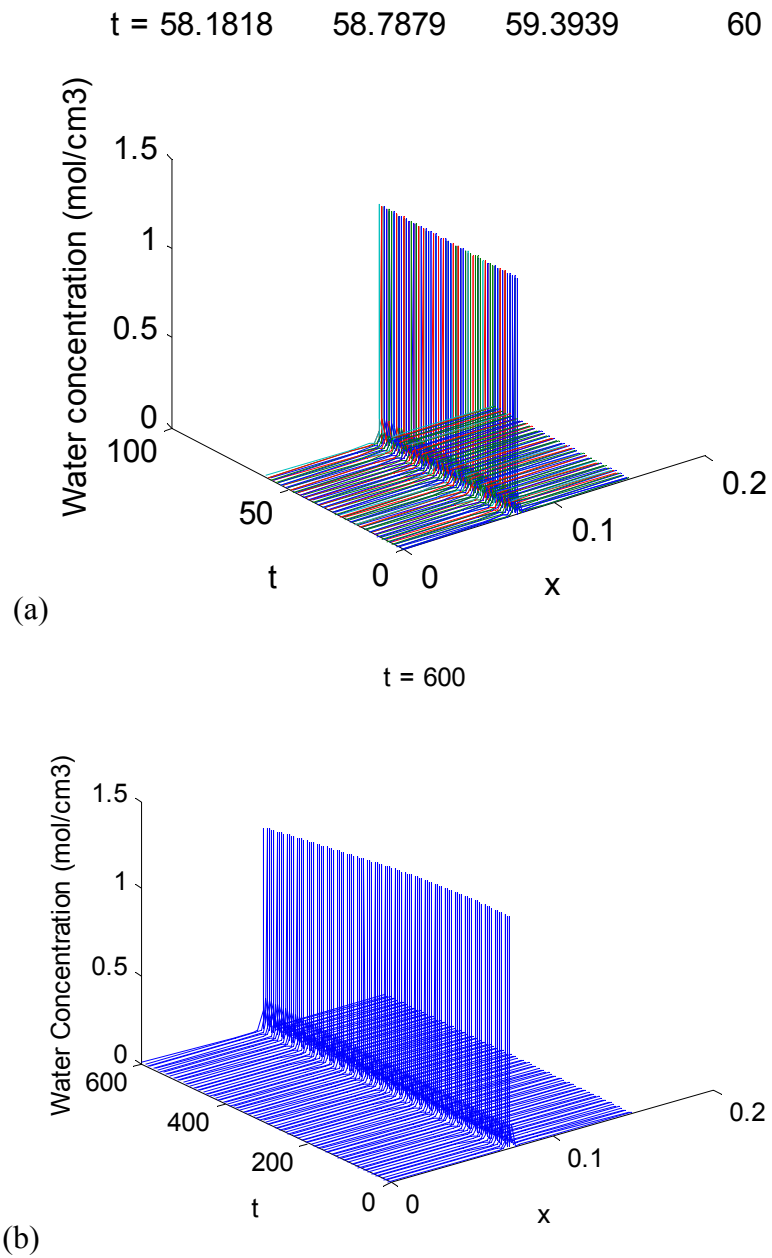
Figure 8.36. Water concentration as a function of time at 3 atm and i = 1 A/cm2, (a) 60 s
and (b) 600 s.

Figure 8.37 shows the distribution of water concentration at the different inlet

flow temperatures at P = 1 atm and a current density of 1.0 A/cm^2. It is found that the

local water activities in the membrane are less than 1.0 when the inlet flow temperatures

are 303 and 313 K. When the stack and gas temperature is lower, the saturation pressure

will drop and the water activities will increase. For the cases with higher inlet

temperature, such as, 333 and 343 K, the gases carry more water vapor into the channel,

and the water activity in the membrane will be greater than 1.0. When the water activities

are large, the membrane conductivity changes will be small. This is because the

membrane is well hydrated, and the speed of electrochemical reaction is faster. As a

result, more oxygen is consumed and the partial pressure of oxygen decreases quickly.
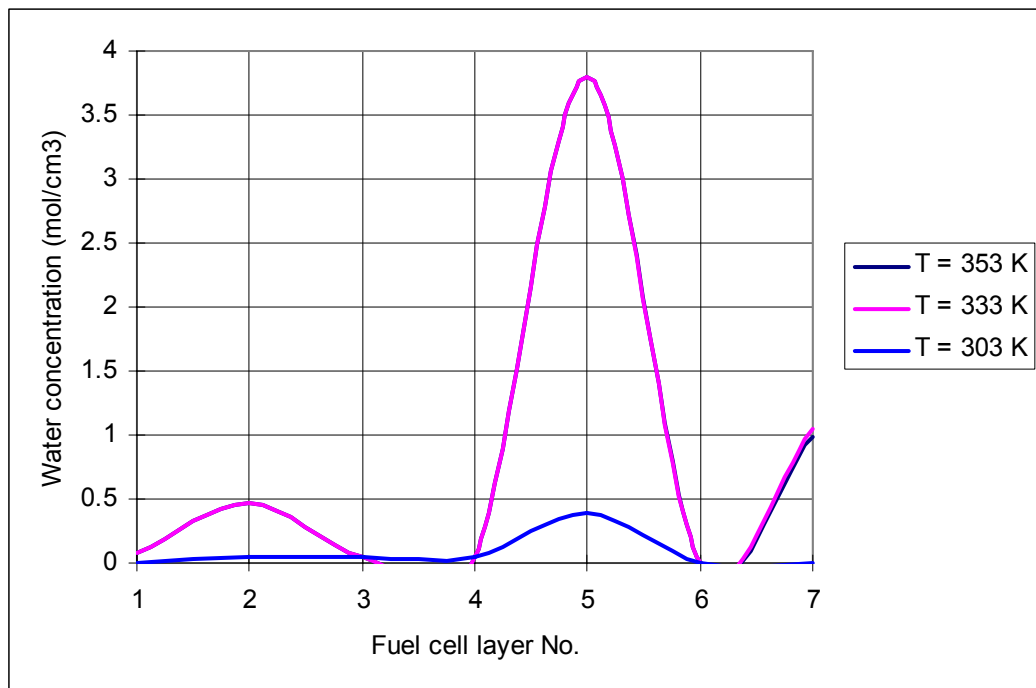
Figure 8.37. The concentration of water in the anode gas flow channel, electrode backing

layer and catalyst layer

Figure 8.38 illustrates the water concentration in each fuel cell layer with varying pressures. The water transport across the polymer electrolyte layer is driven by a water concentration gradient. The amount of water contained in the gas phase and electrolyte can be characterized by the membrane activity and water uptake, as described in Chapter 5.
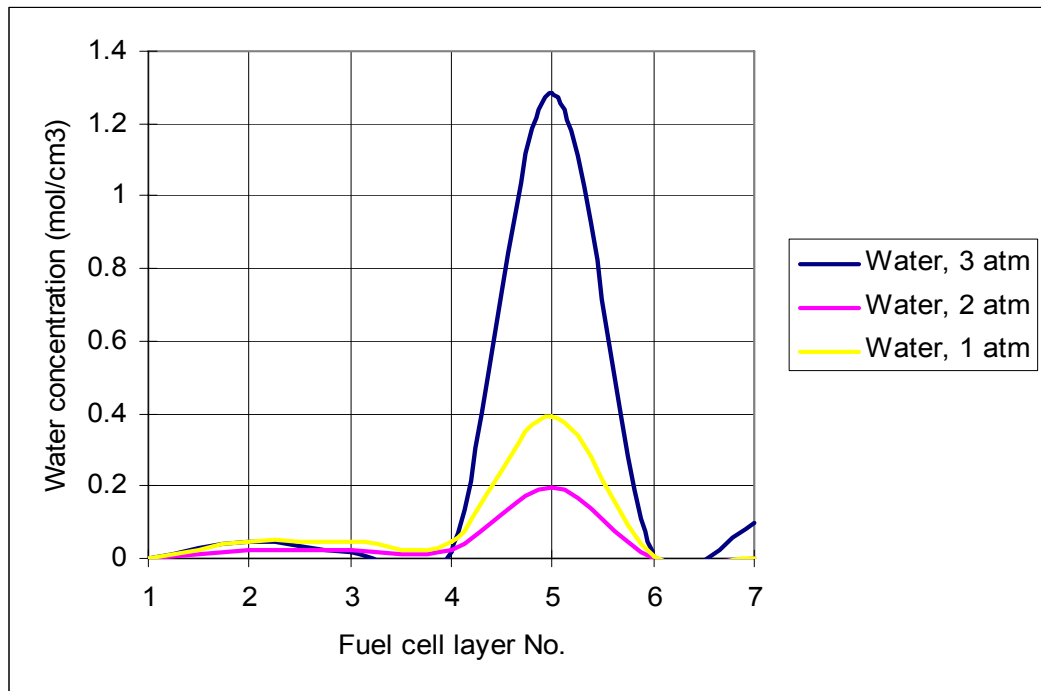
Figure 8.38. Water concentration as a function of pressure

Figure 8.39 shows the hydrogen, oxygen and water concentration at 3 atm at T = 298 K, and the current density is 0.1 A/cm^2. The hydrogen and oxygen concentration decreases slightly from the flow field to the GDL layers, and then again slightly from the GDL to the catalyst layer. The water mole fraction increases from Figure 8.39 to Figure

8.40 from approximately 0.1 mol/cm^3 to 1.2 mol/cm^3 with a current density of 0.1 A/cm^2 to 1.0 A/cm^2.
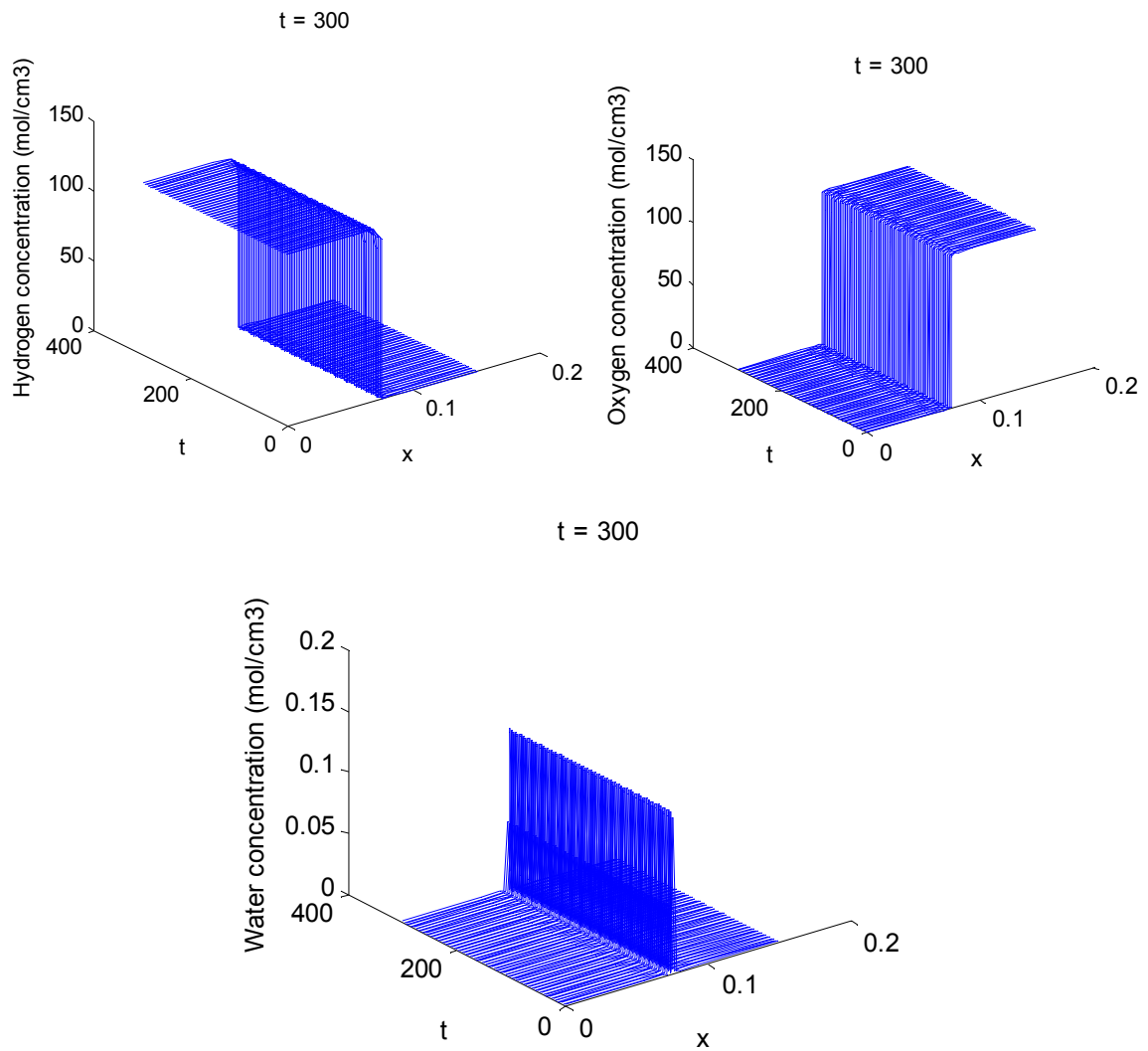
Figure 8.39. Hydrogen, oxygen and water concentration at 3 atm, i = 0.1 A/cm2
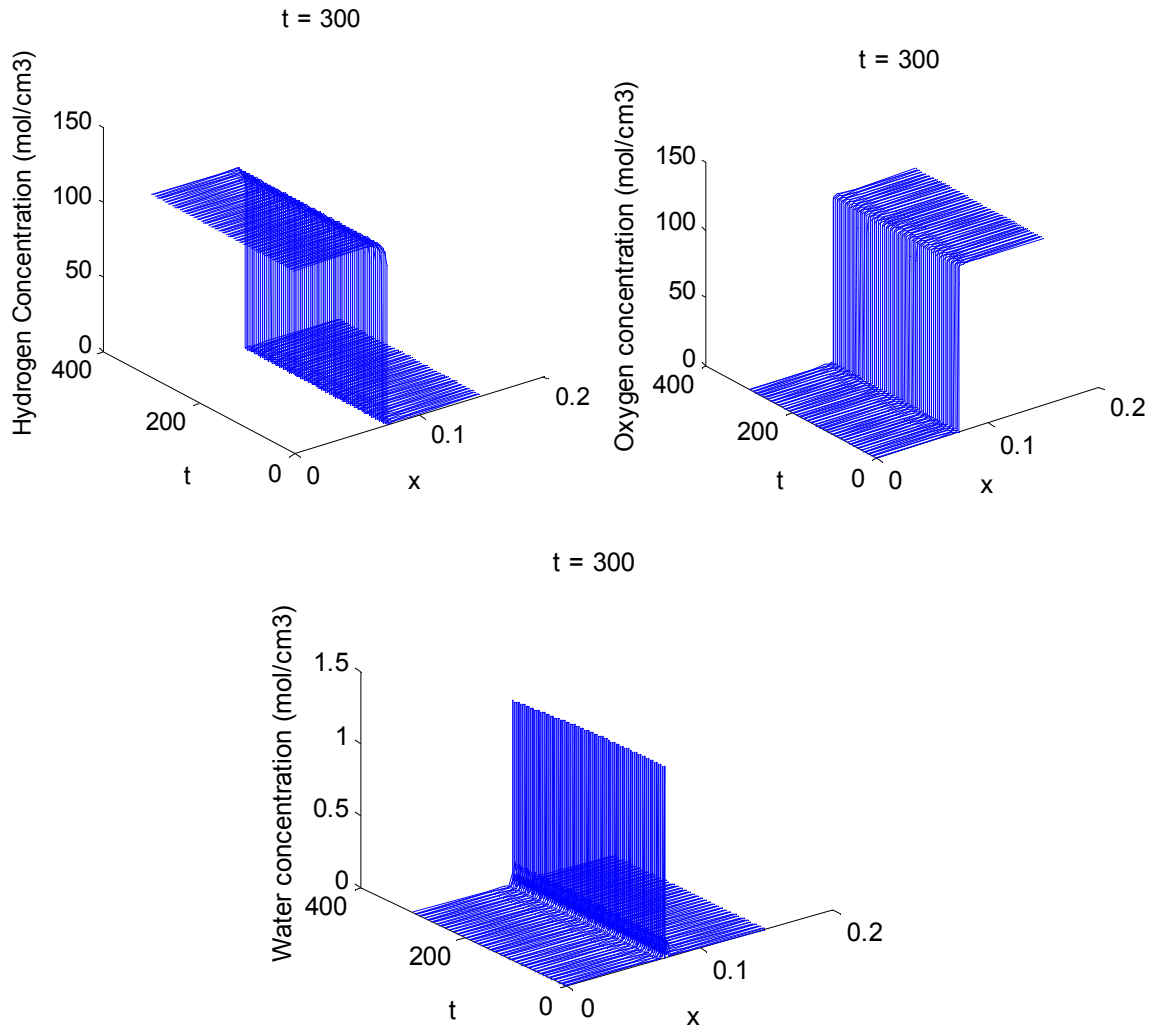
Figure 8.40. Hydrogen, oxygen and water concentration at 3 atm, i = 1 A/cm2

8.3 Membrane Portion of the Overall Fuel Cell Stack Model

The membrane is treated differently than the other layers in the numerical code because the transport phenomena are different due to the membrane properties. Lines 1464 – 1592 calculate the mass flow through the membrane, which includes the calculation of the amount of water in the membrane (water activity), the water uptake, the amount of hydrogen and oxygen that diffused into the membrane, and the hydrogen,

oxygen and water concentrations. The pressure and velocity is calculated in 2301 – 2306, and the membrane temperature is calculated on lines 2765 – 2762. The potential is based on water content, and is calculated on lines 2827 – 2848. A summary of the membrane portion of the code is shown in Figure 8.41.
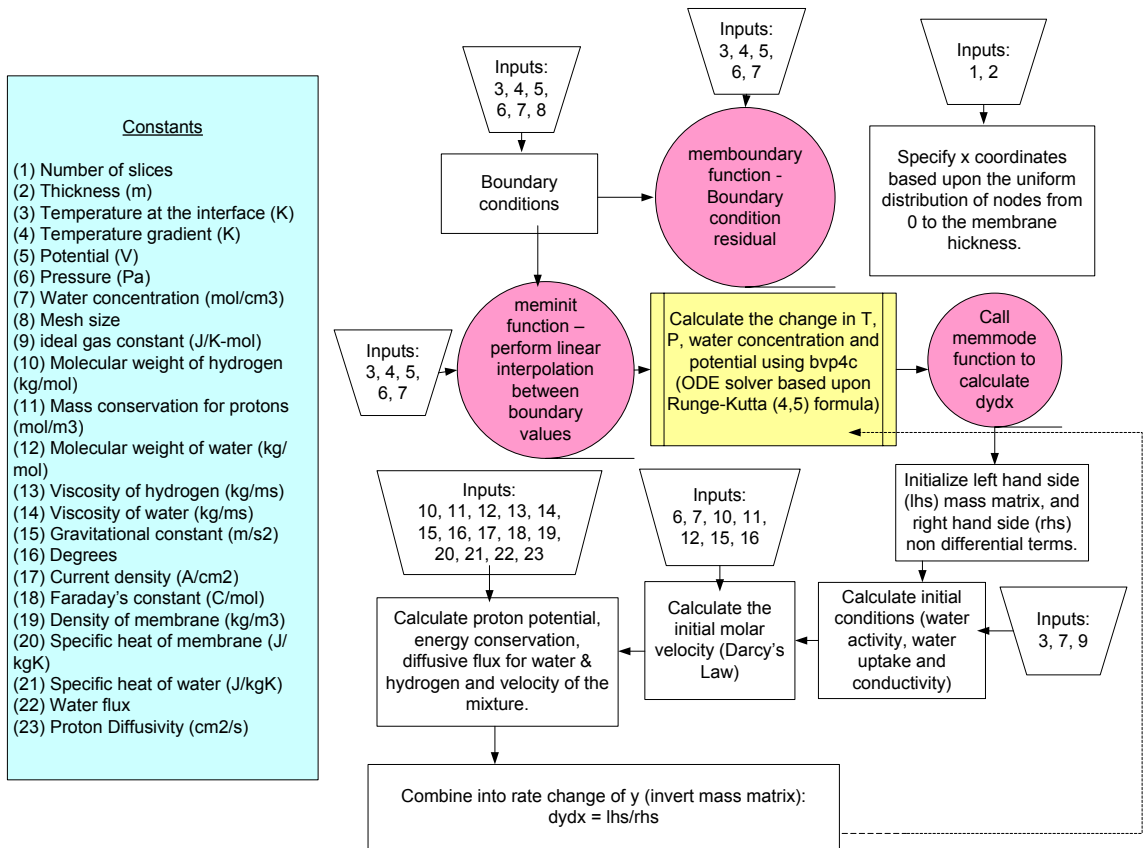
Figure 8.41. Flow chart of membrane model

8.3.1 Effect of Current Density

As the current density increases, protons navigate from the anode where they are produced, to the cathode where they are consumed. As protons migrate, water molecules are dragged through the membrane. The concentration in the membrane changes with time with an applied current density. The solid lines show the water concentration with the specified applied current density. The water concentration on the anode side becomes lower with increased current density. The number of water molecules on the cathode side also is higher with the increased current density. In addition, the overall water content in the membrane is lower with higher current density due to an increased number of protons dragging more water molecules out of the membrane. These phenomena are illustrated in Figure 8.42.
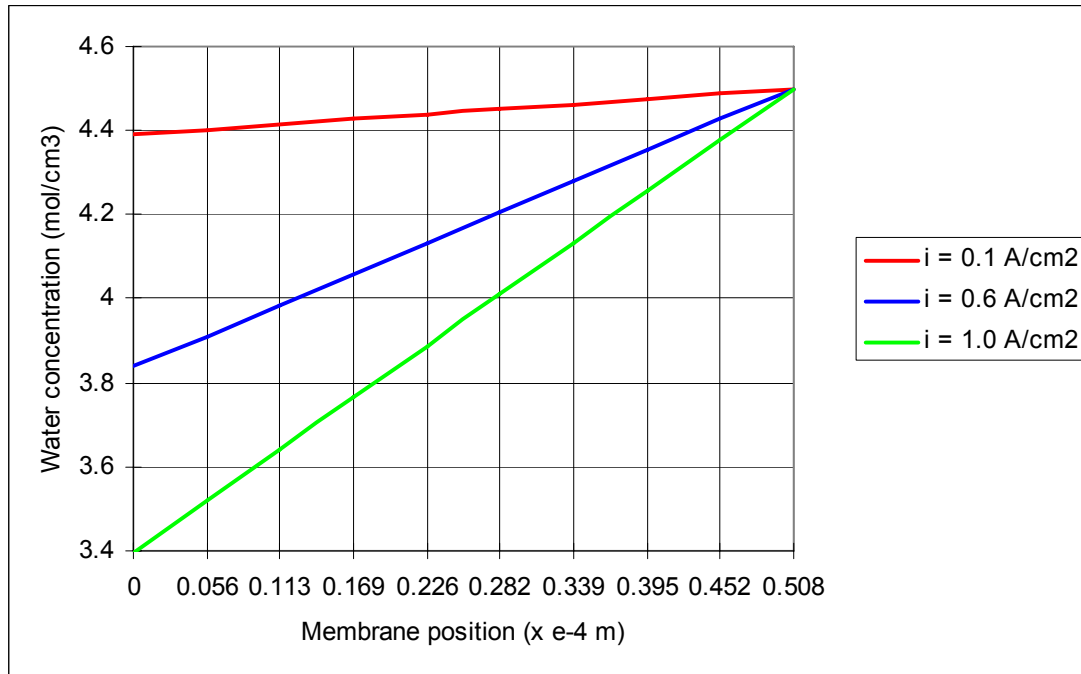
Figure 8.42. Effect of current density on water concentration (a) 0.1 A/cm^2 (b) 0.9 A/cm^2

(c) comparison of 0.1 A/cm^2, 0.5 A/cm^2 and 0.9 cm^2

8.3.2 Effect of Temperature

Figure 8.43 shows how the concentration varies with temperature in the membrane. As the membrane temperature increases, the water concentration across the membrane becomes more uniform – even with high current densities. This indicates the membrane conductivity is better with increased temperatures – as long as the membrane can maintain adequate hydration. The ohmic heating results in a very small temperature increase across the membrane from the initial conditions. As the temperatures become higher, convective transport effects begin to dominate. The ohmic heating still heats up the membrane slightly, however, the convective effects dominate and the temperature decreases across the membrane.
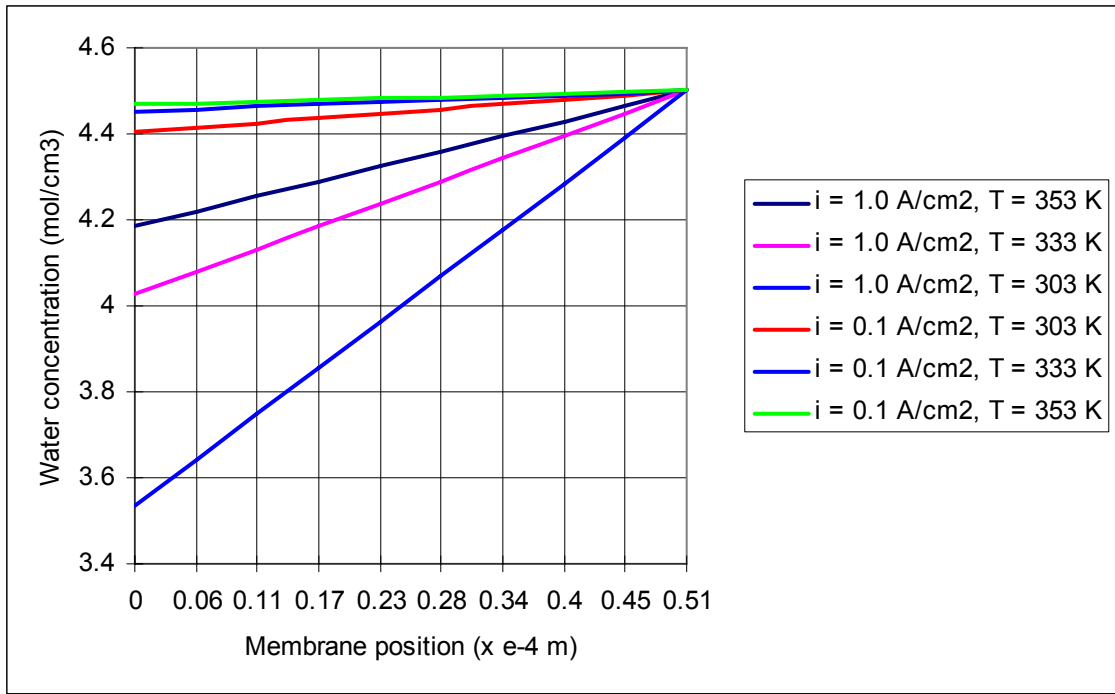
Figure 8.43. Effect of temperature on water concentration (a) 353 K (b) 323 K (c) comparison of 343 K, 348 K, 353 K and 358 K

8.3.3 Effect of Water Activity at the Catalyst/Membrane Interfaces

Figures 8.44 ad 8.45 illustrates the effect of water activity at the catalyst layer/ membrane interfaces with the water concentration across the polymer membrane. If the water activity is 1.0 at the catalyst/membrane interface, the water concentration through the membrane is very uniform. As the water activity at the cathode catalyst interface decreases, the water concentration on the anode side decrease, which means that the membrane conductivity decreases. This same phenomena resulted regardless of the initial membrane concentration.

235
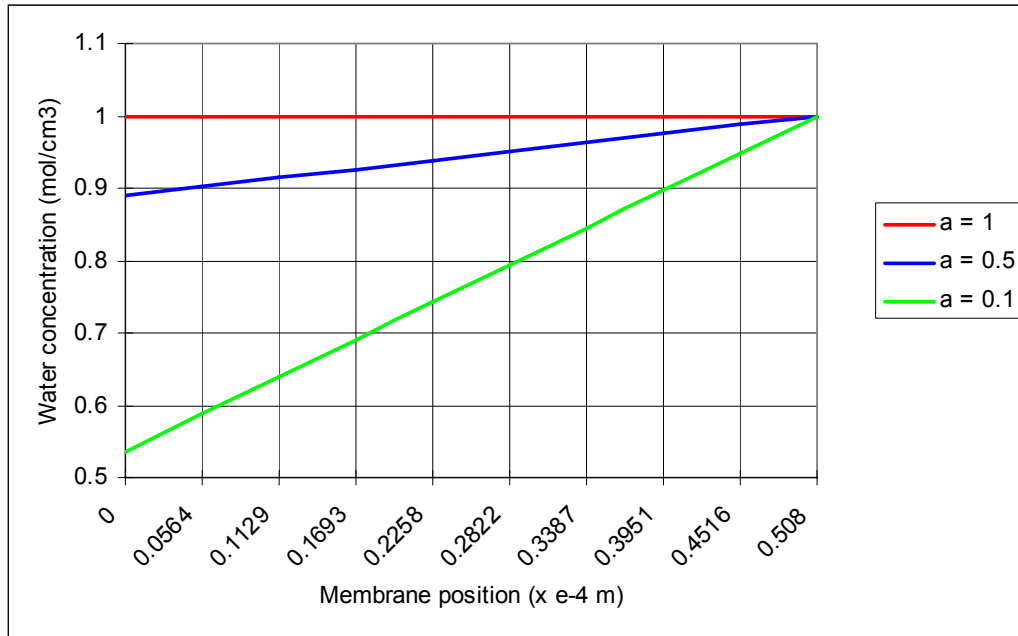
Figure 8.44. Water concentration in the membrane with varying water activity at the

membrane/cathode catalyst layer interface
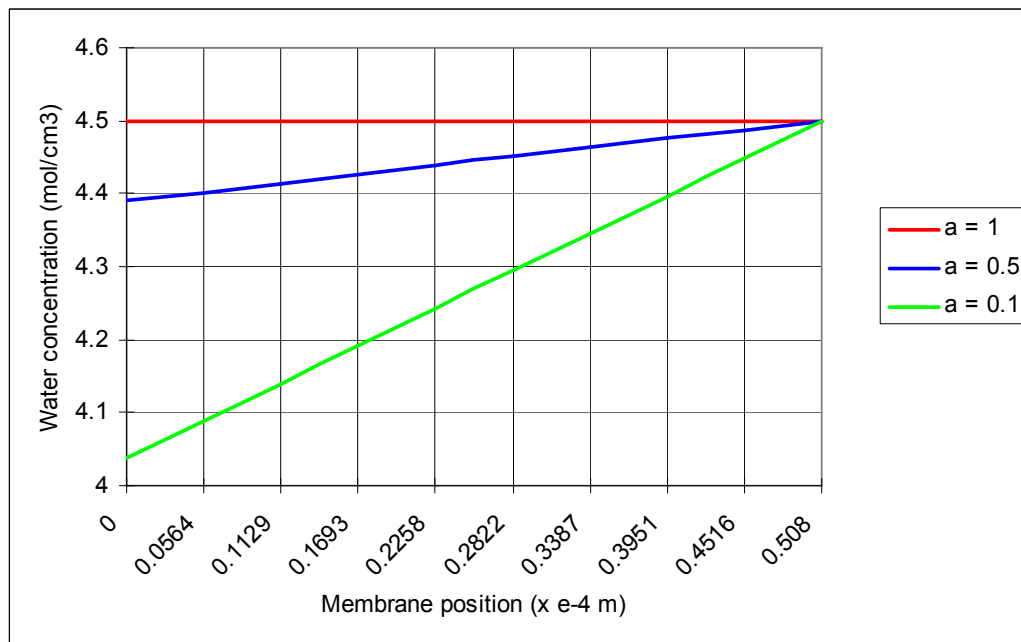
Figure 8.45. Water concentration in the membrane with varying water activity at the

membrane/cathode catalyst layer interface

8.4 Electron Transport

Electrons are produced in the anode catalyst layer, consumed in the cathode catalyst layer, and transported in the solid phase. The electronic current density is zero in the membrane because it is electronically insulative. The current density in the anode catalyst layer is much faster than the reaction at the cathode catalyst layer. Since the oxygen reduction reaction is slower, it requires a larger surface area for the reaction than the cathode catalyst layer. The solid potential distribution for $t = 300$ s is illustrated in Figure 8.46.
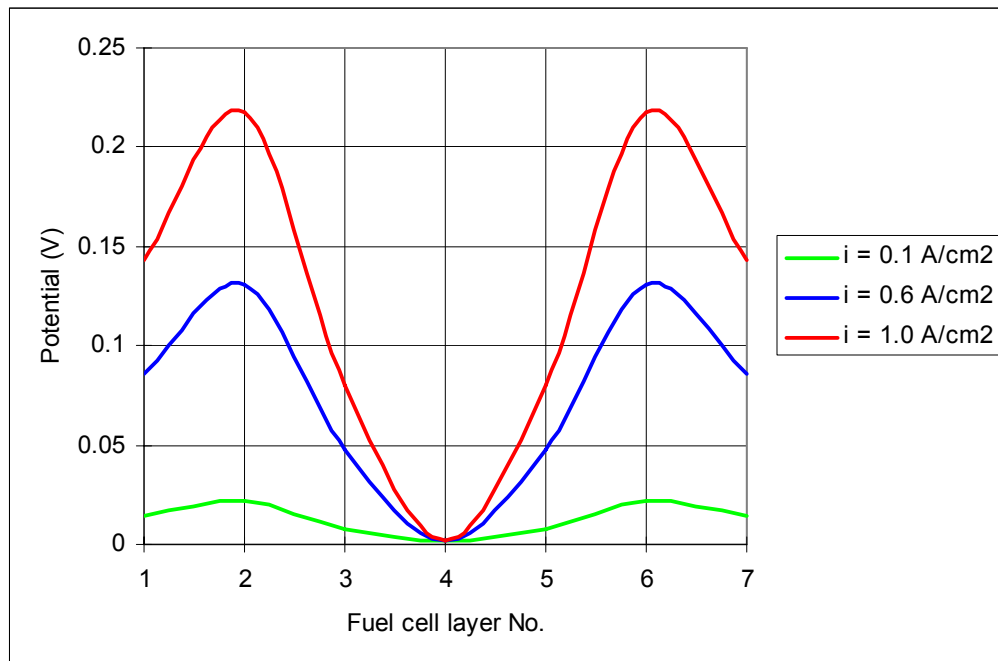
Figure 8.46. The solid phase potential in the PEM fuel cell

The electronic current density is relatively constant in the gas flow channels and gas diffusion layers. The potential varies in each layer based upon the area of the solid

portion of the layer, such as the channel and void space, the thickness and the intrinsic resistivity of the layer.

8.5 Overall Fuel Cell Model Validation

A 16 cm^2 single cell, air breathing fuel cell stack was used for additional fuel cell I-V tests. Five-layered MEAs are used, which are composed of Nafion 112, GDL of carbon cloth material and 1 mg/cm^2 of Pt loading on both anode and cathode. Cell performance tests are conducted with 0.5 to 1.0 standard cubic centimeter per minute (SCCM) of hydrogen from an electrolyzer, with no additional humidification. All tests are taken at 25º C and ambient pressure. I–V curves of these cell performance tests are shown in Figure 8.47, and compared with the model results.
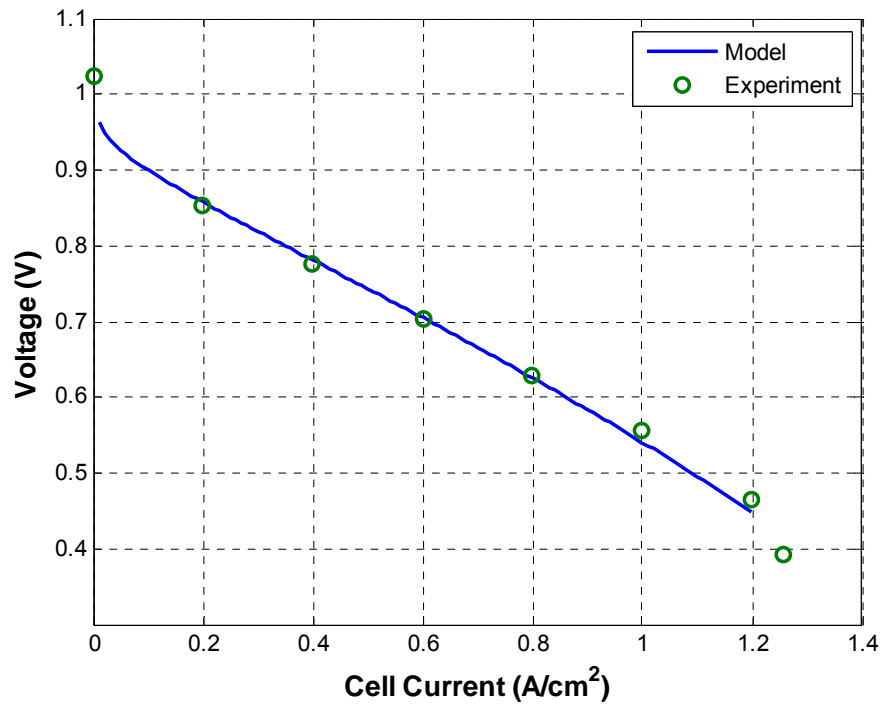
Figure 8.47. Comparison between fuel cell model and experiments at 298 K and 1 bar

Several more IV tests were performed with different fuel cell stack temperatures. As shown in the Figure 8.48, the model results agree well with the actual results obtained with the experiments.
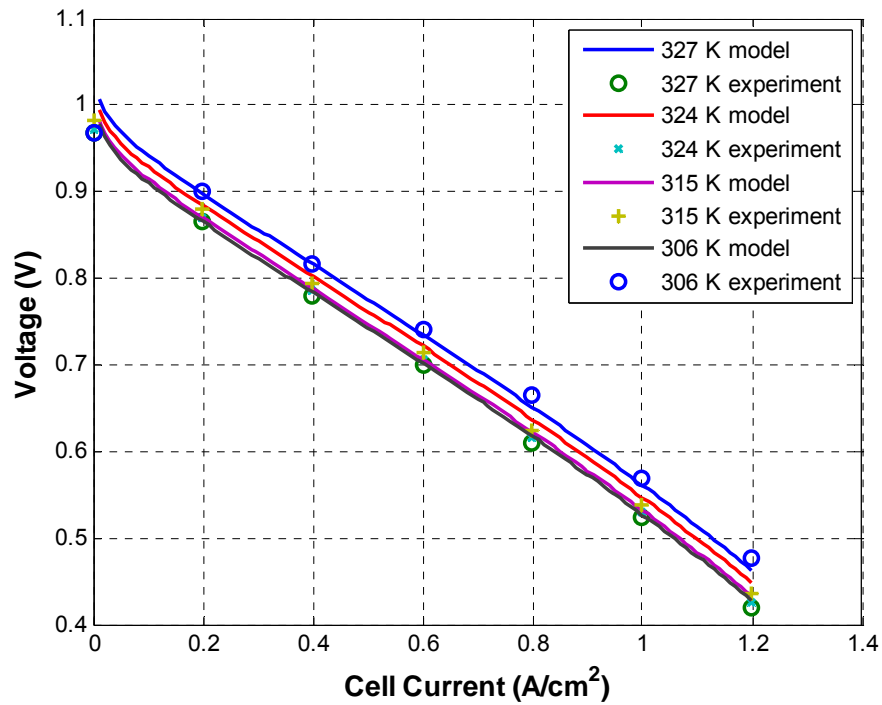
Figure 8.48. Comparison between fuel cell model and experiments at various

temperatures

The overall fuel cell model for predicting electrochemical performance was

created and validated using a 16 cm^2 fuel cell stack. A numerical model included energy,

mass and charge balances for each fuel cell layer. In order to precisely model the

electrochemical reactions, an agglomerate catalyst layer was included in the model using

porous electrode equations. In addition, an empirical membrane model correlating water

content and conductivity was integrated into the model. The experimental validation

consisted of experimentally examining the IV curves of the PEM fuel cell stack.

9
SUMMARY AND FUTURE WORK

The PEM fuel cell consists of several layers where several processes occur simultaneously in the same layer. In the flow field plates, reactant gas flows in the channels, while current flows in the solid portion of the layer. The gas diffusion media also have flow through the porous media, while transporting electrons through the material. The acidic polymer electrolyte layer has both positive ions and water flowing in through the polymer. Like the gas diffusion media, the catalyst layer had reactant gases flowing through the porous structure, while transporting electrons to the gas diffusion layer. In addition, the electro-chemical reactions convert the reactants directly into electrical energy. Heat and water are also produced in this layer. The processes that occur in thee layers are complicated by the thinness of the layers, high temperatures and pressures, and the presence of two phases. The direct measurement of these properties are currently unavailable, therefore, mathematical modeling is needed to help provide insight into the phenomena that is occurring within the fuel cell. There has been an increased interest in modeling fuel cells during the last decade. Although these model are very helpful in trying to understand the transport phenomena that is occurring in the fuel cell, it is difficult to understand how all of the operating variables, such as pressure, temperature, humidity and load requires are affecting the transport phenomena within the fuel cell, and how these transport processes can be improved with new designs.

When considering the formulation of this model, the fuel cell was first considered to be composed of several phases: a multi-component gas phase which includes hydrogen, oxygen, water and sometimes nitrogen and carbon dioxide or carbon monoxide. The liquid phase consists of water, which is produced at the cathode catalyst layer, and is also entering the fuel cell in the reactant streams, the solid portion consists of the layer materials: the end plate, gasket, terminal, gas diffusion media material, catalyst layer material – which is made of carbon and platinum and the polymer electrolyte membrane. The conservation of mass, momentum, energy and charge transport was applied to each node of each layer in the form of traditional engineering mass, energy and charge balances. The effect of pressure drop was also included in the model.

To accomplish the objectives described in this dissertation, detailed models were required for each of the various fuel cell layers. The model developed for this dissertation is complex enough to handle all of the important governing phenomena, but remains simple enough to run in a realistic amount of time. Part of the overall model included a detailed model of the membrane which accounts for many of the effects experimentally observed. It bridges the gap of many models currently in the literature, and allows one to understand how all of the fuel cell parameters affect each other. In this research, both a model for the single PEM fuel cell and the PEM fuel cell stack was developed in MATLAB.

The solution of the numerical model emphasized many of the important processes that occur within the PEM fuel cell. Due to the nature of the electrochemical reactions, the hydrogen and water were removed from the gas phase at a ratio of 1:2, which resulted in the hydrogen concentration increasing in the catalyst layers although it was

being consumed. Water was transported through all of the regions of the fuel cell because it is present in both the gas and liquid phase. Water was consumed in the anode catalyst layer and produced in the cathode catalyst layer. Most of the water consumed in the anode catalyst layer was obtained from the anode gas flow channel, while a large portion of the water produced in the cathode catalyst layer exited the fuel cell through the cathode gas flow channel. However, some of the water produced in the cathode catalyst layer traveled through the polymer electrolyte layer. The relative humidity in the gas phase on the cathode side of the cell was greater than 100%. On the anode side of the cell, the relative humidity was below 100% in the catalyst layers although the reactant flows through the anode gas flow channels were fully humidified. Therefore, these simulations suggest that both liquid water flooding and membrane dehydration could occur simultaneously.

The reaction rate distributions in the anode and cathode catalyst layers illustrate the importance of the mass transport on the conversion of chemical energy to electrical energy in the fuel cell. In the cathode catalyst layer, the reactant gas transport, and the amount of water produced affected the reaction rate. At the anode-side, hydrogen seemed to be aided by convection, which influenced the reaction rate.

The higher the current density, the more water was driven from the anode to the cathode, and out of the membrane. A positive pressure gradient from the anode to the cathode could be used to drive water toward the anode side – which is more likely to dry out. The effect of the water flux into and out of the membrane illustrated that if too much water flows into the membrane, flooding may occur, whereas, if too much water is removed from the membrane, drying may occur. These results seem obvious, but the

243

model allows these phenomena and their effect on temperature and voltage to be studied, and quantified. The model is also capable of predicting transient water, concentration voltage and temperature profiles for transient boundary conditions. This capability will prove useful when attempting to develop a control strategy for the fuel cell, and when investigating highly transient processes such as fuel cell startup on a vehicle.

The bulk gas phase flow acted to hinder the transport of oxygen from the cathode gas flow channels to the cathode catalyst layer. As a result, the concentration of hydrogen increased in the anode catalyst layer, but decreased in the cathode catalyst layer. Water was transported in both the gas phase and as a liquid phase in the polymer electrolyte.

Due to the high conductivity of the solid phase, the potential remained relatively constant in the fuel cell layers. The potential in the electrolyte is influenced purely by the water content of the membrane. Therefore, it is important that water concentration and ion transport is coupled in the polymer model.

Since the humidification of both the anode and cathode sides of the PEM fuel cell are important, the temperature throughout the fuel cell is also very important. Injecting liquid water into the anode channel inlet may be useful for improving fuel cell performance improvement. The optimal amount of liquid water could be determined by using the model and running simulations. Heat can be either added or removed from the fuel cell stack by adjusting the temperature of the reactant gases. However, the fuel cell engineer must take into consideration what the additional equipment cost will be for cooling or heating the fuel cell in this manner. Decreasing the cooling temperature may be helpful in improving fuel cell performance. For many stack designs, it may be advantageous to thermally isolate the fuel cell stack end plates due to the loss of heat at

244

this point in the fuel cell stack. To obtain a uniform heat distribution within the fuel cell stack, it may be useful to heat the bipolar plates, but depending upon the stack design, this may be difficult to implement compared with just heating the end plates. Heating the anode side slightly higher than the cathode-side may be a good option to ensure uniform heat distribution in a fuel cell stack.

The results of this dissertation research suggest several areas of future research. For the heat transfer analysis, it is important to consider the heat transfer in 2-D and 3-D to obtain realistic results. Although both the gaseous and liquid phase of water was studies in this model, there was no relationship introduced between the two phase for the porous GDL and catalyst layers. One option would be the introduction of a simple capillary pressure equation to relate the two phases. In addition, the velocity was calculated for the mixture, but it would be more accurate to calculate the gas and liquid phase velocity separately.

The simulation based on this model can be used to analyze water transport across the membrane, the water phase change effect, the pressure variation along the channel and the energy balance. It can also be used to predict the characteristics of the flows inside the channel and analyze the factors that affect the fuel cell performance. The overall simulations demonstrated that optimal performance in PEMFCs is a balance between different phenomena. Optimization of the right operating conditions and structural properties depends upon the quantification of this interplay. The optimization that can be accomplished with the model are almost endless and depend on the phenomenon being studied.

REFERENCES

[1] Li, X. (2005). *Principles of Fuel Cells*. New York: Taylor & Francis.

[2] Spiegel, C.S. (2007). *Designing and Building Fuel Cells*, 1st ed. New York: McGraw-Hill.

[3] 3M Corporation. (2008). An Exploded View of a Polymer Electrolyte Membrane Fuel Cell Stack. Retrieved from http://www.3m.com/us/mfg_industrial/fuelcells/ overview/pemfc.jhtml

[4] Spiegel, C.S. (2008). *PEM Fuel Cell Modeling and Simulation Using MATLAB*, 1st Ed. New York: Elsevier Science.

[5] Bernardi, D. and Verbrugge, M. (1991). Mathematical model of a gas diffusion electrode bonded to a polymer electrolyte. *AIChE Journal*, 37(8):1151-1163.

[6] Bernardi, D. and Verbrugge, M. (1992). A mathematical model of the solid-polymer-electrolyte fuel cell. *Journal of the Electrochemical Society*, 139(9):2477-2491.

[7] Springer, T., Zawodzinski, T., and Gottesfeld, S. (1991). Polymer electrolyte fuel cell model. *Journal of the Electrochemical Society*, 138(8):2334-2342.

[8] Springer, T., Wilson, M., and Gottesfeld, S. (1993). Modeling and experimental diagnostics in polymer electrolyte fuel cells. . *Journal of the Electrochemical Society*, 140(12):3513-3526.

[9] Weisbrod, K. R, Grot, S.A, and Vanderborgh, N.E (1995). Through-the-electrode model of a proton exchange membrane fuel cell. *Proceedings of the First International Symposium on Proton Conduction Membrane Fuel Cells I,* pages 152-166.

[10] Gloaguen, F. and Durand, R. (1997). Simulations of PEFC cathodes: an effectiveness factor approach. *Journal of Applied Electrochemistry*, 27(9):1029-1035.

[11] Eikerling, M. and Kornyshev, A. (1998). Modeling the performance of the cathode catalyst layer of polymer electrolyte fuel cells. *Journal of Electroanalytical Chemistry*, 453(1-2):89-106.

[12] Marr, C. and Li, X. (1998). An engineering model of proton exchange membrane fuel cell performance. *ARI*, 50:190-200.

[13] Baschuk, J. and Li, X. (2001). Carbon monoxide poisoning of proton exchange membrane fuel cells. *International Journal of Energy Research*, 25(8):695-713.

[14] Pisani, L., Murgia, G., Valentini, M., and D'Aguanno, B. (2002). A working model of polymer electrolyte fuel cells comparisons between theory and experiments. *Journal of the Electrochemical Society*, 149(7):A898-A904.

[15] Bevers, D., Wohr, M., Yasuda, K., and Ogura, K. (1997). Simulation of a polymer electrolyte fuel cell electrode. *Journal of Applied Electrochemistry*, 27(11):1254-1264.

[16] Wohr, M., Bolwin, K., Schnurnberger, M. Fischer, W. Neubrand, and G. Eigenberger. (1998). Dynamic modelling and simulation of a polymer membrane fuel cell including mass transport limitation. *International Journal of Hydrogen Energy*, 23(3):213-218.

[17] Rowe, A. and Li, X. (2001). Mathematical modeling of proton exchange membrane fuel cells. *Journal of Power Sources*, 102(1-2):82-96.

[18] Fuller, T. and Newman, J. (1993). Water and thermal management in solid-polymer-electrolyte fuel cells. *Journal of the Electrochemical Society,* 140(5):1218-1225.

[19] Nguyen, T.V., and White, R.E. (1993). A water and heat management model for proton-exchange- membrane fuel cells. *Journal of the Electrochemical Society*, 140: 2178.

[20] Thirumalai, D. and White, R. (1997). Mathematical modeling of proton-exchange-membrane-fuel-cell stacks. *Journal of the Electrochemical Society*, 144(5):1717-1723.

[21] Yi, J. S. and Nguyen, T. V. (1998). An along-the-channel model for proton exchange membrane fuel cells. *Journal of the Electrochemical Society*, 145(4):1149-1159.

[22] vanBussel, H., Koene, F., and Mallant, R. (1998). Dynamic model of solid polymer fuel cell water management. *Journal of Power Sources*, 71(1-2):218-222.

[23] Singh, D., Lu, D. and Djilali, N. (1999). A two-dimensional analysis of mass transport in proton exchange membrane fuel cells. *International Journal of Engineering Science*, 37(4):431-452.

[24] Kazim, A., Liu, H., and Forges, P. (1999). Modeling of performance of PEM fuel cells with conventional and interdigitated flow fields. *Journal of Applied Electrochemistry*, 29(12):1409-1416.

[25] Bradean, R., Promislow, K., and Wetton, B. (2002). Transport phenomena in the porous cathode of a proton exchange membrane fuel cell. *Numerical Heat Transfer*: Part A: Applications, 42(1-2):121-138.

[26] He, W., Yi, J., and Nguyen, T. (2000). Two-phase flow model of the cathode of PEM fuel cells using interdigitated flow fields. *AIChE Journal*, 46(10):2053-2064.

[27] Natarajan, D., and Nguyen, T. (2001). A two-dimensional, two-phase, multi-component, transient model for the cathode of a proton exchange membrane fuel cell using conventional gas distributors. *Journal of the Electrochemical Society*, 148(12):A1324-A1335.

[28] Natarajan, D. and Nguyen, T. (2003). Three-dimensional effects of liquid water cooling in the cathode of a PEM fuel cell. *Journal of Power Sources*, 115(1):66-80.

[29] Gurau, V., Liu, H., and Kakac, S. (1998). Two-dimensional model for proton exchange membrane fuel cells. *AIChE Journal*, 44(11):2410-2422.

[30] Zhou, T. and Liu, H. (2000). 3-D model of proton exchange membrane fuel cells. American Society of Mechanical Engineers: Heat Transfer Division, (Publication) HTD, 366(1):43-49.

[31] You, L. and Liu, H. (2001). A two-phase and multi-component model for the cathode of PEM fuel cells. American Society of Mechanical Engineers: Heat Transfer Division, (Publication) HTD, 369(4):325-334.

[32] Shimpalee, S., Dutta, S., Lee, W., and Zee, J.V. (1999). Effect of humidity on PEM fuel cell performance part II-numerical simulation. American Society of Mechanical Engineers: Heat Transfer Division, (Publication) HTD, 364(1):367-374.

[33] Shimpalee, S. and Dutta, S. (2000). Numerical prediction of temperature distribution in PEM fuel cells. Numerical Heat Transfer: Part A: Applications, 38(2):111-128.

[34] Shimpalee, S., Lee, W., Zee, J.V., and Naseri-Neshat, H.(2006). Predictingthe transient response of a serpentine flow field PEMFC I: Excess to normal fuel and air. *Journal of Power Sources*, 156(2):355-368.

[35] Shimpalee, S., Lee, W., Zee, J.V., and Naseri-Neshat, H. (2006). Predicting the transient response of a serpentine flow-field PEMFC II: Normal to minimal fuel and air. *Journal of Power Sources*, 156(2):369-374.

[36] Um, S., Wang, C., and Chen, K. (2000). Computational fluid dynamics modeling of proton exchange membrane fuel cells. *Journal of the Electrochemical Society*, 147(12):4485-4493.

[37] Wang, Y. and Wang, C. (2005). Modeling polymer electrolyte fuel cells with large density and velocity changes. *Journal of the Electrochemical Society*, 152(2):A445-A453.

250

[38] Wang, Y. and Wang, C. (2006) Ultra large-scale simulation of polymer electrolyte fuel cells. *Journal of Power Sources*, 153(1):130-135.

[39] Kulikovsky, A. (2003). Quasi-3d modeling of water transport in polymer electrolyte fuel cells. *Journal of the Electrochemical Society*, 150(11):A1432-A1439.

[40] Siegel, N., Ellis, M., Nelson, D., and von Spakovsky, M. (2003). Single domain PEMFC model based on agglomerate catalyst geometry. *Journal of Power Sources*, 115(1):81-89.

[41] Berning, T., Lu, D., Djilali, N. (2002). Three-dimensional computational analysis of transport phenomena in a PEM fuel cell. *Journal of Power Sources*, 106(1-2):284-294.

[42] O'Hayre, R., Cha, S.W., Colella, W., and Prinz, F.B. (2006) *Fuel Cell Fundamentals*. New York: John Wiley and Sons.

[43] Bard, A.J. and Faulkner, L.R. (2001) *Electrochemical Methods: Fundamentals and Applications*, 2nd ed., New York: John Wiley & Sons.

[44] Ay, M., Midilli, A., and Dincer, I. (2006) Thermodynamic modeling of a proton exchange membrane fuel cell. *Int. J. Energy*, 3: 16-44.

[45] Perry, R.H. and Green, D.W. (1997) Perry's Chemical Engineers' Handbook, 7th ed., New York: McGraw Hill.

[46] Barbir, F. (2005). *PEM Fuel Cells: Theory and Practice*. 1st ed., New York: Elsevier Science.

[47] Mench, M., Wang, Y., and Tynell, S.T. (2007). An Introduction to Fuel Cells and Related Transport Phenomena. Department of Mechanical and Nuclear Engineering, Pennsylvania State University. Draft. Retrieved March 4, 2007, from http://mtrl1.mne.psu.edu/Document/jtpoverview.pdf.

[48] Weber, A. Z. (2004). *Modeling Water Management in Polymer Electrolyte Fuel Cells*. [PhD. Dissertation]. University of California, Berkeley:Berkeley, CA.

[49] Askeland, D. R. (1994). *The Science and Engineering of Materials.* 3rd ed., Boston: PWS Publishing Company.

[50] Maggio, G., Recupero, V., and Mantegazza, C. (1996) Modeling of temperature distribution in a solid polymer electrolyte fuel cell stack. *Journal of Power Sources*, 62: 167-174.

[51] Zhang, Y., Minggao, M., Lu, Q., Luo, J., and Li, X. (2004) A model cell stack thermal system. *Applied Thermal English*, 24:501–513.

[52] Park, J., and Li, X. (2006) Effect of flow and temperature distribution on the performance of a PEM fuel cell stack. *Journal of Power Sources*, 162:444–459.

[53] Zong, Y., Zhou, B., and Sobiesiak, A. (2006). Water and thermal management in a single PEM fuel cell with non- uniform stack temperature. Journal of Power Sources, 161:143–159.

[54] Graf, C., Vath, A., and Nicoloso, N. (2006). Modeling of the heat transfer in a portable PEFC system within MATLAB-Simulink. *Journal of Power Sources*, 155: 52–59.

[55] Sundaresan, M. and Moore, R.M. (2005). Polymer electrolyte fuel cell stack thermal model to evaluate sub-freezing startup. *Journal of Power Sources*, 145:534–545.

[56] Shan, Y. and Choe, S.Y. (2006). Modeling and simulation of a PEM fuel cell stack considering temperature effects. *Journal of Power Sources*, 158:274–286.

[57] Shan, Y., Choe, S.Y., and Choi, S.H. (2007). Unsteady 2D PEM fuel cell modeling for a stack emphasizing thermal effects. *Journal of Power Sources*, 165:196–209.

[58] Khandelwal, M. and Mench, M.M. (2006). Direct measurement of through-plane thermal resistance in fuel cell materials. *Journal of Power Sources*, 161: 1106–1115.

[59] Incropera, F.P. and DeWitt, D.P. (1996). *Fundamentals of Heat and Mass Transfer*, (4th ed.). New York:John Wiley & Sons.

[60] Middleman, S. (1998). *An Introduction to Mass and Heat Transfer: Principals of Analysis and Design*, 1st Edition, New York:John Wiley & Sons.

[61] Sanchez, D., Munoz, A., and Sanchez, T. (2007). An assessment on convective and radiative heat transfer modeling in tubular solid oxide fuel cells. *J. Power Sources*, 169:25-34.

[62] Linstrom, P.J. and Mallard, W.G. (2008). NIST Standard Reference Database Number 69, National Institute of Standards and Technology. Retrieved October 19, 2008, from http://webbook.nist.gov.

[63] Felder, R. and Rousseau, R. (1986). *Elementary Principles of Chemical Processes*. 2nd Edition, New York:John Wiley & Sons.

[64] Robinson, R. N. (1996). *Chemical Engineering Reference Manual for the PE Exam*, 5th Edition, Belmont, CA:Professional Publications, Inc.

[65] Zhou, B., Huang, W., Zong, Y., and Sobiesiak, A. (2006). Water and pressure effects on a single PEM fuel cell. *Journal of Power Sources*, 155:190–202.

[66] Schulz, V.P., Becker, J., Wiegmann, A., Mukherjee, P. P., and Wang, C.Y. (2007) Modeling of Two-Phase Behavior in the Gas Diffusion Medium of PEFCs via Full Morphology Approach. *Journal of the Electrochemical Society*. 154:B419-B426.

[67] Massey, B. S. (1989). *Mechanics of Fluids*, 6th Edition, New York:Chapman & Hall.

[68] Ridge, S. J., White, R. E., Tsou, Y., Beaver, R. N., and Eisman, G. A. (1989) Oxygen reduction in a Proton Exchange Membrane Test Cell. *Journal of the Electrochemical Society*. 136:1902.

[69] Suleman, A., Secanell, M., Karan, K. and Dijilali, N. (2007) Multi-variable optimization of PEMFC cathodes using an agglomerate model. *Electrochimica Acta*, 52: 6318.

[70] Karan, K. (2007) Assessment of transport-limited catalyst utilization for engineering of ultra-low Pt loading polymer electrolyte fuel cell anode. *Electrochemistry Communications*, 9: 747.

[71] Song, D., Wang, Q., Liu, Z., Eikerling, M., Xie, Z., Navessin, T., and Holdcroft, S. (2005) A method for optimizing distributions of Nafion and Pt in cathode catalyst layers of PEM fuel cells. *Electrochimica Acta*, 50: 3347.

[72] Verbrugge, M.W. and Hill, R. F. (1990). Ion and solvent transport in ion-exchange membranes. *Journal of the Electrochemical Society*, 137: 886.

[73] Springer, T.E., Zawodzinski, T.A., Wilson, M.S. and Gottesfeld, S. (1996). Characterization of Polymer. *Journal of the Electrochemical Society*, 143:587.

[74] Weisbrod, K. R., Grot, S.A., and Vanderborgh, N. E., (1995). Through the electrode model of a proton exchange membrane fuel cell. The Electrochemical Society Proceedings, Pennington, NJ, 95(23):152.

[75] Yi, J.S., and Nguyen, T. V. (1999). Hydrodynamics of reactant gas in a porous electrode of a PEM. *Journal of the Electrochemical Society*, 146:38.

[76] Gurau, V., Kakac, S., and Liu, H. (1998)*. Mathematical Model for Proton Exchange Membrane Fuel Cells*. [Publication]. ASME Advanced Energy Systems Division, 38:205.

[77] Berning, T., and Djilali, N. J. (2003). , A 3D, multiphase, multicomponent model of the cathode and anode. *Journal of the Electrochemical Society*, 150:A1598.

[78] He, W.S., Lin, G.Y., and Van Nguyen, T. (2003). A Diagnostic Tool to Detect Electrode Flooding in. PEM Fuel Cells. *AIChE Journal*, 49:3221.

[79] Amphlett, J. C., Mann, R.F., Peppley, B.A., Roberge, P.R., and Rodrigues, A. J. (1996). A model of proton exchange membrane fuel cells. *Journal of Power Sources*, 61:183.

[80] Yerramalla, S., Davai, A., Feliachi, A, Biswas, T. (2003). Modeling and simulation of the dynamic behavior of a polymer electrolyte membrane fuel cell. *Journal of Power Sources*, 124:104-113.

[81] Zawodzinski, T.A., et al.(1993). Water uptake by and transport through Nafion 117 membranes. *Journal of Electrochemical Society*, 140(4):1041-1337.

[82] Hinatsu, J.T., Mizuhata, M., and Takenaka, H. (1994) Water Uptake of Perfluorosulfonic Acid Membranes from liquid Water and Water Vapor. *Journal of the Electrochemical Society*, 141:1493.

[83] Weber, A.Z. and Newman, J. (2005). Effects of microporous layers in polymer electrolyte fuel cells. *Journal of the Electrochemical Society*, 152: A677.

[84] Yi, B., Ge, S., Li, X., and Hsing, I. (2005). Absorption, desorption and Transport of Water in Polymer Electrolyte Membranes for Fuel Cells. *Journal of Electrochemical Society*, 152(6):A1149- A1157.

[85] Sakai, T., Takeraka, H., and Torikai, E. (1986). Gas Diffusion in the Dried and Hydrated Nafions. *Journal of the Electrochemical Society*, 133(1):88-92.

[86] Hwang, J.J., and Hwang, H.S. (2004). Parametric studies of a double-cell stack of PEMFC using Grafoil flow-field plates. *Journal of Power Sources* 104**:**24–32.

[87] Al-Huniti, N.S. (2005). Computation of Member Stiffness in Bolted Connections Using the Finite Element Analysis. *Mechanics Based Design of Structures and Machines* 33:331–342.

[88] Alkatan, F., Stephan, P., Daidie, A., and J. Guillot, (2007). Equivalent stiffness of various components in bolted joints subjected to axial loading. *Finite Elements in Analysis and Design,* 43:589-598.

[89] Zhang, O. and Poirier, J.A. (2004). New analytical model of bolted joints. *Journal of Mechanical Design,* 126: 721-728.

[90] Zhou, Y., Lin, G., Shih, A.J., and Hu, S.J. (2007). A Micro-scale Model for predicting contact resistance between Layer in PEM Fuel Cells. *Journal of Power Sources*, 163: 777–783.

[91] Greenwood, J.A. and Williamson, J. (1966). Contact of nominally flat surfaces. Proc. Roy. Soc, London, 295: 300-319.

[92] Puttock, M.J., and Thwaite, E.G. (1969). Elastic Compression of Spheres and Cylinders at Point Line Contact. *NSLTP*, Australia, 25:5-7.

[93] Nitta, I., Hottinen, T., Himanen, O., and Mikkola, M. (2007). Inhomogeneous compression of PEMFC gas diffusion layer Part I. *Journal of Power Sources*, 171:26–36.

[94] Slocum, A. (2002). *Precision Machine Design.* Society of Manufacturing Engineers: New York.

[95] Bickford, J. H. (1990). *An Introduction to the Design and Behavior of Bolted Joints.* 2nd ed. Marcel Dekker, Inc.: New York.

[96] Petele, M. (2007). Prestressed Bolt Connection. Retrieved October 29, 2008, from MITCalc Web site: http://www.mitcalc.com/doc/boltcon/help/en/boltcon.htm

[97] Tirovic, M. and Voller, G.P. (2005). Interface pressure distributions and thermal contact resistance of a bolted joint. *Proceeding of the Royal Society A*, 461:2339-2354.

[98] Spiegel, C. S., Agarwal, R., and Bhansali, S. (2008). Comparision of microchannel dimensions for air-breathing polymer exchange membrane microfuel cells. *Journal of Power Sources*, 182:603–608.

[99] Dyer, C.K. (2002). Fuel cells for portable applications. *Journal of Power Sources*, 106:31–34.

[100] Lee, S. J., Cha, S.W., Liu, Y., O'Hayre, R. and Prinz, F.B. (2000, May) High Power-Density Polymer-Electrolyte Fuel Cells by Microfabrication. *The Electrochemical Society Proceeding Series*, 3.

[101] Yu, J., Cheng, p., Ma, Z. and Yi, B. (2003). Fabrication of miniature silicon wafer fuel cells with improved performance. *Journal of Power Sources*, 124:40–46.

[102] Schmitz, A., Tranitz, M., Wagner, S., Hahn, R. and Hebling, C. (2003). Planar self-breathing fuel cells. *Journal of Power Sources*, 118:162–171.

[103] O'Hayre, R., et al. (2003). Development of portable fuel cell arrays. with printed-circuit technology. *Journal of Power Sources*, 124:459–472.

[104] Cha, S.W., O'Hayre, R., Saito,Y. and Prinz, F.B., (2004). The scaling behavior of flow patterns: a. model investigation. *Journal of Power Sources*, 134:57 – 71.

[105] Wong, C.W., Zhao, T.S., Ye, Q. and Liu, J.G. (2006). *Journal of Power Sources*, 155:291 – 296.

[106] Liu, J.G., Zhao, T.S., Liang, Z.X., and Chen, R. (2006). Effect of membrane thickness on the performance and efficiency of passive direct methanol fuel cells. *Journal of Power Sources*, 153:61 – 67.

[107] Hahn, R.S., Wagner, A., Schmitz, and Reichl, H. (2004). Development of a planar micro fuel cell with thin and micro patterning technologies. *Journal of Power Sources*, 131:73-78.

[108] Hsieh, S.S., Huang, C.F., Kuo, J.K., Tsai, H.H. and Yang, S.H. (2005). SU-8 flow field plates for micro PEMFC. *Journal of Solid State Electrochem*, 9:121 -131.

[109] Lu, Q. and Wang, C.Y. (2005). Development of Micro Direct Methanol Fuel Cells for High *Power* Applications. *Journal of Power Sources*, 144:141 – 145.

[110] Modroukas, D., Modi, V. and Frechette, L.G. (2005). Micromachined silicon structures for free-convection PEM fuel cells. *Journal of Micromechanics and Microengineering*, 15:S193 – S201.

258

[111] Li, W., et al. (2003). Preparation and characterization of multiwalled carbon nanotube-supported platinum for cathode catalysts of direct methanol fuel cells. *Journal of Physical Chemistry*, B107:6292 – 6299.

[112] Lu, Q., Wang, C.Y., Yen, T.J. and Zhang, X. (2004). Development and Characterization of a Silicon-based Micro Direct Methanol Fuel Cell. *Electrochimica Acta*, 49:821 – 828.

[113] Lee, S., Chen, Y., Huang,C. (2005). Electroforming of metallic bipolar plates with micro-featured flow field. *Journal of Power Sources*, 145:369 – 375.

[114] Agarwal, R., Samson, S., Kedia, S. and Bhansali, S. (2007). Fabrication of Integrated Vertical Mirror Surfaces and Transparent Window for Packaging MEMS Devices. *Journal of Microelectromechical Systems,* S. 16(1):122-129.
[115] Khandelwal, M., Lee, S. and Mench, M.M.(2007). One-dimensional thermal model of cold-start in a polymer electrolyte fuel cell stack. Journal of Power Sources, 172:816 – 830.

[116] Shan, Y. and Choe, S.Y. (2006). Modeling and simulation of a PEM fuel cell stack considering temperature effects. *Journal of Power Sources,* 158:274 – 286.

[117] Baschuk, J. J. (2006). *Comprehensive, consistent and systematic approach to the mathematical modeling of PEM fuel cells*. [PhD. Dissertation]. University of Waterloo:Waterloo, ON.

APPENDICES

Appendix A Fuel Cell Layer Parameters Used for Model

Table A.1

Parameters used for the end plate layers

Variable	Notation	Description	Value	Units
Plate area	$A_{a\ end}$	End plate area [118]	0.007225	m^2
Plate width		End plate width [118]	0.085	m
Material	N/A	Clear PVC [118]	N/A	N/A
Thickness	$thick_{a\ end}$	Thickness [118]	0.01	m
Conductivity	$k_{a\ end}$	Conductivity [119]	0.32	W/mK
Density	ρ_{a_end}	Density [120]	1740	kg/m^3
Heat Capacity	$cp_{a\ end}$	Heat Capacity [120]	1460	J/kgK
Specific Resistance	res	Specific Resistance	0	Ohm-m
Coolant radius	r	Inlet channel radius [118]	0.002	m
Coolant length	L	Channel length [118]	0.01	m
Coolant cross-sectional area	A_c	Channel cross-sectional area [118]	$\pi r^2 = 1.256e\text{-}5$	m^2
Coolant perimeter	P_{cs}	Channel perimeter [118]	$2\pi r = 0.01256$	m
Reactant channel radius	r	Inlet channel radius *	0.004	m
Reactant channel length	L	Channel length *	0.01	m
Reactant channel cross-sectional area	A_c	Channel cross-sectional area *	$\pi r^2 = 5.024e\text{-}5$	m^2
Reactant channel perimeter	P_{cs}	Channel perimeter *	$2\pi r = 0.02512$	m

* This parameter was an actual measurement from a fuel cell stack, or it was assumed.

Appendix A (Continued)

Table A.2

Parameters used for the anode end plate

Variable	Notation	Description	Value	Units
H$_2$ Temperature	T_{H2_in}	Initial hydrogen temperature *	298	K
Volumetric flow rate	v_{H2_in}	Volumetric flow rate per cell [118]	1.25e-7	m^3/sec
Humidity	ϕ_{H2_in}	Humidity *	1	N/A
Pressure	P_{H2_in}	Hydrogen pressure *	344,737.864	Pa
Hydrogen density	ρ_{H2_in}	Hydrogen density @ room temp [120]	0.08988	kg/m^3
Hydrogen molecular weight	mw_{H2}	Hydrogen molecular weight	0.0020159	kg/mol
Hydrogen viscosity	mu_{H2_in}	Hydrogen viscosity	8.76e-6	Pa-s
Thermal conductivity	k_{H2_in}	Hydrogen thermal conductivity [120]	0.165	W/mK
Specific heat capacity	cp_{H2_in}	Hydrogen specific heat capacity [120]	14,160	J/kg-K

* This parameter was an actual measurement from a fuel cell stack, or it was assumed.

Appendix A (Continued)

Table A.3

Parameters used for the cathode end plate

Variable	Notation	Description	Value	Units
Oxidant Temperature	T_{O2_in}	Initial oxygen temperature	298	K
Volumetric flow rate	v_{O2_in}	Volumetric flow rate [118]	1.25e-7	m^3/sec
Humidity	ϕ_{O2_in}	Humidity *	1	N/A
Pressure	P_{O2_in}	Oxygen pressure *	344,737.864	Pa
Hydrogen density	ρ_{O2_in}	Oxygen density @ room temp	1.429	kg/m^3
Hydrogen molecular weight	mw_{O2}	Oxygen molecular weight	0.032	kg/mol
Hydrogen viscosity	mu_{O2_in}	Oxygen viscosity	20.18e-6	Pa-s
Thermal conductivity	k_{O2_in}	Oxygen thermal conductivity	0.024	W/mK
Specific heat capacity	cp_{O2_in}	Oxygen specific heat capacity	920	J/kg-K

* This parameter was an actual measurement from a fuel cell stack, or it was assumed.

Appendix A (Continued)

Table A.4

Parameters used for the current collector

Variable	Notation	Description	Value	Units
Plate area	$A_{a\ end}$	Current collector area [118]	0.001289	m^2
Material	N/A	Aluminum 7015 or 6061 *	N/A	N/A
Thickness	$thick_{a\ end}$	Thickness [118]	0.001	m
Conductivity	$k_{a\ end}$	Conductivity *	250	W/mK
Density	ρ_{a_end}	Density *	2720	kg/m^3
Heat Capacity	$cp_{a\ end}$	Heat Capacity *	950	J/kgK
Specific Resistance	res	Specific Resistance *	2.65e-8	Ohm-m
Channel radius	r	Inlet channel radius [118]	0.002	m
Channel length	L	Channel length [118]	0.01	m
Channel cross-sectional area	A_c	Channel cross-sectional area [118]	$\pi r^2 = 1.256e-5$	m^2
Channel perimeter	P_{cs}	Channel perimeter [118]	$2\pi r = 0.01256$	m
Coolant radius	r	Inlet channel radius *	0.004	m
Coolant length	L	Channel length *	0.01	m
Coolant channel cross-sectional area	A_c	Channel cross-sectional area *	$\pi r^2 = 5.024e-5$	m^2
Coolant channel perimeter	P_{cs}	Channel perimeter *	$2\pi r = 0.02512$	m

* This parameter was an actual measurement from a fuel cell stack, or it was assumed.

Appendix A (Continued)

Table A.5

Parameters used for the flow field layers

Variable	Description	Value	Units
Total plate area	Total plate area [118]	0.003025	m^2
Active plate area	Area of plate that has channels [118]	0.001	m^2
Material	Material [118]	Graphite	N/A
Thickness	Thickness [118]	0.0033	m
Conductivity	Conductivity [120]	10	W/mK
Density	Density [120]	1400	kg/m^3
Heat Capacity	Heat Capacity [120]	935	J/kgK
Specific Resistance	Specific Resistance *	1e-4	Ohm-m
Total Length	Total Channel length [118]	0.426	m
"U" bends in channel	No. "U" bends in channel [118]	12	N/A
Avg Bends	Average No. of "L" bends [118] (includes "U" bends)	24	N/A
Length of straight sections	Length of straight channel sections [118]	0.0325	m
No. of channels	No. of channels [118]	13	N/A
Channel depth	Channel depth [118]	0.0015	m
Channel width	Channel width [118]	0.0015	m
Channel area	Channel area *	lw = 6.39e-004	m^2
Perimeter	Channel Perimeter *	0.00471	m

* This parameter was an actual measurement from a fuel cell stack, or it was assumed.

Appendix A (Continued)

Table A.6

Parameters used for cooling channels

Variable	Description	Value	Units
Length	Total Channel length *	0.426	m
"U" bends in channel	No. "U" bends in channel *	12	N/A
Avg Bends	Average No. of "L" bends * (includes "U" bends)	24	N/A
Length of straight sections	Length of straight channel sections *	0.0325	m
No. of channels	No. of channels *	13	N/A
Channel depth	Channel depth *	0.0015	m
Channel width	Channel width *	0.0015	m
Channel area	Channel area *	$lw = 6.39e\text{-}004$	m^2
Perimeter	Channel Perimeter *	0.00471	m

* This parameter was an actual measurement from a fuel cell stack, or it was assumed.

Appendix A (Continued)

Table A.7

Parameters used for surroundings

Variable	Description	Value	Units
Outside Temperature	Ambient temperature *	298	K
Outside pressure	Ambient pressure *	101,325	Pa
Heat coefficient	Convective loss from stack	17	W/K

Table A.8

Parameters used for hydrogen, oxygen and water

Variable	Hydrogen	Air	Water
Temperature of gas or liquid going into stack (K)	298	298	298
Humidity of gas or liquid going into stack	0.5	0.5	N/A
Pressure of gas going into stack (Pa)	101,325.01	101,325.01	N/A
Volumetric flow rate of gas or liquid going into stack (m^3/s)	1.7e-8	1e-8	N/A
Molecular weight (kg/mol)	1e-3		(8e-3
Viscosity (Pa-s)	8.6e-6 (98.8e-7 kg/ms)	8.6e-6	(8.91e-4 kg/ms)
Density (kg/m3)	972	1.3	
Thermal Conductivity (W/m-K)	0.165	0.223	
Specific heat capacity (J/kg-K)	300	1005	4190

Appendix A (Continued)

Table A.9

Parameters used for GDL layer

Variable	Notation	Description	Value	Units
Layer area	$A_{a\ end}$	GDL area [118]	0.001	m^2
Material	N/A	Carbon cloth *	N/A	N/A
Thickness	$thick_{a\ end}$	Thickness [118]	0.0004	m
Conductivity	$k_{a\ end}$	Conductivity *	0.42	W/mK
Density	ρ_{a_end}	Density *	450	kg/m^3
Heat Capacity	$cp_{a\ end}$	Heat Capacity *	710	J/kgK
Specific Resistance	res	Specific Resistance [121]	1e-4	Ohm-m

* This parameter was an actual measurement from a fuel cell stack, or it was assumed.

Appendix A (Continued)

Table A.10

Parameters used for the catalyst layers

Variable	Description	Value	Units
Layer area	Catalyst area [118]	0.001	m^2
Material	Platinum/carbon *	N/A	N/A
Thickness	Thickness [121]	1.5e-3	cm
Conductivity	Thermal Conductivity [120]	0.27	W/mK
Density	Density [121]	Pt: 21.5 C: 2.0	g/cm^3
Heat Capacity	Heat Capacity [120]	710	J/kgK
Electrical conductivity	Electrical conductivity [121]	32.64	S/cm
Anode transfer coefficient	Anode transfer coefficient	1	
Cathode transfer coefficient	Cathode transfer coefficient [121]	0.61	
Henry's constant	Henry's constant [121]	3.1664e10	Pa-cm3/mol
Platinum loading	Platinum loading [121]	0.4	mg/cm2
Pt/C ratio	Pt/C ratio [121]	0.28	
No. of aggregates	No. of aggregates [121]	4	
Aggregate thickness	Aggregate thickness [121]	80	nm
Aggregate radius	Aggregate radius [121]	1	μm
Anode entropy change	Anode entropy change [120]	0.104	J/mol-K
Cathode entropy change	Cathode entropy change [120]	-326.36	J/mol-K

* This parameter was an actual measurement from a fuel cell stack, or it was assumed.

Appendix A (Continued)

Table A.11

Parameters used for the membrane layer

Variable	Description	Value	Units
Initial proton concentration	Initial proton concentration	1.2e-3	mol/m^3
Proton diffusivity	Proton diffusion coefficient	4.5e-5	cm^2/s
Density of membrane	Density of membrane	2,000	kg/m^3
Molecular weight of membrane	Molecular weight of membrane	1.1	Kg/mol SO$_3$
Specific heat of membrane	Specific heat of membrane	852.63	J/kgK
Permeability	Permeability of membrane	1.8e-18	m^2
Initial saturation ratio	Initial saturation ratio	0.02	N/A

Appendix B Diffusion Coefficients

Table B.1

Values for the various gas phase coefficients

Property	Value
Hydrogen/water diffusion coefficient (bar cm^2/s) [122]:	$pD_{H2,H2O} = 0.2470\left(\dfrac{T}{146.55}\right)^{2.334}$
Air/water diffusion coefficient (bar cm^2/s) [122]:	$pD_{air,H2O} = 0.2599\left(\dfrac{T}{299.42}\right)^{2.334}$
Oxygen/water diffusion coefficient (bar cm^2/s) [122]:	$pD_{O2,H2O} = 0.3022\left(\dfrac{T}{323.83}\right)^{2.334}$

Appendix C Derivation of Overall Heat Transfer Coefficient
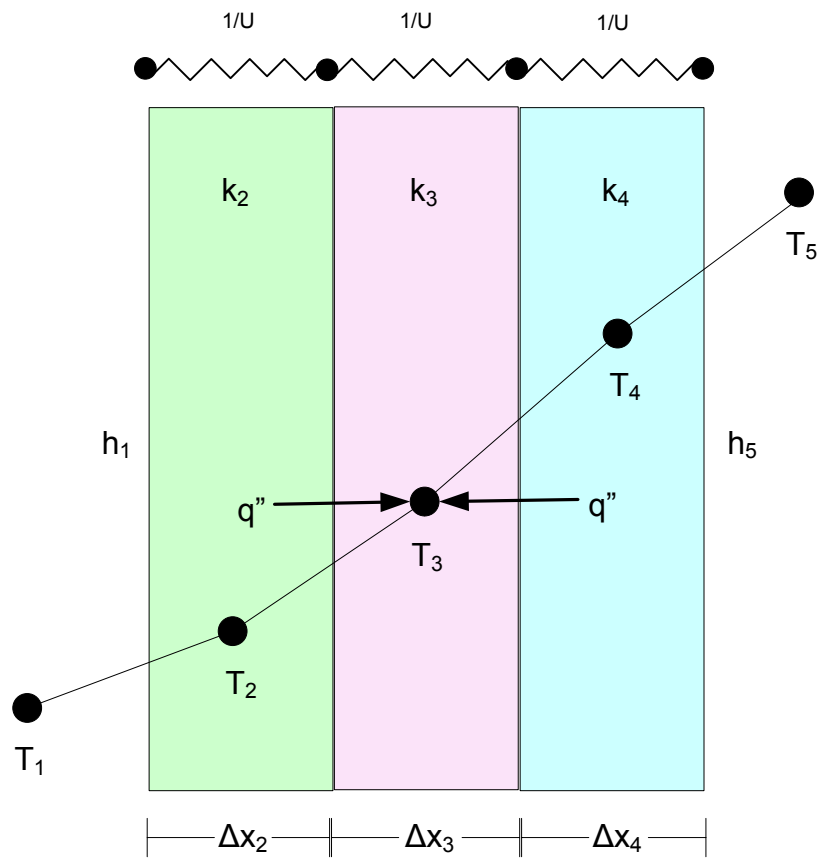
Figure C.1. Schematic for overall heat transfer coefficient derivation

An arbitrary temperature profile, and the thermal resistances for the heat transfer through three nodes is shown in Figure C1. The nodes that define the resistance boundaries have been placed at the center of each section. This method was selected in order to obtain the average temperature in each node. The parameters k and t are the thermal conductivities and layer thickness respectively.

Appendix C (Continued)

Each control volume has conductive heat transfer with each adjacent node in addition to energy storage:

$$\dot{q}_{LHS} + \dot{q}_{RHS} = \frac{dU}{dt}$$

(239)

Each term in Equation 239 must be approximated. The conduction terms from the adjacent nodes are modeled as:

$$q'' = \frac{k_2}{\Delta x_2}(T_{i-1} - T_i)$$

(240)

$$q'' = \frac{k_3}{\Delta x_3}(T_{i+1} - T_i)$$

(241)

Add the heat flux equations together:

$$q'' \frac{\Delta x_2}{k_2} + \frac{\Delta x_3}{k_3} = (T_2 - T_3)$$

(242)

The heat overall heat transfer coefficient is:

$$U = \frac{1}{\dfrac{\Delta x_2}{k_2} + \dfrac{\Delta x_3}{k_3}}$$

(243)

Appendix C (Continued)

For heat transfer on a node from the surroundings and the next node:

$$q'' = \frac{k_2}{\Delta x_2}(T_{i-1} - T_i) \tag{244}$$

$$q'' = h(T_1 - T_i) \tag{245}$$

Add the heat flux equations together:

$$q'' \frac{1}{h} + \frac{\Delta x_2}{k_2} = (T_1 - T_2) \tag{246}$$

The heat overall heat transfer coefficient is:

$$U = \frac{1}{\frac{\Delta x_2}{k_2} + \frac{1}{h}} \tag{247}$$

Appendix D Control Volume Energy Rate Balance

The conservation of energy for a control volume can be introduced by Figure, which shows a system with a fixed quantity of matter, mm that occupies different regions at time t, and a later time $t + \Delta t$. At time, t, the energy of the system can be expressed as:

$$E(t) = E_{cv}(t) + m_i \left(u_i + \frac{V_i^2}{2} + gz_i \right) \qquad (248)$$

where $E_{cv}(t)$ is the sum of the internal, kinetic and gravitational potential energies of the mass contained within the control volume at time t. The specific energy of the mass, m_i, is $u_i + \frac{V_i^2}{2} + gz_i$. In the time interval, Δt, all mass in region i crosses the control volume boundary, and the system at this time can be expressed as:

$$E(t + \Delta t) = E_{cv}(t + \Delta t) + m_e \left(u_e + \frac{V_e^2}{2} + gz_e \right) \qquad (249)$$

At time, t

At time, t + Δt

Region i

$E_{cv}(t)$

Control volume

m_i

$ui + \dfrac{V_i^2}{2} + gz_i$

z_i

Region e

$E_{cv}(t + \Delta t)$

Control volume

m_e

$u_e + \dfrac{V_e^2}{2} + gz_e$

z_e
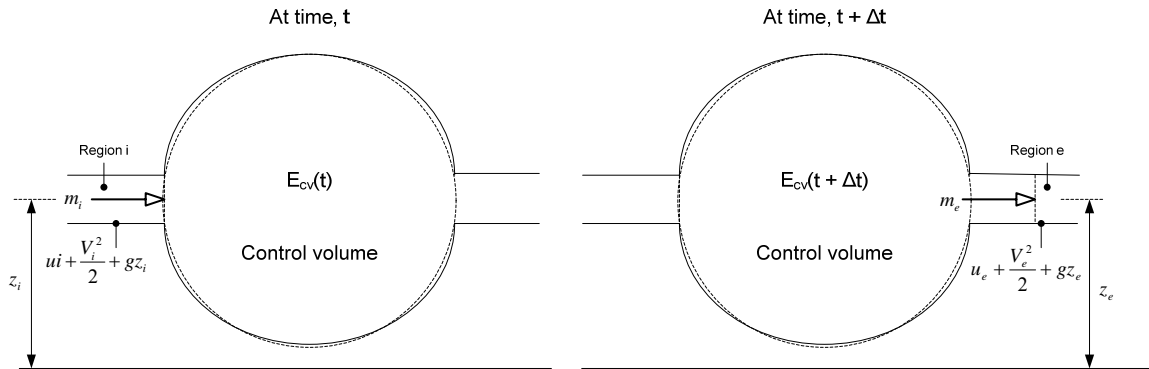
Figure D.1. Illustration of the control volume conservation of energy principle

The mass and energy within the control volume may have changed over the time interval, and the masses m_i and m_e are not necessarily the same. The closed system energy balance can be applied:

$$E(t + \Delta t) - E(t) = Q - W \qquad (250)$$

Introducing and the overall energy balance equation:

$$\left[E_{cv}(t + \Delta t) + m_e \left(u_e + \frac{V_e^2}{2} + gz_e \right) \right] - \left[E_{cv}(t) + m_i \left(u_i + \frac{V_i^2}{2} + gz_i \right) \right] = Q - W \quad (251)$$

Appendix D (Continued)

Rearranging:

$$E_{cv}(t + \Delta t) - E_{cv}(t) = Q - W + m_i \left(u_i + \frac{V_i^2}{2} + gz_i \right) - m_e \left(u_e + \frac{V_e^2}{2} + gz_e \right)$$ (252)

After dividing each term by the time interval, and taking the limit of each term as Δt approaches zero, we obtain:

$$\frac{dE_{cv}}{dt} = \dot{Q} - \dot{W} + m_i \left(u_i + \frac{V_i^2}{2} + gz_i \right) - m_e \left(u_e + \frac{V_e^2}{2} + gz_e \right)$$ (253)

The term $\dfrac{dE_{cv}}{dt}$, represents the total energy associated with the control volume at time, t, and can be written as a volume integral:

$$E_{cv}(t) = \int_v \rho e \, dV = \int_v \rho \left(u + \frac{V^2}{2} + gz \right) dV$$ (254)

The terms accounting for energy transfers accompanying mass flow and flow work at inlets and outlets can be expressed as shown in the following form:

$$\frac{d}{dt} \int_v \rho e \, dV = \dot{Q} - \dot{W} + \sum_i \left[\int_A \left(h_i + \frac{V_i^2}{2} + gz_i \right) \rho V dA \right] - \sum_i \left[\int_A \left(h_e + \frac{V_e^2}{2} + gz_e \right) \rho V dA \right]$$ (255)

Since all of the kinetic and potential energy effects can be ignored, the energy balance can be reduced to:

$$\frac{dU}{dt} = \dot{Q} - \dot{W} + \sum_i m_i h_i - \sum_i m_e h_e \tag{256}$$

The internal energy of the system is the sum of the internal energies of the species in the mixture:

$$U = \sum_i m_i \bar{u}_i(T_i) \tag{257}$$

If the specific heat c, is taken as a constant, then $\bar{u}_i$ can be expressed as:

$$\bar{u}_i = c(T_i - T_{i-1}) \tag{258}$$

The energy balance of a mixture in a control volume can now be written as:

$$\frac{d}{dt}(m_1 c_1 + m_2 c_2 + ... m_i c_i) = \dot{Q} - \dot{W} + \sum_i m_i h_i - \sum_i m_e h_e \tag{259}$$

Appendix E Energy Balances Around Each Node

Energy balances have been defined around each node (control volume). The control volume for the first, last and an arbitrary, internal node is shown in Figure E.1.
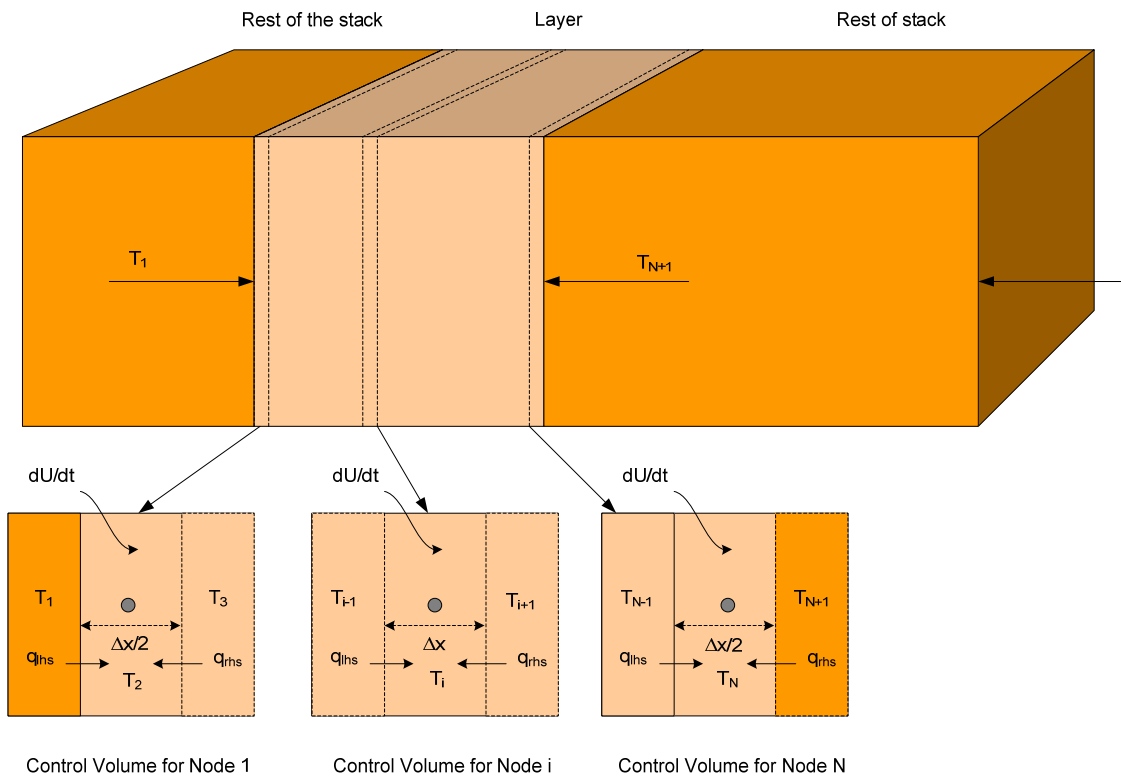
Figure E.1. Schematic of the PEMFC stack and the nodes used for model development

Appendix E (Continued)

Each control volume has conductive heat transfer with each adjacent node in addition to energy storage:

$$\dot{q}_{LHS} + \dot{q}_{RHS} = \frac{dU}{dt}$$

(260)

Each term in Equation 258 must be calculated. The conduction terms from the adjacent nodes are modeled as:

$$\dot{q}_{LHS} = \frac{k\,A\left(T_{i-1} - T_i\right)}{\Delta x}$$

(261)

$$\dot{q}_{RHS} = \frac{k\,A\left(T_{i+1} - T_i\right)}{\Delta x}$$

(262)

where A is the area of the plate. The rate of energy storage is the product of the time rate of change of the nodal temperature and the thermal mass of the control volume:

$$\frac{dU}{dt} = A\,\Delta x\,\rho\,c\,\frac{dT_i}{dt}$$

(263)

Substituting Equations 257 through 260 leads to:

$$A\,\Delta x\,\rho\,c\,\frac{dT_i}{dt} = \frac{k\,A\left(T_{i-1} - T_i\right)}{\Delta x} + \frac{k\,A\left(T_{i-1} - T_i\right)}{\Delta x}$$

(264)

Appendix E (Continued)

Solving for the time rate of the temperature change:

$$\frac{dT_i}{dt} = \frac{k}{\Delta x^2 \rho c}\left(T_{i-1} + T_{i+1} - 2T_i\right) \quad \text{for } i = 2...(N-1)$$

(265)

The control volumes on the edges must be treated separately because they have a smaller volume and experience different energy transfers.

The control volume for the node located at the outer surfaces (node N) provides the energy balance:

$$\frac{dU}{dt} = \dot{q}_{LHS} + \dot{q}_{conv}$$

(266)

or

$$\frac{A\,\Delta x\,\rho c}{2}\frac{dT_N}{dt} = \frac{k\,A\left(T_{N-1} - T_N\right)}{\Delta x} + h\,A\left(T_f - T_N\right)$$

(267)

Solving for the time rate of temperature change for node N:

$$\frac{dT_N}{dt} = \frac{2k}{\rho c\,\Delta x^2}\left(T_{N-1} - T_N\right) + \frac{2h}{\Delta x\,\rho c}\left(T_f - T_N\right)$$

(268)

281

Note that the equations provide the time rate of change for the temperature of every node given the temperatures of the nodes. The energy balance for each control volume provides an equation for the time rate of change of the temperature in terms of the temperature. Therefore, the energy balance written for each control volume has a set of equations for the time rate of change.

The temperature of each node is a function both of position (x) and time (t). The index that specifies the node's position is i where i = 1 corresponds to the adiabatic plate and i = N corresponds to the surface of the plate. A second index, j, is added to each nodal temperature in order to indicate the time (Ti,j); j = 1 corresponds to the beginning of the simulation and j = M corresponds to the end of the simulation. The total simulation time is divided into M time steps; most of the techniques discussed here will divide the simulation time into time steps of equal duration, Δt:

$$\Delta t = \frac{\tau_{sim}}{(M-1)}$$

(269)

The time associated with any time step is:

$$t_j = (j-1)\Delta t \quad \text{for } j = 1...M$$

(270)

Appendix F   Derivation of Mass Transport in the Flow Channels and Through the Porous Media [4]

Mass transport in the fuel cell flow structures is dominated by convection and the laws of fluid dynamics since the flow channels are macroscale (usually in millimeters or centimeters). The mass transport of the fuel cell electrodes occur on a microscale and are dominated by diffusion.

Convection is stirring or hydrodynamic transport. Fluid flow generally occurs because of natural convection, which is the movement of the fluid due to density gradients. Forced convection is characterized by laminar or turbulent flow and stagnant regions. The convective forces that dominate mass transfer in the flow channels are imposed by the fuel, while the oxidant flow rates are imposed by the user. High flow rates can ensure a good distribution of reactants, but may cause other problems in the fuel cell stack, such as high pressures, fuel cell membrane rupture, and many others.

The diffusive forces that occur in the electrode/catalyst layer are shielded from the convective forces in the flow channels. The velocity of the reactants tends to slow down near the gas diffusion/catalyst layers where the diffusion regime of the reactants begins. Figure F1 illustrates convective flow in the reactant flow channel and diffusive flow through the gas diffusion and catalyst layers.
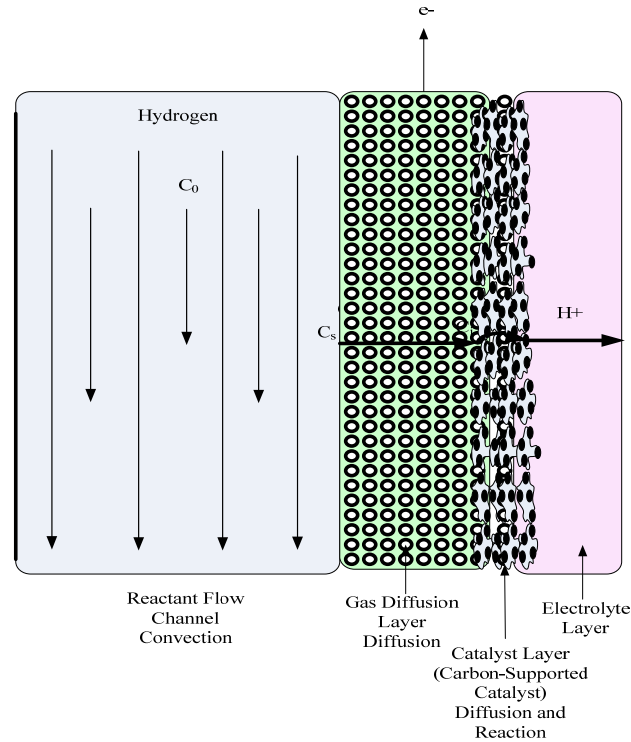
Figure F.1. Fuel cell layers (flow field, gas diffusion layer, catalyst layer) that have

convective and diffusive mass transport

F.1. Convective Mass Transport From Flow Channels to Electrode

As shown in Figure F.1, the reactant is supplied to the flow channel at a

concentration C_0, and it is transported from the flow channel to the concentration at the

electrode surface C_s through convection. The rate of mass transfer is then:

$$\dot{m} = A_{elec}h_m(C_0 - C_s) \tag{271}$$

where A_{elec} is the electrode surface area, and h_m is the mass transfer coefficient.

Appendix F (Continued)

The value of h_m is dependent upon the channel geometry, the physical properties of species i and j, and the wall conditions. H_m can be found from the Sherwood number:

$$h_m = Sh \frac{D_{i,j}}{D_h} \tag{272}$$

Sh is the Sherwood number, D_h is the hydraulic diameter, and D_{ij} is the binary diffusion coefficient for species i and j. The Sherwood number depends upon channel geometry, and can be expressed as:

$$Sh \equiv \frac{h_H D_h}{k} \tag{273}$$

where Sh = 5.39 for uniform surface mass flux ($\dot{m}$ = constant)., and Sh = 4.86 for uniform surface concentration (C_s = constant).

F.2 Diffusive Mass Transport in Fuel Cell Electrodes

As shown in Figure F.1, the diffusive flow occurs at the electrode backing and catalyst layer, where the mass transfer occurs at the micro level. The electrochemical reaction in the catalyst layer can lead to reactant depletion, which can affect fuel cell performance through losses due to reactant depletion (as predicted by the Nernst equation) and activation losses. To determine the size of the concentration loss, the amount the catalyst layer reactant and product concentrations differ from the bulk values needs to be found.

Appendix F (Continued)

The rate of mass transfer by diffusion of the reactants to the catalyst layer ($\dot{m}$) can be calculated as shown in equation 274:

$$\dot{m} = -D\frac{dC}{dx} \tag{274}$$

where D is the bulk diffusion coefficient and C is the concentration of reactants. Using Fick's law, the diffusional transport through the electrode backing layer at steady-state is:

$$\dot{m} = A_{elec} D^{eff} \frac{C_s - C_i}{\delta} \tag{275}$$

where C_i is the reactant concentration at the backing layer/catalyst interface, and δ is the electrode-backing layer thickness, and D^{eff} is the effective diffusion coefficient for the porous electrode backing layer, which is dependent upon the bulk diffusion coefficient D, and the pore structure. Assuming uniform pore size the backing layer is free from flooding of water or liquid electrolyte, D^{eff} can be defined as:

$$D^{eff} = D\phi^{3/2} \tag{276}$$

where ϕ is the electrode porosity. The total resistance to the transport of the reactant to the reaction sites can be expressed by combining Equations 275 and 276:

$$\dot{m} = \frac{C_0 - C_i}{\left(\dfrac{1}{h_m A_{elec}} + \dfrac{\delta}{D^{eff} A_{elec}}\right)} \tag{277}$$

where $\dfrac{1}{h_m A_{elec}}$ is the resistance to the convective mass transfer, and $\dfrac{L}{D^{eff} A_{elec}}$ is the resistance to the diffusional mass transfer through the electrode backing layer.

Appendix F (Continued)

When the fuel cell is turned on, it begins producing electricity at a fixed current density i. The reactant and product concentrations in the fuel cell are constant. As soon as the fuel cell begins producing current, the electrochemical reaction leads to the depletion of reactants at the catalyst layer. The flux of reactants and products will match the consumption/depletion rate of reactants and products at the catalyst layer as described by the following equation:

$$i = \frac{nF\dot{m}}{A_{elec}} \tag{278}$$

where i is the fuel cell's operating current density, F is the Faraday constant, n is the number of electrons transferred per mol of reactant consumed, and $\dot{m}$ is the rate of mass transfer by diffusion of reactants to the catalyst layer. Substituting Equation 277 into 278 yields:

$$i = -nF \frac{C_0 - C_i}{\left(\frac{1}{h_m} + \frac{\delta}{D^{eff}}\right)} \tag{279}$$

The reactant concentration in the backing layer/catalyst interface is less than the reactant concentration supplied to the flow channels, which depends upon i, δ, and D^{eff}. The higher the current density, the worse the concentration losses will be. These concentration losses can be improved if the diffusion layer thickness is reduced, or the effective diffusivity is increased.

The limiting current density of the fuel cell is the point where the current density becomes so large the reactant concentration falls to zero. The limiting current density (i_L)

of the fuel cell can be calculated if the minimum concentration at the backing catalyst

layer interface is $C_i = 0$ as follows:

$$i_L = -nF \frac{C_0}{\left(\dfrac{1}{h_m} + \dfrac{\delta}{D^{eff}} \right)} \tag{280}$$

When designing a fuel cell, the limiting current density can be increased by

ensuring that C_0, is high, which is accomplished by designing good flow structures to

evenly distribute the reactants, and ensuring that D^{eff} is large and δ is small by optimizing

fuel cell operating conditions (such as temperature, pressure), electrode structure and

flooding, and diffusion layer thickness.

The typical limiting current density is 1 to 10 A/cm^2. The fuel cell will not be able

to produce a higher current density than its limiting current density. However, other types

of losses may limit the fuel cell voltage to zero before the limiting current density does.

F.3 Convective Mass Transport in Flow Structures

Fuel cell flow structures are designed to distribute reactants across a fuel cell. The

typical fuel cell has a series of small flow fields to evenly distribute reactants, and to keep

mass transport losses to a minimum. The next couple of sections demonstrate the

derivations for the mass transport in the flow channels.

Appendix F (Continued)

F.3.1 Mass Transport in Flow Channels

The mass transport in flow channels can be modeled using a control volume for reactant flow from the flow channel to the electrode layer as shown in Figure F.2.
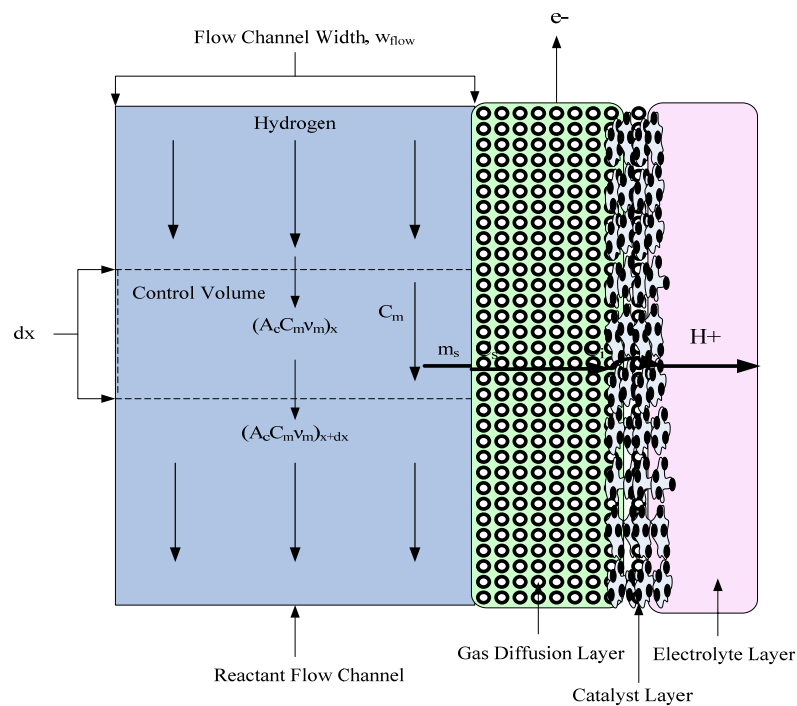
Figure F.2. Control volume for reactant flow from the flow channel to the electrode layer

The rate of convective mass transfer at the electrode surface ($\dot{m}_s$) can be expressed as:

$$\dot{m}_s = h_m (C_m - C_s) \tag{281}$$

where C_m is the mean concentration of the reactant in the flow channel (averaged over the channel cross-section, and decreases along the flow direction, x), and C_s is the concentration at the electrode surface.

As shown in Figure F.2, the reactant moves at the molar flow rate, $A_c C_m v_m$ at the position x, where A_c is the channel cross-sectional area and v_m is the mean flow velocity in the flow channel. This can be expressed as:

$$\frac{d}{dx}\left(A_c C_m v_m\right) = -\dot{m}_s w_{elec} \tag{282}$$

where w_{elec} is the width of the electrode surface. If the flow in the channel is assumed to be steady, then the velocity is constant, and the concentration is constant, then:

$$\frac{d}{dx} C_m = \frac{-\dot{m}_s}{v_m w_{flow}} \tag{283}$$

The current density is small ($i < 0.5\ i_L$), it can be assumed constant. Using Faraday's law, $\dot{m}_s = \dfrac{i}{nF}$ and integrating:

$$C_m(x) = C_{m,in}(x) - \frac{\left(\dfrac{i}{nF}\right)}{v_m w_{flow}} x \tag{284}$$

where $C_{m,in}$ is the mean concentration at the flow channel inlet.

If the current density is large ($i > 0.5\ i_L$), the condition at the electrode surface can be approximated by assuming the concentration at the surface (C_s) is constant. This can be written as follows:

$$\frac{d}{dx}\left(C_m - C_s\right) = \frac{-h_m}{v_m w_{flow}}\left(C_m - C_s\right) \tag{285}$$

After integrating from the channel inlet to location x in the flow channel, equation becomes:

$$\frac{C_m - C_s}{\left(C_m - C_s\right)_{in}} = \exp\frac{-h_m x}{v_m w_{flow}} \tag{286}$$

At the channel outlet, x = H, and equation becomes:

$$\frac{C_{m,out} - C_s}{C_{m,in} - C_s} = \exp\frac{-h_m H}{v_m w_{flow}} \tag{287}$$

where $C_{m,out}$ is the mean concentration at the flow channel outlet.

A simple expression can be derived if the entire flow channel is assumed to be the control volume as shown in Figure F.3:

$$\begin{aligned}
\dot{m}_s &= v_m w_{flow} w_{elec}\left(C_{in} - C_{out}\right) \\
\dot{m}_s &= v_m w_{flow} w_{elec}\left(\Delta C_{in} - \Delta C_{out}\right)
\end{aligned} \tag{288}$$
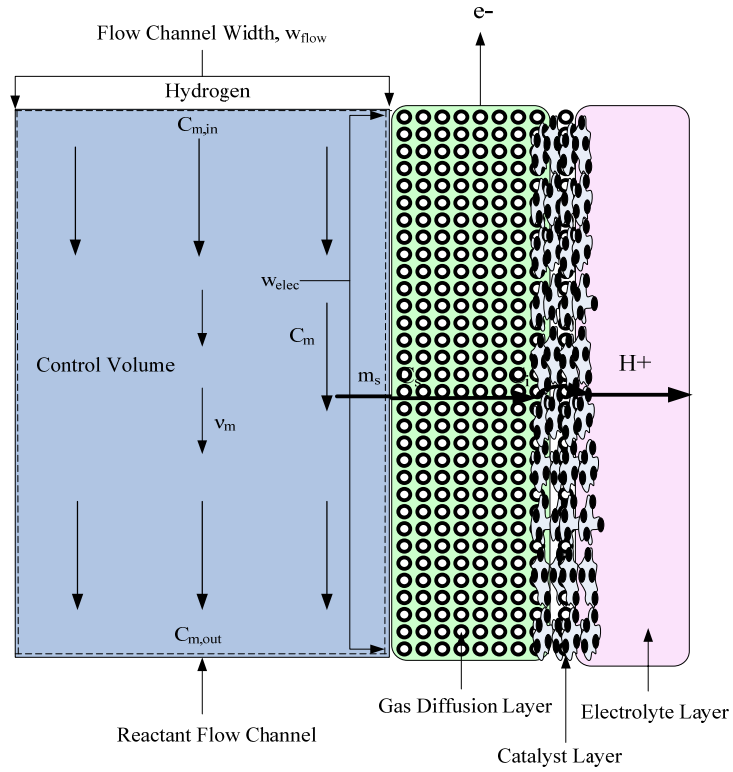
Figure F.3. Entire channel as the control volume for reactant flow from the flow channel to the electrode layer

If C_s is constant, substituting for $w_{flow} w_{elec}$:

$$\dot{m}_s = A h_m \Delta C_{lm} \tag{289}$$

where

$$\Delta C_{lm} = \frac{\Delta C_{in} - \Delta C_{out}}{\ln\left(\dfrac{\Delta C_{in}}{\Delta C_{out}}\right)} \tag{290}$$

The local current density corresponding to the rate of mass transfer is:

$$i(x) = nFh_m\left(C_m - C_s\right)\exp\left(\frac{-h_m x}{v_m w_{flow}}\right) \tag{291}$$

The current density averaged over the electrode surface is:

$$\bar{i} = nFh_m \Delta C_{lm} \tag{292}$$

The limiting current density when C_s approaches 0 is:

$$i_L(x) = nFh_m C_{m,in} \exp\left(\frac{-h_m x}{v_m w_{flow}}\right) \tag{293}$$

$$\bar{i}_L = nFh_m \left[\frac{\Delta C_{in} - \Delta C_{out}}{\ln\left(\dfrac{\Delta C_{in}}{\Delta C_{out}}\right)}\right] \tag{294}$$

Both the current density and limiting current density decrease exponentially along the channel length.

Appendix G Heat Transfer Model

Table G.1

Heat transfer equations for the end plate, manifold and gasket layers

Main Parameters	Equations
Inputs: ρ density (kg/m^3) $A_{i,s}$ solid area of layer (m^2) A_{void} void area of layer (m^2) Δx thickness of the node (m) cp specific heat (J/Kg-K) x mole fraction n_{tot} total molar flow rate of mixture (mol/s) T_i temperature of the node (K) k thermal conductivity of node i (W/m-K) h_{surr} convective loss from the stack to the air *Calculated:* $c_{p,mix}$ specific heat of mixture (J/Kg-K) U_{surr} overall heat transfer coefficient for the surroundings U_{i-1} overall heat transfer coefficient for the left node $\dot{q}_{surr}$ heat flow from the surroundings $\dot{q}_{i-1}$ heat flow from the left node H_i enthalpy of component i	$(c_{p,mix}n_{tot} + \rho A_{i,s}\Delta x\ cp)\dfrac{dT_i}{dt} = \dot{q}_{i-1} + \dot{q}_{i+1} +$ $H_{H2,i} + H_{H2Ov,i} + H_{H2Ol,i} -$ $H_{H2,i+1} - H_{H2Ov,i+1} - H_{H2Ol,i+1} -$ $H_{H2\_out} - H_{H2Ov\_out} - H_{H2Ol\_out}$ Specific heat of mixture: $$c_{p,mix} = x_i c_{p,i} + x_j c_{p,j}$$ Heat flow from surroundings: $$\dot{q}_{surr} = U_{surr}A_{i,s}(T_{surr} - T_i)$$ $$U_{surr} = \dfrac{1}{\dfrac{\Delta x_i}{k_i} + \dfrac{1}{h_{surr}}}$$ Heat flow from left node: $$\dot{q}_{i-1} = U_{i-1}(T_{i-1} - T_i)$$ $$U_{i-1} = \dfrac{1}{\dfrac{\Delta x_i}{k_i A_{i,s}} + \dfrac{\Delta x_{i-1}}{k_{i-1}A_{i-1,s}}}$$

Appendix G (Continued)

Table G.1 *(continued)*

Main Parameters	Equations
Inputs: ρ density of the layer (kg/m³) $A_{i,s}$ solid area of layer (m²) A_{void} void area of layer (m²) Δx thickness of the node (m) cp specific heat of layer (J/Kg-K) T_i temperature of the node (K) k thermal conductivity of node I (W/m-K) h_{surr} convective loss from the stack to the air w_{chan} channel width (m) L_{chan} channel length (m) *Calculated:* $U_{i,f}$ overall heat transfer coefficient from the fluid U_{i+1} overall heat transfer coefficient for the right node $\dot{q}_{i+1}$ heat flow from the right node $\dot{q}_{i,f}$ heat flow from the gases/fluids	Heat flow from right node: $$\dot{q}_{i+1} = U_{i+1}(T_{i+1} - T_i)$$ $$U_{i+1} = \frac{1}{\dfrac{\Delta x_{i+1}}{k_{i+1}A_{i+1,s}} + \dfrac{\Delta x_i}{k_i A_{i,s}}}$$ Heat flow from fluid/gases to solid $$\dot{q}_{i,f} = U_{i,f}(T_i - T_{i,f})$$ $$U_{i,f} = \frac{1}{\dfrac{\Delta x_i}{k_i A_{i,s}} + \dfrac{1}{h_f A_{void}}}$$ Area of solid portion of the layer: $$A_{i,s} = A - A_{void}$$ Channel area: $$A_{void} = w_{chan} \times L_{chan}$$

Appendix G (Continued)

Table G.2

Gas temperature calculations for the end plate, manifold and gasket layers

Main Parameters	Equations
Inputs: $c_{p,mix}$ specific heat of mixture (J/Kg-K) n_{tot} total molar flow rate of mixture (mol/s) $A_{i,s}$ solid area of layer (m^2) A_{void} void area of layer (m^2) k thermal conductivity of node I (W/m-K) Δx thickness of the node (m) *Calculated:* U_{i-1} overall heat transfer coefficient for the left node U_{i+1} overall heat transfer coefficient for the right node $\dot{q}_{i-1}$ heat flow from the left node $\dot{q}_{i+1}$ heat flow from the right node $\dot{q}_{i,s}$ heat flow from the solid portion of the layer $T_{i,f}$ temperature of gas/fluid mixture H_i enthalpy of component i	$(c_{p,mix}n_{tot})\dfrac{dT_{i,f}}{dt} = \dot{q}_{i-1} + \dot{q}_{i+1} + \dot{q}_{i,s}$ $H_{H2,i} + H_{H2Ov,i} + H_{H2Ol,i} -$ $H_{H2,i+1} - H_{H2Ov,i+1} - H_{H2Ol,i+1} -$ $H_{H2\_out} - H_{H2Ov\_out} - H_{H2Ol\_out}$ Specific heat of mixture: $c_{p,mix} = x_i c_{p,i} + x_j c_{p,j}$ Heat flow from left node: $\dot{q}_{i-1} = U_{i-1}(T_{i-1} - T_i)$ $U_{i-1} = \dfrac{1}{\dfrac{\Delta x_i}{k_i A_{i,s}} + \dfrac{\Delta x_{i-1}}{k_{i-1} A_{i-1,s}}}$ Heat flow from right node: $\dot{q}_{i+1} = U_{i+1}(T_{i+1} - T_i)$ $U_{i+1} = \dfrac{1}{\dfrac{\Delta x_{i+1}}{k_{i+1} A_{i+1,s}} + \dfrac{\Delta x_i}{k_i A_{i,s}}}$

Appendix G (Continued)

Table G.2 *(continued)*

Main Parameters	Equations
Inputs: $c_{p,mix}$ specific heat of mixture (J/Kg-K) n_{tot} total molar flow rate of mixture (mol/s) w_{chan} channel width (m) L_{chan} channel length (m) n_i molar flow rate of component i (mol/s) *Calculated:* $U_{i,s}$ overall heat transfer coefficient from solid to gases/fluid $\dot{q}_{i,s}$ heat flow from the solid portion of the layer $A_{i,s}$ solid area of layer (m²) A_{void} void area of layer (m²) H_i enthalpy of component i T_i temperature of the node (K)	Heat flow from solid to fluid/gases: $$\dot{q}_{i,s} = U_{i,s}(T_{i,s} - T_i)$$ $$U_{i,s} = \frac{1}{\dfrac{\Delta x_i}{k_i A_{i,s}} + \dfrac{1}{h_f A_{void}}}$$ Enthalpies of each gas/liquid flow: $$H_i = n_i h_i T_i$$ Area of solid portion of the layer: $$A_{i,s} = A - A_{void}$$ Channel area: $$A_{void} = w_{chan} \times L_{chan}$$

Appendix G (Continued)

Table G.3

Heat transfer coefficient for the end plate, manifold and gasket layers

Main Parameters	Equations
Inputs:	Calculate Reynold's number:
v_m is the characteristic velocity of the flow (m/s)	$$\mathrm{Re}_i = \frac{\rho v_m D_h}{\mu} = \frac{v_m D_h}{v}$$
ρ is the fluid density (kg/m^3)	
μ is the fluid viscosity (kg/(m*s))	
P_{cs} is the perimeter	Hydraulic diameter for a circular flow field:
d_c channel depth (m)	
w_c channel width (m)	$$D_{h,i} = \frac{4 \times A_{ch}}{P_{cs}}$$
A_{ch} cross-sectional area of the channel (m^2)	
Pr is the Prandtl number	Hydraulic diameter for a rectangular flow field:
L length of channel at node i (m)	
	$$D_{h,i} = \frac{2 w_c d_c}{w_c + d_c}$$
Calculated:	
D_h is the hydraulic diameter (m)	
Nu Nusselt number	Nusselt number:
Re$_i$ Reynold's number at node i	
f friction factor	$$Nu = \frac{(f/8)(\mathrm{Re}-1000)\,\mathrm{Pr}}{1+12.7\sqrt{(f/8)}(\mathrm{Pr}^{2/3}-1)}\left(1+\left(\frac{D_h}{L}\right)^{2/3}\right)$$
h convective heat transfer coefficient	
	The friction factor can be defined by:
	$$f = \frac{1}{0.79\ln(\mathrm{Re})-1.64}$$
	The convective heat transfer coefficient is:
	$$h = \frac{Nu \cdot k}{D_h}$$

Appendix G (Continued)

Table G.4

Heat transfer calculations for the flow field plate layers

Main Parameters	Equations
Inputs: ρ density (kg/m³) $A_{i,s}$ solid area of layer (m²) A_{void} void area of layer (m²) Δx thickness of the node (m) cp specific heat of layer (J/Kg-K) T_i temperature of the node (K) k thermal conductivity of node i (W/m-K) n_{tot} total molar flow rate of mixture (mol/s) *Calculated:* $U_{i-1,f}$ overall heat transfer coefficient for the gases/fluids in the left node U_{i-1} overall heat transfer coefficient for the left node U_{i+1} overall heat transfer coefficient for the right node $\dot{q}_{i-1,f}$ heat flow from fluid/gases in left node $\dot{q}_{i-1}$ heat flow from the left node $\dot{q}_{i+1}$ heat flow from the right node $\dot{q}_{i,f}$ heat flow from the gases/fluids $c_{p,mix}$ specific heat of mixture (J/Kg-K) H_i enthalpy of component i T_i temperature of the node (K)	$(c_{p,mix}n_{tot} + \rho A_{i,s}\Delta x\ cp)\dfrac{dT_i}{dt} = \dot{q}_{i-1} + \dot{q}_{i+1} + \dot{q}_{i-1,f} +$ $\dot{q}_{i+1,f} + \dot{q}_{i,f} + \dot{q}_{res,i} + H_{H2,i} + H_{H2Ov,i} + H_{H2Ol,i} -$ $H_{H2,i+1} - H_{H2Ov,i+1} - H_{H2Ol,i+1} -$ $H_{H2\_out} - H_{H2Ov\_out} - H_{H2Ol\_out}$ Heat flow from left node: $\dot{q}_{i-1} = U_{i-1}(T_{i-1} - T_i)$ $U_{i-1} = \dfrac{1}{\dfrac{\Delta x_i}{k_i A_{i,s}} + \dfrac{\Delta x_{i-1}}{k_{i-1}A_{i-1,s}}}$ Heat flow from fluid/gases in left node: $\dot{q}_{i-1,f} = U_{i-1,f}(T_{i-1} - T_i)$ $U_{i-1,f} = \dfrac{1}{\dfrac{\Delta x_i}{k_i A_{i,s}} + \dfrac{1}{h_{i-1,f}A_{i-1,void}}}$ Heat flow from right node: $\dot{q}_{i+1} = U_{i+1}(T_{i+1} - T_i)$ $U_{i+1} = \dfrac{1}{\dfrac{\Delta x_{i+1}}{k_{i+1}A_{i+1,s}} + \dfrac{\Delta x_i}{k_i A_{i,s}}}$

Table G.4 *(continued)*

Main Parameters	Equations

Inputs:

ρ density of the layer (kg/m^3)

$A_{i,s}$ solid area of layer (m^2)

A_{void} void area of layer (m^2)

Δx thickness of the node (m)

cp specific heat of layer (J/Kg-K)

T_i temperature of the node (K)

k thermal conductivity of node I (W/m-K)

w_{chan} channel width (m)

L_{chan} channel length (m)

$\rho_{res,i}$ resistivity of solid portion of node i

i current density (A/m^2)

Calculated:

$U_{i+1,f}$ overall heat transfer coefficient for fluid/gases in right node

U_{i+1} overall heat transfer coefficient for the right node

$U_{i,f}$ overall heat transfer coefficient for fluid/gases to solid

$\dot{q}_{i+1,f}$ heat flow from fluid/gases in right node

$\dot{q}_{i+1}$ heat flow from the right node

$\dot{q}_{i,f}$ heat flow from the gases/fluids

$\dot{q}_{res,i}$ heat flow due to ohmic heating

Heat flow from fluid/gases in right node:

$$\dot{q}_{i+1,f} = U_{i+1,f}(T_{i+1,f} - T_i)$$

$$U_{i+1,f} = \cfrac{1}{\cfrac{1}{h_{i+1,f} A_{i+1,void}} + \cfrac{\Delta x_i}{k_i A_{i,s}}}$$

Heat flow from fluid/gases to solid

$$\dot{q}_{i,f} = U_{i,f}(T_i - T_{i,f})$$

$$U_{i,f} = \cfrac{1}{\cfrac{\Delta x_i}{k_i A_{i,s}} + \cfrac{1}{h_{i,f} A_{void}}}$$

Area of solid portion of the layer:

$$A_{i,s} = A - A_{void}$$

Channel area:

$$A_{void} = w_{chan} \times L_{chan}$$

Ohmic heating:

$$\dot{q}_{res,i} = i^2 \left(\frac{\rho_{res,i} \Delta x_i}{A_i} \right)$$

Appendix G (Continued)

Table G.5

Gas temperature calculations for the flow field plate layers

Main Parameters	Equations
Inputs: $c_{p,mix}$ specific heat of mixture (J/Kg-K) n_{tot} total molar flow rate of mixture (mol/s) $A_{i,s}$ solid area of layer (m²) A_{void} void area of layer (m²) k thermal conductivity of node I (W/m-K) Δx thickness of the node (m)	$(c_{p,mix}n_{tot})\dfrac{dT_i}{dt} = \dot{q}_{i-1} + \dot{q}_{i+1} + \dot{q}_{i-1,f} + \dot{q}_{i+1,f} +$ $\dot{q}_{i,f} + H_{H2,i} + H_{H2Ov,i} + H_{H2Ol,i} -$ $H_{H2,i+1} - H_{H2Ov,i+1} - H_{H2Ol,i+1} -$ $H_{H2\_out} - H_{H2Ov\_out} - H_{H2Ol\_out}$ Specific heat of mixture: $c_{p,mix} = x_i c_{p,i} + x_j c_{p,j}$
Calculated: U_{i-1} overall heat transfer coefficient for the left node U_{i+1} overall heat transfer coefficient for the right node $U_{i-1,f}$ overall heat transfer coefficient for the gases/fluids in the left node $\dot{q}_{i-1}$ heat flow from the left node $\dot{q}_{i+1}$ heat flow from the right node $\dot{q}_{i,s}$ heat flow from the solid portion of the layer $\dot{q}_{i-1,f}$ heat flow from fluid/gases in left node $T_{i,f}$ temperature of gas/fluid mixture H_i enthalpy of component i	Heat flow from left node: $\dot{q}_{i-1} = U_{i-1}(T_{i-1} - T_i)$ $U_{i-1} = \dfrac{1}{\dfrac{\Delta x_i}{k_i A_{i,s}} + \dfrac{\Delta x_{i-1}}{k_{i-1} A_{i-1,s}}}$ Heat flow from fluid/gases in left node: $\dot{q}_{i-1,f} = U_{i-1,f}(T_{i-1} - T_i)$ $U_{i-1,f} = \dfrac{1}{\dfrac{\Delta x_i}{k_i A_{i,s}} + \dfrac{1}{h_{i-1,f} A_{i-1,void}}}$

Table G.5 *(continued)*

Main Parameters	Equations
Inputs: $A_{i,s}$ solid area of layer (m²) A_{void} void area of layer (m²) k thermal conductivity of node I (W/m-K) Δx thickness of the node (m) *Calculated:* U_{i+1} overall heat transfer coefficient for the right node $U_{i+1,f}$ overall heat transfer coefficient from fluid/gases $\dot{q}_{i+1,f}$ heat flow from fluid/gases in right node $\dot{q}_{i+1}$ heat flow from the right node $\dot{q}_{i,s}$ heat flow from the solid portion of the layer $T_{i,f}$ temperature of gas/fluid mixture	Heat flow from right node: $$\dot{q}_{i+1} = U_{i+1}(T_{i+1} - T_i)$$ $$U_{i+1} = \cfrac{1}{\cfrac{\Delta x_{i+1}}{k_{i+1} A_{i+1,s}} + \cfrac{\Delta x_i}{k_i A_{i,s}}}$$ Heat flow from fluid/gases in right node: $$\dot{q}_{i+1,f} = U_{i+1,f}(T_{i+1,f} - T_i)$$ $$U_{i+1,f} = \cfrac{1}{\cfrac{1}{h_{i+1,f} A_{i+1,void}} + \cfrac{\Delta x_i}{k_i A_{i,s}}}$$ Heat flow from solid to fluid/gases: $$\dot{q}_{i,s} = U_{i,s}(T_{i,s} - T_i)$$ $$U_{i,s} = \cfrac{1}{\cfrac{\Delta x_i}{k_i A_{i,s}} + \cfrac{1}{h_f A_{void}}}$$

Appendix G (Continued)

Table G.5 *(continued)*

Main Parameters	Equations
Inputs: w_{chan} channel width (m) L_{chan} channel length (m) *Calculated:* $T_{i,f}$ temperature of gas/fluid mixture H_i enthalpy of component i $A_{i,s}$ solid area of layer (m^2) A_{void} void area of layer (m^2)	Enthalpies of each gas/liquid flow: $$H_i = n_i h_i T_{i,f}$$ Area of solid portion of the layer: $$A_{i,s} = A - A_{void}$$ Channel area: $$A_{void} = w_{chan} \times L_{chan}$$

Table G.6

Heat transfer coefficient for the flow field plate layers

Main Parameters	Equations
Inputs:	Calculate Reynold's number:

Inputs:

v_m is the characteristic velocity of the flow (m/s)

ρ is the fluid density (kg/m³)

μ is the fluid viscosity (kg/(m*s))

P_{cs} is the perimeter

d_c channel depth (m)

w_c channel width (m)

A_{ch} cross-sectional area of the channel (m²)

Pr is the Prandtl number

L length of channel at node i (m)

Calculated:

D_h is the hydraulic diameter (m)

Nu Nusselt number

Re_i Reynold's number at node i

f friction factor

h convective heat transfer coefficient

Calculate Reynold's number:

$$Re_i = \frac{\rho v_m D_h}{\mu} = \frac{v_m D_h}{v}$$

Hydraulic diameter for a circular flow field:

$$D_{h,i} = \frac{4 \times A_{ch}}{P_{cs}}$$

Hydraulic diameter for a rectangular flow field:

$$D_{h,i} = \frac{2 w_c d_c}{w_c + d_c}$$

Nusselt number:

$$Nu = \frac{(f/8)(Re-1000)\,Pr}{1+12.7\sqrt{(f/8)}(Pr^{2/3}-1)}\left(1+\left(\frac{D_h}{L}\right)^{2/3}\right)$$

The friction factor can be defined by:

$$f = \frac{1}{0.79\ln(Re)-1.64}$$

The convective heat transfer coefficient is:

$$h = \frac{Nu \cdot k}{D_h}$$

Appendix G (Continued)

Table G.7

Heat transfer equations for the gas diffusion layers

Main Parameters	Equations
Inputs:	$$(c_{p,mix}n_{tot} + \rho A \Delta x \; cp)\frac{dT_i}{dt} = \dot{q}_{i-1} + \dot{q}_{i-1,f} + \dot{q}_{i+1} + \dot{q}_{res,i} + \dot{\imath}$$

Inputs:
ρ density of the layer (kg/m^3)
$A_{i,s}$ solid area of layer (m^2)
A_{void} void area of layer (m^2)
Δx thickness of the node (m)
cp specific heat of layer (J/Kg-K)
T_i temperature of the node (K)
k thermal conductivity of node i (W/m-K)

Calculated:
U_{i-1} overall heat transfer coefficient for the left node
U_{i+1} overall heat transfer coefficient for the right node
$U_{i-1,f}$ overall heat transfer coefficient for the gases/fluids in the left node
$\dot{q}_{i-1}$ heat flow from the left node
$\dot{q}_{i+1}$ heat flow from the right node
$\dot{q}_{i,s}$ heat flow from the solid portion of the layer
$\dot{q}_{i-1,f}$ heat flow from fluid/gases in left node
H_i enthalpy of component i
T_i temperature of the node (K)

$$(c_{p,mix}n_{tot} + \rho A \Delta x \; cp)\frac{dT_i}{dt} = \dot{q}_{i-1} + \dot{q}_{i-1,f} + \dot{q}_{i+1} + \dot{q}_{res,i} + \dot{\imath}$$

$$H_{H2Ov,i} + H_{H2Ol,i} - H_{H2,i+1} - H_{H2Ov,i+1} - H_{H2Ol,i+1}$$

Heat flow from left node:

$$\dot{q}_{i-1} = U_{i-1}(T_{i-1} - T_i)$$

$$U_{i-1} = \frac{1}{\dfrac{\Delta x_i}{k_i A_{i,s}} + \dfrac{\Delta x_{i-1}}{k_{i-1} A_{i-1,s}}}$$

Heat flow from fluid/gases in left node:

$$\dot{q}_{i-1,f} = U_{i-1,f}(T_{i-1} - T_i)$$

$$U_{i-1,f} = \frac{1}{\dfrac{\Delta x_i}{k_i A_{i,s}} + \dfrac{1}{h_{i-1,f} A_{i-1,void}}}$$

Heat flow from right node:

$$\dot{q}_{i+1} = U_{i+1}(T_{i+1} - T_i)$$

$$U_{i+1} = \frac{1}{\dfrac{\Delta x_{i+1}}{k_{i+1} A_{i+1,s}} + \dfrac{\Delta x_i}{k_i A_{i,s}}}$$

305

Table G.7 *(continued)*

Main Parameters	Equations
Inputs: ρ density of the layer (kg/m^3) $A_{i,s}$ solid area of layer (m^2) A_{void} void area of layer (m^2) Δx thickness of the node (m) cp specific heat of layer (J/Kg-K) T_i temperature of the node (K) k thermal conductivity of node I (W/m-K) w_{chan} channel width (m) L_{chan} channel length (m) $\rho_{res,i}$ resistivity of solid portion of node i i current density (A/m^2) *Calculated:* $U_{i+1,f}$ overall heat transfer coefficient for fluid/gases in right node U_{i+1} overall heat transfer coefficient for the right node $U_{i,f}$ overall heat transfer coefficient for fluid/gases to solid $\dot{q}_{i+1,f}$ heat flow from fluid/gases in right node $\dot{q}_{i+1}$ heat flow from the right node $\dot{q}_{i,f}$ heat flow from the gases/fluids $\dot{q}_{res,i}$ heat flow due to ohmic heating	Heat flow from fluid/gases in right node: $$\dot{q}_{i+1,f} = U_{i+1,f}(T_{i+1,f} - T_i)$$ $$U_{i+1,f} = \cfrac{1}{\cfrac{1}{h_{i+1,f}A_{i+1,void}} + \cfrac{\Delta x_i}{k_i A_{i,s}}}$$ Heat flow from fluid/gases to solid $$\dot{q}_{i,f} = U_{i,f}(T_i - T_{i,f})$$ $$U_{i,f} = \cfrac{1}{\cfrac{\Delta x_i}{k_i A_{i,s}} + \cfrac{1}{h_{i,f}A_{void}}}$$ Area of solid portion of the layer: $$A_{i,s} = A - A_{void}$$ Channel area: $$A_{void} = w_{chan} \times L_{chan}$$ Ohmic heating: $$\dot{q}_{res,i} = i^2\left(\frac{\rho_{res,i}\Delta x_i}{A_i}\right)$$

Appendix G (Continued)

Table G.8

Gas temperature heat transfer equations for the gas diffusion layers

Main Parameters	Equations
Inputs: $c_{p,mix}$ specific heat of mixture (J/Kg-K) n_{tot} total molar flow rate of mixture (mol/s) $A_{i,s}$ solid area of layer (m^2) A_{void} void area of layer (m^2) k thermal conductivity of node I (W/m-K) Δx thickness of the node (m)	$(c_{p,mix}n_{tot})\dfrac{dT_i}{dt} = \dot{q}_{i-1} + \dot{q}_{i+1} + \dot{q}_{i-1,f} + \dot{q}_{i+1,f} +$ $\dot{q}_{i,f} + H_{H2,i} + H_{H2Ov,i} + H_{H2Ol,i} -$ $H_{H2,i+1} - H_{H2Ov,i+1} - H_{H2Ol,i+1} -$ $H_{H2\_out} - H_{H2Ov\_out} - H_{H2Ol\_out}$ Specific heat of mixture: $c_{p,mix} = x_i c_{p,i} + x_j c_{p,j}$
Calculated: U_{i-1} overall heat transfer coefficient for the left node U_{i+1} overall heat transfer coefficient for the right node $U_{i-1,f}$ overall heat transfer coefficient for the gases/fluids in the left node $\dot{q}_{i-1}$ heat flow from the left node $\dot{q}_{i+1}$ heat flow from the right node $\dot{q}_{i,s}$ heat flow from the solid portion of the layer $\dot{q}_{i-1,f}$ heat flow from fluid/gases in left node $T_{i,f}$ temperature of gas/fluid mixture H_i enthalpy of component i	Heat flow from left node: $\dot{q}_{i-1} = U_{i-1}(T_{i-1} - T_i)$ $U_{i-1} = \dfrac{1}{\dfrac{\Delta x_i}{k_i A_{i,s}} + \dfrac{\Delta x_{i-1}}{k_{i-1} A_{i-1,s}}}$ Heat flow from fluid/gases in left node: $\dot{q}_{i-1,f} = U_{i-1,f}(T_{i-1} - T_i)$ $U_{i-1,f} = \dfrac{1}{\dfrac{\Delta x_i}{k_i A_{i,s}} + \dfrac{1}{h_{i-1,f} A_{i-1,void}}}$

Appendix G (Continued)

Table G.8 *(continued)*

Main Parameters	Equations
Inputs: ρ density of the layer (kg/m^3) $A_{i,s}$ solid area of layer (m^2) A_{void} void area of layer (m^2) Δx thickness of the node (m) cp specific heat of layer (J/Kg-K) T_i temperature of the node (K) k thermal conductivity of node I (W/m-K) *Calculated:* $U_{i+1,f}$ overall heat transfer coefficient for fluid/gases in right node U_{i+1} overall heat transfer coefficient for the right node $U_{i,f}$ overall heat transfer coefficient for fluid/gases to solid $\dot{q}_{i+1,f}$ heat flow from fluid/gases in right node $\dot{q}_{i+1}$ heat flow from the right node	Heat flow from right node: $\dot{q}_{i+1} = U_{i+1}(T_{i+1} - T_i)$ $U_{i+1} = \dfrac{1}{\dfrac{\Delta x_{i+1}}{k_{i+1} A_{i+1,s}} + \dfrac{\Delta x_i}{k_i A_{i,s}}}$ Heat flow from fluid/gases in right node: $\dot{q}_{i+1,f} = U_{i+1,f}(T_{i+1,f} - T_i)$ $U_{i+1,f} = \dfrac{1}{\dfrac{1}{h_{i+1,f} A_{i+1,void}} + \dfrac{\Delta x_i}{k_i A_{i,s}}}$ Heat flow from solid to fluid/gases: $\dot{q}_{i,s} = U_{i,s}(T_{i,s} - T_i)$ $U_{i,s} = \dfrac{1}{\dfrac{\Delta x_i}{k_i A_{i,s}} + \dfrac{1}{h_f A_{void}}}$

Appendix G (Continued)

Table G.8 *(continued)*

Main Parameters	Equations
Inputs: w_{chan} channel width (m) L_{chan} channel length (m) *Calculated:* $T_{i,f}$ temperature of gas/fluid mixture H_i enthalpy of component i $A_{i,s}$ solid area of layer (m^2) A_{void} void area of layer (m^2)	Enthalpies of each gas/liquid flow: $H_i = n_i h_i T_{i,f}$ Area of solid portion of the layer: $A_{i,s} = A - A_{void}$ Channel area: $A_{void} = w_{chan} \times L_{chan}$

Appendix G (Continued)

Table G.9

Heat transfer equations for the catalyst layers

Main Parameters	Equations
Inputs: ρ density of the layer (kg/m^3) $A_{i,s}$ solid area of layer (m^2) A_{void} void area of layer (m^2) Δx thickness of the node (m) cp specific heat of layer (J/Kg-K) T_i temperature of the node (K) k thermal conductivity of node i (W/m-K) *Calculated:* U_{i-1} overall heat transfer coefficient for the left node U_{i+1} overall heat transfer coefficient for the right node $U_{i-1,f}$ overall heat transfer coefficient for the gases/fluids in the left node $\dot{q}_{i-1}$ heat flow from the left node $\dot{q}_{i+1}$ heat flow from the right node $\dot{q}_{i,s}$ heat flow from the solid portion of the layer $\dot{q}_{i-1,f}$ heat flow from fluid/gases in left node H_i enthalpy of component i T_i temperature of the node (K)	$(c_{p,mix} n_{tot} + \rho A \Delta x \ cp)\dfrac{dT_i}{dt} = \dot{q}_{i-1} + \dot{q}_{i-1,f} + \dot{q}_{i+1} + \dot{q}_{res,i} + $ $H_{H2Ov,i} + H_{H2Ol,i} - H_{H2,i+1} - H_{H2Ov,i+1} - H_{H2Ol,i+1}$ Heat flow from left node: $\dot{q}_{i-1} = U_{i-1}(T_{i-1} - T_i)$ $U_{i-1} = \dfrac{1}{\dfrac{\Delta x_i}{k_i A_{i,s}} + \dfrac{\Delta x_{i-1}}{k_{i-1} A_{i-1,s}}}$ Heat flow from fluid/gases in left node: $\dot{q}_{i-1,f} = U_{i-1,f}(T_{i-1} - T_i)$ $U_{i-1,f} = \dfrac{1}{\dfrac{\Delta x_i}{k_i A_{i,s}} + \dfrac{1}{h_{i-1,f} A_{i-1,void}}}$ Heat flow from right node: $\dot{q}_{i+1} = U_{i+1}(T_{i+1} - T_i)$ $U_{i+1} = \dfrac{1}{\dfrac{\Delta x_{i+1}}{k_{i+1} A_{i+1,s}} + \dfrac{\Delta x_i}{k_i A_{i,s}}}$

Table G.9 *(continued)*

Main Parameters	Equations
Inputs: ρ density of the layer (kg/m^3) $A_{i,s}$ solid area of layer (m^2) A_{void} void area of layer (m^2) Δx thickness of the node (m) cp specific heat of layer (J/Kg-K) T_i temperature of the node (K) k thermal conductivity of node I (W/m-K) w_{chan} channel width (m) L_{chan} channel length (m) $\rho_{res,i}$ resistivity of solid portion of node i i current density (A/m^2) *Calculated:* $U_{i+1,f}$ overall heat transfer coefficient for fluid/gases in right node $U_{i,f}$ overall heat transfer coefficient for fluid/gases to solid $\dot{q}_{i+1,f}$ heat flow from fluid/gases in right node $\dot{q}_{i,f}$ heat flow from the gases/fluids $\dot{q}_{res,i}$ heat flow due to ohmic heating	Heat flow from fluid/gases in right node: $$\dot{q}_{i+1,f} = U_{i+1,f}(T_{i+1,f} - T_i)$$ $$U_{i+1,f} = \cfrac{1}{\cfrac{1}{h_{i+1,f} A_{i+1,void}} + \cfrac{\Delta x_i}{k_i A_{i,s}}}$$ Heat flow from fluid/gases to solid $$\dot{q}_{i,f} = U_{i,f}(T_i - T_{i,f})$$ $$U_{i,f} = \cfrac{1}{\cfrac{\Delta x_i}{k_i A_{i,s}} + \cfrac{1}{h_{i,f} A_{void}}}$$ Area of solid portion of the layer: $$A_{i,s} = A - A_{void}$$ Channel area: $$A_{void} = w_{chan} \times L_{chan}$$ Ohmic heating: $$\dot{q}_{res,i} = i^2 \left(\frac{\rho_{res,i} \Delta x_i}{A_i} \right)$$

Appendix G (Continued)

Table G.10

Gas temperature heat transfer equations for the catalyst layers

Main Parameters	Equations
Inputs: $c_{p,mix}$ specific heat of mixture (J/Kg-K) n_{tot} total molar flow rate of mixture (mol/s) $A_{i,s}$ solid area of layer (m²) A_{void} void area of layer (m²) k thermal conductivity of node I (W/m-K) Δx thickness of the node (m)	$$(c_{p,mix}n_{tot})\frac{dT_i}{dt} = \dot{q}_{i-1} + \dot{q}_{i+1} + \dot{q}_{i-1,f} + \dot{q}_{i+1,f} +$$ $$\dot{q}_{i,f} + H_{H2,i} + H_{H2Ov,i} + H_{H2Ol,i} -$$ $$H_{H2,i+1} - H_{H2Ov,i+1} - H_{H2Ol,i+1} -$$ $$H_{H2\_out} - H_{H2Ov\_out} - H_{H2Ol\_out}$$ Heat flow from left node: $$\dot{q}_{i-1} = U_{i-1}(T_{i-1} - T_i)$$

Calculated:
U_{i-1} overall heat transfer coefficient for the left node
U_{i+1} overall heat transfer coefficient for the right node
$U_{i-1,f}$ overall heat transfer coefficient for the gases/fluids in the left node
$\dot{q}_{i-1}$ heat flow from the left node
$\dot{q}_{i+1}$ heat flow from the right node
$\dot{q}_{i,s}$ heat flow from the solid portion of the layer
$\dot{q}_{i-1,f}$ heat flow from fluid/gases in left node
$T_{i,f}$ temperature of gas/fluid mixture
H_i enthalpy of component i

$$U_{i-1} = \frac{1}{\dfrac{\Delta x_i}{k_i A_{i,s}} + \dfrac{\Delta x_{i-1}}{k_{i-1} A_{i-1,s}}}$$

Heat flow from fluid/gases in left node:

$$\dot{q}_{i-1,f} = U_{i-1,f}(T_{i-1} - T_i)$$

$$U_{i-1,f} = \frac{1}{\dfrac{\Delta x_i}{k_i A_{i,s}} + \dfrac{1}{h_{i-1,f} A_{i-1,void}}}$$

Heat flow from right node:

$$\dot{q}_{i+1} = U_{i+1}(T_{i+1} - T_i)$$

$$U_{i+1} = \frac{1}{\dfrac{\Delta x_{i+1}}{k_{i+1} A_{i+1,s}} + \dfrac{\Delta x_i}{k_i A_{i,s}}}$$

Appendix G (Continued)

Table G.10 *(continued)*

Main Parameters	Equations
Inputs: ρ density of the layer (kg/m³) $A_{i,s}$ solid area of layer (m²) A_{void} void area of layer (m²) Δx thickness of the node (m) cp specific heat of layer (J/Kg-K) T_i temperature of the node (K) k thermal conductivity of node I (W/m-K) w_{chan} channel width (m) L_{chan} channel length (m) *Calculated:* $U_{i+1,f}$ overall heat transfer coefficient for fluid/gases in right node U_{i+1} overall heat transfer coefficient for the right node $U_{i,f}$ overall heat transfer coefficient for fluid/gases to solid $\dot{q}_{i+1,f}$ heat flow from fluid/gases in right node $\dot{q}_{i+1}$ heat flow from the right node $\dot{q}_{i,f}$ heat flow from the gases/fluids	Heat flow from fluid/gases in right node: $\dot{q}_{i+1,f} = U_{i+1,f}(T_{i+1,f} - T_i)$ $U_{i+1,f} = \dfrac{1}{\dfrac{1}{h_{i+1,f} A_{i+1,void}} + \dfrac{\Delta x_i}{k_i A_{i,s}}}$ Heat flow from solid to fluid/gases: $\dot{q}_{i,s} = U_{i,s}(T_{i,s} - T_i)$ $U_{i,s} = \dfrac{1}{\dfrac{\Delta x_i}{k_i A_{i,s}} + \dfrac{1}{h_f A_{void}}}$ Enthalpies of each gas/liquid flow: $H_i = n_i h_i T_i$ Area of solid portion of the layer: $A_{i,s} = A - A_{void}$ Channel area: $A_{void} = w_{chan} \times L_{chan}$

Table G.11

Heat transfer equations for the membrane layer

Main Parameters	Equations
Inputs: ρ density of the layer (kg/m^3) $A_{i,s}$ solid area of layer (m^2) A_{void} void area of layer (m^2) Δx thickness of the node (m) cp specific heat of layer (J/Kg-K) T_i temperature of the node (K) k thermal conductivity of node i (W/m-K) *Calculated:* U_{i-1} overall heat transfer coefficient for the left node U_{i+1} overall heat transfer coefficient for the right node $U_{i-1,f}$ overall heat transfer coefficient for the gases/fluids in the left node $\dot{q}_{i-1}$ heat flow from the left node $\dot{q}_{i+1}$ heat flow from the right node $\dot{q}_{i,s}$ heat flow from the solid portion of the layer $\dot{q}_{i-1,f}$ heat flow from fluid/gases in left node H_i enthalpy of component i T_i temperature of the node (K)	$(c_{p,mix}n_{tot} + \rho A \Delta x \ cp)\dfrac{dT_i}{dt} = \dot{q}_{i-1} + \dot{q}_{i+1} + \dot{q}_{res,i} + \dot{q}_{int,i}$ $H_{H2Ov,i} + H_{H2Ol,i} - H_{H+,i+1} - H_{H2Ov,i+1} - H_{H2Ol,i+1}$ Heat flow from left node: $\dot{q}_{i-1} = U_{i-1}(T_{i-1} - T_i)$ $U_{i-1} = \dfrac{1}{\dfrac{\Delta x_i}{k_i A_{i,s}} + \dfrac{\Delta x_{i-1}}{k_{i-1} A_{i-1,s}}}$ Heat flow from fluid/gases in left node: $\dot{q}_{i-1,f} = U_{i-1,f}(T_{i-1} - T_i)$ $U_{i-1,f} = \dfrac{1}{\dfrac{\Delta x_i}{k_i A_{i,s}} + \dfrac{1}{h_{i-1,f} A_{i-1,void}}}$ Heat flow from right node: $\dot{q}_{i+1} = U_{i+1}(T_{i+1} - T_i)$ $U_{i+1} = \dfrac{1}{\dfrac{\Delta x_{i+1}}{k_{i+1} A_{i+1,s}} + \dfrac{\Delta x_i}{k_i A_{i,s}}}$

Table G.11 *(continued)*

Main Parameters	Equations
Inputs: ρ density of the layer (kg/m^3) $A_{i,s}$ solid area of layer (m^2) A_{void} void area of layer (m^2) Δx thickness of the node (m) cp specific heat of layer (J/Kg-K) T_i temperature of the node (K) k thermal conductivity of node I (W/m-K) w_{chan} channel width (m) L_{chan} channel length (m) $\rho_{res,i}$ resistivity of solid portion of node i i current density (A/m^2) *Calculated:* $U_{i+1,f}$ overall heat transfer coefficient for fluid/gases in right node $U_{i,f}$ overall heat transfer coefficient for fluid/gases to solid $\dot{q}_{i+1,f}$ heat flow from fluid/gases in right node $\dot{q}_{i,f}$ heat flow from the gases/fluids $\dot{q}_{res,i}$ heat flow due to ohmic heating	Heat flow from fluid/gases in right node: $$\dot{q}_{i+1,f} = U_{i+1,f}(T_{i+1,f} - T_i)$$ $$U_{i+1,f} = \cfrac{1}{\cfrac{1}{h_{i+1,f} A_{i+1,void}} + \cfrac{\Delta x_i}{k_i A_{i,s}}}$$ Heat flow from fluid/gases to solid $$\dot{q}_{i,f} = U_{i,f}(T_i - T_{i,f})$$ $$U_{i,f} = \cfrac{1}{\cfrac{\Delta x_i}{k_i A_{i,s}} + \cfrac{1}{h_{i,f} A_{void}}}$$ Area of solid portion of the layer: $$A_{i,s} = A - A_{void}$$ Channel area: $$A_{void} = w_{chan} \times L_{chan}$$ Ohmic heating: $$\dot{q}_{res,i} = i^2\left(\frac{\rho_{res,i}\Delta x_i}{A_i}\right)$$

Table G.11 *(continued)*

Main Parameters	Equations
Inputs:	$$(c_{p,mix}n_{tot})\frac{dT_i}{dt} = \dot{q}_{i-1} + \dot{q}_{i+1} + \dot{q}_{i-1,f} + \dot{q}_{i+1,f} +$$
$c_{p,mix}$ specific heat of mixture (J/Kg-K)	
n_{tot} total molar flow rate of mixture (mol/s)	$$\dot{q}_{i,f} + H_{H2,i} + H_{H2Ov,i} + H_{H2Ol,i} -$$
$A_{i,s}$ solid area of layer (m^2)	$$H_{H2,i+1} - H_{H2Ov,i+1} - H_{H2Ol,i+1} -$$
A_{void} void area of layer (m^2)	$$H_{H2\_out} - H_{H2Ov\_out} - H_{H2Ol\_out}$$
k thermal conductivity of node I (W/m-K)	Specific heat of mixture:
Δx thickness of the node (m)	$$c_{p,mix} = x_i c_{p,i} + x_j c_{p,j}$$
Calculated:	Heat flow from left node:
U_{i-1} overall heat transfer coefficient for the left node	
U_{i+1} overall heat transfer coefficient for the right node	$$\dot{q}_{i-1} = U_{i-1}(T_{i-1} - T_i)$$
$U_{i-1,f}$ overall heat transfer coefficient for the gases/fluids in the left node	$$U_{i-1} = \frac{1}{\dfrac{\Delta x_i}{k_i A_{i,s}} + \dfrac{\Delta x_{i-1}}{k_{i-1} A_{i-1,s}}}$$
$\dot{q}_{i-1}$ heat flow from the left node	
$\dot{q}_{i+1}$ heat flow from the right node	Heat flow from fluid/gases in left node:
$\dot{q}_{i,s}$ heat flow from the solid portion of the layer	$$\dot{q}_{i-1,f} = U_{i-1,f}(T_{i-1} - T_i)$$
$\dot{q}_{i-1,f}$ heat flow from fluid/gases in left node	$$U_{i-1,f} = \frac{1}{\dfrac{\Delta x_i}{k_i A_{i,s}} + \dfrac{1}{h_{i-1,f} A_{i-1,void}}}$$
$T_{i,f}$ temperature of gas/fluid mixture	
H_i enthalpy of component i	

Table G.11 *(continued)*

Main Parameters	Equations
Inputs: ρ density of the layer (kg/m^3) $A_{i,s}$ solid area of layer (m^2) A_{void} void area of layer (m^2) Δx thickness of the node (m) cp specific heat of layer (J/Kg-K) T_i temperature of the node (K) k thermal conductivity of node I (W/m-K) w_{chan} channel width (m) L_{chan} channel length (m) *Calculated:* $U_{i+1,f}$ overall heat transfer coefficient for fluid/gases in right node U_{i+1} overall heat transfer coefficient for the right node $U_{i,f}$ overall heat transfer coefficient for fluid/gases to solid $\dot{q}_{i+1,f}$ heat flow from fluid/gases in right node $\dot{q}_{i+1}$ heat flow from the right node $\dot{q}_{i,f}$ heat flow from the gases/fluids	Heat flow from right node: $$\dot{q}_{i+1} = U_{i+1}(T_{i+1} - T_i)$$ $$U_{i+1} = \cfrac{1}{\cfrac{\Delta x_{i+1}}{k_{i+1}A_{i+1,s}} + \cfrac{\Delta x_i}{k_i A_{i,s}}}$$ Heat flow from fluid/gases in right node: $$\dot{q}_{i+1,f} = U_{i+1,f}(T_{i+1,f} - T_i)$$ $$U_{i+1,f} = \cfrac{1}{\cfrac{1}{h_{i+1,f}A_{i+1,void}} + \cfrac{\Delta x_i}{k_i A_{i,s}}}$$ Heat flow from solid to fluid/gases: $$\dot{q}_{i,s} = U_{i,s}(T_{i,s} - T_i)$$ $$U_{i,s} = \cfrac{1}{\cfrac{\Delta x_i}{k_i A_{i,s}} + \cfrac{1}{h_f A_{void}}}$$

Table G.11 *(continued)*

Main Parameters	Equations
Inputs: w_{chan} channel width (m) L_{chan} channel length (m) *Calculated:* $T_{i,f}$ temperature of gas/fluid mixture H_i enthalpy of component i $A_{i,s}$ solid area of layer (m^2) A_{void} void area of layer (m^2)	Enthalpies of each gas/liquid flow: $$H_i = n_i h_i T_{i,f}$$ Area of solid portion of the layer: $$A_{i,s} = A - A_{void}$$ Channel area: $$A_{void} = w_{chan} \times L_{chan}$$

Appendix H   Mass Transfer Analysis

Table H.1

Mass transfer equations for the end plate, manifold and gasket layers

Main Parameters	Equations
Inputs: n_{tot_in} inlet molar flow rate (mol/s) P_{in} inlet pressure (Pa) υ_{in} inlet volumetric flow rate (m³/s) T_{in} inlet temperature (K) R ideal gas constant (m³-Pa/K-mol) *Calculated:* n_{tot} total molar flow rate of mixture x_{H2} mole fraction of hydrogen x_{H2O} mole fraction of water x_{O2} mole fraction of oxygen $n_{H2Ov,i}$ molar flow rate of water vapor $n_{H2Ol,i}$ molar flow rate of liquid water $n_{H2O,i}$ total water molar flow rate $n_{H2,i}$ molar flow rate of hydrogen	Convert volumetric flow rate to molar flow rate: $$n_{tot\_in} = \frac{P_{in}\upsilon_{in}}{RT_{in}}$$ Total molar accumulation: $$\frac{dn_{tot}}{dt} = n_{tot,i} - n_{tot,i+1}$$ The rate of H_2 accumulation is: $$\frac{d}{dt}(x_{H2}n_{tot}) = x_{H2,i}n_{tot,i} - x_{H2,i+1}n_{tot,i+1}$$ The rate of H_2O accumulation is: $$\frac{d}{dt}(x_{H2O}n_{tot}) = x_{H2O,i}n_{tot,i} - x_{H2O,i+1}n_{tot,i+1}$$ The rate of O_2 accumulation is: $$\frac{d}{dt}(x_{O2}n_{tot}) = x_{O2,i}n_{tot,i} - x_{O2,i+1}n_{tot,i+1}$$

Appendix H (Continued)

Table H.2

Mole fraction calculations for the end plate, manifold and gasket layers

Main Parameters	Equations
Inputs: $P_{sat}(T_{i,f})$ saturation pressure at the gas/fluid temperature at node i (Pa) ϕ_{in} inlet humidity of the gas stream M_{H2O} molecular weight of water (kg/mol) M_{H2} molecular weight of hydrogen (kg/mol) $P_{tot,i}$ Total pressure at node i (Pa) d_c channel depth (m) w_c channel width (m) k_c evaporation and condensation rate constant (s^{-1}) R ideal gas constant (m^3-Pa/K-mol) $T_{i,f}$ temperature of gas/liquid mixture at node i (K) Δx thickness of node i (m) *Calculated:* n_{tot} total molar flow rate of mixture x_{H2} mole fraction of hydrogen x_{H2O} mole fraction of water $p_{H2O,i}$ vapor pressure of the inlet water vapor H is the humidity $n_{H2Ov,i}$ molar flow rate of water vapor $n_{H2Ol,i}$ molar flow rate of liquid water $n_{H2O,i}$ total water molar flow rate	Calculate the vapor pressure of the inlet water vapor: $$p_{H2O,i} = \phi_{in} P_{sat}(T_{i,f})$$ Calculate humidity: $$H = \frac{M_{H2O}\, p_{H2O,i}}{M_{H2}(P_{tot,i} - p_{H2O,i})}$$ The mole fraction of the water vapor is: $$x_{H2Ov,i} = \frac{\dfrac{H}{M_{H2O}}}{\dfrac{1}{M_{H2}} + \dfrac{H}{M_{H2O}}}$$ The molar flow rate of water vapor is: $$n_{H2Ov,i} = x_{H2Ov,i} n_{tot,i}$$ Water condensation and evaporation: $$n_{H2Ol,i+1} = \left(\frac{k_c w_c d_c}{RT_{i,f}}\right)\frac{n_{H2Ov,i+1}}{n_{tot,i+1}}\left(P_{tot,i} - P_{sat}(T_{i,f})\right)$$ The total molar flow rate of water is: $$n_{H2O,i} = n_{H2Ov,i} + n_{H2Ol,i}$$

Appendix H (Continued)

Table H.2 *(continued)*

Main Parameters	Equations
Inputs: R ideal gas constant (m^3-Pa/K-mol) $P_{sat}(T_{i,f})$ saturation pressure at the gas/fluid temperature at node i (Pa) $P_{tot,i}$ Total pressure at node i (Pa) *Calculated:* n_{tot} total molar flow rate of mixture x_{H2} mole fraction of hydrogen x_{H2O} mole fraction of water H is the humidity $n_{H2Ov,i}$ molar flow rate of water vapor $n_{H2Ol,i}$ molar flow rate of liquid water $n_{H2O,i}$ total water molar flow rate $n_{H2,i}$ molar flow rate of hydrogen RH Relative humidity RW Relative water content $T_{i,f}$ temperature of gas/liquid mixture at node i (K)	The total mole fraction of water is: $$x_{H2O,i} = \frac{n_{H2O,i}}{n_{tot,i}}$$ The mole fraction of hydrogen is: $$x_{H2,i} = 1 - x_{H2O,i}$$ The molar flow rate of hydrogen is: $$n_{H2,i} = x_{H2,i} n_{tot,i}$$ Total flowrate out of the layer is: $$n_{tot,i+1} = n_{H2,i+1} + n_{H2O,i+1}$$ Relative humidity: $$RH = \frac{n_{H2Ov,i+1}}{n_{tot,i+1}} \frac{P_{tot,i}}{P_{sat}(T_{i,f})}$$ Relative water content: $$RW = \frac{n_{H2O,i+1}}{n_{tot,i+1}} \frac{P_{tot,i}}{P_{sat}(T_{i,f})}$$

Appendix H (Continued)

Table H.3

Mass transfer calculations for the flow field layers

Main Parameters	Equations
Inputs: n_{tot_in} inlet molar flow rate (mol/s) P_{in} inlet pressure (Pa) υ_{in} inlet volumetric flow rate (m³/s) T_{in} inlet temperature (K) R ideal gas constant (m³-Pa/K-mol) *Calculated:* n_{tot} total molar flow rate of mixture $n_{tot,2}$ total molar flow rate leaving the plate, and going back to the manifold x_{H2} mole fraction of hydrogen x_{H2O} mole fraction of water x_{O2} mole fraction of oxygen $n_{H2Ov,i}$ molar flow rate of water vapor $n_{H2Ol,i}$ molar flow rate of liquid water $n_{H2O,i}$ total water molar flow rate $n_{H2,i}$ molar flow rate of hydrogen	Convert volumetric flow rate to molar flow rate: $$n_{tot\_in} = \frac{P_{in}\upsilon_{in}}{RT_{in}}$$ Total molar accumulation: $$\frac{dn_{tot}}{dt} = n_{tot,i} - n_{tot,i+1} - n_{tot,2}$$ The rate of H_2 accumulation is: $$\frac{d}{dt}(x_{H2}n_{tot}) = x_{H2,i}n_{tot,i} - x_{H2,i+1}n_{tot,i+1} - x_{H2,2}n_{tot,2}$$ The rate of H_2O accumulation is: $$\frac{d}{dt}(x_{H2O}n_{tot}) = x_{H2O,i}n_{tot,i} - x_{H2O,i+1}n_{tot,i+1} - x_{H2O,2}n_{tot,2}$$ The rate of O_2 accumulation is: $$\frac{d}{dt}(x_{O2}n_{tot}) = x_{O2,i}n_{tot,i} - x_{O2,i+1}n_{tot,i+1} - x_{O2,2}n_{tot,2}$$

Appendix H (Continued)

Table H.3 *(continued)*

Main Parameters	Equations
Inputs: $P_{sat}(T_{i,f})$ saturation pressure at the gas/fluid temperature at node i (Pa) ϕ_{in} inlet humidity of the gas stream M_{H2O} molecular weight of water (kg/mol) M_{H2} molecular weight of hydrogen (kg/mol) $P_{tot,i}$ Total pressure at node I (Pa) d_c channel depth (m) w_c channel width (m) k_c evaporation and condensation rate constant (s^{-1}) *Calculated:* n_{tot} total molar flow rate of mixture x_{H2} mole fraction of hydrogen x_{H2O} mole fraction of water x_{O2} mole fraction of oxygen $p_{H2O,i}$ vapor pressure of the inlet water vapor H is the humidity $n_{H2Ov,i}$ molar flow rate of water vapor $n_{H2Ol,i}$ molar flow rate of liquid water $n_{H2O,i}$ total water molar flow rate $n_{H2,i}$ molar flow rate of hydrogen	Calculate the vapor pressure of the inlet water vapor: $$p_{H2O,i} = \phi_{in} P_{sat}(T_{i,f})$$ Calculate humidity: $$H = \frac{M_{H2O} \, p_{H2O,i}}{M_{H2}(P_{tot,i} - p_{H2O,i})}$$ The mole fraction of the water vapor is: $$x_{H2Ov,i} = \frac{\dfrac{H}{M_{H2O}}}{\dfrac{1}{M_{H2}} + \dfrac{H}{M_{H2O}}}$$ The molar flow rate of water vapor is: $$n_{H2Ov,i} = x_{H2Ov,i} n_{tot,i}$$ The molar flow rate for water condensation and evaporation is: $$n_{H2Ol,i+1} = \left(\frac{k_c w_c d_c}{RT_{i,f}}\right)\frac{n_{H2Ov,i+1}}{n_{tot,i+1}}\left(P_{tot,i} - P_{sat}(T_{i,f})\right)$$ The total molar flow rate of water is: $$n_{H2O,i} = n_{H2Ov,i} + n_{H2Ol,i}$$

Appendix H (Continued)

Table H.3 *(continued)*

Main Parameters	Equations
Inputs: $P_{tot,i}$ Total pressure at node i (Pa) D_h hydraulic diameter (m) Sh Sherwood number $u_{m,i}$ velocity of mixture (m/s) b distance between flow channels and gas diffusion layer x_H height of gas diffusion layer *Calculated:* n_{tot} total molar flow rate of mixture x_{H2} mole fraction of hydrogen x_{H2O} mole fraction of water x_{O2} mole fraction of oxygen $n_{H2Ov,i}$ molar flow rate of water vapor $n_{H2Ol,i}$ molar flow rate of liquid water $n_{H2O,i}$ total water molar flow rate $n_{H2,i}$ molar flow rate of hydrogen h_m mass transfer coefficient $D_{i,j}$ diffusion coefficient (m²/s) $C_{i,out}$ Outlet average concentration $T_{i,f}$ temperature of gas/liquid mixture at node i (K)	The total mole fraction of water is: $$x_{H2O,i} = \frac{n_{H2O,i}}{n_{tot,i}}$$ The mole fraction of hydrogen is: $$x_{H2,i} = 1 - x_{H2O,i}$$ The molar flow rate of hydrogen is: $$n_{H2,i} = x_{H2,i} n_{tot,i}$$ The concentrations are calculated at the node inlet: $$C_{H2O,i} = x_{H2O,i} \left(\frac{P_{tot,i}}{RT_{i,f}} \right)$$ $$C_{H2,i} = x_{H2,i} \left(\frac{P_{tot,i}}{RT_{i,f}} \right)$$ Mass transfer coefficient: $$h_m = Sh \frac{D_{i,j}}{D_h}$$

Table H.3 *(continued)*

Main Parameters	Equations
Inputs: $P_{tot,i}$ Total pressure at node i (Pa) D_h hydraulic diameter (m) Sh Sherwood number	Outlet average concentration for hydrogen: $$C_{H2,i+1} = C_{H2,i} \exp\left(\frac{-h_m x_H}{b u_{m,i}}\right)$$
Calculated: n_{tot} total molar flow rate of mixture x_{H2} mole fraction of hydrogen x_{H2O} mole fraction of water x_{O2} mole fraction of oxygen $p_{H2O,i}$ vapor pressure of the inlet water vapor H is the humidity $n_{H2Ov,i}$ molar flow rate of water vapor $n_{H2Ol,i}$ molar flow rate of liquid water $n_{H2O,i}$ total water molar flow rate $n_{H2,i}$ molar flow rate of hydrogen h_m mass transfer coefficient $D_{i,j}$ diffusion coefficient (m2/s) $C_{i,out}$ Outlet average concentration	Average limiting current density: $$\bar{i}_L = nFh_m \left[\frac{C_{H2,i} - C_{H2,i+1}}{\ln\left(\dfrac{C_{H2,i}}{C_{H2,i+1}}\right)} \right]$$ Outlet molar flow: $$n_{H2,i+1} = A_i h_m (C_{H2,i} - C_{H2,i+1})$$ Total flowrate out of the layer is: $$n_{tot,i+1} = n_{H2,i+1} + n_{H2O,i+1}$$ The total mole fraction of hydrogen is: $$x_{H2,i+1} = \frac{n_{H2,i+1}}{n_{tot,i+1}}$$

Appendix H (Continued)

Table H.3 *(continued)*

Main Parameters	Equations
Inputs: $P_{tot,i}$ Total pressure at node i (Pa) $P_{sat}(T_{i,f})$ saturation pressure at the gas/fluid temperature at node i (Pa) $n_{H2Ov,i}$ molar flow rate of water vapor n_{tot} total molar flow rate of mixture $n_{H2O,i}$ total water molar flow rate *Calculated:* x_{H2O} mole fraction of water RH Relative humidity RW Relative water content	The total mole fraction of water is: $$x_{H2O,i+1} = \frac{n_{H2O,i+1}}{n_{tot,i+1}}$$ Relative humidity: $$RH = \frac{n_{H2Ov,i+1}}{n_{tot,i+1}} \frac{P_{tot,i}}{P_{sat}(T_{i,f})}$$ Relative water content: $$RW = \frac{n_{H2O,i+1}}{n_{tot,i+1}} \frac{P_{tot,i}}{P_{sat}(T_{i,f})}$$

Appendix H (Continued)

Table H.4

Mass transfer calculations for the gas diffusion layers

Main Parameters	Equations
Inputs: $P_{tot,i}$ Total pressure at node i (Pa) *Calculated:* n_{tot} total molar flow rate of mixture x_{H2} mole fraction of hydrogen x_{H2O} mole fraction of water x_{O2} mole fraction of oxygen $n_{H2Ov,i}$ molar flow rate of water vapor $n_{H2Ol,i}$ molar flow rate of liquid water $n_{H2O,i}$ total water molar flow rate $n_{H2,i}$ molar flow rate of hydrogen	Total molar accumulation: $$\frac{dn_{tot}}{dt} = n_{tot,i} - n_{tot,i+1}$$ The rate of H_2 accumulation is: $$\frac{d}{dt}(x_{H2}n_{tot}) = x_{H2,i}n_{tot,i} - x_{H2,i+1}n_{tot,i+1}$$ The rate of H_2O accumulation is: $$\frac{d}{dt}(x_{H2O}n_{tot}) = x_{H2O,i}n_{tot,i} - x_{H2O,i+1}n_{tot,i+1}$$ The rate of O_2 accumulation is: $$\frac{d}{dt}(x_{O2}n_{tot}) = x_{O2,i}n_{tot,i} - x_{O2,i+1}n_{tot,i+1}$$

Appendix H (Continued)

Table H.4 *(continued)*

Main Parameters	Equations
Inputs: $P_{sat}(T_{i,f})$ saturation pressure at the gas/fluid temperature at node i (Pa) ϕ_{in} inlet humidity of the gas stream M_{H2O} molecular weight of water (kg/mol) M_{H2} molecular weight of hydrogen (kg/mol) $P_{tot,i}$ Total pressure at node I (Pa) d_c channel depth (m) w_c channel width (m) k_c evaporation and condensation rate constant (s^{-1}) *Calculated:* n_{tot} total molar flow rate of mixture x_{H2O} mole fraction of water x_{O2} mole fraction of oxygen $p_{H2O,i}$ vapor pressure of the inlet water vapor H is the humidity $n_{H2Ov,i}$ molar flow rate of water vapor $n_{H2Ol,i}$ molar flow rate of liquid water $n_{H2O,i}$ total water molar flow rate $T_{i,f}$ temperature of gas/liquid mixture at node i (K)	Calculate the vapor pressure of the inlet water vapor: $$p_{H2O,i} = \phi_{in} P_{sat}(T_{i,f})$$ Calculate humidity: $$H = \frac{M_{H2O}\, p_{H2O,i}}{M_{H2}(P_{tot,i} - p_{H2O,i})}$$ The mole fraction of the water vapor is: $$x_{H2Ov,i} = \frac{\dfrac{H}{M_{H2O}}}{\dfrac{1}{M_{H2}} + \dfrac{H}{M_{H2O}}}$$ The molar flow rate of water vapor is: $$n_{H2Ov,i} = x_{H2Ov,i} n_{tot,i}$$ The molar flow rate for water condensation and evaporation is: $$n_{H2Ol,i+1} = \left(\frac{k_c w_c d_c}{RT_{i,f}}\right)\frac{n_{H2Ov,i+1}}{n_{tot,i+1}}\left(P_{tot,i} - P_{sat}(T_{i,f})\right)$$ The total molar flow rate of water is: $$n_{H2O,i} = n_{H2Ov,i} + n_{H2Ol,i}$$

Appendix H (Continued)

Table H.4 *(continued)*

Main Parameters	Equations
Inputs: $P_{tot,i}$ total pressure at node i (Pa) d_c channel depth (m) w_c channel width (m) k_c evaporation and condensation rate constant (s^{-1}) Δx thickness of node i (m) $u_{m,i}$ velocity of mixture (m/s) b distance between flow channels and gas diffusion layer x_H height of gas diffusion layer ϕ is the electrode porosity *Calculated:* n_{tot} total molar flow rate of mixture x_{H2} mole fraction of hydrogen x_{H2O} mole fraction of water $n_{H2O,i}$ total water molar flow rate $n_{H2,i}$ molar flow rate of hydrogen $C_{H2O,i}$ Concentration of water at node i $C_{H2,i}$ Concentration of hydrogen at node i $\bar{i}_L$ average limiting current density $D_{i,j}^{eff}$ effective diffusion coefficient $D_{i,j}$ diffusion coefficient $T_{i,f}$ temperature of gas/liquid mixture at node i (K)	The concentration at the node inlet is: $$C_{H2,i} = x_{H2,i}\left(\frac{P_{tot,i}}{RT_{i,f}}\right)$$ Outlet average concentration for hydrogen: $$C_{H2,i+1} = C_{H2,i}\exp\left(\frac{-h_m x_H}{bu_{m,i}}\right)$$ Average limiting current density: $$\bar{i}_L = \frac{nFD_{i,j}C_{H2,i+1}}{\Delta x_i}$$ Outlet molar flow: $$n_{H2,i+1} = \frac{A_i D_{i,j}(C_{H2,i} - C_{H2,i+1})}{\Delta x_i}$$ Effective diffusion coefficient: $$D_{i,j}^{eff} = D_{i,j}\phi^{3/2}$$ Total flowrate out of the layer is: $$n_{tot,i+1} = n_{H2,i+1} + n_{H2O,i+1}$$

Appendix H (Continued)

Table H.4 *(continued)*

Main Parameters	Equations
Inputs: $P_{sat}(T_{i,f})$ saturation pressure at the gas/fluid temperature at node I (Pa) $P_{tot,i}$ Total pressure at node I (Pa) *Calculated:* n_{tot} total molar flow rate of mixture x_{H2} mole fraction of hydrogen x_{H2O} mole fraction of water $n_{H2Ov,i}$ molar flow rate of water vapor $n_{H2Ol,i}$ molar flow rate of liquid water $n_{H2O,i}$ total water molar flow rate $n_{H2,i}$ molar flow rate of hydrogen RH Relative humidity RW Relative water content $C_{H2O,i}$ Concentration of water at node i $C_{H2,i}$ Concentration of hydrogen at node i $T_{i,f}$ temperature of gas/liquid mixture at node i (K)	The total mole fraction of hydrogen is: $$x_{H2,i+1} = \frac{n_{H2,i+1}}{n_{tot,i+1}}$$ The total mole fraction of water is: $$x_{H2O,i+1} = \frac{n_{H2O,i+1}}{n_{tot,i+1}}$$ Outlet concentration of water: $$C_{H2O,i+1} = x_{H2O,i+1}\left(\frac{P_{tot,i}}{RT_{i,f}}\right)$$ Relative humidity: $$RH = \frac{n_{H2Ov,i+1}}{n_{tot,i+1}}\frac{P_{tot,i}}{P_{sat}(T_{i,f})}$$ Relative water content: $$RW = \frac{n_{H2O,i+1}}{n_{tot,i+1}}\frac{P_{tot,i}}{P_{sat}(T_{i,f})}$$

Appendix H (Continued)

Table H.5

Mass transfer calculations for the catalyst layers

Main Parameters	Equations
Inputs: $P_{sat}(T_{i,f})$ saturation pressure at the gas/fluid temperature at node I (Pa) ϕ_{in} inlet humidity of the gas stream M_{H2O} molecular weight of water (kg/mol) M_{H2} molecular weight of hydrogen (kg/mol) $P_{tot,i}$ Total pressure at node I (Pa) *Calculated:* n_{tot} total molar flow rate of mixture x_{H2} mole fraction of hydrogen x_{H2O} mole fraction of water x_{O2} mole fraction of oxygen $p_{H2O,i}$ vapor pressure of the inlet water vapor H is the humidity $n_{H2Ov,i}$ molar flow rate of water vapor $n_{H2Ol,i}$ molar flow rate of liquid water $n_{H2O,i}$ total water molar flow rate $n_{H2,i}$ molar flow rate of hydrogen	Total molar accumulation: $$\frac{dn_{tot}}{dt} = n_{tot,i} - n_{tot,i+1}$$ The rate of H_2 accumulation is: $$\frac{d}{dt}(x_{H2}n_{tot}) = x_{H2,i}n_{tot,i} - x_{H2,i+1}n_{tot,i+1}$$ The rate of H_2O accumulation is: $$\frac{d}{dt}(x_{H2O}n_{tot}) = x_{H2O,i}n_{tot,i} - x_{H2O,i+1}n_{tot,i+1}$$ The rate of O_2 accumulation is: $$\frac{d}{dt}(x_{O2}n_{tot}) = x_{O2,i}n_{tot,i} - x_{O2,i+1}n_{tot,i+1}$$ Calculate the vapor pressure of the inlet water vapor: $$p_{H2O,i} = \phi_{in}P_{sat}(T_{i,f})$$ Calculate humidity: $$H = \frac{M_{H2O}\,p_{H2O,i}}{M_{H2}(P_{tot,i} - p_{H2O,i})}$$

Table H.5 *(continued)*

Main Parameters	Equations
Inputs: $P_{sat}(T_{i,f})$ saturation pressure at the gas/fluid temperature at node i (Pa) M_{H2O} molecular weight of water (kg/mol) M_{H2} molecular weight of hydrogen (kg/mol) $P_{tot,i}$ Total pressure at node i (Pa) d_c channel depth (m) w_c channel width (m) k_c evaporation and condensation rate constant (s^{-1})	The mole fraction of the water vapor is: $$x_{H2Ov,i} = \frac{\dfrac{H}{M_{H2O}}}{\dfrac{1}{M_{H2}} + \dfrac{H}{M_{H2O}}}$$ The molar flow rate of water vapor is: $$n_{H2Ov,i} = x_{H2Ov,i} n_{tot,i}$$
Calculated: n_{tot} total molar flow rate of mixture x_{H2O} mole fraction of water x_{O2} mole fraction of oxygen H is the humidity $n_{H2Ov,i}$ molar flow rate of water vapor $n_{H2Ol,i}$ molar flow rate of liquid water $n_{H2O,i}$ total water molar flow rate $C_{H2O,i}$ Concentration of water at node i $C_{H2,i}$ Concentration of hydrogen at node i $T_{i,f}$ temperature of gas/liquid mixture at node i (K)	The molar flow rate for water condensation and evaporation is: $$n_{H2Ol,i+1} = \left(\frac{k_c w_c d_c}{RT_{i,f}} \right) \frac{n_{H2Ov,i+1}}{n_{tot,i+1}} \left(P_{tot,i} - P_{sat}(T_{i,f}) \right)$$ The total molar flow rate of water is: $$n_{H2O,i} = n_{H2Ov,i} + n_{H2Ol,i}$$ The concentrations at the node inlet: $$C_{H2O,i} = x_{H2O,i} \left(\frac{P_{tot,i}}{RT_{i,f}} \right)$$ $$C_{H2,i} = x_{H2,i} \left(\frac{P_{tot,i}}{RT_{i,f}} \right)$$

Table H.5 *(continued)*

Main Parameters	Equations
Inputs:	Outlet average concentration for hydrogen:
$P_{tot,i}$ Total pressure at node I (Pa)	
ϕ is the electrode porosity	$$C_{H2,i+1} = C_{H2,i}\, \exp\left(\frac{-h_m x_H}{b u_{m,i}}\right)$$
Δx thickness of node i (m)	
$u_{m,i}$ velocity of mixture (m/s)	
b distance between flow channels and gas diffusion layer	Average limiting current density:
x_H height of gas diffusion layer	$$\bar{i}_L = \frac{nFD_{i,j}C_{H2,i+1}}{\Delta x_i}$$
ϕ is the electrode porosity	
Calculated:	Outlet molar flow:
n_{tot} total molar flow rate of mixture	
x_{H2} mole fraction of hydrogen	$$n_{H2,i+1} = \frac{A_i D_{i,j}(C_{H2,i} - C_{H2,i+1})}{\Delta x_i}$$
x_{H2O} mole fraction of water	
x_{O2} mole fraction of oxygen	
$n_{H2Ov,i}$ molar flow rate of water vapor	Effective diffusion coefficient:
$n_{H2Ol,i}$ molar flow rate of liquid water	$$D_{i,j}^{eff} = D_{i,j}\phi^{3/2}$$
$n_{H2O,i}$ total water molar flow rate	
$n_{H2,i}$ molar flow rate of hydrogen	Total flowrate out of the layer is:
$C_{H2O,i}$ Concentration of water at node i	
$C_{H2,i}$ Concentration of hydrogen at node i	$$n_{tot,i+1} = n_{H2,i+1} + n_{H2O,i+1}$$
$\bar{i}_L$ average limiting current density	The total mole fraction of hydrogen is:
$D_{i,j}^{eff}$ effective diffusion coefficient	$$x_{H2,i+1} = \frac{n_{H2,i+1}}{n_{tot,i+1}}$$
$D_{i,j}$ diffusion coefficient	

Table H.5 *(continued)*

Main Parameters	Equations
Inputs: $P_{sat}(T_{i,f})$ saturation pressure at the gas/fluid temperature at node i (Pa) $P_{tot,i}$ Total pressure at node i (Pa) *Calculated:* n_{tot} total molar flow rate of mixture x_{H2O} mole fraction of water $n_{H2Ov,i}$ molar flow rate of water vapor $n_{H2O,i}$ total water molar flow rate RH Relative humidity RW Relative water content $C_{H2O,i}$ Concentration of water at node i $T_{i,f}$ temperature of gas/liquid mixture at node i (K)	The total mole fraction of water is: $$x_{H2O,i+1} = \frac{n_{H2O,i+1}}{n_{tot,i+1}}$$ Outlet concentration of water: $$C_{H2O,i+1} = x_{H2O,i+1}\left(\frac{P_{tot,i}}{RT_{i,f}}\right)$$ Relative humidity: $$RH = \frac{n_{H2Ov,i+1}}{n_{tot,i+1}}\frac{P_{tot,i}}{P_{sat}(T_{i,f})}$$ Relative water content: $$RW = \frac{n_{H2O,i+1}}{n_{tot,i+1}}\frac{P_{tot,i}}{P_{sat}(T_{i,f})}$$

Appendix I Pressure Drop Analysis

Table I.1

Pressure drop calculations for the end plate, terminal and gasket layers

Main Parameters	Equations
Inputs: υ_{in} inlet volumetric flow rate (m³/s) A_{ch} cross-sectional area of the channel (m²) f is the friction factor ρ fluid density (kg/m³) $\bar{v}$ average velocity (m/s) K_L local resistance P_{cs} perimeter d_c channel depth (m) w_c channel width (m) N_{ch} number of parallel channels ρ density (kg/m³) $P_{tot,i}$ total pressure at node i (Pa) *Calculated:* v_i velocity (m/s) n_{tot} total molar flow rate of mixture ΔP_{i+1} pressure drop L_{chan} channel length (m) D_H hydraulic diameter or characteristic length (m)	The velocity (m/s) in the fuel cell channel near the entrance of the cell is: $$v_i = \frac{\upsilon_{in}}{A_{ch}}$$ Pressure drop: $$\Delta P_{i+1} = f \frac{L_{chan}}{D_H} \rho \frac{\bar{v}^2}{2} + \sum K_L \rho \frac{\bar{v}^2}{2}$$ Hydraulic diameter for a circular flow field: $$D_{H,i} = \frac{4 \times A_{ch}}{P_{cs}}$$ For rectangular channels, the hydraulic diameter is: $$D_{H,i} = \frac{2 w_c d_c}{w_c + d_c}$$

Table I.1 *(continued)*

Main Parameters	Equations
Inputs: D_H hydraulic diameter or characteristic length (m) ρ fluid density (kg/m^3) μ fluid viscosity (kg/(m*s)) v_m characteristic velocity of the flow (m/s) ν kinematic viscosity (m^2/s) *Calculated:* $P_{tot,i}$ total pressure at node i (Pa) Re$_i$ Reynold's number f_i friction factor	The channel length can be defined as: $$L_{chan} = \frac{A_{cell,i}}{N_{ch}(w_c + w_L)}$$ The friction factor can be defined by: $$f_i = \frac{56}{\text{Re}}$$ Reynold's number: $$\text{Re}_i = \frac{\rho v_m D_H}{\mu} = \frac{v_m D_H}{\nu}$$ Pressure at outlet node: $$P_{tot,i+1} = P_{tot,i} - \int_0^x \left[\frac{dP_{tot}}{dx} \right] dx$$

Appendix I (Continued)

Table I.2

Pressure drop calculations for the flow field layers

Main Parameters	Equations
Inputs: υ_{in} inlet volumetric flow rate (m³/s) A_{ch} cross-sectional area of the channel (m²) f_i friction factor ρ fluid density (kg/m³) $\bar{v}$ average velocity (m/s) K_L local resistance P_{cs} perimeter d_c channel depth (m) w_c channel width (m) A_{cell} cell active area (m²) N_{ch} number of parallel channels w_L space between channels (m) ρ density (kg/m³) $P_{tot,i}$ total pressure at node i (Pa) *Calculated:* v_i velocity (m/s) n_{tot} total molar flow rate of mixture ΔP_{i+1} pressure drop L_{chan} channel length (m) D_H hydraulic diameter or characteristic length (m) Re_i Reynold's number f_i friction factor	The velocity (m/s) in the entrance of the flow field layer is: $$v_i = \frac{\left(\dfrac{n_{tot,i} * T_{f,i} * R}{P_{tot,i}}\right)}{N_{ch}}$$ The velocity (m/s) in each fuel cell channel is: $$v_{chan} = \frac{\upsilon_{in}}{A_{ch}} \quad \text{where} \quad A_{ch} = \frac{1}{2}\pi r^2$$ Molar flow rate in each channel: $$n_{tot\_in} = \frac{P_{in}\upsilon_{in}}{RT_{in}}$$ Pressure drop: $$\frac{dP_{tot}}{dx} = f\frac{L_{chan}}{D_H}\rho\frac{\bar{v}^2}{2} + \sum K_L \rho \frac{\bar{v}^2}{2}$$ Hydraulic diameter for a circular flow field: $$D_{H,i} = \frac{4 \times A_c}{P_{cs}}$$

Appendix I (Continued)

Table I.2 *(continued)*

Main Parameters	Equations
Inputs: f_i friction factor ρ fluid density (kg/m^3) $\bar{v}$ average velocity (m/s) K_L local resistance P_{cs} perimeter d_c channel depth (m) w_c channel width (m) A_{cell} cell active area (m^2) N_{ch} number of parallel channels w_L space between channels (m) ρ density (kg/m^3) $P_{tot,i}$ total pressure at node i (Pa) v_m characteristic velocity of the flow (m/s) v kinematic viscosity (m^2/s) *Calculated:* v_i velocity (m/s) n_{tot} total molar flow rate of mixture ΔP_{i+1} pressure drop L_{chan} channel length (m) D_H hydraulic diameter or characteristic length (m)	For rectangular channels, the hydraulic diameter is: $$D_{H,i} = \frac{2 w_c d_c}{w_c + d_c}$$ The channel length can be defined as: $$L_{chan} = \frac{A_{cell,i}}{N_{ch}(w_c + w_L)}$$ The friction factor can be defined by: $$f_i = \frac{56}{\mathrm{Re}}$$ Reynold's number: $$\mathrm{Re}_i = \frac{\rho v_m D_{ch}}{\mu} = \frac{v_m D_{ch}}{v}$$ Pressure at outlet node: $$P_{tot,i+1} = P_{tot,i} - \int_0^x \left[\frac{dP_{tot}}{dx} \right] dx$$

Appendix I (Continued)

Table I.3

Pressure drop calculations for the gas diffusion layers

Main Parameters	Equations
Inputs: μ viscosity (Pa-s) v volumetric flow rate (m³/s) k permeability (m²) A cross-sectional area (m²) ε void fraction Δx thickness of node i (m) k permeability (m²) μ viscosity (Pa-s) Δx thickness of node i (m) $\Delta P_{tot,i}$ change in total pressure (Pa) *Calculated:* $\Delta P_{tot,i}$ change in total pressure (Pa) $u_{m,i}$ velocity of mixture (m/s)	Pressure drop: $$\Delta P_{tot,i} = \frac{\mu_i v_i}{k_i A \varepsilon} \Delta x$$ Volumetric flow rate: $$v_i = \frac{n_{tot,i} * T_{f,i} * R}{P_{tot,i}}$$ Velocity of the mixture in the membrane: $$u_{m,i} = \frac{k_i}{\mu_i \Delta x} \Delta P_{tot,i}$$

Appendix I (Continued)

Table I.4

Pressure drop calculations for the catalyst layers

Main Parameters	Equations
Inputs: μ viscosity (Pa-s) v volumetric flow rate (m^3/s) k permeability (m^2) A cross-sectional area (m^2) ε void fraction Δx thickness of node i (m) k permeability (m^2) μ viscosity (Pa-s) Δx thickness of node i (m) $\Delta P_{tot,i}$ change in total pressure (Pa) *Calculated:* $\Delta P_{tot,i}$ change in total pressure (Pa) $u_{m,i}$ velocity of mixture (m/s)	Pressure drop: $$\Delta P_{tot,i} = \frac{\mu_i v_i}{k_i A \varepsilon} \Delta x$$ Volumetric flow rate: $$v_i = \frac{n_{tot,i} * T_{f,i} * R}{P_{tot,i}}$$ Velocity of the mixture in the membrane: $$u_{m,i} = \frac{k_i}{\mu_i \Delta x} \Delta P_{tot,i}$$

Appendix J Polymer Membrane Layer

Table J.1

Polymer electrolyte membrane layer mass balance equations

Main Parameters	Equations
Inputs:	Convert volumetric flow rate to molar flow rate:
n_{tot_in} inlet molar flow rate (mol/s)	
P_{in} inlet pressure (Pa)	$$n_{tot\_in} = \frac{P_{in}\upsilon_{in}}{RT_{in}}$$
υ_{in} inlet volumetric flow rate (m³/s)	
T_{in} inlet temperature (K)	Total molar accumulation:
R ideal gas constant (m³-Pa/K-mol)	
$P_{sat}(T_{i,f})$ saturation pressure at the gas/fluid temperature at node i (Pa)	$$\frac{dn_{tot}}{dt} = n_{tot,i} - n_{tot,i+1}$$
Calculated:	The rate of H_2 accumulation is:
n_{tot} total molar flow rate of mixture	
$n_{H2O,i}$ total water molar flow rate	$$\frac{d}{dt}(x_{H2}n_{tot}) = x_{H2,i}n_{tot,i} - x_{H2,i+1}n_{tot,i+1}$$
$n_{H2,i}$ molar flow rate of hydrogen	
x_{H2} mole fraction of hydrogen	The rate of H_2O accumulation is:
x_{H2O} mole fraction of water	
x_{O2} mole fraction of oxygen	$$\frac{d}{dt}(x_{H2O}n_{tot}) = x_{H2O,i}n_{tot,i} - x_{H2O,i+1}n_{tot,i+1}$$
	The rate of O_2 accumulation is:
	$$\frac{d}{dt}(x_{O2}n_{tot}) = x_{O2,i}n_{tot,i} - x_{O2,i+1}n_{tot,i+1}$$

Appendix J (Continued)

Table J.2

Calculation of mole fractions and molar flow rates for the PEM layer

Main Parameters	Equations
Inputs: $P_{sat}(T_{i,f})$ saturation pressure at the gas/fluid temperature at node i (Pa) ϕ_{in} inlet humidity of the gas stream M_{H2O} molecular weight of water (kg/mol) M_{H2} molecular weight of hydrogen (kg/mol) $P_{tot,i}$ total pressure at node i (Pa) d_c channel depth (m) w_c channel width (m) k_c evaporation and condensation rate constant (s^{-1}) *Calculated:* n_{tot} total molar flow rate of mixture x_{H2} mole fraction of hydrogen x_{H2O} mole fraction of water x_{O2} mole fraction of oxygen $p_{H2O,i}$ vapor pressure of the inlet water vapor H is the humidity $n_{H2Ov,i}$ molar flow rate of water vapor $n_{H2Ol,i}$ molar flow rate of liquid water $n_{H2O,i}$ total water molar flow rate	Calculate the vapor pressure of the inlet water vapor: $$p_{H2O,i} = \phi_{in} P_{sat}(T_{i,f})$$ Calculate humidity: $$H = \frac{M_{H2O}\, p_{H2O,i}}{M_{H2}(P_{tot,i} - p_{H2O,i})}$$ The mole fraction of the water vapor is: $$x_{H2Ov,i} = \frac{\dfrac{H}{M_{H2O}}}{\dfrac{1}{M_{H2}} + \dfrac{H}{M_{H2O}}}$$ The molar flow rate of water vapor is: $$n_{H2Ov,i} = x_{H2Ov,i} n_{tot,i}$$ The molar flow rate for water condensation and evaporation is: $$n_{H2Ol,i+1} = \left(\frac{k_c w_c d_c}{RT_{i,f}}\right)\frac{n_{H2Ov,i+1}}{n_{tot,i+1}}\left(P_{tot,i} - P_{sat}(T_{i,f})\right)$$ The total molar flow rate of water is: $$n_{H2O,i} = n_{H2Ov,i} + n_{H2Ol,i}$$

Table J.2 *(continued)*

Main Parameters	Equations
Inputs: $P_{sat}(T_{i,f})$ saturation pressure at the gas/fluid temperature at node I (Pa) $P_{tot,i}$ Total pressure at node I (Pa) *Calculated:* n_{tot} total molar flow rate of mixture x_{H2} mole fraction of hydrogen x_{H2O} mole fraction of water $n_{H2Ov,i}$ molar flow rate of water vapor $n_{H2Ol,i}$ molar flow rate of liquid water $n_{H2O,i}$ total water molar flow rate $n_{H2,i}$ molar flow rate of hydrogen RH Relative humidity RW Relative water content	The total molar flow rate of water is: $$n_{H2O,i} = n_{H2Ov,i} + n_{H2Ol,i}$$ The total mole fraction of water is: $$x_{H2O,i} = \frac{n_{H2O,i}}{n_{tot,i}}$$ The mole fraction of hydrogen is: $$x_{H2,i} = 1 - x_{H2O,i}$$ The molar flow rate of hydrogen is: $$n_{H2,i} = x_{H2,i} n_{tot,i}$$ Total flowrate out of the layer is: $$n_{tot,i+1} = n_{H2,i+1} + n_{H2O,i+1}$$ Relative humidity: $$RH = \frac{n_{H2Ov,i+1}}{n_{tot,i+1}} \frac{P_{tot,i}}{P_{sat}(T_{i,f})}$$ Relative water content: $$RW = \frac{n_{H2O,i+1}}{n_{tot,i+1}} \frac{P_{tot,i}}{P_{sat}(T_{i,f})}$$

Appendix J (Continued)

Table J.3

Diffusive flux and potential relations for the PEM layer

Main Parameters	Equations

Inputs:

a_w water activity

R ideal gas constant (m^3-Pa/K-mol)

$P_{sat}(T_{i,f})$ saturation pressure at the gas/fluid temperature at node i (Pa)

$P_{tot,i}$ Total pressure at node i (Pa)

$C_{H2O,i}$ Concentration of water at node i

ρ_{dry}^m dry membrane density (kg/m^3)

M^m membrane molecular mass (kg/mol)

$c_1 - c_5$ constants for the activity of water molecules

Calculated:

n_{tot} total molar flow rate of mixture

x_{H2} mole fraction of hydrogen

x_{H2O} mole fraction of water

x_{O2} mole fraction of oxygen

λ water uptake

σ ionic conductivity

$\dfrac{\partial \Phi_m}{\partial x}$ proton potential

Calculate water uptake:

$$\lambda(a_w, T_{f,i}) = \begin{cases} 0.043 + 17.8 a_w - 39.85(a_w)^2 + 36(a_w)^3 & \text{at } = 303\,\text{K} \\ 0.3 + 10.8 a_w - 16(a_w)^2 + 14.1(a_w)^3 & \text{at } = 353\,\text{K} \end{cases}$$

$$\lambda(a_w, T_{f,i}) = \lambda(a_w, 303) + (\lambda(a_w, 353) - \lambda(a_w, 303))\left(\frac{T_{f,i} - 303}{50}\right)$$

Calculate ionic conductivity:

$$\sigma = (0.005139\lambda - 0.00326)\exp\left[1268\left(\frac{1}{303} - \frac{1}{T}\right)\right]$$

Proton potential:

$$\frac{\partial \Phi_m}{\partial x} = -\frac{i}{\sigma_m} + \frac{F}{\sigma_m}c_{H+}u^m$$

Diffusion coefficient:

$$D_{cH_2O,i} = D' e^{2416\left(\frac{1}{303} - \frac{1}{T}\right)} \frac{\lambda_{H_2O/SO_3}}{a(17.81 - 78.9a + 108a^2)}$$

$$D = \begin{cases} 2.642276\times10^{-13}\lambda_{H_2O/SO_3} & \lambda_{H_2O/SO_3} \leq 1.23 \\ 7.75\times10^{-11}\lambda_{H_2O/SO_3} - 9.5\times10^{-11} & 1.23 < \lambda_{H_2O/SO_3} \leq 6 \\ 2.5625\times10^{-11}\lambda_{H_2O/SO_3} - 2.1625\times10^{-10} & 6 < \lambda_{H_2O/SO_3} \leq 14 \end{cases}$$

Appendix J (Continued)

Table J.4

Pressure, velocity and diffusive flux equations for the PEM layer

Main Parameters	Equations
Inputs: $D_{cH_2O,i}$ diffusion coefficient D_{H+} proton diffusion coefficient $c^m_{H_2O}$ water concentration c_{H+} proton concentration Φ_m potential F Faraday's constant R ideal gas constant k permeability (m^2) μ viscosity (Pa-s) Δx thickness of node i (m) $\Delta P_{tot,i}$ change in total pressure (Pa) $P_{tot,i}$ total pressure at node i (Pa) *Calculated:* $J^M_{H_2O}$ diffusive molar flux for water J_{H+} diffusive molar flux for protons $u_{m,i}$ velocity of mixture (m/s) $P_{tot,i+1}$ pressure at outlet node (Pa)	Diffusive molar flux for water: $$J^M_{H_2O} = -D_{cH_2O,T}\frac{\partial c^m_{H_2O}}{\partial x} + n_{drag}\frac{i_x}{F}$$ Diffusive molar flux for protons: $$J_{H+} = -\frac{F}{RT}D_{H+}c_{H+}\frac{\partial \Phi_m}{\partial x}$$ Velocity of the mixture in the membrane: $$u_{m,i} = \frac{k_i}{\mu_i \Delta x}\Delta P_{tot,i}$$ Pressure at node i: $$P_{tot,i} = \frac{P_{tot,i+1} - P_{tot,i-1}}{\Delta x_i}$$ Pressure at outlet node: $$P_{tot,i+1} = P_{tot,i} - \int_0^x\left[\frac{dP_{tot}}{dx}\right]dx$$

Appendix J (Continued)

Table J.5

Gas permeation equations for the PEM layer

Main Parameters	Equations
Inputs: $T_{i,f}$ temperature of gas/liquid mixture at node i (K) *Calculated:* P_m permeability S_{O2} oxygen solubility D_{H2} hydrogen diffusivity (cm^2 s^{-1}) D_{O2} oxygen diffusivity (cm^2 s^{-1}) $n_{O2,i}$ oxygen molar flow rate (mol/s) $n_{H2,i}$ hydrogen molar flow rate (mol/s)	Permeability: $$P_m = D \times S$$ Oxygen solubility $$S_{O2} = 7.43 \times 10^{-12} \exp\left(\frac{666}{T_{f,i}}\right)$$ Oxygen diffusivity: $$D_{O2} = 0.0031 \exp\left(-\frac{2768}{T_{f,i}}\right)$$ Hydrogen diffusivity: $$D_{H2} = 0.0041 \exp\left(-\frac{2602}{T_{f,i}}\right)$$ Hydrogen molar flow rate: $$n_{H2,i} = \frac{P_{H2} A_i P_{tot,i}}{\Delta x_i}$$ Oxygen molar flow rate: $$n_{O2,i} = \frac{P_{O2} A_i P_{tot,i}}{\Delta x_i}$$

Appendix K Parameters for 16 cm2 Fuel Cell Stack

Table K.1

Material properties used for the anode layers of the 16 cm^2 fuel cell stack

Fuel Cell Layer	Material	Thickness (m)	Area (m^2)	Area of void (m^2)	Density (kg/m^2)	Thermal Conductivity (W/m-K)	Specific heat capacity (J/kg-K)	Specific Resistance (ohm-m)
End plate	Polycarbonate	0.01	0.0064	0	1300	0.2	1200	0
Gasket	Black Conductive Rubber	0.001	0.001704	0	1400	1.26	1000	0
Flow field plate	SS	0.0005	0.003385	0.0016925	8000	16	500	7.2e-7
Diffusion media	Carbon Cloth	0.0004	0.0016	0.00128	2000	65	840	0.000014
Catalyst	Pt/C	0.000065	0.0016	0.00112	387	0.2	770	0.000014
Membrane	Nafion	0.00005	0.0016	0	1740	0.21	1100	0.1

Table K.2

Material properties used for the cathode layers of the 16 cm^2 fuel cell stack

Fuel Cell Layer	Material	Thickness (m)	Area (m^2)	Area of void (m^2)	Density (kg/m^2)	Thermal Conductivity (W/m-K)	Specific heat capacity (J/kg-K)	Specific Resistance (ohm-m)
Catalyst	Pt/C	0.000065	0.0016	0.00112	387	0.2	770	0.000014
Diffusion media	Carbon Cloth	0.0004	0.0016	0.00128	2000	65	840	0.000014
Flow field plate	SS	0.0005	0.003385	0.0016925	8000	16	500	7.2e-7
Gasket	Black Conductive Rubber	0.001	0.001704	0	1400	1.26	1000	0
End plate	Polycarbonate	0.01	0.0064	0	1300	0.2	1200	0
Hydrogen	-	-	-	-	0.090	0.165	14,160	-
Air	-	-	-	-	1.30	0.0223	1005	-

Appendix L Typical Outputs for Each Fuel Cell Layer

Table L.1

Typical outputs of the anode end plate, terminal and cooling channel layer after 30 sec

Fuel cell layer	Inlet	Outlet
Left end plate	Flow rate: 0.1628 mol/s	Flow rate: 0.1628 mol/s
	Pressure: 344,737.864 Pa	Pressure: 344,737.864 Pa
	Velocity: 3.6079 m/s	Velocity: 3.6079 m/s
	Temperature: 313 K	Temperature: 313 K
Terminal/gasket layers	Flow rate: 0.1628 mol/s	Flow rate: 0.1628 mol/s
	Pressure: 344,737.864 Pa	Pressure: 344,734.864 Pa
	Velocity: 3.6079 m/s	Velocity: 0.6882 m/s
Cooling channel layer	Flow rate: 0.0779 mol/s	Flow rate: 0.0779 mol/s
	Pressure: 202,650.02 Pa	Pressure: 70,100 Pa
	Velocity: 1.9808 m/s	Velocity: 1.9808 m/s
	Temperature: 326.5 K	Temperature: 326.5 K

Appendix L (Continued)

Table L.2

Typical outputs of the anode flow field and GDL layers after 30 sec

Fuel cell layer	Inlet	Outlet
Anode Flow Field	*In each inlet*	*In each outlet*
	Flow rate: 0.0203 mol/s	Flow rate: 0.0203 mol/s
	Pressure: 344,737.864 Pa	Pressure: 344,737.864 Pa
	Velocity: 0.0032 m/s	Velocity: 0.0032 m/s
	In each of the channels	*Going to GDL layer*
	Flow rate: 0.0051 mol/s	Flow rate: 0.0021 mol/s
	Pressure: 344,080 Pa	Pressure: 240,720 Pa
	Velocity: 113.34 m/s	Velocity: 0.0083 m/s
	Pressure at the end of the flow channels (due to pressure drop): 240,720 Pa	Temperature: 331 K
	Temperature: 331 K	
Anode GDL	Flow rate: 0.0021 mol/s	Flow rate: 0.0021 mol/s
	Pressure: 240,720 Pa	Pressure: 239,630 Pa
	Velocity: 0.0083 m/s	Velocity: 0.3492 m/s
	Temperature: 331 K	Temperature: 331 K

Table L.3

Typical outputs of the anode catalyst and membrane layers after 30 sec

Fuel cell layer	Inlet	Outlet
Anode Catalyst	Flow rate: 0.0021 mol/s	Flow rate: 0.0010 mol/s
	Pressure: 239,630 Pa	Pressure: 225,880 Pa
	Velocity: 0.3492 m/s	Velocity: 0.5741 m/s
	Temperature: 331 K	Temperature: 331 K
Membrane (Nafion 115)	*Total hydrogen flow rate into membrane due to permeability*	*Total flow rate in anode catalyst layer*
		Flow rate: 0.0021 mol/s
	Flow rate: 9.7707e-007 mol/s	
	Total oxygen flow rate into membrane due to permeability	*Total flow rate in cathode catalyst layer*
		Flow rate: 0.0015 mol/s
	Flow rate: 1.1293e-007 mol/s	
	Temperature: 331 K	
	Pressure: 14,930 Pa	

Appendix L (Continued)

Table L.4

Typical outputs of the cathode catalyst and GDL layers after 30 sec

Fuel cell layer	Inlet	Outlet
Cathode Catalyst	Flow rate: 0.0021 mol/s	Flow rate: 0.0015 mol/s
	Pressure: 265,750 Pa	Pressure: 226,450 Pa
	Velocity: 0.4458 m/s	Velocity: 0.5194 m/s
	Temperature: 331 K	Temperature: 331 K
Cathode GDL	Flow rate: 0.0021 mol/s	Flow rate: 0.0021 mol/s
	Pressure: 270,890 Pa	Pressure: 265,750 Pa
	Velocity: 0.0026 m/s	Velocity: 0.4458 m/s
	Temperature: 331 K	Temperature: 331 K

Appendix L (Continued)

Table L.5

Typical outputs of the cathode flow field layer after 30 sec

Inlet	Outlet
In each inlet	*In each outlet*
Flow rate: 0.0145 mol/s	Flow rate: 0.0145 mol/s
Pressure: 344,737.864 Pa	Pressure: 344,737.864 Pa
Velocity: 0.0023 m/s	Velocity: 0.0023 m/s
In each of the channels	*Going to GDL layer*
Flow rate: 0.0036 mol/s	Flow rate: 0.00094 mol/s
Pressure: 344,400 Pa	Pressure: 270,890 Pa
Velocity: 80.97 m/s	Velocity: 0.0026 m/s
Pressure at the end of the flow channels	
(due to pressure drop): 270,890 Pa	
Temperature: 331 K	

Table L.6

Typical outputs of the cathode end plate, terminal and cooling layers after 30 sec

Fuel cell layer	Inlet	Outlet
Cooling channel layer	Flow rate: 0.0779 mol/s	Flow rate: 0.0779 mol/s
	Pressure: 202,650.02 Pa	Pressure: 70,100 Pa
	Velocity: 1.9808 m/s	Velocity: 1.9808 m/s
	Temperature: 330 K	Temperature: 330 K
Manifold layer	Flow rate: 0.1159 mol/s	Flow rate: 0.1159 mol/s
	Pressure: 344,737.864 Pa	Pressure: 344,734.864 Pa
	Velocity: 2.5687 m/s	Velocity: 0.4900 m/s
	Temperature: 326.5 K	Temperature: 326.5 K
Right end plate	Flow rate: 0.1159 mol/s	Flow rate: 0.1159 mol/s
	Pressure: 344,737.864 Pa	Pressure: 344,737.864 Pa
	Velocity: 2.5687 m/s	Velocity: 2.5687 m/s
	Temperature: 313 K	Temperature: 313 K

ABOUT THE AUTHOR

Colleen S. Spiegel, received a BSChE and MSChE in chemical engineering from the University of South Florida in 2001 and 2003 respectively. She has been an R&D manager, chemical engineer and engineering consultant for a total of eight years, and her expertise is in the areas of design and modeling. Mrs. Spiegel has worked in several areas of research and process development and was instrumental in establishing new ideas for several companies.

Mrs. Spiegel is the author of "Designing and Building Fuel Cells" (McGraw-Hill), and "PEM Fuel Cell Modeling and Simulation with MATLAB" (Elsevier Science). She is the founder of Clean Fuel Cell Energy, LLC, which offers fuel cell components to engineers and scientists globally. She is a member of the American Institute of Chemical Engineers (AICHE), the Institute of Electrical & Electronics Engineers (IEEE) and the National Association of Science Writers (NASW).